

**DOCTORAL THESIS**

# Development of Computational and Statistical Methods for Fluorescence-Based Diffusion Measurements

Hamed Karimi

TALLINN UNIVERSITY OF TECHNOLOGY  
DOCTORAL THESIS  
26/2026

**Development of Computational and  
Statistical Methods for  
Fluorescence-Based Diffusion  
Measurements**

HAMED KARIMI



TALLINN UNIVERSITY OF TECHNOLOGY  
School of Science  
Department of Cybernetics

**The dissertation was accepted for the defence of the degree of Doctor of Philosophy in Applied Physics and Mathematics on 14 April 2026**

**Supervisor:** Professor Marko Vendelin  
Laboratory of Systems Biology  
Tallinn University of Technology  
Tallinn, Estonia

**Co-supervisor:** Assistant Professor Martin Laasmaa  
Laboratory of Systems Biology  
Tallinn University of Technology  
Tallinn, Estonia

**Opponents:** Assistant Professor Falk Schneider  
Fluorescence and Membrane Dynamics (FMD) Lab  
University of Warwick  
Coventry, UK  
  
Dr. Sergei Kopantšuk  
Institute of Chemistry  
University of Tartu  
Tartu, Estonia

**Defence of the thesis:** 12 May 2026, Tallinn

**Declaration:**

*Hereby I declare that this doctoral thesis, my original investigation and achievement, submitted for the doctoral degree at Tallinn University of Technology, has not been submitted for any academic degree elsewhere.*

Hamed Karimi

---

signature



Copyright: Hamed Karimi, 2026  
ISSN 2585-6898 (publication)  
ISBN 978-9916-80-491-9 (publication)  
ISSN 2585-6901 (PDF)  
ISBN 978-9916-80-492-6 (PDF)  
DOI <https://doi.org/10.23658/taltech.26/2026>

Karimi, H. (2026). *Development of Computational and Statistical Methods for Fluorescence-Based Diffusion Measurements* [TalTech Press]. <https://doi.org/10.23658/taltech.26/2026>

TALLINNA TEHNIKAÜLIKOOL  
DOKTORITÖÖ  
26/2026

# **Fluorestsentsipõhiste difusioonimõõtmiste arvutuslike ja statistiliste meetodite väljatöötamine**

HAMED KARIMI



# Contents

List of Publications .....	7
Author's Contributions to the Publications .....	8
Abbreviations.....	9
Introduction .....	10
1 Physical Basis of Molecular Transport in Cells.....	12
1.1 Fundamental Principles of Diffusion .....	12
1.2 Fick's Laws and Brownian Motion .....	12
1.3 Diffusion in Cellular Environments .....	14
2 Fluorescence-Based Diffusion Measurement Techniques .....	16
2.1 Fluorescence Correlation Spectroscopy (FCS) .....	16
2.1.1 Principles and Theory .....	16
2.1.2 Advantages .....	18
2.1.3 Limitations .....	18
2.2 Raster Image Correlation Spectroscopy (RICS).....	18
2.2.1 Principles and Theory .....	18
2.2.2 Advantages .....	19
2.2.3 Limitations .....	19
2.3 Bayesian Approach to Direct Analysis of Fluorescence Intensity Traces .....	20
2.3.1 Principles and Theory .....	20
2.3.2 Bayesian Inference .....	21
2.3.3 Markov Chain Monte Carlo .....	21
2.3.4 Advantages .....	22
2.3.5 Limitations .....	23
2.4 Methodological Challenges and Motivation .....	23
2.4.1 Experimental Artifacts and Data Quality .....	23
2.4.2 Biological Complexity and Non-Ideal Diffusion .....	24
2.4.3 Statistical Modeling Deficiencies .....	24
2.4.4 Correlation-Based Software Limitations.....	24
2.4.5 Beyond Correlation: Direct Intensity Analysis.....	25
Aims of the Thesis .....	26
3 Unified Platform for FCS and RICS Analysis (IOCBIO FCS) .....	27
3.1 Overview .....	27
3.2 Visualizing Raw RICS/FCS Datasets .....	27
3.3 Calculating Autocorrelation Functions .....	27
3.4 Data Filtering and Model-Based Parameter Estimation.....	28
3.5 Results .....	33
4 Fluorescence Intensity Trace Statistical Analysis (FITSA) .....	35
4.1 Overview and Motivation .....	35
4.2 Methodological Framework .....	35
4.3 Practical Advantages and Scope .....	35
4.4 Validation and Results.....	36

5 Discussion .....	37
5.1 Statistical Rigor in Correlation-Based Analysis: Challenges and Solutions ...	37
5.2 Beyond Correlation: Direct Intensity Analysis with FITSA .....	38
5.3 IOCBIO FCS Platform: Addressing Critical Gaps in Correlation Analysis .....	39
5.4 Limitations, and Future Directions .....	40
Conclusions .....	42
References .....	43
Acknowledgements .....	49
Abstract .....	50
Kokkuvõte .....	52
Appendix 1 .....	55
Appendix 2 .....	77
Appendix 3 .....	103
Curriculum Vitae .....	122
Elulookirjeldus .....	124

## List of Publications

The present Ph.D. thesis is based on the following publications that are referred to in the text by Roman numbers.

- I **Hamed Karimi**, Otto Gustavson, Irina Česnokova, Jelena Branovets, Rikke Birkedal, Martin Laasmaa, and Marko Vendelin. A Unified Platform for FCS and RICS Analysis with Advanced Statistical Inference. *ACS Omega*, 2026
- II Robert Risti, Kathryn H. Gunn, Kristofer Hiis-Hommuk, Natjan-Naatan Seeba, **Hamed Karimi**, Ly Villo, Marko Vendelin, Saskia B. Neher, and Aivar Löökene. Combined action of albumin and heparin regulates lipoprotein lipase oligomerization, stability, and ligand interactions. *PLOS ONE*, 18(4):e0283358, 2023
- III **Hamed Karimi**, Martin Laasmaa, Margus Pihlak, and Marko Vendelin. Statistical analysis of fluorescence intensity transients with Bayesian methods. *Science Advances*, 11(16):eads4609, 2025

## Author's Contributions to the Publications

- I The author contributed to the conceptualization and methodological design, assembled the experimental setup, conducted the measurements, and participated in the investigation and data curation. The author developed and applied software tools for analysis, performed the formal data analysis and visualization, drafted the original manuscript, and contributed to subsequent review and editing.
- II The author received the samples, performed RICS measurements, and analysed the resulting data using software tools developed by the author. The contributions included experimental investigation, diffusion analysis, extraction of diffusion coefficients, and interpretation of the results.
- III The author contributed to the conceptualization and methodology of the study together with other co-authors and initiated the project by testing an existing Matlab-based software developed by another research group, identifying its limitations, which motivated the development of a new Python-based framework. The author developed the initial version of the Python software and contributed to the development and validation of the simulation and analysis software as part of a team effort. The author carried out formal analysis jointly with collaborators, curated and prepared the data, and contributed to the generation of visualizations. The author contributed to performing experiments in cardiomyocytes and preparing the experimental solutions. The author also contributed to the manuscript through review and editing.

## Abbreviations

ACF	Autocorrelation Function
DC	Diffusion Coefficient
DL	Deep Learning
FCF	Fluorescence Correlation Spectroscopy
FITSA	Fluorescence Intensity Trace Statistical Analysis
GLS	Generalized Least Squares
HMC	Hamiltonian Monte Carlo
MCMC	Markov Chain Monte Carlo
ML	Machine Learning
MSD	Mean Square Displacement
NLS	Nonlinear Least Squares
NUTS	No-U-Turn Sampler
OLS	Ordinary Least Squares
PSF	Point Spread Function
RICS	Raster Image Correlation Spectroscopy
SSR	Sum of Squared Residuals
TSA	Triplet-State Amplitude
WLS	Weighted Least Squares
2D	Two-Dimensional
3D	Three-Dimensional
$\Delta x$	Pixel Shift
$\hat{R}$	Potential Scale Reduction Factor
$\tau$	Lag Time
$\tau_T$	Triplet-State Relaxation Time

## Introduction

Cardiomyocytes, the contractile cells of the heart, rely on a precise spatial and temporal organization of molecular processes to maintain normal cardiac function [4, 5]. These cells exhibit a highly structured intracellular architecture, characterized by ordered sarcomeres, an extensive sarcoplasmic reticulum, and densely packed mitochondria [5, 6]. Together, these structures support coordinated calcium handling, energy production, and force generation required for periodic contraction [4, 5, 7]. This pronounced structural organization leads to intracellular compartmentalization, where biochemical reactions and molecular transport are spatially restricted rather than uniformly distributed throughout the cytosol [8, 9]. Compartmentalization in cardiomyocytes arises from both physical barriers, such as myofilaments and membrane-bound organelles, and functional organization, including localized enzyme systems and metabolite channeling [10–12]. Several studies have shown that this compartmentalization plays an important role in regulating energy transfer pathways, such as creatine kinase and adenylate kinase systems, thereby contributing to efficient excitation–contraction coupling and metabolic homeostasis [4, 5, 8, 9, 11–14].

Within this complex and crowded intracellular environment, the diffusion of proteins, metabolites, and signaling molecules is not isotropic or uniform [15, 16]. Instead, molecular diffusion can be direction-dependent and spatially heterogeneous, reflecting the underlying cellular architecture. Experimental studies using fluorescence correlation-based techniques have demonstrated anisotropic diffusion of metabolites such as ATP in cardiomyocytes, with diffusion properties differing along and across the myofibrillar axis [15, 16]. Such findings highlight the close relationship between intracellular structure, diffusion dynamics, and functional compartmentalization [9, 14].

Alterations in cellular architecture, compartmentalization, or molecular mobility may therefore influence key physiological processes, including excitation–contraction coupling, metabolic substrate delivery, and intracellular signaling [8, 17, 18]. Whether disrupted diffusion dynamics contribute to cardiac pathologies remains an open question, though changes in intracellular organization and molecular transport have been proposed as potential mechanisms in conditions such as heart failure and arrhythmias [5]. Understanding molecular diffusion in cardiomyocytes is therefore essential not only for clarifying fundamental aspects of cardiac physiology but also for informing the development of therapeutic strategies that may target subcellular transport mechanisms [9].

When approximating a cardiomyocyte as a cylindrical geometry—reflecting its elongated morphology with typical dimensions of 100–150  $\mu\text{m}$  in length and 10–25  $\mu\text{m}$  in diameter [19, 20]—the measurement of diffusion coefficients presents both conceptual and technical challenges [15]. Molecular diffusion within different compartments of this cellular cylinder, including the cytosol, specific organelles, and membrane-proximal regions, may exhibit distinct characteristics due to local viscosity variations, molecular crowding effects, and interactions with the organized cytoskeletal network [21–23].

Fluorescence correlation spectroscopy (FCS) has emerged as a powerful technique for measuring diffusion coefficients by analyzing temporal fluorescence intensity fluctuations in a small observation volume, typically created by a focused laser beam in a confocal microscope [24–26]. Raster image correlation spectroscopy (RICS) extends this approach by performing spatial and temporal correlation analysis on image series acquired during laser scanning, enabling mapping of diffusion parameters across cellular regions [27–29]. Both techniques provide single-molecule sensitivity and can characterize diffusion in live cells [30, 31].

This thesis presents computational and statistical advances in fluorescence-based diffusion measurements through three interconnected studies. Paper I introduces IOCBIO FCS,

a unified open-source platform integrating FCS and RICS analysis with GPU-accelerated computation, Bayesian inference, and experimentally measured point spread functions. Paper II applies this platform to investigate lipoprotein lipase oligomerization, where I contributed by performing RICS analysis to determine diffusion coefficients in heterogeneous samples. Paper III presents fluorescence intensity trace statistical analysis (FITSA), a Bayesian method that analyzes fluorescence intensity traces directly, achieving comparable precision to FCS with substantially fewer photons.

The thesis is organized as follows. Chapter 1 establishes the theoretical foundation by presenting fundamental principles of diffusion, introducing key equations governing molecular transport, and examining diffusion processes in cellular environments with emphasis on the constraints imposed by biological complexity. Chapter 2 provides a review of fluorescence-based diffusion measurement techniques, the theoretical basis and practical implementation of FCS and RICS, presenting the Bayesian approach to direct analysis of fluorescence intensity traces, critically examining limitations of these methods, and defining the specific aims addressed by the present work. Chapter 3 describes the unified FCS/RICS analysis platform, emphasizing implementation of advanced statistical methods and key innovations that extend the capabilities of conventional analysis tools. Chapter 4 presents FITSA, outlining the conceptual framework for direct intensity trace analysis, the Bayesian statistical approach, and comparative advantages over autocorrelation-based methods. Chapter 5 presents the discussion of this thesis, summarizing its main contributions, placing them in the context of quantitative fluorescence microscopy, and highlighting their relevance for reducing phototoxicity and improving diffusion measurements.

# 1 Physical Basis of Molecular Transport in Cells

Diffusion is a fundamental physical process underlying molecular transport in biological systems [32]. In cellular environments, diffusion governs the movement of metabolites, proteins, and signaling molecules and therefore plays a central role in cellular function [21, 22]. The focus of this thesis is on the development of experimental and computational techniques for estimating diffusion parameters from fluorescence measurements, motivated by the challenges of characterizing molecular transport in complex cellular environments.

To establish a rigorous foundation for these later applications, this chapter first introduces diffusion from a physical and statistical mechanics perspective. Classical descriptions of diffusion are presented to clarify the assumptions, parameters, and limitations inherent in standard diffusion models. These concepts are subsequently extended and revisited in the context of intracellular environments, where structural organization, molecular crowding, and compartmentalization lead to deviations from idealized diffusion behavior. This physical framework provides the basis for the diffusion models and data analysis approaches developed and applied in the following chapters.

## 1.1 Fundamental Principles of Diffusion

Diffusion is the spontaneous net movement of particles from regions of higher concentration to regions of lower concentration, driven by the random thermal motion of molecules [33]. This fundamental transport phenomenon arises from the statistical behavior of large ensembles of particles, each possessing kinetic energy proportional to the absolute temperature of the system. At the molecular level, particles undergo continuous collisions with surrounding molecules, resulting in random directional changes that, when averaged over many particles and sufficient time, produce macroscopic concentration gradients that dissipate, driving the system toward a state of dynamic equilibrium according to predictable laws, such as Fick's laws of diffusion. The thermodynamic basis of diffusion lies in the second law of thermodynamics, which dictates that isolated systems evolve toward states of maximum entropy—for a concentration gradient, this corresponds to uniform distribution of particles throughout the available volume [32, 33].

The driving force for diffusion can be expressed in terms of the chemical potential gradient. In this case, particles move from regions of high chemical potential to low chemical potential, and under near-equilibrium conditions, the flux is proportional to this gradient [33].

The diffusion coefficient ( $DC$ ), a fundamental parameter characterizing the rate of diffusive transport, depends on both the intrinsic properties of the diffusing species, such as molecular size and shape, and the properties of the medium, including viscosity, temperature, and molecular crowding effects [32, 33]. The Einstein relation connects the diffusion coefficient to the molecular mobility and thermal energy through  $DC = \mu k_B T$ , where  $\mu$  is the mobility,  $k_B$  is Boltzmann's constant, and  $T$  is the absolute temperature, establishing a direct link between microscopic thermal fluctuations and macroscopic transport properties.

## 1.2 Fick's Laws and Brownian Motion

The mathematical description of diffusion is provided by Fick's laws, which relate concentration gradients to particle flux [34]. Fick's first law states that the flux  $\mathbf{J}$  (number of particles crossing a unit area per unit time) is proportional to the negative concentration

gradient:

$$\mathbf{J} = -DC \nabla c(\mathbf{r}, t) \quad (1)$$

where  $DC$  is the diffusion coefficient,  $c(\mathbf{r}, t)$  is the concentration at position  $\mathbf{r}$  and time  $t$ , and the negative sign indicates that flux occurs in the direction of decreasing concentration.

Fick's second law describes the time evolution of concentration distributions by combining the first law with the continuity equation (conservation of mass) [34]:

$$\frac{\partial c(\mathbf{r}, t)}{\partial t} = DC \nabla^2 c(\mathbf{r}, t) \quad (2)$$

This partial differential equation governs diffusion dynamics. In an unbounded domain, its fundamental solution (Green's function) is known analytically and generates solutions for arbitrary initial conditions [33]. For instance, the solution for an initial point source of  $N$  particles at the origin in an unbounded three-dimensional (3D) medium is the Gaussian distribution [32–34]:

$$c(\mathbf{r}, t) = \frac{N}{(4\pi DC t)^{3/2}} \exp\left(-\frac{r^2}{4DC t}\right) \quad (3)$$

which demonstrates that the concentration profile broadens as  $\sqrt{DC t}$  and the peak concentration decreases as  $t^{-3/2}$ . In an unbounded domain, Eq. 3 is the Green's function of the diffusion equation. Therefore, the solution for any initial concentration distribution  $c(\mathbf{r}, t = 0)$  can be obtained by convolution with this Gaussian kernel [32, 33].

The microscopic foundation of diffusion is provided by the theory of Brownian motion, which describes the random trajectories of individual particles subjected to thermal fluctuations. A stochastic description of particle motion based on the Langevin equation leads, upon ensemble averaging over noise realizations, to the Fokker–Planck equation for the probability density [35, 36]. For free diffusion, the corresponding Fokker–Planck equation reduces to Fick's second law, establishing the formal equivalence between microscopic stochastic dynamics and macroscopic diffusion. Einstein's seminal work on Brownian motion established that a particle undergoing random collisions with solvent molecules executes a random walk, with the mean square displacement (MSD) growing linearly with time [34]:

$$MSD = \langle (\mathbf{r}(t) - \mathbf{r}(0))^2 \rangle = 2 d DC t \quad (4)$$

where  $d$  is the spatial dimensionality (e.g.,  $d = 3$  for 3D diffusion,  $d = 2$  for diffusion confined to a plane). This relationship directly connects the macroscopic diffusion coefficient to microscopic particle trajectories and forms the basis for single-particle tracking experiments. For spherical particles of radius  $a$  diffusing in a medium of viscosity  $\eta$ , the Stokes–Einstein relation relates the diffusion coefficient to these physical parameters [32, 33]:

$$DC = \frac{k_B T}{6\pi\eta a} \quad (5)$$

demonstrating that diffusion is enhanced at higher temperatures and reduced viscosities, and that larger particles diffuse more slowly.

The random walk model reveals essential features of diffusive motion: in the continuous Brownian limit trajectories are non-differentiable (infinitely jagged at all scales), displacements over non-overlapping time intervals are statistically independent, and displacements are Gaussian distributed; for discrete random walks this Gaussian form emerges after many steps via the central limit theorem [32].

Deviations from this idealized behavior, termed anomalous diffusion, occur when  $\langle r^2(t) \rangle \propto t^\alpha$  with  $\alpha \neq 1$ , and are commonly observed in complex biological environments due to molecular crowding, binding interactions, and active transport processes [21, 22]. It should be noted that the anomalous exponent  $\alpha$  serves here as a phenomenological descriptor of deviation from normal diffusion and does not uniquely identify the underlying stochastic transport mechanism.

### 1.3 Diffusion in Cellular Environments

Diffusion in living cells deviates substantially from the idealized conditions assumed in classical diffusion theory due to the highly organized, crowded, and compartmentalized nature of the intracellular environment [32]. The cytoplasm contains macromolecular concentrations reaching 300–400 g/L, creating a crowded milieu [23]. This molecular crowding means that large macromolecules block accessible pathways, reducing the free space available for diffusion and increasing the effective viscosity experienced by diffusing molecules. This macromolecular crowding typically reduces diffusion coefficients by factors of 2–10 compared to dilute aqueous solutions, with the magnitude of reduction depending on the size of the diffusing species relative to the crowding agents [22].

Furthermore, the cytoskeleton—comprising actin filaments, microtubules, and intermediate filaments—creates a dynamic meshwork that can obstruct diffusion, create barriers to free motion, and in some cases facilitate directed transport through motor protein activity [21]. Membrane-bounded organelles partition the cell into distinct compartments with different physical and chemical properties, and molecules must traverse these membranes, either by passive diffusion through lipid bilayers or via protein channels and transporters, to access different cellular regions [19, 20]. Many cellular proteins exhibit transient binding to structural elements or other molecules, leading to anomalous subdiffusion characterized by MSDs that grow more slowly than linearly with time [22].

These physical barriers to diffusion—macromolecular crowding, cytoskeletal obstruction, membrane-bounded organelles, and transient binding—do not merely slow molecular motion; they also create functional spatial organization within cells [21]. When diffusion is sufficiently restricted, it can limit the rate at which substrates reach enzymes or the distance over which signaling molecules can effectively communicate, thereby creating distinct functional microdomains even in the absence of physical membrane barriers [8, 37]. This diffusion-mediated compartmentalization has been proposed as a key mechanism for controlling intracellular energy transfer pathways and maintaining signaling specificity, particularly in highly structured cells such as cardiomyocytes [9, 38].

In cardiomyocytes specifically, diffusion processes are linked to the specialized function of these cells in cardiac contraction [5]. The highly ordered sarcomeric structure creates a periodic obstruction pattern that can anisotropically affect diffusion—molecules may diffuse more readily parallel to the long axis of the sarcomeres than perpendicular to it [16, 38]. The extensive sarcoplasmic reticulum network, which occupies a substantial fraction of cellular volume and is responsible for calcium storage and release during excitation-contraction coupling, creates a complex 3D network through which metabolites and signaling molecules must navigate [6, 14]. Mitochondria, occupying approximately 40% of cardiomyocyte volume and arranged in regular arrays between sarcomeres, further restrict diffusion pathways [6].

From the perspective of intracellular regulation, these structural constraints imply that diffusion can directly influence the efficiency and robustness of excitation-contraction coupling and energy supply-demand matching [4, 38]. A central question addressed by our laboratory is how diffusion limitations and compartmentalization shape the interaction

between ATP-producing and ATP-consuming processes, and how these interactions adapt to changing physiological conditions [9, 10].

Electrostatic interactions introduce additional complexity to diffusion in cellular environments, particularly for charged molecules such as ions, charged metabolites, and proteins with net positive or negative charge [39]. Fixed negative charges on proteins, nucleic acids, and membrane phospholipids create local electric fields that couple electrical potential gradients to concentration gradients, giving rise to electrodiffusion where the flux of charged species depends on both [7, 17, 39].

The combination of geometric constraints, macromolecular crowding, and electrostatic effects means that effective diffusion coefficients in cardiomyocytes can vary substantially depending on the specific subcellular location and local environment [9, 10, 12, 13, 40]. Quantitative characterization of diffusion in cardiomyocytes is therefore essential for linking intracellular transport properties to cellular function. However, obtaining such measurements in live cells remains challenging due to structural heterogeneity and the coexistence of multiple transport mechanisms.

To address the challenge of quantifying molecular transport in complex intracellular environments, several experimental approaches have been developed. These approaches ranging from ensemble methods that measure average properties over large populations of molecules to single-molecule techniques that resolve individual trajectories [25]. Fluorescence-based methods have emerged as particularly powerful tools due to their non-invasive nature, single-molecule sensitivity, applicability to both in vitro and in vivo systems, and the capacity for spatial mapping of diffusion parameters [26, 31]. These techniques can be applied to characterize diffusion in simple buffer solutions for biophysical studies of protein interactions and conformational dynamics, as well as in complex biological environments including live cells where they can probe molecular transport with minimal perturbation [30].

Among these techniques, FCS [24, 25] and RICS [27, 28] have become established methods for quantifying diffusion coefficients through analysis of fluorescence intensity fluctuations arising from molecules diffusing through a defined observation volume or across a scanned image field. A review of these fluorescence-based diffusion measurement techniques, their theoretical foundations, practical implementations, and current limitations are presented in the following chapter. The limitations of existing fluorescence-based diffusion measurement techniques provide a key motivation for the work presented in this thesis, which focuses on improving data analysis strategies and developing alternative approaches for extracting diffusion parameters in cellular environments.

## 2 Fluorescence-Based Diffusion Measurement Techniques

Quantitative measurement of molecular diffusion in living cells requires experimental techniques capable of resolving stochastic molecular motion in complex and heterogeneous environments. Fluorescence-based methods have become central tools for this purpose due to their high sensitivity, non-invasive nature, and applicability to live-cell systems. This chapter introduces the main fluorescence-based techniques used to quantify diffusion coefficients from intensity fluctuation data. The underlying principles and theoretical foundations of each method are presented, followed by a discussion of their advantages and inherent limitations. Particular emphasis is placed on challenges that arise when these techniques are applied to intracellular environments, which motivate the methodological developments presented in this thesis.

### 2.1 Fluorescence Correlation Spectroscopy (FCS)

#### 2.1.1 Principles and Theory

FCS is a single-molecule technique that measures the temporal fluctuations of fluorescence intensity arising from molecules diffusing through a small observation volume (Figure 1), typically defined by a diffraction-limited focused laser beam in a confocal microscope configuration [24, 25].

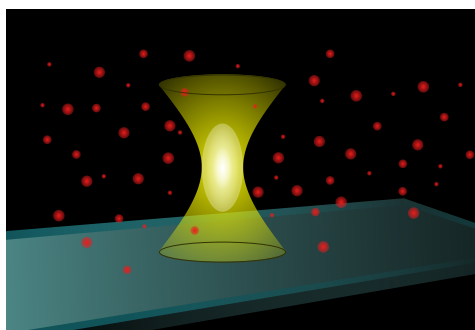


Figure 1: Schematic illustration of the confocal detection volume in a confocal fluorescence microscope. The yellow hourglass shape represents the focused laser excitation beam, and the central yellow ellipsoid denotes the effective confocal detection volume. Red spheres correspond to diffusing fluorescent particles of different sizes. The coverslip positioned above the microscope objective is shown at the bottom.

The fundamental principle of FCS relies on analyzing the temporal autocorrelation function (ACF) of fluorescence intensity fluctuations,  $G(\tau) = \langle \delta F(t) \delta F(t + \tau) \rangle / \langle F(t) \rangle^2$ , where  $\delta F(t)$  represents the deviation of fluorescence intensity from its mean value at time  $t$ , and  $\tau$  is the lag time [24, 25]. When fluorescent molecules diffuse through the observation volume, they create stochastic fluctuations in the detected fluorescence signal. For freely diffusing molecules without interactions, the characteristic decay time of these fluctuations, quantified by the ACF, is directly related to the diffusion coefficient:  $\tau_D = \omega^2 / (4 DC)$ , where  $\omega$  is the characteristic dimension of the observation volume (lateral beam waist radius) and  $DC$  is the diffusion coefficient [26].

In FCS, fluorescence detection is spatially weighted by the microscope detection efficiency profile, given by the product of excitation and collection efficiency. This weighting is

commonly approximated by a 3D Gaussian function, [41]

$$PSF(x, y, z) = \exp\left(-\frac{2x^2}{\omega_{xy}^2} - \frac{2y^2}{\omega_{xy}^2} - \frac{2z^2}{\omega_z^2}\right), \quad (6)$$

where  $\omega_{xy}$  and  $\omega_z$  are the lateral and axial radii. The FCS observation volume is the effective volume defined by this weighting function rather than a sharp physical boundary.

For 3D Gaussian observation volumes, the ACF for freely diffusing molecules takes the analytical form:

$$G(\tau) = \frac{1}{N} \left(1 + \frac{\tau}{\tau_D}\right)^{-1} \left(1 + \frac{\tau}{s^2 \tau_D}\right)^{-1/2}, \quad (7)$$

where  $N$  is the average number of molecules in the observation volume and  $s$  is the structure parameter (ratio of axial to lateral dimensions of the observation volume). By fitting this theoretical model to autocorrelation curves calculated from experimentally recorded fluorescence intensity traces, one can extract both the diffusion coefficient and the local concentration of fluorescent molecules, making FCS a powerful tool for studying molecular dynamics, binding interactions, and conformational changes in solution and in living cells [30, 31].

The ACF can be extended to account for photophysical processes, particularly triplet-state kinetics, which occur when fluorophores undergo intersystem crossing to a non-fluorescent triplet state before relaxing back to the ground state [41, 42]. The presence of triplet-state dynamics introduces an additional fast decay component in the ACF, modifying the standard diffusion model to [41]:

$$G(\tau) = \frac{1}{N} \left(1 + \frac{TSA}{1-TSA} \exp\left(\frac{-\tau}{\tau_T}\right)\right) \left(1 + \frac{\tau}{\tau_D}\right)^{-1} \left(1 + \frac{\tau}{s^2 \tau_D}\right)^{-1/2}, \quad (8)$$

where  $TSA$  is the triplet-state amplitude, representing the fraction of molecules in the triplet state at equilibrium and  $\tau_T$  is the triplet-state relaxation time. This 3D diffusion model with triplet-state correction is essential for accurately extracting diffusion coefficients from FCS measurements of fluorescent dyes, which exhibit triplet-state dynamics with relaxation times in the microsecond range [42]. Furthermore, FCS models can be extended to multi-component systems where multiple species with different diffusion coefficients contribute to the correlation function, with the total ACF represented as a weighted sum of individual components [41].

From a theoretical perspective, the fluorescence intensity fluctuations analyzed in FCS can be interpreted in terms of the diffusion Green's function, often referred to as the diffusion propagator. For freely diffusing, non-interacting molecules undergoing Brownian motion, the diffusion process is fully characterized by the conditional probability density  $P(\mathbf{r}, t | \mathbf{r}_0, 0)$ , which gives the probability of finding a molecule at position  $\mathbf{r}$  at time  $t$ , given that it was located at  $\mathbf{r}_0$  at the initial time  $t = 0$ . For an initial point source of  $N$  particles, the ensemble-averaged concentration profile is related to this propagator through  $c(\mathbf{r}, t) = NP(\mathbf{r}, t | \mathbf{r}_0, 0)$ , such that the Gaussian solution of Fick's diffusion equation derived in Eq. 3 corresponds to the diffusion Green's function (propagator) multiplied by the total particle number  $N$ .

In FCS, the temporal autocorrelation function arises from integrating this propagator over the confocal observation volume defined by the microscope point spread function (PSF), such that the characteristic decay time of the ACF directly reflects the diffusive spreading encoded in the propagator. The same propagator forms the theoretical foundation of other correlation-based techniques, including RICS, which probe diffusion through different spatiotemporal sampling schemes.

### 2.1.2 Advantages

FCS offers several key advantages for diffusion measurements: single-molecule sensitivity enabling detection at nanomolar to picomolar concentrations, rapid data acquisition with typical measurement times of seconds to minutes, and the ability to extract both diffusion coefficients and absolute molecular concentrations from a single measurement [26]. The technique requires minimal sample preparation and can be applied to both in vitro solutions and specific locations within live cells, making it a versatile tool for studying molecular dynamics across diverse biological contexts. Additionally, FCS provides access to fast dynamic processes on microsecond to millisecond timescales, and the small observation volume (femtoliters) enables characterization of local microenvironments that may differ substantially from bulk cellular properties.

### 2.1.3 Limitations

Despite its advantages, FCS faces several significant limitations. The technique requires relatively high laser intensities to achieve sufficient signal-to-noise ratios, particularly when mapping spatial variations across cellular regions, which increases cumulative laser exposure and associated phototoxicity effects in live cells [43]. A fundamental statistical issue arises in conventional FCS analysis: the ACF data points at different lag times are not statistically independent, yet standard fitting procedures using ordinary least squares (OLS) or maximum likelihood methods assume this independence [44–47]. This incorrect assumption leads to overconfident parameter estimates with underestimated uncertainties, making it difficult to rigorously assess goodness-of-fit or compare models of different complexities—for instance, distinguishing between single-component and multi-component diffusion becomes statistically ambiguous.

While generalized least squares (GLS) approaches can address correlated errors by incorporating the full covariance matrix, estimating this covariance reliably may require thousands of repeated measurements under identical conditions [48, 49], which is often impractical in live-cell experiments due to phototoxicity, cell movement, and viability constraints over the extended acquisition periods.

Alternatively, structured covariance estimation approaches—such as shrinkage estimators that regularize the empirical covariance matrix to improve conditioning and reduce estimation error [48, 50], as well as parametric covariance models or low-rank approximations [51]—can exploit the known structure of ACF errors and reduce the number of repeated measurements required for covariance estimation. In addition, the randomly sampled segmented ACF (rsACF) method reduces correlations between ACF data points and improves the statistical validity of goodness-of-fit evaluation [47]. However, all of these approaches still require repeated measurements to reliably characterize error correlations, which remains challenging in live-cell experiments due to limitations in acquisition time and phototoxicity.

Furthermore, FCS provides single-point measurements, necessitating sequential scanning to map spatial heterogeneity, which further increases total laser exposure time and limits throughput for characterizing complex biological systems.

## 2.2 Raster Image Correlation Spectroscopy (RICS)

### 2.2.1 Principles and Theory

RICS extends the correlation analysis approach of FCS to laser scanning microscopy by exploiting both the spatial and temporal information contained in image series acquired during raster scanning [27, 28]. The fundamental principle of RICS is to calculate spatial ACFs from fluorescence intensity images, where the correlation is computed as a function

of pixel displacement in both the horizontal ( $\xi$ ) and vertical ( $\psi$ ) directions:  $G(\xi, \psi) = \langle I(x, y) I(x + \xi, y + \psi) \rangle / \langle I(x, y) \rangle^2$ , with the resulting correlation function reflecting the combined effects of molecular diffusion during the scanning process and the PSF.

The key innovation of RICS is the realization that the raster-scanning process of laser scanning microscopy inherently encodes temporal information into the spatial structure of an image. During image acquisition, neighboring pixels along the fast scan direction are recorded sequentially and are separated in time by the pixel dwell time, while pixels in adjacent scan lines are separated by the line scan time. As a result, spatial correlations between pixels correspond to well-defined time delays, enabling diffusion dynamics to be extracted from spatial correlation functions.

The theoretical RICS correlation function combines the spatial structure of the microscope PSF with the temporal evolution of molecular diffusion during raster scanning. For a Gaussian PSF, the spatiotemporal autocorrelation function can be written as [16, 27, 28]:

$$G(\Delta, \tau) = \frac{1}{N} \prod_{i \in \{x, y, z\}} \left[ \frac{1}{\sqrt{\pi (4DC_i \tau + \omega_i^2)}} \exp\left(-\frac{\Delta_i^2}{4DC_i \tau + \omega_i^2}\right) \right], \quad (9)$$

where  $\Delta = (\Delta x, \Delta y, \Delta z)$  is the spatial displacement,  $DC_i$  denotes the diffusion coefficient along axis  $i \in \{x, y, z\}$ , and  $\omega_i$  are the Gaussian PSF widths along the corresponding axes.

In RICS analysis, spatial lags are sampled in the imaging plane so that  $\Delta x = \xi \delta_x$ ,  $\Delta y = \psi \delta_y$ , and  $\Delta z = 0$ , with  $\delta_x$  and  $\delta_y$  denoting the pixel sizes in the horizontal and vertical image directions, respectively. The correlation lag time  $\tau(\xi, \psi)$  is determined by the scanning process, with  $\tau(\xi, \psi) = \xi t_{\text{pix}} + \psi t_{\text{line}}$ , where  $t_{\text{pix}}$  is pixel dwell time, and  $t_{\text{line}}$  is line scan time.

Unlike FCS which provides a single-point measurement, RICS enables spatial mapping of diffusion coefficients across the entire imaged region by calculating local correlation functions from image subregions [16, 27–29].

Similar to FCS, RICS correlation functions can be extended to account for triplet-state kinetics and multi-component diffusion, enabling characterization of complex systems with multiple diffusing species or photophysical processes [28].

### 2.2.2 Advantages

RICS combines the molecular sensitivity of correlation spectroscopy with the spatial mapping capabilities of laser scanning microscopy, enabling simultaneous measurement of diffusion coefficients across entire cellular regions rather than at single points [27, 29]. This spatial mapping capability makes RICS particularly valuable for characterizing heterogeneous biological systems where diffusion properties vary between subcellular compartments. RICS can detect anisotropic diffusion by performing measurements at multiple scanning angles, providing directional information about molecular transport in organized structures such as in the cardiomyocytes [15, 16]. The technique utilizes the raster scanning process of laser scanning confocal microscopes for temporal sampling, requiring no additional instrumentation beyond a standard laser scanning confocal microscope, and the distributed laser exposure across the scan field can reduce local photodamage compared to the continuous illumination at a single point in FCS.

### 2.2.3 Limitations

RICS faces challenges that extend beyond those of FCS due to the increased complexity of spatiotemporal data acquisition. The statistical issues affecting FCS, particularly correlations between ACF data points, are also present in RICS, but estimating the covariance

structure for rigorous GLS-based fitting is significantly more challenging. A typical RICS analysis involves calculating spatial ACFs from image stacks, yielding a two-dimensional (2D) correlation surface that is cropped and flattened into a vector of several hundred points for fitting. Reliable covariance estimation for such high-dimensional data would require acquiring thousands of independent image stacks under identical scanning conditions (image size, pixel dwell time, scanning speed, and angle), which is practically infeasible in live-cell experiments where maintaining stable conditions over the required acquisition time is impossible due to phototoxicity and cell viability constraints.

Additionally, RICS data acquisition is inherently slower than FCS because of the flyback periods during line scanning when no useful data are collected, further extending experimental duration. The technique is also sensitive to artifacts from large particles, cellular movements, or photobleaching that occur during frame acquisition, requiring careful quality control and filtering strategies. While RICS provides spatial maps of diffusion, the spatial resolution of these maps is limited by the need for sufficient statistics within each analyzed subregion, creating a trade-off between spatial detail and measurement precision.

## 2.3 Bayesian Approach to Direct Analysis of Fluorescence Intensity Traces

### 2.3.1 Principles and Theory

Several years ago, an alternative framework for FCS was proposed by *Pressé* and colleagues [52–55] that fundamentally departed from the correlation-based paradigm of FCS. Instead of calculating and fitting the ACF of fluorescence intensity fluctuations, this approach applies Bayesian inference directly to the raw photon count data, constructing a probabilistic model that describes the physical processes underlying signal formation. The method models individual fluorescent molecules diffusing through the confocal observation volume, with each molecule's contribution to the detected signal depending on its position relative to the PSF at each time point. By fitting this physical model directly to the recorded fluorescence intensity transient, the approach yields posterior probability distributions for parameters such as the diffusion coefficient and molecular brightness (maximum photon emission rate for a molecule at the center of the observation volume), providing a complete characterization of parameter uncertainty within a rigorous statistical framework.

At the timescale of interest (e.g., 1  $\mu$ s), individual photon detections occur stochastically and independently, with the total photon count  $w_k$  between successive time assessments following Poisson statistics [53]:

$$w_k \sim \text{Poisson} \left( (t_k - t_{k-1}) \left( \mu_{\text{back}} + \sum_n \mu_k^n \right) \right) \quad (10)$$

where the index  $k$  denotes discrete time steps in the measurement sequence with corresponding physical times  $t_k$ ,  $\mu_{\text{back}}$  is the background photon emission rate, and  $\sum_n \mu_k^n$  represents the sum of photon emission rates from individual fluorescent molecules indexed by  $n = 1, 2, \dots$  at time step  $k$ . The time interval  $(t_k - t_{k-1})$  represents the duration over which photons are collected at each assessment step. The number of molecules contributing to the signal is not known a priori and must be inferred from the data, which is addressed through Bayesian non-parametric methods. Each molecular emission rate  $\mu_k^n$  depends on the molecule's position  $(x_k^n, y_k^n, z_k^n)$  at time step  $k$  relative to the center of the confocal volume and is expressed as [53]:

$$\mu_k^n = \mu_{\text{mol}} \text{PSF}(x_k^n, y_k^n, z_k^n) \quad (11)$$

where  $\mu_{\text{mol}}$  represents the molecular brightness, and PSF characterizing the spatial detection efficiency. Molecular motion is modeled as free Brownian diffusion, with positions at

successive time points drawn from normal distributions:

$$\begin{aligned}x_k^n &\sim \text{Normal}(x_{k-1}^n, 2(t_k - t_{k-1})DC) \\y_k^n &\sim \text{Normal}(y_{k-1}^n, 2(t_k - t_{k-1})DC) \\z_k^n &\sim \text{Normal}(z_{k-1}^n, 2(t_k - t_{k-1})DC)\end{aligned}\tag{12}$$

where  $DC$  is the diffusion coefficient, assumed identical for all molecules in the basic formulation, and  $\text{Normal}(\mu, \sigma^2)$  denotes a normal distribution with mean  $\mu$  and variance  $\sigma^2$ , with probability density function

$$p(x | \mu, \sigma^2) = \frac{1}{\sqrt{2\pi\sigma^2}} \exp\left(-\frac{(x - \mu)^2}{2\sigma^2}\right).\tag{13}$$

The model can be extended to accommodate multiple diffusing species with distinct diffusion coefficients, as demonstrated in [53].

### 2.3.2 Bayesian Inference

Bayesian inference provides a fundamentally different statistical paradigm compared to the frequentist approach. In the frequentist framework, parameters such as the diffusion coefficient are treated as fixed but unknown quantities, and the goal is to find point estimates (e.g., through least squares or maximum likelihood methods) along with confidence intervals based on the sampling distribution of the estimator [48, 49]. Frequentist confidence intervals do not represent probability statements about the parameter itself but rather describe the long-run frequency with which such intervals would contain the true parameter value across many hypothetical repetitions of the experiment [56].

In contrast, Bayesian inference treats parameters as random variables in the statistical sense, assigning probability distributions that quantify our uncertainty about their values given limited and noisy data. For parameters that are fixed physical constants (e.g., diffusion coefficients under fixed conditions), these distributions represent epistemic uncertainty, whereas for quantities that inherently fluctuate (e.g., the number of molecules in the observation volume) they may also describe intrinsic stochastic variability [57].

Prior distributions encode initial beliefs or information about parameters before observing data, and Bayes' theorem updates these priors to posterior distributions that incorporate the evidence provided by the measured data:  $p(\theta|data) \propto p(data|\theta)p(\theta)$ , where  $\theta$  represents model parameters,  $data$  is the observed data,  $p(data|\theta)$  is the likelihood function, and  $p(\theta)$  is the prior [56, 57]. The posterior distribution  $p(\theta|data)$  directly quantifies our uncertainty about parameters given the observed data, enabling intuitive probabilistic statements through credible intervals or quantile ranges—for example, the central 95% credible interval represents the range within which the parameter lies with 95% probability, computed from the 2.5th and 97.5th percentiles of the posterior distribution. This Bayesian framework naturally handles complex models with many parameters and unknown model structures (such as the uncertain number of molecules in the observation volume), providing a principled approach to model comparison and parameter inference that explicitly accounts for all sources of uncertainty [58].

### 2.3.3 Markov Chain Monte Carlo

For complex models where posterior distributions cannot be computed analytically, Markov Chain Monte Carlo (MCMC) methods enable practical implementation of Bayesian inference by generating samples from the posterior distribution through iterative simulation [57]. MCMC algorithms construct a Markov chain—a sequence of parameter values where each

new value depends only on the previous one—whose stationary distribution is the desired posterior distribution. The chain typically starts from an arbitrary initial point that may be far from the high-probability region of the posterior. The burn-in period refers to the initial samples that are discarded because the chain has not yet converged to the target distribution. After burn-in, subsequent samples provide an empirical representation of the posterior from which parameter estimates, credible intervals, and other quantities of interest can be computed.

Various MCMC sampling algorithms have been developed, each with different computational properties and efficiency characteristics. The Metropolis–Hastings algorithm [59] is a general-purpose approach that proposes new parameter values from a proposal distribution and accepts or rejects them based on the ratio of posterior probabilities, ensuring detailed balance and convergence to the target posterior. Gibbs sampling is a special case that updates one parameter at a time by sampling from its conditional distribution given all other parameters, which is particularly efficient when these conditional distributions have closed-form expressions but requires careful implementation to avoid slow mixing when parameters are highly correlated [57].

Hamiltonian Monte Carlo (HMC) methods exploit gradient information and introduce auxiliary momentum variables to guide proposals through parameter space more efficiently, reducing random walk behavior and enabling better exploration of high-dimensional posteriors with correlated parameters [57]. No-U-Turn Sampler (NUTS), an extension of HMC, automatically tunes the simulation length to balance exploration efficiency with computational cost, eliminating the need for manual tuning of trajectory length parameters [60]. Slice sampling provides another alternative that adaptively adjusts the proposal distribution by sampling uniformly from regions under the posterior density, offering robustness without requiring gradient calculations or careful tuning of proposal distributions [57].

The choice of sampling algorithm depends on the specific characteristics of the posterior distribution, the availability of gradient information, and computational constraints, with HMC and NUTS generally providing superior performance for high-dimensional problems with smooth posteriors, while Metropolis–Hastings and Gibbs sampling remain valuable for problems with discrete parameters or when gradient computation is impractical. The *Jazani et al.* implementation MCMC exploits a Gibbs sampling [53].

#### 2.3.4 Advantages

The direct Bayesian analysis of fluorescence intensity traces offers several advantages over traditional correlation-based methods. Most notably, the approach achieves a remarkable reduction in required experimental time—*Jazani et al.* demonstrated that accurate diffusion coefficient estimation can be obtained from measurement durations orders of magnitude shorter than those needed for conventional FCS analysis [53].

This reduction stems from the more efficient extraction of information directly from photon count fluctuations rather than from the derived ACF, which involves information loss through the averaging inherent in correlation calculation.

The Bayesian framework provides rigorous quantification of parameter uncertainties through posterior probability distributions. These complete posterior distributions directly reveal the number of diffusing components through the structure of the diffusion coefficient posterior: single-component systems exhibit a single peak, while multi-component systems show distinct, separated peaks corresponding to each population. Additionally, the approach naturally handles complex scenarios such as unknown numbers of molecules and time-varying molecular brightness, incorporating these as additional parameters to be inferred rather than requiring pre-specification.

### 2.3.5 Limitations

Despite its theoretical advantages, the Bayesian direct analysis approach faces several practical limitations that have hindered its widespread adoption. The model implementation available in the literature [53] does not support triplet-state kinetics, a significant photophysical process that affects most fluorophores and must be included in the model to obtain accurate diffusion coefficients from typical FCS measurements.

When we installed and tested the most recently implemented version [53], we found the computational performance to be prohibitively slow for routine analysis, with single-chain MCMC runs requiring minutes to hours depending on the number of sampling steps and the complexity of the data. The implementation is written in MATLAB and does not support parallel execution of multiple chains within a single MATLAB session, which is problematic for assessing chain convergence through the Gelman–Rubin statistic  $\hat{R}$  (also known as the potential scale reduction factor, which compares within-chain and between-chain variances to diagnose whether multiple chains have converged to the same posterior distribution) [61].

To evaluate convergence, we manually executed multiple independent runs and saved samples for post-hoc  $\hat{R}$  calculation, but found that chains frequently failed to converge (exhibiting high  $\hat{R}$  values) even for simulated data with known ground-truth diffusion coefficients. More concerning, we observed cases where chains appeared to converge based on  $\hat{R}$  diagnostics but converged to incorrect parameter values, particularly when a different molecular brightness range was used as the prior distribution, demonstrating sensitivity to prior selection. Examples of these convergence failures are documented in Paper III. These computational and convergence limitations represent significant barriers to the practical application of this promising approach and motivated the development of alternative methods that retain the advantages of direct intensity analysis while addressing these implementation challenges.

## 2.4 Methodological Challenges and Motivation

Despite their widespread adoption and proven utility, the analysis of FCS and RICS data faces substantial computational and methodological challenges that limit both accessibility and scientific reliability. These challenges span multiple domains, from fundamental data quality issues to statistical modeling limitations and the absence of critical capabilities in existing software tools. Additionally, while direct intensity analysis approaches offer theoretical advantages, existing implementation faces significant practical limitations that hinder their adoption for routine experimental work. The following subsections detail these challenges and establish the motivation for the methodological developments presented in this thesis.

### 2.4.1 Experimental Artifacts and Data Quality

Raw fluorescence signals are inherently susceptible to numerous experimental artifacts that can severely compromise analysis results. Detector noise, photobleaching, photoblinking, mechanical drift, and slow intensity trends can significantly distort correlation functions and bias parameter estimation if not properly accounted for. In solution measurements, rare but bright fluorescent aggregates or “blobs”—originating from impurities, aggregation, or incomplete labeling—can dominate intensity fluctuations and lead to spurious correlation amplitudes and diffusion times. These artifacts are particularly problematic because they are difficult to detect and systematically exclude within conventional correlation-based analysis frameworks, yet their presence can invalidate the physical interpretation of measured parameters. Advanced filtering strategies that can identify and remove

contaminated measurements before parameter estimation are therefore essential for robust analysis of both solution and cellular measurements.

#### **2.4.2 Biological Complexity and Non-Ideal Diffusion**

In biologically relevant systems, additional complexity arises from pronounced spatial heterogeneity, anisotropic transport properties imposed by cellular ultrastructure, and non-ideal diffusion behaviors such as anomalous diffusion, transient binding, or the coexistence of multiple diffusing populations. Anisotropic diffusion, in particular, is prevalent in highly structured cellular environments such as cardiomyocytes, where molecular transport is constrained by organized cytoskeletal networks and membrane systems. Although RICS analyses incorporating variable scanning speeds and angles have been previously implemented for characterizing anisotropic diffusion [15, 16], to date, no open-source software offering these analytical capabilities has been made publicly accessible.

Accurate characterization of direction-dependent diffusion requires not only appropriate theoretical models but also precise knowledge of the 3D PSF of the microscope system. The use of experimentally measured PSFs becomes critical in anisotropic environments, where even small deviations from idealized Gaussian approximations can lead to systematic errors in extracted diffusion coefficients and structural parameters. Despite this clear need, existing analysis tools either rely exclusively on analytical PSF models or provide no mechanism for incorporating experimentally determined PSFs into the fitting procedure.

#### **2.4.3 Statistical Modeling Deficiencies**

From a modeling perspective, traditional fitting approaches based on OLS optimization remain widely used due to their computational efficiency, but they neglect the strong statistical correlations between ACF data points and the inherently heteroscedastic noise structure of correlation functions. As a result, uncertainty estimates obtained from OLS fits are often unreliable, and goodness-of-fit metrics may provide misleading assessments of model adequacy, particularly when comparing models that differ in complexity [47].

Although advanced statistical treatments such as GLS and Bayesian inference are well established in principle, to our knowledge no currently available open-source software implements these methods for FCS or RICS analysis. While Guo and colleagues previously developed a Bayesian and GLS implementation for FCS [49], the software is no longer accessible. This absence of statistically rigorous frameworks prevents researchers from obtaining reliable uncertainty quantification, incorporating prior knowledge, or performing principled model comparison.

#### **2.4.4 Correlation-Based Software Limitations**

The current open-source software ecosystem for FCS and RICS analysis [29, 62–70] lacks critical capabilities required for rigorous analysis of complex biological systems. Only a single implementation currently offers GPU acceleration for ACF computation [70], which is essential for high-throughput or large-scale analyses. These platforms collectively lack support for experimentally measured PSFs, multiple-angle RICS analysis for anisotropic diffusion characterization, advanced statistical frameworks including Bayesian inference and GLS error treatment, and systematic filtering strategies for identifying and removing artifact-contaminated measurements. The absence of these capabilities in accessible, maintained software limits the ability of researchers to perform statistically rigorous and comprehensive analysis of molecular transport in structured cellular environments. To address these limitations, we developed the IOCBIO FCS platform, as detailed in Paper I.

#### **2.4.5 Beyond Correlation: Direct Intensity Analysis**

However, even with enhanced analysis methods, correlation-based techniques face fundamental limitations related to photon requirements and phototoxicity in live-cell applications. The Bayesian direct analysis approach proposed by *Pressé* and colleagues offered a promising alternative by analyzing intensity traces directly rather than through derived correlation functions, theoretically enabling accurate parameter estimation from shorter measurements [53]. Yet practical implementation of this approach suffered from computational inefficiency, convergence difficulties, and sensitivity to prior specification, hindering its adoption for routine experimental work. To overcome these limitations, we developed FITSA, as presented in Paper III.

## Aims of the Thesis

This thesis aims to develop improved methods for measuring molecular diffusion in cardiomyocytes by addressing fundamental limitations in existing fluorescence-based diffusion measurement techniques. By integrating physical models of diffusion in complex cellular environments with statistically rigorous and computationally efficient analysis methods, this work seeks to enable reliable estimation of molecular transport parameters in structurally heterogeneous and anisotropic intracellular systems. The specific aims are:

- To develop a unified, open-source platform that addresses computational and statistical limitations of existing FCS and RICS analysis tools.
- To develop a computationally efficient Bayesian method for direct analysis of fluorescence intensity traces that overcomes photon requirement and phototoxicity limitations of correlation-based approaches while providing reliable parameter estimation and uncertainty quantification.

## 3 Unified Platform for FCS and RICS Analysis (IOCBIO FCS)

### 3.1 Overview

In Paper I, we developed IOCBIO FCS as an open-source, Python-based platform with a command-line interface for analyzing fluorescence intensity traces and images obtained from FCS and RICS experiments. The platform addresses critical gaps in existing analysis tools by providing a unified framework that integrates modern computational methods with rigorous statistical inference approaches, supporting the complete workflow from raw data visualization through autocorrelation calculation to model fitting and parameter estimation.

Key capabilities include GPU-accelerated computation of ACFs, flexible model fitting with support for anisotropic diffusion and experimentally measured 3D PSFs, and a comprehensive suite of statistical methods within both frequentist and Bayesian inference frameworks. The platform is designed with modularity and extensibility in mind, allowing researchers to adapt analysis workflows to specific experimental requirements. The following subsections describe the key capabilities and selected features of the software; complete technical documentation and validation studies are provided in Paper I.

### 3.2 Visualizing Raw RICS/FCS Datasets

Before performing correlation analysis, it is essential to assess the quality and stability of raw fluorescence data to identify potential experimental artifacts that could compromise subsequent parameter estimation. The IOCBIO FCS platform provides comprehensive visualization capabilities for both FCS and RICS datasets, enabling users to examine individual measurements and detect systematic issues such as photobleaching, sample drift, illumination inhomogeneities, or mechanical instabilities. For FCS experiments, the software can display individual fluorescence intensity traces showing temporal fluctuations as well as summary statistics across multiple sequential traces that reveal long-term trends in signal intensity or measurement stability. Similarly, for RICS experiments, users can visualize individual confocal scan frames to assess spatial intensity distributions and pixel-level signal quality and examine averaged intensities across entire image series to detect temporal variations in fluorescence signal. These visualization modes provide essential diagnostic tools that enable early-stage quality control by revealing problematic datasets requiring exclusion or systematic trends needing correction prior to autocorrelation analysis, thereby ensuring that subsequent correlation analysis and parameter estimation are conducted on high-quality data for more reliable and reproducible diffusion coefficient measurements.

### 3.3 Calculating Autocorrelation Functions

The computation of ACFs is the central step in converting raw fluorescence data into quantitative information about molecular dynamics. The IOCBIO FCS platform implements efficient algorithms for calculating ACFs from both FCS intensity traces and RICS image series, with support for CPU-based and GPU-accelerated computation to accommodate different hardware configurations and dataset sizes.

The software provides flexible data selection and preprocessing options to adapt the analysis to specific experimental conditions. Individual or grouped fluorescence traces (FCS) and images or image series (RICS) can be selected, enabling targeted inspection and refinement of the data prior to further processing. For FCS measurements, fluorescence traces can be restricted to selected time intervals to exclude segments affected by artifacts identified during visualization. For RICS datasets, image series can be subdivided

into smaller spatial regions to enable spatially resolved analysis of heterogeneous samples or grouped according to acquisition parameters such as scanning angle or speed for comparative analysis.

For FCS datasets comprising multiple sequential traces, the software can compute and visualize the covariance matrix of ACFs calculated from individual traces (Figure 2), explicitly revealing the correlation structure of statistical noise across different lag times. The strong diagonal elements indicate high variance at each individual lag time, while the off-diagonal structure reveals systematic correlations between nearby lag times—this non-diagonal structure demonstrates that autocorrelation data points are not statistically independent, violating a key assumption of OLS fitting approaches commonly used in FCS analysis. This covariance information is essential for implementing GLS fitting that properly accounts for the correlated error structure, leading to statistically rigorous parameter estimates and realistic uncertainty quantification.

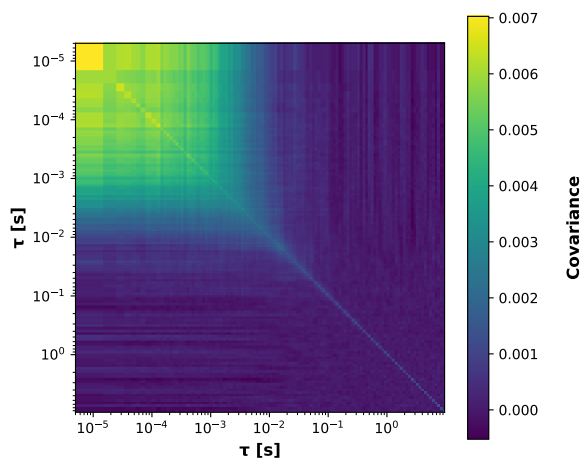


Figure 2: Covariance matrix of ACFs computed from 120 individual FCS traces, revealing the correlation structure of statistical noise across different lag times. Each element  $(i, j)$  of this matrix represents the covariance between autocorrelation values at lag times  $\tau_i$  and  $\tau_j$ , quantifying the extent to which fluctuations in the ACF at one lag time are statistically related to fluctuations at another lag time.

### 3.4 Data Filtering and Model-Based Parameter Estimation

Following autocorrelation computation, the analysis framework provides multiple levels of data filtering designed to exclude inappropriate contributions prior to final parameter estimation. For both FCS and RICS, very short lag times dominated by detector-related artifacts and long lag times where noise dominates can be excluded, and visualization tools are provided to assess ACF quality before fitting. Filtering can also be applied based on acquisition parameters such as scanning angle and scanning speed, enabling removal of technical artifacts while preserving the underlying diffusion information.

A second, conceptually distinct filtering stage is implemented through pre-analysis of diffusion coefficient and concentration. In this approach, preliminary parameter estimates are computed independently for individual FCS traces or RICS images and visualized as distributions and scatter plots. This step enables identification of transient artifacts caused by large, slowly diffusing particles or aggregates entering the observation volume, which cannot be reliably detected from fluorescence intensity alone.

To illustrate this workflow, we analyzed a RICS dataset comprising 720 images acquired

at three different line times (2.0, 3.5, and 6.0 ms, corresponding to fast, medium, and slow scanning speeds) from a protein solution prone to forming large aggregates (see Paper II for experimental details). Large, slowly diffusing particles or aggregates can transiently enter the observation volume, producing localized high-intensity regions within individual images (Figure 3A and B). These events manifest as characteristic elongated high-intensity features in the affected image regions (Figure 3C), in contrast to the uniform intensity distribution observed under normal conditions (Figure 3D).

When ACFs are computed from the complete dataset without filtering, the resulting ACF exhibits systematic deviations that cannot be adequately described by standard diffusion models. Fit quality is assessed using the sum of squared residuals (SSR), where smaller values indicate better agreement between model and data; in all cases (Figure 4A–D), the fits were performed on averaged ACFs containing the same number of lag-time points, ensuring that SSR values are directly comparable across datasets. The unfiltered dataset yields  $SSR = 11.83$  (Figure 4A).

Standard filtering strategies based on mean intensity were found insufficient for identifying such events. While manual exclusion of high-intensity images before or after ACF calculation is possible through command-line options, this approach requires subjective threshold selection and becomes impractical for large datasets.

The diffusion-concentration pre-analysis provides a more systematic solution. By fitting each image individually and visualizing the resulting parameter estimates (Figure 5), characteristic patterns emerge: intensity peaks (Figure 5D) correspond to anomalously low concentration estimates (Figure 5C), which also appear as the low-concentration points in the scatter plot (Figure 5A, left region). This inverse relationship between intensity and estimated concentration arises from the nature of correlation analysis: the autocorrelation amplitude is inversely proportional to the number of independently diffusing entities in the observation volume. When a large, bright aggregate is present, it dominates the fluorescence signal while behaving as a single slowly diffusing object, resulting in elevated autocorrelation amplitude and consequently an underestimated concentration. Based on this visualization, users can define concentration thresholds (min and max) that specifically exclude images affected by large particles. Applying a minimum threshold of 3.6 nM excludes 135 of 720 images and substantially improves fit quality (Figure 4B;  $SSR = 0.04$ ).

The minimum concentration threshold was determined by gradually increasing the cutoff from low values until a stable global fit was achieved, as judged by convergence behavior, improvement in SSR, and stabilization of the estimated diffusion coefficient. Users can similarly define filtering ranges for diffusion coefficients to exclude images with anomalously fast or slow apparent diffusion. The apparent positive trend between diffusion coefficient and concentration in Figure 5A is a fitting artifact arising from the projection of a multi-component system onto a single-component model and does not indicate a physical concentration dependence of diffusivity.

In datasets where large particles are present throughout much of the acquisition, concentration-based filtering at the whole-image level may exclude a substantial fraction of data, reducing the statistical reliability of parameter estimates. For example, when analyzing only images 500–600 from the demonstration dataset (a region with frequent intensity peaks), concentration filtering excludes 49 of 100 images, discarding approximately 50% of the available data (Figure 4C;  $SSR = 0.14$ ).

To preserve more data in such challenging cases, the platform supports subdivision of RICS images into spatial sectors before ACF calculation. This approach substantially increases the number of individual correlation functions available for pre-analysis. Importantly, large particles typically affect only a subset of sectors within each image, enabling ex-

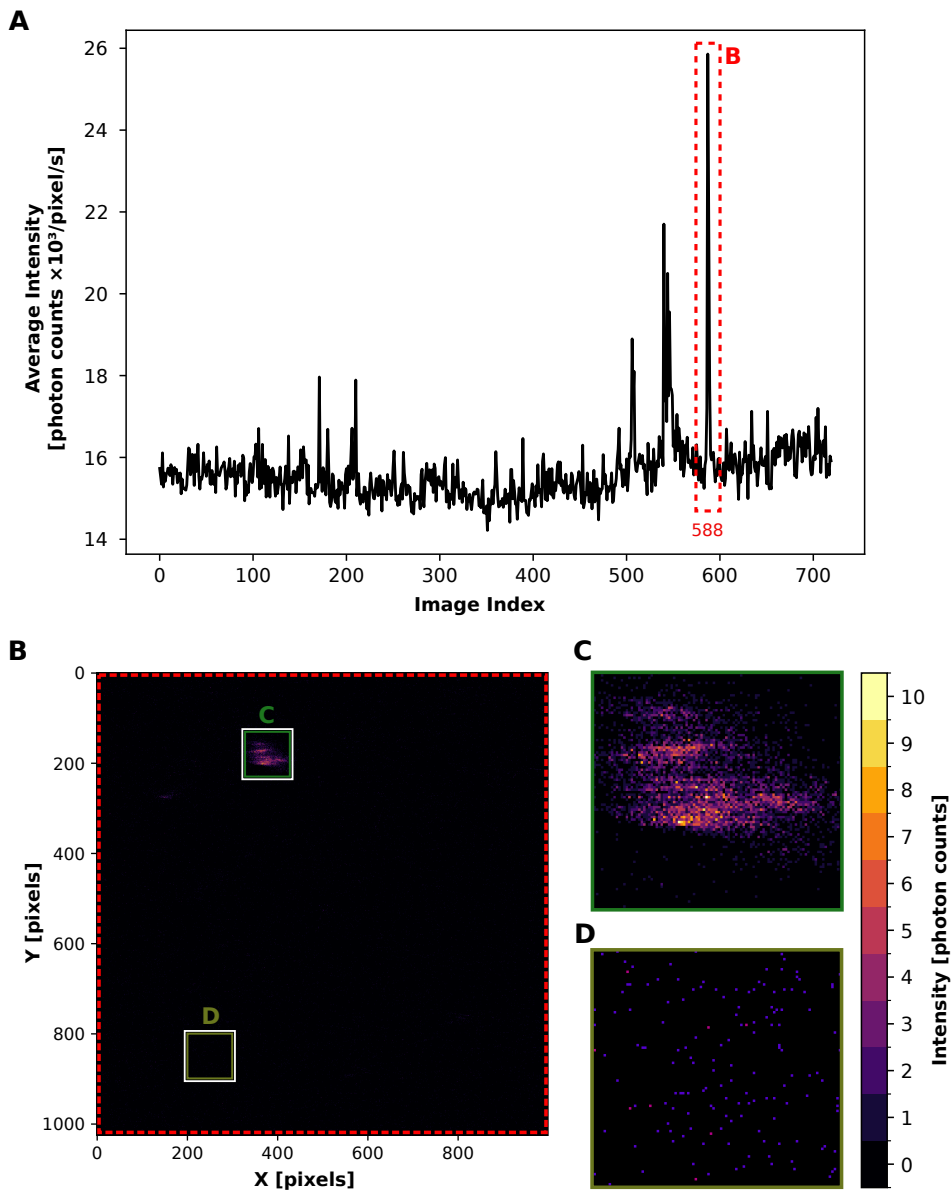


Figure 3: Overview of a RICS acquisition containing transient intensity artifacts. (A) Average fluorescence intensity per pixel per second across 720 consecutively acquired RICS images; the red dashed region highlights the intensity peak corresponding to the image shown in panel B. (B) RICS image at index 588, exhibiting a localized high-intensity region caused by a large particle or aggregate traversing the observation volume; green boxes indicate the areas enlarged in panels C and D. (C) Enlarged view of the high-intensity region, showing a characteristic elongated intensity feature. (D) Enlarged view of a representative region with uniform intensity distribution.

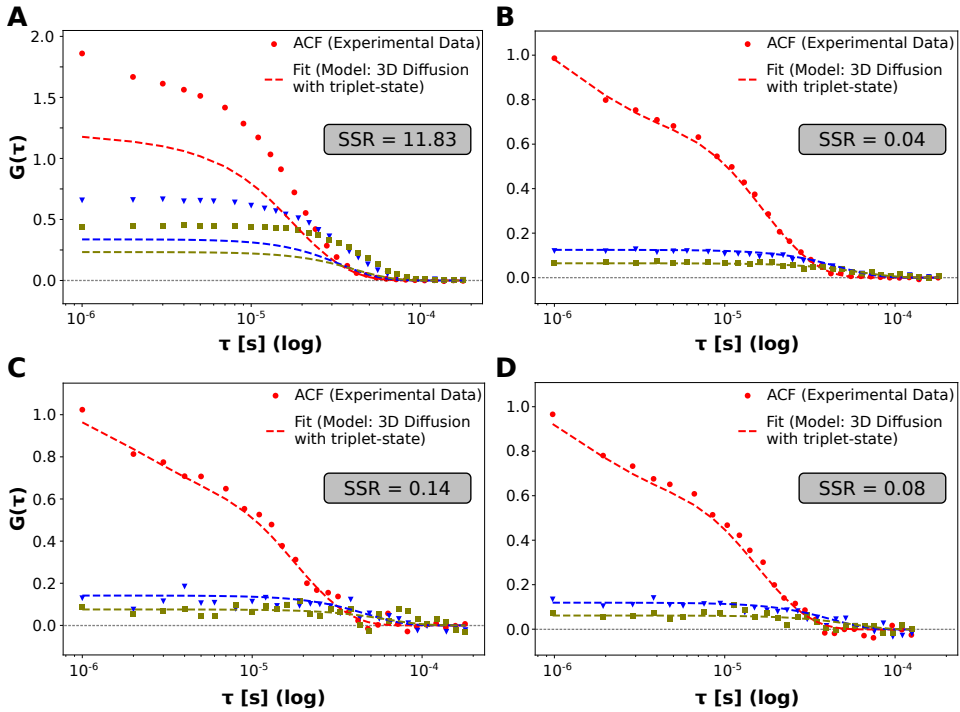


Figure 4: Autocorrelation function fitting using a 3D diffusion model with triplet-state kinetics under different filtering conditions. Each panel displays the ACF for the medium scanning speed (line time 3.5 ms); SSR values reported in each panel are computed from combined fits across all three scanning configurations (line times 2.0, 3.5, and 6.0 ms). Different colors represent spatial lags  $\Delta y = 0$  (red circles),  $\Delta y = 1$  (blue triangles), and  $\Delta y = 2$  (olive squares); dashed lines show the corresponding model fits. (A) Fit to ACF computed from all 720 images without filtering. (B) Fit after excluding images with concentration below 3.6 nM, retaining 585 of 720 images. (C) Fit using a subset of 100 images (indices 500–600) after concentration-based filtering, retaining 51 images. (D) Fit using the same 100-image subset divided into  $6 \times 6$  sectors (3600 total), after concentration-based filtering, retaining 3463 sectors.

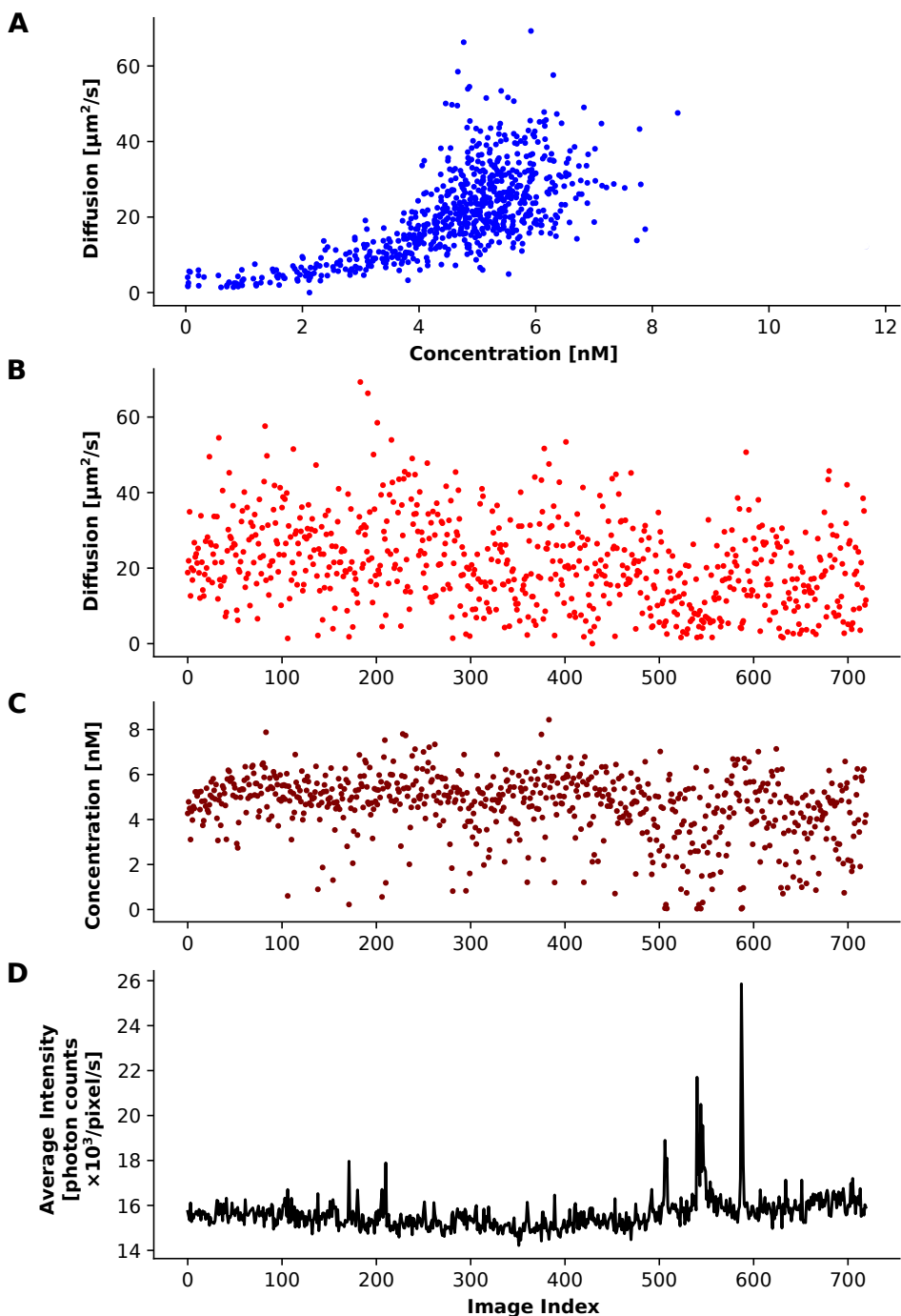


Figure 5: Diffusion-concentration pre-analysis of 720 individual RICS images. (A) Scatter plot of diffusion coefficient versus concentration for each image. (B) Diffusion coefficient as a function of image index. (C) Concentration as a function of image index. (D) Average fluorescence intensity per pixel per second across 720 consecutively acquired RICS images.

clusion of contaminated regions while retaining unaffected areas for analysis. For example, dividing the same 100 images into  $6 \times 6$  sectors yields 3600 individual ACFs; concentration-based filtering then excludes only 137 sectors (3.8%), preserving the vast majority of data. This approach yields improved fit quality (Figure 4D; SSR = 0.08) with parameter estimates (concentration:  $7.73 \pm 0.26$  nM; diffusion coefficient:  $15.64 \pm 0.50$   $\mu\text{m}^2/\text{s}$ ; triplet amplitude:  $0.44 \pm 0.04$ ; triplet relaxation time:  $1.31 \pm 0.22$   $\mu\text{s}$ ; mean  $\pm$  SD) consistent with those obtained from the larger filtered dataset (Figure 4C and B).

An early version of this filtering strategy was successfully applied in Paper II, which investigated the combined action of albumin and heparin in regulating lipoprotein lipase oligomerization. The RICS pre-analysis capabilities enabled accurate determination of diffusion coefficients by identifying and excluding large fluorescent aggregates from measurements containing heterogeneous oligomeric structures.

Following pre-analysis and identification of parameter values or datasets to be excluded, final parameter inference is performed using a flexible fitting framework supporting multiple diffusion models and statistical inference approaches. Implemented models include single- and two-component isotropic diffusion with optional triplet-state kinetics, formulated using either an idealized 3D Gaussian PSF or experimentally measured PSFs. This capability is critical for accurate parameter extraction in biological systems where idealized PSF approximations can introduce systematic biases. All models support anisotropic diffusion analysis, including RICS measurements acquired at multiple laser scanning angles, enabling characterization of direction-dependent transport in structured cellular environments.

To accommodate different noise characteristics and analysis goals, the platform implements a comprehensive suite of statistical methods, including OLS, weighted least squares (WLS), and GLS, each available within both nonlinear least squares (NLS) and Bayesian inference frameworks. This yields six distinct estimation approaches, allowing researchers to select the most appropriate method for their data characteristics and uncertainty quantification needs.

All ACF fitting results shown in Figure 4 were obtained using nonlinear least squares with weighted least squares error model (NLS-WLS) and an experimentally measured PSF. Guidance on selecting appropriate statistical frameworks for fitting, error models, and diffusion models for specific experimental conditions is provided in the discussion section of Paper I.

### 3.5 Results

The results presented in Paper I demonstrate that reliable inference of molecular diffusion parameters from FCS and RICS data depends critically on both the statistical treatment of noise and the flexibility of the analysis framework. Systematic comparisons using synthetic and experimental datasets show that commonly used OLS fitting can substantially underestimate parameter uncertainty. In contrast, weighted and generalized least-squares approaches explicitly account for non-uniform and correlated noise in ACFs, leading to more realistic uncertainty estimates. Bayesian inference further extends this framework by propagating noise structure into full posterior distributions, providing reliable confidence intervals and enabling principled model comparison through information criteria and Bayes factors.

The results highlight that the structure of noise correlations varies substantially with experimental conditions, such as diffusion speed, and directly impacts parameter reliability. By incorporating covariance-aware error models and Bayesian evidence evaluation, the platform enables objective selection of diffusion models, which is particularly important for

distinguishing between single-component, multi-component, and triplet-state models.

Beyond statistical rigor, the results establish the practical relevance of advanced RICS capabilities implemented in the software. The ability to analyze anisotropic diffusion using experimentally measured PSFs and to generate spatially resolved diffusion and concentration maps reveals heterogeneity that is inaccessible to conventional, spatially averaged analyses. Comprehensive visualization capabilities support all stages of analysis, including pre-analysis scatter plots for identifying outliers, fitted ACFs with residual diagnostics, posterior distribution summaries for Bayesian fits, angular dependence plots for multiple-angle RICS measurements, and spatially resolved parameter maps from sector-based analysis. These results show that IOCBIO FCS enables both efficient point estimation and statistically rigorous uncertainty quantification, providing quantitatively reliable insights into molecular transport in complex biological environments.

Representative fitting results, comparative analysis of statistical approaches, and validation studies are presented in Paper I. A broader interpretation and implications for diffusion analysis in biological systems is provided in the Discussion chapter. Comprehensive documentation, including usage examples and command-line interface specifications, is available at <https://iocbio.gitlab.io/fcs>.

## 4 Fluorescence Intensity Trace Statistical Analysis (FITSA)

### 4.1 Overview and Motivation

As discussed in Chapter 2, the Bayesian approach to direct intensity trace analysis proposed by Pressé and colleagues offered theoretical advantages over correlation-based methods, including reduced photon requirements and rigorous uncertainty quantification [53]. However, practical implementation suffered from computational inefficiency, convergence difficulties, and sensitivity to prior specification. While we initially investigated whether these limitations could be addressed through parameter tuning and algorithmic optimization of the existing framework, we found that the fundamental design of the method necessitated a complete reconceptualization. To address these deep-rooted challenges while retaining the benefits of direct intensity analysis, we developed FITSA—a fundamentally new Bayesian method built from first principles that achieves robust parameter estimation from fluorescence intensity traces with substantially improved computational efficiency and stability. As detailed in the following sections, FITSA differs from previous approaches in critical aspects.

### 4.2 Methodological Framework

FITSA introduces several critical innovations that enable practical application of direct Bayesian analysis to experimental fluorescence data. The method distinguishes between signal components originating from particles passing through the confocal volume and background emissions by identifying portions of the signal with elevated photon counts. A key innovation is adaptive signal binning that dynamically adjusts temporal resolution based on local photon emission rates: regions with high photon counts indicating particle presence are binned into short time intervals to capture rapid molecular movements, while regions dominated by background emissions are binned into longer intervals. The algorithm creates smooth transitions between different bin sizes, enabling efficient tracking of particles as they enter, traverse, and exit the confocal observation volume. Because particle diffusion events are assumed to be statistically independent, the fluorescence trace is segmented into distinct subsections by identifying low-photon regions that serve as natural division points between particle transit events, allowing separate analysis of each event while maintaining computational tractability.

For MCMC sampling of the posterior distribution, FITSA employs HMC with NUTS, which leverages gradient information to efficiently navigate the parameter space. Unlike the Gibbs sampling approach used in the *Jazani et al.* implementation [53], which samples parameters sequentially and can suffer from slow mixing in correlated parameter spaces, NUTS proposes joint updates across all parameters using Hamiltonian dynamics, substantially improving sampling efficiency [60].

Beyond computational efficiency, the fundamental methodological changes in FITSA—including the signal preprocessing and gradient-based sampling strategy—yield substantially improved robustness to prior specification. Detailed convergence diagnostics, posterior distributions, and sensitivity analyses are presented in Paper III.

### 4.3 Practical Advantages and Scope

The methodological design of FITSA achieves a critical advantage for practical diffusion measurements in biological systems: the method provides comparable precision to conventional FCS while requiring substantially fewer detected photons, enabling accurate diffusion coefficient estimation from measurement durations orders of magnitude shorter than

those needed for traditional correlation analysis. This efficiency gain stems from FITSA's direct analysis of intensity fluctuations, which extracts information from the complete photon arrival pattern rather than compressing it into a correlation function.

By reducing photon requirements, FITSA directly addresses phototoxicity concerns in live-cell experiments—a fundamental limitation of correlation-based techniques where extended measurements or spatial mapping across cellular regions necessitate cumulative laser exposure that can compromise cell viability and alter the biological processes under investigation.

#### 4.4 Validation and Results

The performance and robustness of FITSA were systematically validated through comprehensive analysis of both synthetic and experimental data, as detailed in Paper III. Using simulated fluorescence traces, we demonstrated FITSA's superior convergence behavior and robustness to prior specification across different diffusion coefficients and molecular brightness values. Direct comparison with the earlier implementation [53] revealed that FITSA achieves reliable convergence with substantially fewer iterations while maintaining accurate parameter recovery across a wide range of prior distributions; that implementation exhibited sensitivity to prior choice and convergence difficulties.

Precision analysis using synthetic data confirmed that FITSA achieves comparable accuracy to conventional FCS while requiring substantially fewer photons. This efficiency gain remained consistent across different molecular brightness conditions, with precision primarily determined by total photon count for both methods.

Experimental validation using Alexa Fluor 647 Dextran 10K in glycerol-water mixtures demonstrated FITSA's practical applicability to real fluorescence measurements. Analysis of subsections from extended recordings revealed that FITSA produced substantially more consistent diffusion coefficient estimates across different temporal segments compared to FCS, indicating improved stability for short-duration measurements. Systematic investigation of the effects of laser power and dye concentration (0.1 and 1 nM) confirmed the expected relationship between photon flux and estimation precision, with FITSA maintaining accurate parameter recovery under conditions where correlation analysis becomes unreliable due to insufficient photon statistics. Finally, application to diffusion measurements in rat cardiomyocytes established FITSA's capability for analyzing molecular transport in complex biological environments, where short measurement durations are essential to minimize phototoxicity while capturing spatially heterogeneous diffusion dynamics.

These experimental demonstrations confirm that FITSA provides a practical and robust alternative to FCS for quantifying molecular diffusion in biological systems, particularly where photon budget constraints or phototoxicity concerns limit the applicability of traditional methods.

The detailed performance evaluation, experimental validation, and comparative analyses of FITSA are presented in Paper III. The significance of these results in the context of fluorescence-based diffusion measurements and their broader methodological implications are discussed in the Discussion chapter.

## 5 Discussion

Measuring molecular diffusion in cardiomyocytes presents unique challenges due to the highly organized cellular architecture. The sarcomeric structure, extensive sarcoplasmic reticulum, and densely packed mitochondria create an environment where molecular diffusion is neither isotropic nor spatially uniform [15, 16]. Understanding this compartmentalization and anisotropic transport is essential for energy metabolism and excitation-contraction coupling research [4, 8, 9, 11].

However, fluorescence-based diffusion measurements face a central trade-off: achieving statistically rigorous parameter estimation requires extended measurements, while live-cell experiments demand minimal laser exposure to avoid phototoxicity. This discussion examines how the methods developed in this thesis address this trade-off, evaluates when each approach is most appropriate, and considers future directions for quantitative molecular transport analysis.

### 5.1 Statistical Rigor in Correlation-Based Analysis: Challenges and Solutions

The central methodological challenge in FCS and RICS analysis lies in the statistical structure of autocorrelation data. While the non-independence of ACF data points has been recognized for some time [47, 49], practical applications typically ignore these correlations during model fitting. This widespread practice has profound consequences: parameter uncertainties are systematically underestimated, goodness-of-fit metrics become unreliable, and model selection procedures favor overly complex models that capture noise rather than underlying physical processes. The problem is not merely technical but reflects a fundamental limitation of the correlation-based approach when applied under realistic experimental conditions.

The IOCBIO FCS platform addresses these statistical challenges by providing the first open-source implementation integrating multiple statistical frameworks—OLS, WLS, and GLS (available only for FCS)—within both NLS and Bayesian inference approaches. This comprehensive suite enables researchers to select methods appropriate for their data characteristics and experimental constraints. OLS assumes identical error across all ACF points and independence between measurements, leading to artificially narrow parameter distributions but remaining useful for rapid preliminary analysis. WLS accounts for heteroscedastic errors using point-wise variance estimates, offering a practical compromise applicable to both FCS and RICS. GLS accounts for both heteroscedasticity and temporal correlations, providing the most reliable metrics when covariance can be estimated from replicate measurements.

Bayesian inference yields full posterior distributions that reveal parameter correlations. When sufficient repeated measurements are available, GLS fitting within the Bayesian inference framework provides statistically rigorous uncertainty quantification by properly accounting for correlated and heteroscedastic noise.

However, proper implementation of these advanced statistical treatments reveals the depth of the challenge. Properly accounting for statistical correlations through covariance estimation requires datasets orders of magnitude larger than those typically acquired. For FCS, estimating a reliable covariance matrix demands thousands of repeated measurements under strictly stable conditions—experiments lasting tens to hundreds of hours (approximately 100 hours for a single *in vitro* experiment in Paper I) with rigorous precautions to minimize room-scale temperature and airflow variability. Such stability is achievable only in simplified *in vitro* systems. In live-cell environments, the extended laser

exposure required for such high photon counts introduces prohibitive challenges. Beyond threats to cell viability, photobleaching progressively depletes fluorophore populations and biases diffusion estimates, while photoblinking creates artificial fluctuations that distort correlation functions [71–74]. Over these extended acquisition periods, mechanical drift inevitably shifts the observation volume, compromising spatial localization and introducing spurious correlations.

For RICS, the situation is even more severe. Reliable estimation of such a covariance matrix would require thousands of independent RICS images acquired under identical conditions (image size, scanning speed, and scanning angle)—practically infeasible in live-cell experiments given the additional constraints of flyback periods that extend acquisition times. Consequently, GLS fitting is currently not implemented for RICS, restricting model comparison to WLS-based metrics or residual assessment.

The fundamental challenge is clear: achieving statistical rigor in correlation-based analysis requires dataset sizes that are achievable only in highly controlled *in vitro* conditions and for live-cell experiments, the long acquisition times are practically infeasible. This incompatibility between statistical requirements and biological constraints cannot be resolved through better statistical methods alone—it demands a fundamentally different approach to extracting diffusion parameters from fluorescence data. The need for a method capable of obtaining reliable diffusion coefficients from substantially shorter experiments became evident as a critical requirement for advancing live-cell molecular transport analysis.

## 5.2 Beyond Correlation: Direct Intensity Analysis with FITSA

FITSA represents a conceptual departure from correlation-based analysis by treating fluorescence intensity traces as primary data rather than as inputs for correlation function calculation. This fundamental shift addresses both the statistical limitations of ACF-based methods and their photon efficiency constraints. By analyzing complete photon arrival patterns rather than compressing them into correlation functions, FITSA extracts information more efficiently and avoids the problematic statistical structure inherent to autocorrelation data.

While earlier implementation of direct intensity analysis by *Jazani* and colleagues [53] established the conceptual foundation for this approach, they faced significant practical limitations that hindered routine experimental adoption. This implementation required substantially more MCMC iterations to achieve convergence, exhibited sensitivity to prior specification that could lead to biased parameter estimates when priors deviated from true values, and proved computationally demanding for analyzing longer fluorescence traces. These limitations prevented direct intensity analysis from becoming a practical alternative to FCS despite its theoretical advantages.

FITSA's key innovations—adaptive signal binning, subsection segmentation treating particle transits as independent events, strategic seed point selection at maximum photon emission, and implementation of HMC with NUTS rather than Gibbs sampling—enable substantially improved convergence and substantially greater robustness to prior specification. The sectioning approach addresses a fundamental challenge in direct trajectory analysis: when reconstructing complete particle trajectories, coordinate positions become strongly correlated throughout the trajectory, with any change at the beginning affecting all subsequent positions. This correlation is particularly problematic when combined with varying position precision—high when particles are near the focal point and low when they are distant. FITSA overcomes this challenge by confining coordinate correlations within short segments and initiating sampling from well-constrained positions, enabling efficient

posterior exploration that earlier methods could not achieve.

The photon efficiency comparison between FITSA and FCS requires careful interpretation in light of the statistical issues discussed above. Standard FCS analysis assuming independent residuals yields artificially narrow confidence intervals—an incorrect assessment that creates the appearance of precision without corresponding accuracy [47, 49]. When properly accounting for correlations through covariance estimation, FCS requires vastly larger datasets. Considering these statistical requirements, FITSA estimates diffusion coefficients using substantially fewer photons than FCS, with advantages more pronounced for slower diffusion coefficients typical of intracellular environments [15, 16].

This substantial photon reduction has immediate practical implications for live-cell research by directly addressing the experimental challenges described above. Shorter measurements enabled by FITSA's photon efficiency mitigate these artifacts while enabling extensive spatial mapping across cellular regions without cumulative damage, establishing FITSA as a practical alternative to FCS for diffusion measurements in live-cell applications.

### 5.3 IOCBIO FCS Platform: Addressing Critical Gaps in Correlation Analysis

Given the current limitations of FITSA discussed in the following subsection, correlation-based methods (FCS and RICS) remain essential for complex diffusion models, multi-component systems, triplet-state dynamics, and anisotropic transport. Existing open-source FCS and RICS software [29, 62–70] lack several critical capabilities: none support multiple-angle RICS analysis for characterizing anisotropic diffusion; none incorporate experimentally measured 3D PSFs into fitting procedures; only one implementation provides GPU acceleration for ACF calculation; and none implement Bayesian inference for correlation data analysis.

The IOCBIO FCS platform addresses these critical gaps through several unique capabilities. First, it provides the first open-source implementation of Bayesian inference for correlation-based analysis, enabling principled model comparison through Bayes factors while properly incorporating prior knowledge. Proper error modeling is critical for model selection: as demonstrated with synthetic data in Paper I, neglecting the correlated noise structure in correlation data can lead to selection of incorrect models or result in Bayes factor differences below the threshold required for confident model selection [47, 49, 56].

Second, the platform enables direct incorporation of experimentally measured 3D PSFs into fitting procedures. Experimentally measured PSFs substantially improve fit quality compared to analytical Gaussian models. This capability is essential for accurate parameter extraction in anisotropic systems such as cardiomyocytes [15, 16]. The platform allows flexible voxel downsampling of PSFs to balance accuracy and computational efficiency, enabling users to optimize the accuracy-speed tradeoff based on PSF resolution and computational resources.

Third, The platform's support for multiple-angle RICS analysis represents another critical innovation for characterizing anisotropic diffusion. By acquiring RICS data at different scanning angles within the same sample, researchers can characterize direction-dependent transport patterns that reflect cellular ultrastructure. The combination of multiple-angle RICS with experimentally measured PSFs enables quantification of anisotropic diffusion that remains hidden when using single-angle acquisitions or idealized PSF models. Application to cardiomyocyte measurements (shown in Paper I) revealed clear directional dependencies in molecular diffusion that reflect sarcomeric organization, demonstrating the platform's capability for characterizing anisotropic transport in highly structured cells.

GPU-accelerated autocorrelation computation substantially reduces processing time for large datasets, achieving 19-fold speedup for FCS analysis and 8-fold speedup for RICS

processing, making high-throughput analysis and extensive spatial mapping practically feasible by reducing processing.

Spatial mapping through region-based RICS analysis reveals subcellular domains with distinct diffusion and concentration properties. This capability enables investigation of compartmentalization in energy metabolism pathways [4, 8, 9, 11], where localized enzyme systems and restricted molecular mobility contribute to efficient metabolic regulation.

The platform also implements diffusion coefficient and concentration pre-analysis and filtering strategies to identify and exclude poor-quality measurements before main parameter estimation, improving robustness in heterogeneous biological samples. These capabilities collectively enable rigorous quantitative characterization of molecular transport in complex biological systems.

## 5.4 Limitations, and Future Directions

The FITSA method currently faces limitations that constrain its applicability despite its advantages in photon efficiency and convergence reliability. The method is restricted to relatively simple diffusion models—specifically, 3D single-component isotropic diffusion without triplet-state kinetics—limiting its ability to analyze more complex scenarios such as multi-component diffusion, anomalous diffusion, or systems where photophysical processes significantly affect fluorescence signals. Current FITSA implementation requires low fluorophore concentrations (below approximately 1 nM) to maintain the assumption of independent particle transit events and enable reliable background identification. At higher concentrations where multiple particles continuously contribute to the signal, the method faces challenges in determining background emission levels and separating overlapping particle events. Additionally, while FITSA is computationally more efficient than earlier direct intensity analysis implementation, it remains more demanding than conventional FCS analysis, particularly for longer traces or large experimental datasets.

Future development of direct analysis methods should prioritize extending model complexity to address these constraints. Integration of triplet-state kinetics, multi-component diffusion, anomalous diffusion models, and realistic PSF shapes would substantially broaden FITSA's applicability. Handling higher fluorophore concentrations through multi-particle trajectory reconstruction represents another important direction, potentially enabling analysis of more complex biological systems.

For FCS method, implementing segmented and randomized ACF approaches [47] represents a promising direction for future development of the IOCBIO FCS platform. These methods reduce correlations between ACF data points, enabling reliable goodness-of-fit evaluation with shorter experiments and partially resolving the conflict between statistical rigor and experimental feasibility in live-cell applications.

Currently, PSFs are characterized in solution rather than within live cells; future development of methods for in-cell PSF characterization would improve accuracy, particularly for detecting anisotropy where systematic PSF errors can approach or exceed the magnitude of directional diffusion differences. As a current practical solution, the IOCBIO FCS platform allows PSF scale as an additional free parameter during fitting to accommodate calibration uncertainties. Additionally, extending GPU acceleration to Bayesian inference frameworks could substantially reduce the computational time currently required for posterior sampling [75].

Machine learning (ML) and deep learning (DL) approaches have recently been explored for FCS applications [76]. Convolutional neural networks trained on simulated data can predict diffusion parameters directly from intensity traces, reducing data requirements and enabling near real-time inference [77]. ML approaches have also been applied for artifact

filtering [74] and anomalous diffusion classification [78]. However, these approaches face limitations: training on simulated data may not generalize to real experimental conditions that vary across microscopes; learned representations lack physical interpretability, hindering failure diagnosis; and integrated uncertainty quantification is limited. ML/DL methods are thus complementary to correlation-based approaches—excelling at rapid screening when training data exist, while correlation methods provide interpretable, physically grounded parameters with rigorous statistical inference.

The choice among approaches depends on experimental constraints and scientific goals, with each method offering distinct advantages for different scenarios. The IOCBIO FCS platform is optimal for anisotropic diffusion characterization, multi-component diffusion, triplet-state kinetics, spatial parameter mapping, and moderate-to-high concentrations. Current FITSA implementation excels for brief measurements at low concentrations with simple single-component isotropic diffusion. ML/DL methods suit real-time analysis and classification tasks.

## Conclusions

This thesis developed two computational approaches for fluorescence-based diffusion measurements: the IOCBIO FCS platform for correlation-based analysis and FITSA for direct Bayesian analysis of intensity traces.

- IOCBIO FCS provides the first open-source implementation combining Bayesian inference for FCS/RICS analysis, experimentally measured PSF support, and multiple-angle RICS capabilities for anisotropic diffusion characterization.
- Rigorous statistical treatment of autocorrelation data requires impractically large datasets for live-cell experiments, representing a fundamental limitation of correlation-based approaches.
- FITSA achieves comparable precision to FCS with substantially fewer photons by analyzing intensity traces directly, enabling shorter measurements that reduce phototoxicity in live-cell applications.
- These approaches serve complementary roles: IOCBIO FCS for complex scenarios (multi-component diffusion, triplet-state dynamics, anisotropic transport), FITSA for photon-limited single-component measurements.

## References

- [1] **Hamed Karimi**, Otto Gustavson, Irina Česnokova, Jelena Branovets, Rikke Birkedal, Martin Laasmaa, and Marko Vendelin. A Unified Platform for FCS and RICS Analysis with Advanced Statistical Inference. *ACS Omega*, 2026.
- [2] Robert Risti, Kathryn H. Gunn, Kristofer Hiis-Hommuk, Natjan-Naatan Seeba, **Hamed Karimi**, Ly Villo, Marko Vendelin, Saskia B. Neher, and Aivar Lõokene. Combined action of albumin and heparin regulates lipoprotein lipase oligomerization, stability, and ligand interactions. *PLOS ONE*, 18(4):e0283358, 2023.
- [3] **Hamed Karimi**, Martin Laasmaa, Margus Pihlak, and Marko Vendelin. Statistical analysis of fluorescence intensity transients with Bayesian methods. *Science Advances*, 11(16):eads4609, 2025.
- [4] A. Kaasik, V. Veksler, E. Boehm, M. Novotova, A. Minajeva, and R. Ventura-Clapier. Energetic crosstalk between organelles: Architectural integration of energy production and utilization. *Circ.Res.*, 89(2):153–159, 2001.
- [5] Rikke Birkedal, Martin Laasmaa, Jelena Branovets, and Marko Vendelin. Ontogeny of cardiomyocytes: Ultrastructure optimization to meet the demand for tight communication in excitation–contraction coupling and energy transfer. *Philosophical Transactions of the Royal Society B: Biological Sciences*, 377(1864):20210321, 2022.
- [6] Pauline M. Bennett, Elisabeth Ehler, and Amanda J. Wilson. Sarcoplasmic reticulum is an intermediary of mitochondrial and myofibrillar growth at the intercalated disc. *Journal of Muscle Research and Cell Motility*, 37(3):55–69, 2016.
- [7] Sanjeewa A. Goonasekera and Jeffery D. Molkenstin. Unraveling the secrets of a double life: Contractile versus signaling Ca<sup>2+</sup> in a cardiac myocyte. *Journal of Molecular and Cellular Cardiology*, 52(2):317–322, 2012.
- [8] Alexey E. Alekseev, Santiago Reyes, Vitaly A. Selivanov, Petras P. Dzeja, and Andre Terzic. Compartmentation of membrane processes and nucleotide dynamics in diffusion-restricted cardiac cell microenvironment. *Journal of Molecular and Cellular Cardiology*, 52(2):401–409, 2012.
- [9] Rikke Birkedal, Jelena Branovets, and Marko Vendelin. Compartmentalization in cardiomyocytes modulates creatine kinase and adenylate kinase activities. *FEBS Letters*, 598(21):2623–2640, 2024.
- [10] Hena R. Ramay and Marko Vendelin. Diffusion Restrictions Surrounding Mitochondria: A Mathematical Model of Heart Muscle Fibers. *Biophysical Journal*, 97(2):443–452, 2009.
- [11] Mervi Sepp, Marko Vendelin, Heiki Vija, and Rikke Birkedal. ADP Compartmentation Analysis Reveals Coupling between Pyruvate Kinase and ATPases in Heart Muscle. *Biophysical Journal*, 98:2785–2793, 2010.
- [12] Päivo Simson, Natalja Jepihhina, Martin Laasmaa, Pearu Peterson, Rikke Birkedal, and Marko Vendelin. Restricted ADP movement in cardiomyocytes: Cytosolic diffusion obstacles are complemented with a small number of open mitochondrial voltage-dependent anion channels. *Journal of Molecular and Cellular Cardiology*, 97:197–203, 2016.

- [13] Natalja Jephina, Nathalie Beraud, Mervi Sepp, Rikke Birkedal, and Marko Vendelin. Permeabilized Rat Cardiomyocyte Response Demonstrates Intracellular Origin of Diffusion Obstacles. *Biophysical Journal*, 101(9):2112–2121, 2011.
- [14] Rikke Birkedal, Martin Laasmaa, and Marko Vendelin. The location of energetic compartments affects energetic communication in cardiomyocytes. *Frontiers in Physiology*, 5, 2014.
- [15] Marko Vendelin and Rikke Birkedal. Anisotropic diffusion of fluorescently labeled ATP in rat cardiomyocytes determined by raster image correlation spectroscopy. *American Journal of Physiology-Cell Physiology*, 295(5):C1302–C1315, 2008.
- [16] Ardo Illaste, Martin Laasmaa, Pearu Peterson, and Marko Vendelin. Analysis of Molecular Movement Reveals Latticelike Obstructions to Diffusion in Heart Muscle Cells. *Biophysical Journal*, 102(4):739–748, 2012.
- [17] Alessandra Ghigo and Delphine Mika. cAMP/PKA signaling compartmentalization in cardiomyocytes: Lessons from FRET-based biosensors. *Journal of Molecular and Cellular Cardiology*, 131:112–121, 2019.
- [18] Ting-Yu Lin, Quynh N. Mai, Hao Zhang, Emily Wilson, Huan-Chieh Chien, Sook Wah Yee, Kathleen M. Giacomini, Jeffrey E. Olgin, and Roshanak Irannejad. Cardiac contraction and relaxation are regulated by distinct subcellular cAMP pools. *Nature Chemical Biology*, 20(1):62–73, 2024.
- [19] Seong S. Han. *Cell Biology*. McGraw-Hill, New York, 1979.
- [20] K. Hopkin, A.D. Johnson, D. Morgan, M. Raff, K. Roberts, and P. Walter. *Essential Cell Biology: Fifth International Student Edition*. W.W. Norton, 2018.
- [21] K. Luby-Phelps. Cytoarchitecture and physical properties of cytoplasm: Volume, viscosity, diffusion, intracellular surface area. *International Review of Cytology*, 192:189–221, 2000.
- [22] Alan S Verkman. Solute and macromolecule diffusion in cellular aqueous compartments. *Trends in Biochemical Sciences*, 27(1):27–33, 2002.
- [23] Steven B. Zimmerman and Stefan O. Trach. Estimation of macromolecule concentrations and excluded volume effects for the cytoplasm of *Escherichia coli*. *Journal of Molecular Biology*, 222(3):599–620, 1991.
- [24] Elliot L Elson and Douglas Magde. Fluorescence correlation spectroscopy. i. conceptual basis and theory. *Biopolymers*, 13(1):1–27, 1974.
- [25] Elliot L. Elson. Fluorescence Correlation Spectroscopy: Past, Present, Future. *Biophysical Journal*, 101(12):2855–2870, 2011.
- [26] Elke Haustein and Petra Schwill. Fluorescence Correlation Spectroscopy: Novel Variations of an Established Technique. *Annual Review of Biophysics*, 36(Volume 36, 2007):151–169, 2007.
- [27] Michelle A. Digman, Claire M. Brown, Parijat Sengupta, Paul W. Wiseman, Alan R. Horwitz, and Enrico Gratton. Measuring Fast Dynamics in Solutions and Cells with a Laser Scanning Microscope. *Biophysical Journal*, 89(2):1317–1327, 2005.

- [28] Michelle A. Digman and Enrico Gratton. Analysis of diffusion and binding in cells using the RICS approach. *Microscopy Research and Technique*, 72(4):323–332, 2009.
- [29] Molly J. Rossow, Jennifer M. Sasaki, Michelle A. Digman, and Enrico Gratton. Raster image correlation spectroscopy in live cells. *Nature Protocols*, 5(11):1761–1774, 2010.
- [30] Kirsten Bacia, Sally A. Kim, and Petra Schwille. Fluorescence cross-correlation spectroscopy in living cells. *Nature Methods*, 3(2):83–89, 2006.
- [31] Sally A. Kim, Katrin G. Heinze, and Petra Schwille. Fluorescence correlation spectroscopy in living cells. *Nature Methods*, 4(11):963–973, 2007.
- [32] Howard C. Berg. *Random Walks in Biology*. Princeton University Press, 1993.
- [33] John Crank. *The Mathematics of Diffusion*. Clarendon Press, 1979.
- [34] M. H. Jacobs. *Diffusion Processes*. Springer-Verlag, New York, 1967.
- [35] Hannes Risken. *The Fokker-Planck Equation: Methods of Solution and Applications*, volume 18 of *Springer Series in Synergetics*. Springer, Berlin, Heidelberg, 1996.
- [36] C. W. Gardiner. *Handbook of Stochastic Methods*. Springer, 4 edition, 2009.
- [37] Manuela Zaccolo and Tullio Pozzan. Discrete Microdomains with High Concentration of cAMP in Stimulated Rat Neonatal Cardiac Myocytes. *Science*, 295(5560):1711–1715, 2002.
- [38] Marko Vendelin, Olav Kongas, and Valdur Saks. Regulation of mitochondrial respiration in heart cells analyzed by reaction-diffusion model of energy transfer. *Am J Physiol Cell Physiol*, 278(4):C747–764, 2000.
- [39] Bertil Hille. *Ion Channels of Excitable Membranes (3rd Edition)*. Sinauer Associates, 2001.
- [40] Mark Richards, Oliver Lomas, Kees Jalink, Kerrie L. Ford, Richard D. Vaughan-Jones, Konstantinos Lefkimmiatis, and Pawel Swietach. Intracellular tortuosity underlies slow cAMP diffusion in adult ventricular myocytes. *Cardiovascular Research*, 110(3):395–407, 2016.
- [41] E. P. Petrov and P. Schwille. State of the Art and Novel Trends in Fluorescence Correlation Spectroscopy. In Ute Resch-Genger, editor, *Standardization and Quality Assurance in Fluorescence Measurements II: Bioanalytical and Biomedical Applications*, Springer Series on Fluorescence, pages 145–197. Springer, 2008.
- [42] Jerker Widengren, Uelo Mets, and Rudolf Rigler. Fluorescence correlation spectroscopy of triplet states in solution: A theoretical and experimental study. *The Journal of Physical Chemistry*, 99(36):13368–13379, 1995.
- [43] Jaroslav Icha, Michael Weber, Jennifer C. Waters, and Caren Norden. Phototoxicity in live fluorescence microscopy, and how to avoid it. *BioEssays*, 39(8):1700003, 2017.
- [44] Dennis E. Koppel. Statistical accuracy in fluorescence correlation spectroscopy. *Physical Review A*, 10(6):1938–1945, 1974.
- [45] Thorsten Wohland, Rudolf Rigler, and Horst Vogel. The Standard Deviation in Fluorescence Correlation Spectroscopy. *Biophysical Journal*, 80(6):2987–2999, 2001.

- [46] Saveez Saffarian and Elliot L. Elson. Statistical Analysis of Fluorescence Correlation Spectroscopy: The Standard Deviation and Bias. *Biophysical Journal*, 84(3):2030–2042, 2003.
- [47] John Kohler, Kwang-Ho Hur, and Joachim Dieter Mueller. Statistical analysis of the autocorrelation function in fluorescence correlation spectroscopy. *Biophysical Journal*, 123(6):667–680, 2024.
- [48] Jun He, Syuan-Ming Guo, and Mark Bathe. Bayesian Approach to the Analysis of Fluorescence Correlation Spectroscopy Data I: Theory. *Anal. Chem.*, 84(9):3871–3879, 2012.
- [49] Syuan-Ming Guo, Jun He, Nilah Monnier, Guangyu Sun, Thorsten Wohland, and Mark Bathe. Bayesian Approach to the Analysis of Fluorescence Correlation Spectroscopy Data II: Application to Simulated and In Vitro Data. *Anal. Chem.*, 2012.
- [50] Olivier Ledoit and Michael Wolf. A well-conditioned estimator for large-dimensional covariance matrices. *Journal of Multivariate Analysis*, 88(2):365–411, 2004.
- [51] Jianqing Fan, Yuan Liao, and Han Liu. An overview of the estimation of large covariance and precision matrices. *The Econometrics Journal*, 19(1):C1–C32, 2016.
- [52] Sina Jazani, Ioannis Sgouralis, and Steve Pressé. A method for single molecule tracking using a conventional single-focus confocal setup. *The Journal of Chemical Physics*, 150(11):114108, 2019.
- [53] Sina Jazani, Ioannis Sgouralis, Omer M. Shafraz, Marcia Levitus, Sanjeevi Sivasankar, and Steve Pressé. An alternative framework for fluorescence correlation spectroscopy. *Nature Communications*, 10(1):3662, 2019.
- [54] Meysam Tavakoli, Sina Jazani, Ioannis Sgouralis, Omer M. Shafraz, Sanjeevi Sivasankar, Bryan Donaphon, Marcia Levitus, and Steve Pressé. Pitching Single-Focus Confocal Data Analysis One Photon at a Time with Bayesian Nonparametrics. *Physical Review X*, 10(1):011021, 2020.
- [55] Sina Jazani, Lance W. Q. Xu, Ioannis Sgouralis, Douglas P. Shepherd, and Steve Pressé. Computational Proposal for Tracking Multiple Molecules in a Multifocus Confocal Setup. *ACS Photonics*, 9(7):2489–2498, 2022.
- [56] Sir Harold Jeffreys and Sir Harold Jeffreys. *The Theory of Probability*. Oxford Classic Texts in the Physical Sciences. Oxford University Press, Oxford, New York, third edition, third edition edition, 1998.
- [57] Steve Brooks, Andrew Gelman, Galin Jones, and Xiao-Li Meng, editors. *Handbook of Markov Chain Monte Carlo*. Chapman and Hall/CRC, New York, 2011.
- [58] James O. Berger and William H. Jefferys. The application of robust Bayesian analysis to hypothesis testing and Occam’s Razor. *Journal of the Italian Statistical Society*, 1(1):17–32, 1992.
- [59] W. K. Hastings. Monte Carlo Sampling Methods Using Markov Chains and Their Applications. *Biometrika*, 57(1):97–109, 1970.

- [60] Matthew D. Hoffman and Andrew Gelman. The No-U-Turn Sampler: Adaptively Setting Path Lengths in Hamiltonian Monte Carlo. *Journal of Machine Learning Research*, 15(47):1593–1623, 2014.
- [61] Andrew Gelman and Donald B. Rubin. Inference from Iterative Simulation Using Multiple Sequences. *Statistical Science*, 7(4):457–472, 1992.
- [62] Jagadish Sankaran, Xianke Shi, Liang Yoong Ho, Ernst H. K. Stelzer, and Thorsten Wohland. ImFCS: A software for Imaging FCS data analysis and visualization. *Optics Express*, 18(25):25468–25481, 2010.
- [63] Johannes Schindelin, Ignacio Arganda-Carreras, Erwin Frise, Verena Kaynig, Mark Longair, Tobias Pietzsch, Stephan Preibisch, Curtis Rueden, Stephan Saalfeld, Benjamin Schmid, Jean-Yves Tinevez, Daniel James White, Volker Hartenstein, Kevin Eliceiri, Pavel Tomancak, and Albert Cardona. Fiji: An open-source platform for biological-image analysis. *Nature Methods*, 9(7):676–682, 2012.
- [64] Paul Müller, Petra Schwille, and Thomas Weidemann. PyCorrFit—generic data evaluation for fluorescence correlation spectroscopy. *Bioinformatics*, 30(17):2532–2533, 2014.
- [65] Dominic Waithe, Falk Schneider, Jakub Chojnacki, Mathias P. Clausen, Dilip Shrestha, Jorge Bernardino de la Serna, and Christian Eggeling. Optimized processing and analysis of conventional confocal microscopy generated scanning FCS data. *Methods*, 140–141:62–73, 2018.
- [66] Antonio Z. Politi, Yin Cai, Nike Walther, M. Julius Hossain, Birgit Koch, Malte Wachsmuth, and Jan Ellenberg. Quantitative mapping of fluorescently tagged cellular proteins using FCS-calibrated four-dimensional imaging. *Nature Protocols*, 13(6):1445–1464, 2018.
- [67] Waldemar Schrimpf, Anders Barth, Jelle Hendrix, and Don C. Lamb. PAM: A Framework for Integrated Analysis of Imaging, Single-Molecule, and Ensemble Fluorescence Data. *Biophysical Journal*, 114(7):1518–1528, 2018.
- [68] R Pinto-Cámara, A Linares, D. S Moreno-Gutiérrez, H. O Hernández, J. D Martínez-Reyes, J. M Rendón-Mancha, C. D Wood, and A Guerrero. FCSlib: An open-source tool for fluorescence fluctuation spectroscopy analysis for mobility, number and molecular brightness in R. *Bioinformatics*, 37(13):1930–1931, 2021.
- [69] Shawn Yoshida, William Schmid, Nam Vo, William Calabrese, and Lydia Kisley. Computationally-efficient spatiotemporal correlation analysis super-resolves anomalous diffusion. *Optics Express*, 29(5):7616–7629, 2021.
- [70] Jagadish Sankaran, Harikrushnan Balasubramanian, Wai Hoh Tang, Xue Wen Ng, Adrian Röllin, and Thorsten Wohland. Simultaneous spatiotemporal super-resolution and multi-parametric fluorescence microscopy. *Nature Communications*, 12(1):1748, 2021.
- [71] Vivien Octeau, Laurent Cognet, Laurence Duchesne, David Lasne, Nicolas Schaeffer, David G. Fernig, and Brahim Lounis. Photothermal Absorption Correlation Spectroscopy. *ACS Nano*, 3(2):345–350, 2009.

- [72] Cameron Hodges, Rudra P. Kafle, J. Damon Hoff, and Jens-Christian Meiners. Fluorescence Correlation Spectroscopy with Photobleaching Correction in Slowly Diffusing Systems. *Journal of Fluorescence*, 28(2):505–511, 2018.
- [73] Lili Zhang, Carmina Perez-Romero, Nathalie Dostatni, and Cécile Fradin. Using FCS to accurately measure protein concentration in the presence of noise and photobleaching. *Biophysical Journal*, 120(19):4230–4241, 2021.
- [74] Alva Seltmann, Pablo Carravilla, Katharina Reglinski, Christian Eggeling, and Dominic Waithe. Neural network informed photon filtering reduces fluorescence correlation spectroscopy artifacts. *Biophysical Journal*, 123(6):745–755, 2024.
- [75] Andrew L. Beam, Sujit K. Ghosh, and Jon Doyle. Fast Hamiltonian Monte Carlo Using GPU Computing. *Journal of Computational and Graphical Statistics*, 25(2):536–548, 2016.
- [76] Jörg Enderlein. Machine learning and advanced statistical analysis for fluorescence correlation spectroscopy. *Biophysical Journal*, 123(6):651–652, 2024.
- [77] Wai Hoh Tang, Shao Ren Sim, Daniel Ying Kia Aik, Ashwin Venkata Subba Nelanuthala, Thamarailingam Athilingam, Adrian Röllin, and Thorsten Wohland. Deep learning reduces data requirements and allows real-time measurements in imaging FCS. *Biophysical Journal*, 123(6):655–666, 2024.
- [78] Nathan Quiblier, Jan-Michael Rye, Pierre Leclerc, Henri Truong, Abdelkrim Hannou, Laurent Heliot, and Hugues Berry. Enhancing fluorescence correlation spectroscopy with machine learning to infer anomalous molecular motion. *Biophysical Journal*, 124(5):844–856, 2025.

## Acknowledgements

First and foremost, I would like to express my deepest gratitude to my main supervisor, Marko Vendelin. I truly owe this work to his guidance, trust, and continuous support throughout my PhD. Marko gave me the freedom to explore ideas independently while always being available with thoughtful advice, sharp scientific insight, and calm encouragement when challenges arose. His patience, integrity, and deep understanding of science shaped not only this thesis but also my development as a researcher. Above all, I am grateful for the trust he placed in me over these four years, which allowed me to grow with confidence and motivation. I could not have asked for a better supervisor.

I would also like to sincerely thank my co-supervisor, Martin Laasmaa, for his valuable scientific input, constructive discussions, and support during this work.

I am grateful to my colleagues Rikke Birkedal, Jelena Branovets, Irina Česnokova, and Otto Gustavson, who made significant contributions to the work presented in this thesis. Thank you for your dedication, collaboration, and the many helpful discussions. I wish you all the very best in your future paths. I also thank my other colleagues and collaborators who contributed to this work and helped me.

I sincerely thank my wife and my family for their patience, encouragement, and constant support throughout my PhD.

This research was supported by the Estonian Research Council (grant PRG1127). I am grateful for the opportunity to conduct my doctoral studies in Estonia and for the supportive research environment provided during this work. This work was carried out in the Laboratory of Systems Biology at the Institute of Cybernetics, Tallinn University of Technology (TalTech).

The grammar and language of this thesis were refined with the assistance of AI tools (Claude and ChatGPT).

## Abstract

# Development of Computational and Statistical Methods for Fluorescence-Based Diffusion Measurements

Molecular diffusion plays a fundamental role in cellular physiology, yet accurate measurement of diffusion coefficients in living cells remains challenging due to limitations in existing analysis methods and phototoxicity constraints from prolonged laser exposure. This thesis addresses these challenges through development of two computational approaches for fluorescence-based diffusion measurements: IOCBIO FCS, an enhanced platform for correlation spectroscopy analysis, and fluorescence intensity trace statistical analysis (FITSA), a novel method based on direct Bayesian analysis of intensity traces.

Fluorescence correlation spectroscopy (FCS) and raster image correlation spectroscopy (RICS) are established techniques for measuring molecular dynamics through analysis of fluorescence intensity fluctuations. However, current analysis methods suffer from critical limitations. More fundamentally, conventional fitting approaches based on OLS incorrectly assume identical error variance across all autocorrelation function (ACF) data points and statistical independence between measurements, leading to underestimated uncertainties and unreliable model selection.

To address these software limitations in correlation-based methods, we developed IOCBIO FCS, a unified open-source Python platform integrating GPU-accelerated autocorrelation computation, comprehensive statistical inference frameworks (Bayesian and frequentist approaches with ordinary, weighted, and generalized least-squares error treatment), support for experimentally measured 3D PSFs, and capabilities for multiple-angle RICS analysis at variable scanning speeds. The platform enables spatial mapping of diffusion parameters across heterogeneous samples and characterization of anisotropic diffusion in organized cellular structures. Validation studies demonstrate that proper error modeling substantially affects parameter uncertainty estimates and model selection outcomes, with neglect of correlation structure leading to unreliable conclusions about system complexity.

The platform implements diffusion-concentration pre-analysis for quality control, enabling identification and exclusion of measurements contaminated by artifacts such as large fluorescent aggregates or unstable fluorescence before main parameter estimation. For RICS measurements, image-splitting strategies combined with concentration-based filtering systematically detect and remove images affected by rare high-intensity events that would otherwise distort spatial correlation analysis. Application of these RICS pre-analysis capabilities to study lipoprotein lipase oligomerization demonstrated practical utility of the filtering algorithms for characterizing diffusion in samples containing mixtures of different oligomeric states in the presence of large particle artifacts.

Proper treatment of correlated and heteroscedastic errors through covariance estimation requires thousands of repeated measurements under stable conditions—practically infeasible in live-cell experiments due to phototoxicity and cell viability constraints. To address the fundamental photon efficiency limitations of correlation-based techniques, we developed FITSA, a Bayesian method that analyzes fluorescence intensity traces directly rather than through derived ACFs. Key innovations include adaptive signal binning that adjusts temporal resolution based on local photon emission rates, subsection segmentation treating particle transits as independent events, and strategic seed point selection at maximum photon emission enabling efficient posterior sampling. Comparative analysis demonstrates that FITSA achieves convergence with substantially fewer iterations than earlier direct intensity analysis implementation, providing faster computation with improved robustness to prior specification. When comparing to FCS with rigorous covariance

estimation—which requires thousands of repeated measurements—FITSA estimates diffusion coefficients with substantially fewer total photons, with advantages more pronounced for slower diffusion characteristic of intracellular environments. This substantial photon reduction enables shorter measurement durations, directly addressing phototoxicity concerns that limit live-cell applications of correlation spectroscopy.

These complementary tools address different experimental needs: IOCBIO FCS for complex scenarios including multi-component diffusion, triplet-state dynamics, and anisotropic transport; FITSA for photon-limited measurements where phototoxicity is critical.

## Kokkuvõte

### Fluorestsentsipõhiste difusioonimõõtmiste arvutuslike ja statistiliste meetodite väljatöötamine

Molekulaarne difusioon mängib raku füsioloogias fundamentaalset rolli, kuid difusioonikonstandi täpne mõõtmine elusrakkudes on endiselt keeruline olemasolevate analüüsimeetodite piirangute ning pikaajalisest laserkiirgusest tuleneva fototoksilisuse tõttu. Käesolev väitekiri käsitleb neid väljakutseid kahe arvutusliku lähenemise arendamise kaudu fluorestsentsil põhinevate difusioonimõõtmiste jaoks: IOCBIO FCS — korrelatsioonispektroskoopia analüüsplatvorm — ning fluorestsentsi intensiivsuse jälgimise statistiline analüüs (FITSA), uude meetodeid, mis põhineb mõõteandmete otsesel Bayesi analüüsil.

Fluorestsentskorrelatsioonispektroskoopia (FCS) ja rasterkujutise korrelatsioonispektroskoopia (RICS) on väljakujunenud tehnikad molekulaarse dünaamika mõõtmiseks fluorestsentsi intensiivsuse fluktuatsioonide analüüsi kaudu. Paraku on praegustel analüüsimeetodidel mitmeid kriitilisi piiranguid. Fundamentaalsel tasandil eeldavad tavapärased lähenemismeetodid identset dispersiooni kõigi autokorrelatsioonifunktsiooni andmepunktide jaoks ning mõõtmiste statistilist sõltumatust, mis põhjustab parameetrite määramatuste alahindamist ja viib ebausaldusväärse mudelivalikuni.

Nende piirangute ületamiseks korrelatsioonipõhistes meetodites töötati välja IOCBIO FCS — ühtne, avatud lähtekoodiga ja Pythonil põhinev platvorm, mis integreerib GPU-kiirendatud autokorrelatsiooni arvutuse, põhjalikud järeldava statistika raamistikud (Bayesi ja sagedusstatistilised lähenemised koos hariliku, kaalutud ja üldistatud vähimruutude veatõotlusega), toe eksperimentaalselt mõõdetud 3D PSF-idele ning võimalused üldistatud RICS-analüüsiks. Platvorm võimaldab parameetrite ruumilist kaardistamist heterogeensetes proovides ning anisotroopse difusiooni iseloomustamist organiseeritud rakustruktuurides. Valideerimisuuringud näitavad, et korrektne veamodelleerimine mõjutab oluliselt parameetrite määramatuste hinnanguid ja mudelivaliku tulemusi, kusjuures kovariatsiooni eiramine viib ebausaldusväärsete järeldusteni süsteemi keerukuse kohta.

Platvorm rakendab difusiooni ja kontsentratsiooni eelanalüüsi kvaliteedikontrolliks, võimaldades tuvastada ja välistada mõõtmisi, mis on saastunud artefaktidega, nagu suured fluorestsentseeruvad agregaadid, enne peamist parameetrite hindamist. RICS-mõõtmiste puhul võimaldavad piltide jagamise strateegiad koos kontsentratsioonipõhise filtreerimisega süstemaatiliselt tuvastada ja eemaldada pildid, mida mõjutavad harvad kõrge intensiivsusega sündmused, mis muudu moonutaksid ruumilist korrelatsioonianalüüsi. Nende RICS-i eelanalüüsi võimaluste rakendamine lipoproteiini lipaasi oligomerisatsiooni uurimisel demonstreeris filtreerimisalgoritmide praktilist kasulikkust difusiooni iseloomustamisel proovides, mis sisaldavad erinevate oligomeeride olekute segusid suurte osakeste artefaktide olemasolul.

Korrelatsiooniliste ja muutuva hajuvusega vigade korrektne käsitlemine kovariatsiooni hindamise kaudu nõuab tuhandeid kordusmõõtmisi stabiilsetes tingimustes, mis on elusrakkude eksperimentides fototoksilisuse ja rakkude eluvõime piirangute tõttu praktiliselt teostamatu. Nende korrelatsioonipõhiste meetodite fundamentaalsete footoniefektiivsuse piirangute ületamiseks töötati välja Bayesi statistikal põhinev meetod FITSA, mis analüüsib fluorestsentsi intensiivsuse ajajälgi otse, mitte autokorrelatsioonifunktsioonide kaudu. Võrdlev analüüs näitab, et FITSA koondub oluliselt väiksema iteratsioonide arvuga kui varasemad otsese intensiivsuse analüüsi meetodid, pakkudes kiiremat arvutust ja paremat robustsust eelteadmiste spetsifikatsiooni suhtes. Võrreldes FCS-iga vajab FITSA oluliselt vähem footoneid, kusjuures eelised on eriti väljendunud aeglase difusiooni korral, mis on iseloomulik rakusisestele keskkondadele. See märkimisväärne footonite arvu vähenemine

võimaldab lühemaid mõõtmisaegu, leevendades otseselt fototoksilisuse probleeme, mis piiravad elusrakkude korrelatsioonispektroskoopia rakendusi.

Need teineteist täiendavad tööriistad vastavad erinevatele eksperimentaalsetele vajadustele: IOCBIO FCS keerukate stsenaariumide jaoks, sealhulgas mitmekomponentne difusioon, triplet-oleku dünaamika ja anisotroopne transport, ning FITSA footonpiiratud mõõtmiste jaoks, kus fototoksilisus on kriitiline.



## Appendix 1

I

**Hamed Karimi**, Otto Gustavson, Irina Česnokova, Jelena Branovets, Rikke Birkedal, Martin Laasmaa, and Marko Vendelin. A Unified Platform for FCS and RICS Analysis with Advanced Statistical Inference. *ACS Omega*, 2026



# A Unified Platform for FCS and RICS Analysis with Advanced Statistical Inference

Hamed Karimi, Otto Gustavson, Irina Česnokova, Jelena Branovets, Rikke Birkedal, Martin Laasmaa, and Marko Vendelin\*

Cite This: <https://doi.org/10.1021/acsomega.5c12269>

Read Online

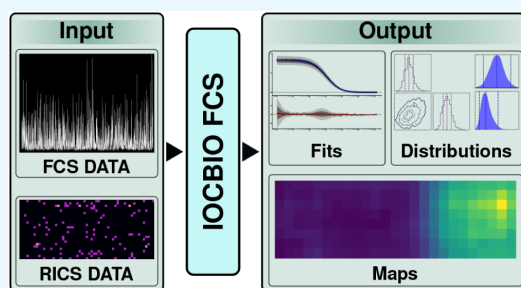
ACCESS |

Metrics & More

Article Recommendations

Supporting Information

**ABSTRACT:** Fluorescence correlation spectroscopy (FCS) and raster image correlation spectroscopy (RICS) are powerful techniques for measuring molecular diffusion, concentration, and dynamics in biological systems, yet current analysis tools lack unified frameworks that combine advanced statistical methods with high-performance computing. We present an open-source Python platform, IOCBIO FCS, that integrates FCS and RICS analysis with GPU-accelerated autocorrelation function calculation, robust statistical inference, and realistic optical modeling. The platform uniquely provides capabilities absent from existing open-source tools: direct incorporation of experimentally measured 3D point spread functions into fitting procedures, comprehensive statistical frameworks encompassing Bayesian inference alongside generalized, weighted, and ordinary least-squares methods for rigorous uncertainty quantification, and combined multiple-angle RICS analysis for characterizing anisotropic diffusion in complex biological systems. Additional features include image partitioning for spatial parameter mapping, advanced filtering strategies for data quality control, and comprehensive visualization of fitted results, residuals, posterior distributions, and parameter maps. This platform establishes a reproducible workflow bridging modern fluorescence microscopy with quantitative analysis of molecular transport across biophysics, biochemistry, and cell biology research.



## INTRODUCTION

The quantitative characterization of molecular transport phenomena and intermolecular interactions represents a fundamental challenge in modern biophysics, biochemistry, and cellular biology. Understanding how molecules move, interact, and organize within complex biological environments is essential for elucidating cellular processes ranging from signal transduction and enzymatic reactions to membrane dynamics and organelle function.<sup>1–4</sup> For example, in specialized cells such as cardiomyocytes (CMs), diffusion is significantly restricted, impacting intracellular energy transfer and signaling.<sup>5–15</sup>

Advanced fluorescence-based correlation techniques have emerged as powerful methodological approaches to address these questions, providing unprecedented insights into molecular behavior at physiologically relevant concentrations and under cellular conditions.

Fluorescence correlation spectroscopy (FCS) and raster image correlation spectroscopy (RICS) have established themselves as indispensable tools for quantifying molecular dynamics in living and solution-based systems.<sup>16–20</sup> FCS exploits the inherent fluorescence intensity fluctuations arising from molecular motion and interactions within an observation volume, enabling precise determination of diffusion coeffi-

cients, molecular concentrations, and binding kinetics with single-molecule sensitivity. Complementarily, RICS extends correlation analysis to scanning fluorescence microscopy by analyzing intensity fluctuations across raster-scanned images, thereby providing spatially resolved measurements of molecular transport properties.

The biological significance of these techniques is evidenced by their widespread application across diverse research domains. In membrane biology, FCS and RICS have revealed the complex dynamics of lipid rafts, membrane protein clustering, and receptor–ligand interactions, providing crucial insights into cellular signaling mechanisms.<sup>21–24</sup> In cellular transport studies, these methods have elucidated anomalous diffusion phenomena in the cytoplasm and nucleus, revealing how macromolecular crowding, active transport processes, and intracellular barriers influence molecular mobility.<sup>25–28</sup> Furthermore, in biochemical research, correlation spectroscopy

Received: November 25, 2025

Revised: March 3, 2026

Accepted: March 6, 2026

has proven invaluable for studying protein folding dynamics, enzyme–substrate interactions, and drug-target binding kinetics both *in vitro* and in living cells.<sup>29,30</sup>

Despite their widespread adoption and proven utility, the analysis of FCS and RICS data presents substantial computational and methodological challenges that limit their accessibility and reliability.<sup>31,32</sup> Raw fluorescence signals are inherently susceptible to experimental artifacts including detector noise, photobleaching, photoblinking, and mechanical drift, all of which can significantly distort correlation functions and compromise parameter extraction.<sup>33–36</sup> The presence of immobile fractions, heterogeneous populations, or anomalous diffusion behaviors further complicates data interpretation and requires sophisticated analytical approaches. Additionally, biological systems frequently exhibit spatial heterogeneity and anisotropic transport properties that necessitate advanced correlation analysis methods capable of resolving directional dependencies and local variations in molecular dynamics.<sup>27,37</sup>

Traditional fitting approaches based on least-squares optimization are relatively fast but often fail to provide reliable uncertainty estimates and may converge to local minima, especially when dealing with noisy data or complex multi-component systems.<sup>38</sup> By contrast, Bayesian inference frameworks for parameter estimation provide superior uncertainty quantification and model selection capabilities, enabling more rigorous and interpretable analysis of correlation data.<sup>39–41</sup>

The software landscape for FCS and RICS remains limited. Although RICS analyses incorporating variable scanning speeds and angles have been previously implemented<sup>27,37</sup> to date, no open-source software offering these analytical capabilities has been made publicly accessible. Other existing open-source tools are restricted to either FCS or RICS analysis, often rely exclusively on CPU-based computation for autocorrelation function (ACF) calculation, omit modern statistical approaches for robust uncertainty quantification, lack support for Bayesian inference, and do not allow fitting with experimentally measured 3D point spread functions (PSFs).<sup>42–50</sup>

To overcome these limitations, the present work introduces a unified, open-source platform that integrates several critical capabilities into a reproducible and statistically rigorous workflow for molecular transport analysis: 1—visualization tools for quality control, data exploration, and data filtering before ACF calculation; 2—flexible ACF computation with support for both CPU and GPU acceleration, and multiple correlation modes optimized for different experimental geometries, with additional functionality for image splitting to enable parameter mapping and support for laser scanning at arbitrary angles and speeds; 3—advanced data filtering strategies after ACF calculation, including pre-analysis of diffusion coefficient and concentration for systematic exclusion of unreliable measurements prior to fitting; 4—flexible diffusion modeling supporting both experimentally measured 3D PSFs and analytical 3D Gaussian ellipsoid approximations; 5—robust fitting frameworks incorporating least-squares methods alongside Bayesian inference with multiple noise models; 6—comprehensive visualization of fitted results with support for parameter mapping, residual analysis, and posterior distribution visualization for estimated parameters.

The primary methodological novelty of the present platform lies in its unified open-source implementation that, for the first time, combines RICS analysis with arbitrary scan angles and speeds, Bayesian inference with support for generalized least-

squares (GLS) to account for correlated errors in parameter estimation and uncertainty quantification, fitting with experimentally measured 3D PSFs, and an advanced filtering strategy based on diffusion-concentration pre-analysis within a single reproducible workflow supporting both FCS and RICS. The ability to incorporate experimentally measured PSFs and to support RICS acquisition at arbitrary scan angles is particularly important in anisotropic systems such as cardiomyocytes, where molecular transport is spatially constrained and deviations from idealized PSF geometry can significantly bias extracted diffusion coefficients. Additionally, the platform incorporates GPU-accelerated ACF computation, which significantly reduces processing time for large data sets while maintaining full compatibility with CPU-based operation. By bringing these capabilities together in a statistically rigorous and computationally scalable framework, the platform enables new biological insights into spatially heterogeneous and anisotropic molecular dynamics that were previously difficult to obtain reliably with existing tools.

## METHODS

### Overview

The Methods section outlines the implementation of the software framework for FCS and RICS analysis. The workflow comprises three major components: calculation of ACFs; fitting of ACFs with different models that support both Gaussian and experimentally measured PSFs, implemented within frequentist and Bayesian inference frameworks; and visualization of data across all stages of analysis. Experimental measurements were performed using solution measurements as well as live and fixed cell preparations where mitochondria were fluorescently labeled. The software was developed in Python with a command line interface, relying on widely used scientific packages for numerical computation, data management, and visualization. This enables scriptable, reproducible workflows and deployment on computing clusters where graphical interfaces are impractical. For some tasks, interactive cursor-based menus support parameter filtering (scanning angles, speeds) and RICS spatial map visualization. This hybrid approach balances automation with interactivity.

### ACF Calculation

The software computes the ACF to quantify fluctuations in fluorescence intensity in both FCS and RICS data sets. For FCS, the ACF is calculated as a function of lag time ( $\tau$ ), capturing correlations of the fluorescence intensity  $I(t)$  according to

$$G(\tau) = \frac{\langle \delta I(t) \delta I(t + \tau) \rangle}{\langle I \rangle^2} \quad (1)$$

where  $\delta I(t) = I(t) - \langle I \rangle$  represents deviations from the mean. The correlation is normalized by the square of the mean photon count, producing a dimensionless function suitable for quantitative analysis.<sup>16,17</sup>

For RICS, the software computes a spatial ACF in which temporal information is intrinsically encoded by the scanning pattern. The spatial ACF is defined as

$$G(\xi, \psi) = \frac{\langle \delta I(x, y) \delta I(x + \xi, y + \psi) \rangle_{x,y}}{\langle I(x, y) \rangle_{x,y}^2},$$

$$\text{with } \delta I(x, y) = I(x, y) - \langle I(x, y) \rangle_{x,y} \quad (2)$$

Here,  $\xi$  and  $\psi$  denote pixel displacements (spatial lags) along the fast- and slow-scan axes, respectively, and  $\langle \cdot \rangle_{x,y}$  indicates averaging over all spatial locations in both  $x$  and  $y$  directions.

Temporal information is encoded in the scanning process: a displacement of  $\xi$  pixels along the  $x$ -axis corresponds to an effective delay of  $\xi t_{\text{pix}}$ , while a displacement of  $\psi$  lines along the  $y$ -axis corresponds to  $\psi t_{\text{line}}$ . Thus, the effective lag time is

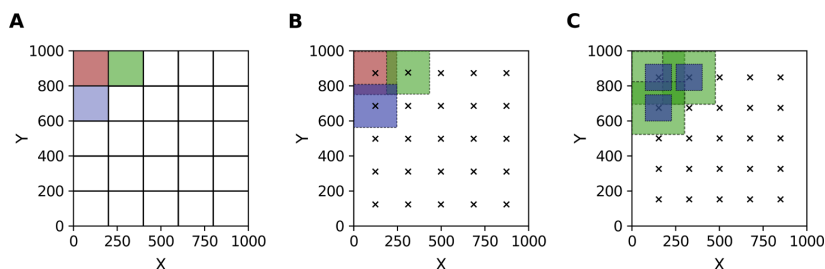


**Figure 1.** Image-splitting configurations for spatially resolved autocorrelation analysis in RICS data sets (1000 × 1000 pixels). (A) Sector self-correlation, where the autocorrelation function (ACF) is computed for each sector with itself. Colored squares indicate example correlation areas. (B) Larger-area self-correlation, where the ACF is computed for each larger area with itself. Colored squares indicate example correlation areas, and cross symbols mark sector centers. (C) Pair-correlation between smaller and larger areas (blue and green squares, respectively). Cross symbols mark sector centers.

$$\tau(\xi, \psi) = \xi t_{\text{pix}} + \psi t_{\text{line}} \quad (3)$$

Although the ACF in RICS is expressed in spatial coordinates, each spatial lag can be mapped to an effective temporal lag.<sup>19</sup>

For RICS data sets acquired in structured environments such as cells, the user can choose to subtract the background to remove nonspecific fluorescence and stationary contributions before normalization. In this case, images are grouped by acquisition conditions, and an average image for each group is subtracted from individual frames. The resulting arrays are then normalized by dividing by the squared variance of the background-subtracted signal. In cases such as diffusion in solution, where background is negligible, each image is normalized by subtracting its mean and dividing by the squared mean intensity. These normalization procedures yield a robust, dimensionless measure of correlation that is suitable for extraction of diffusion and dynamic parameters across different experimental conditions.

For RICS data sets, the software implements three configurations for spatially resolved autocorrelation analysis via image splitting. The image series is divided into user-defined sectors along the horizontal and vertical axes, ensuring that all sectors are fully contained within the image and evenly distributed across the imaged area. Sector centers are determined based on these restrictions, and Figure 1 illustrates the three available configurations. In the first configuration, sector self-correlation, the ACF is computed for each sector with itself, enabling direct mapping of local heterogeneities when photon counts are sufficient (Figure 1A). In the second configuration, larger-area self-correlation, a larger area centered on each sector is correlated with itself, thereby increasing the sampling volume and improving statistical averaging (Figure 1B). This approach is particularly useful when photon counts are limited.<sup>51</sup> In the third configuration, pair-correlation, a smaller reference area is correlated with a larger concentric area, providing sensitivity to directional transport and spatial connectivity between different scales (Figure 1C). Together, these modes enable multiscale mapping of molecular dynamics, from local fluctuations to anisotropic or active transport processes within cells.

## Diffusion Models

The theoretical fit of the ACF relies on the PSF of the microscope. The PSF is handled in three different ways: first, the experimentally measured PSF can be directly<sup>52</sup> used in the integrals of the correlation model (numerical evaluation, computationally slower), second, the experimental PSF can be reduced to an equivalent Gaussian ellipsoid by extracting the waist parameters  $\omega_x$ ,  $\omega_y$ , and  $\omega_z$ , which are then used in the analytical formulas, or third, the user may directly set  $\omega_x$ ,  $\omega_y$ , and  $\omega_z$  to desired values. For all three options, an additional PSF-scale factor can be applied in the range 0–2 (default value 1), allowing further flexibility in fitting.

The 3D Gaussian ellipsoid approximation of the PSF is given by<sup>17,53</sup>

$$\text{PSF}(x, y, z) = \exp\left(-\frac{2x^2}{\omega_x^2} - \frac{2y^2}{\omega_y^2} - \frac{2z^2}{\omega_z^2}\right) \quad (4)$$

The effective focal volume is defined by<sup>17,54</sup>

$$V_{\text{eff}} = \frac{[\int \text{PSF}(\mathbf{r}) dV]^2}{\int \text{PSF}^2(\mathbf{r}) dV} \quad (5)$$

and is used to determine the molecular occupancy within the observation region. Here,  $\mathbf{r} = (x, y, z)$  denotes the spatial coordinates in the focal volume  $V$ .

For RICS, the autocorrelation depends both on the spatial lag (pixel displacements mapped into sample coordinates) and on the lag time introduced by the raster scan. In the anisotropic Gaussian PSF approximation, the spatiotemporal ACF for a displacement  $\Delta = (\Delta x, \Delta y, \Delta z)$  and lag time  $\tau$  can be written as,<sup>19,20,27</sup>

$$G(\Delta, \tau) = \frac{1}{V_{\text{eff}}(C)} \prod_{i \in \{x, y, z\}} \left[ \frac{1}{\sqrt{\pi(4DC_i\tau + \omega_i^2)}} \exp\left(-\frac{\Delta_i^2}{4DC_i\tau + \omega_i^2}\right) \right] \quad (6)$$

where  $\langle C \rangle$  is the mean concentration,  $DC_i$  the diffusion coefficient along axis  $i \in \{x, y, z\}$ , and  $\omega_i$  the PSF width along axis  $i$ . The product runs over the three spatial axes to account for anisotropic diffusion and the 3D PSF. In this formulation, diffusion is direction dependent with  $DC_x$ ,  $DC_y$ , and  $DC_z$ . Because RICS samples spatial lags only in the imaging plane ( $\Delta x, \Delta y$ ) while  $\Delta z = 0$ , the acquisition geometry does not impose any equality between  $DC_x$  and the in-plane coefficients. Axial diffusion contributes via the 3D PSF to the temporal evolution of the ACF, and  $DC_z$  may equal  $DC_x$  or  $DC_y$  only under sample-specific assumptions (e.g., isotropic 3D:  $DC_x = DC_y = DC_z$ ; quasi-2D:  $DC_z = 0$ ; uniaxial anisotropy:  $DC_x \neq DC_y = DC_z$ ). A two-component anisotropic extension is obtained by a linear mixture of two component contributions (fraction  $f$  for component 1):

$$G(\Delta, \tau) = \frac{1}{V_{\text{eff}}(C)} \left[ f \prod_{i \in \{x, y, z\}} \frac{1}{\sqrt{\pi(4DC_{1,i}\tau + \omega_i^2)}} \exp\left(-\frac{\Delta_i^2}{4DC_{1,i}\tau + \omega_i^2}\right) + (1-f) \prod_{i \in \{x, y, z\}} \frac{1}{\sqrt{\pi(4DC_{2,i}\tau + \omega_i^2)}} \exp\left(-\frac{\Delta_i^2}{4DC_{2,i}\tau + \omega_i^2}\right) \right] \quad (7)$$

with  $DC_{1,i}$  and  $DC_{2,i}$  the axis-dependent diffusion coefficients of components 1 and 2, respectively (the isotropic two-component form is recovered when  $DC_{1,i} \equiv DC_1$  and  $DC_{2,i} \equiv DC_2$ ).

To account for fluorophore triplet dynamics, the correlation function is multiplied by<sup>17</sup>

$$\left(1 + \frac{TSA}{1 - TSA} \exp\left(-\frac{\tau}{\tau_T}\right)\right) \quad (8)$$

where  $TSA$  denotes the triplet-state amplitude and  $\tau_T$  the triplet-state relaxation time.

The sample-frame displacements  $\Delta x$ ,  $\Delta y$ ,  $\Delta z$  are obtained from pixel displacements  $(\xi, \psi, \zeta)$  and the pixel sizes by a rotation by the scan angle  $\alpha$ :

$$\begin{bmatrix} \Delta x \\ \Delta y \\ \Delta z \end{bmatrix} = \begin{bmatrix} \cos \alpha & -\sin \alpha & 0 \\ \sin \alpha & \cos \alpha & 0 \\ 0 & 0 & 1 \end{bmatrix} \begin{bmatrix} \xi s_\xi \\ \psi s_\psi \\ \zeta s_\zeta \end{bmatrix} \quad (9)$$

where  $s_\xi$ ,  $s_\psi$ ,  $s_\zeta$  denote the pixel sizes along the corresponding axes in physical units.

The correlation lag time in RICS  $\tau(\xi, \psi)$  is determined by the scanning process, with  $\tau(\xi, \psi) = \xi^2 t_{\text{pix}} + \psi^2 t_{\text{line}}$  as defined above. The pixel sizes  $s_\xi$ ,  $s_\psi$ ,  $s_\zeta$  are instead used to relate spatial displacements to the physical dimensions of the PSF.

Evaluating eq 6 (or eq 7) at zero spatial lag,  $\Delta x = \Delta y = \Delta z = 0$ , removes the exponential spatial terms and reduces the expression to the purely temporal ACF used in point FCS. Thus, FCS corresponds to the special case of the RICS formulation with vanishing spatial lag and direct specification of the temporal lag  $\tau$ . Extensions to two-component diffusion or the inclusion of triplet dynamics can be incorporated.

For the experimentally measured PSF, the same diffusion equations as in<sup>27</sup> are applied for the different models.

## Fitting Frameworks

The software implements six complementary parameter estimation approaches by combining two statistical frameworks—frequentist and Bayesian inference—with three error treatment methods.

The frequentist framework estimates parameters by minimizing the chi-squared statistic

$$\chi^2(\theta) = [y - f(x, \theta)]^T W [y - f(x, \theta)] \quad (10)$$

where  $y$  represents the observed data,  $f(x, \theta)$  is the model function,  $\theta$  are the parameters to be estimated, and  $W$  is the weight matrix determined by the error structure.

For ordinary least-squares (OLS) with uniform errors, the optimization problem reduces to minimizing the sum of squared residuals  $S(\theta) = \sum_{i=1}^n [y_i - f(x_i, \theta)]^2$ , which is equivalent to using  $W = I$  (identity matrix) in the chi-squared formulation. The common error variance is subsequently estimated from the optimal residuals as  $\hat{\sigma}^2 = \frac{1}{n-p} S(\hat{\theta})$ , where  $\hat{\theta}$  are the fitted parameters,  $n$  is the number of data points, and  $p$  is the number of parameters. This approach assumes uniform weighting across all data points. When measurement uncertainties vary across data points, weighted least-squares (WLS)

employs  $W = \text{diag}\left(\frac{1}{\sigma_1^2}, \frac{1}{\sigma_2^2}, \dots, \frac{1}{\sigma_n^2}\right)$ , providing optimal parameter estimates under heteroscedastic conditions. For correlated measurement errors with known covariance matrix  $\Sigma$ , generalized least-squares (GLS) uses  $W = \Sigma^{-1}$  to account for both heteroscedasticity and correlation structure, ensuring efficient parameter estimation when errors exhibit complex dependencies.<sup>39,40,55–57</sup>

The covariance matrix  $\Sigma$  for FCS is empirically estimated from  $N$  independent traces acquired under identical experimental conditions. Each trace  $k$  yields an ACF, and the sample covariance matrix is computed as

$$\Sigma_{i,j} = \frac{1}{N-1} \sum_{k=1}^N [G_k(\tau_i) - \bar{G}(\tau_i)][G_k(\tau_j) - \bar{G}(\tau_j)] \quad (11)$$

where  $G_k(\tau_i)$  is the ACF value at lag time  $\tau_i$  for trace  $k$  and  $\bar{G}(\tau_i) = \frac{1}{N} \sum_{k=1}^N G_k(\tau_i)$  is the mean ACF. Diagonal elements  $\Sigma_{i,i}$  quantify variance at each lag time, while off-diagonal elements  $\Sigma_{i,j}$  ( $i \neq j$ ) capture correlations between different lag times. These correlations arise from temporal overlap in the correlation calculation and photon detection statistics. Reliable covariance estimation requires  $N$  to be substantially larger than the number of ACF points to ensure matrix stability.<sup>40</sup>

The Bayesian framework treats parameters as random variables and characterizes their posterior distribution through  $p(\theta|y) \propto p(y|\theta)p(\theta)$ , where  $p(y|\theta)$  is the likelihood function and  $p(\theta)$  represents prior information. For uniform errors, the likelihood function assumes Gaussian distributions

$$p(y|\theta, \sigma) = \prod_{i=1}^n \frac{1}{\sqrt{2\pi\sigma^2}} \exp\left(-\frac{[y_i - f(x_i, \theta)]^2}{2\sigma^2}\right) \quad (12)$$

When individual error estimates are available, the heteroscedastic likelihood incorporates these uncertainties

$$p(y|\theta) = \prod_{i=1}^n \frac{1}{\sqrt{2\pi\sigma_i^2}} \exp\left(-\frac{[y_i - f(x_i, \theta)]^2}{2\sigma_i^2}\right) \quad (13)$$

For correlated errors, the likelihood utilizes the full covariance structure<sup>40</sup>

$$p(y|\theta) = \frac{1}{\sqrt{(2\pi)^n |\Sigma|}} \exp\left(-\frac{1}{2} [y - f(x, \theta)]^T \Sigma^{-1} [y - f(x, \theta)]\right) \quad (14)$$

In this expression,  $y - f(x, \theta)$  represents the residual vector containing all  $n$  data points. The covariance matrix  $\Sigma$  accounts for correlations among these residuals,  $\Sigma^{-1}$  denotes its inverse, and  $|\Sigma|$  its determinant, which ensures proper normalization of the multivariate Gaussian likelihood.

In the Bayesian inference framework implemented in our software, this likelihood is combined with prior distributions to compute the posterior probability of the model parameters. The Bayesian evidence ( $Z$ ) quantifies the marginal likelihood obtained by integrating the likelihood over the parameter space and serves as a basis for objective model comparison, naturally implementing Occam's razor.<sup>58–60</sup>

## Confocal Microscopy System

Experiments were conducted on a custom-built confocal microscope,<sup>27</sup> equipped with a water-immersion 60 $\times$  objective lens (UPLSAPO; NA 1.2; Olympus). For FCS and RICS measurements, Alexa Fluor 647 fluorophores were excited using a 633 nm laser source (05-LHP-151, Melles Griot, US) focused onto the sample plane. Dye was selected to minimize impact of autofluorescence in cardiomyocytes which is significant at shorter wavelengths.

Fluorescence signals were collected through a long-pass filter (F76-631, Semrock, Rochester, NY) and detected using an avalanche photodiode detector (SPCMAQRH-54, Excelitas Technologies, Pittsburgh, PA), using a PCIe data acquisition board with temporal sampling of 1 and 3  $\mu\text{s}$  (PCIe-6353, National Instruments, Austin, TX). For mitochondrial imaging experiments, MitoTracker Green-labeled cells were excited using a 488 nm laser (0488L11A-NI-NT-NF, Integrated Optics UAB, Lithuania), and fluorescence was captured through a bandpass filter (550/88 nm; FF01-550/88-25, Semrock, Rochester, NY) with 30  $\mu\text{s}$  pixel time.

## Solution Experiments

Experiments were performed using filtered Alexa Fluor 647 Dextran 10K in water or a glycerol/water mixture at room temperature (22 $^\circ\text{C}$ ). Samples were allowed to equilibrate for 10 min to ensure sedimentation and stability before measurements. A temporal

sampling of 1  $\mu\text{s}$  was used for all experiments, unless explicitly stated otherwise.

### Cardiomyocyte Experiments

All animal studies were conducted in compliance with Directive 2010/63/EU of the European Parliament regarding the protection of laboratory animals and received approval from the Project Authorisation Committee for Animal Experiments of the Estonian Ministry of Rural Affairs.

For live cell experiments, ventricular CMs were freshly isolated from female Wistar Han rats (61 days old; Envigo RMS, 5961 NM Horst, The Netherlands) for determining diffusion coefficients. Cell isolation followed the protocol described earlier;<sup>61</sup> wash solution composition described in ref 62. CMs were subsequently transferred to a reusable silicone chamber (94.6077.434, flexiPERM, SARSTEDT AG & Co. KG, Nümbrecht, Germany) mounted on a coverslip and bathed in an intracellular-like medium. This solution comprised 0.5 mM EGTA, 3.0 mM  $\text{KH}_2\text{PO}_4$ , 3.0 mM  $\text{MgCl}_2$ , 20 mM Hepes, 110 mM sucrose, 20 mM taurine, 0.5 mM dithiothreitol, 60 mM lactobionate, 5 mM glutamate, 2 mM malate, 5.0 mM MgATP, 10 mM PCr, and 10 nM Alexa Fluor 647 Dextran 10K, supplemented with bovine serum albumin (5 mg/mL) and adjusted to pH 7.1 at 25°C using KOH.

For fixed cell experiments, ventricular CMs were obtained from a male mouse (221 days old) with arginine-glycine amidinotransferase (AGAT) heterozygosity on a pure C57BL/6J genetic background.<sup>62,63</sup> Isolation procedure is described in ref 62. Freshly isolated CMs were fixed in 4% paraformaldehyde (PFA) for 10 min, washed and stored in PBS at 4°C until further use. Fixed CMs were transferred to a reusable silicone chamber, mounted on a coverslip coated with Cell-Tak cell adhesive (354240, Corning, US), and bathed in a solution containing PBS and 50 nM Alexa Fluor 647 Dextran 10K.

For both live and fixed experiments, prior to measurements, CMs were incubated with MitoTracker Green FM (M7514, Invitrogen, Eugene, OR) at 250 nM for 10 min to visualize mitochondrial networks. Cell membrane permeabilization was achieved using a glass micropipette controlled by a precision micromanipulator (SMXS-K-L-EUR, Sensapex, Oulu, Finland). The micropipettes, featuring tip diameters of 0.5  $\mu\text{m}$ , were fabricated from 1.0 mm glass capillaries (TW100F-3, World Precision Instruments, Sarasota, US) using a micropipette puller (PC-10, Narishige, Japan). After approximately 5 min to allow cell adherence to the coverslip within the silicone chamber, individual cells were selected for analysis. After membrane permeabilization, cells were allowed to equilibrate with the external medium for 5 min. Confocal imaging of the mitochondrial architecture was first performed, followed by selection of discrete square regions within the cell for subsequent diffusion analysis.

### PSF Characterization

PSF measurements were performed using TetraSpeck microsphere test slides prepared according to the protocol described in ref 64. The stock suspension (T7279, Invitrogen, Eugene, OR) was diluted 1:10,000 in distilled water, and a droplet of the diluted solution was deposited onto a 0.17 mm coverslip and dried at room temperature. After drying, the sample was mounted with immersion oil (Carl Zeiss Immersol W, Oberkochen, Germany; refractive index  $n = 1.334$  at 23°C) and sealed with a glass slide. Images were acquired in regions containing well-separated microspheres to avoid overlapping Airy patterns near the focal plane. The acquisition settings included lateral pixel sizes below 40 nm and axial step sizes of 100 nm. Multiple 3D stacks were collected for subsequent analysis. Individual microspheres were localized within each stack and aligned based on centroid positions obtained by least-squares optimization (eq 4). The averaged point source profile was then fitted with eq 4 to extract  $\omega_x$ ,  $\omega_y$ , and  $\omega_z$  used in the correlation analysis.

### Synthetic Trace

Synthetic fluorescence traces were generated using the simulation package provided in FITSA.<sup>65</sup> For single-trace FCS, 100 particles freely diffusing in a  $2.5 \times 2.5 \times 7 \mu\text{m}^3$  box ( $x, y, z$ ) with diffusion coefficient  $DC = 100 \mu\text{m}^2 \text{s}^{-1}$  were simulated over 80 s with a time

step of 1  $\mu\text{s}$ . For multitrace FCS, 25 particles in a larger  $8 \times 8 \times 12 \mu\text{m}^3$  box with  $DC = 20 \mu\text{m}^2 \text{s}^{-1}$  were simulated to produce 2000 traces, each 30 s long with the same time step. In both cases, a symmetric Gaussian PSF with lateral waist  $\omega_y = 0.3$  and axial waist  $\omega_z = 1.1 \mu\text{m}$  was used consistently for data generation and model fitting.

### Benchmarking

Computational performance benchmarking was evaluated using Linux PC with AMD Ryzen 9 9950X CPU, NVIDIA GeForce RTX 4080 SUPER with 16 GB GDDR6X memory GPU, 128 GB DDR5 RAM, Debian GNU/Linux 12, Python 3.11.2, NumPy 2.4.1, SciPy 1.16.3, CuPy 13.6.0, Cython 3.2.4, CUDA Toolkit 13.1, NVIDIA Driver 590.48.01.

GPU memory requirements for ACF calculation scale differently for FCS and RICS protocols. For FCS, memory consumption is  $\sim 80$  bytes per time point (e.g., 60-million-point trace, equivalent to 1 min acquisition at 1  $\mu\text{s}$  time resolution, requires  $\sim 4.8$  GB). For RICS, memory consumption is  $\sim 120$  bytes per pixel for single-image analysis (higher than FCS due to 2D array handling and sector processing overhead; e.g.,  $1000 \times 1000$  images require  $\sim 120$  MB), and  $\sim 320$  bytes per pixel for 30-image background slots (e.g., 30 images of  $1000 \times 1000$  require  $\sim 320$  MB). The sector splitting does not increase memory requirements as sectors are processed sequentially. For RICS experiments, GPU memory requirements are determined by the number of images per slot (when background subtraction is enabled) rather than the total number of images in the experiment, as images and slots are processed sequentially.

Performance times correspond to elapsed real time measured under the hardware and software conditions described above. Total runtime for complete analysis tasks (e.g., ACF calculation and full fitting workflows) was measured using bash shell `time` keyword. The duration of the model fitting stage was measured separately within the analysis code using Python `time` module, enabling separation of fixed overhead components (data loading and output writing) from fitting computation.

### Data Format

The software uses HDF5 as the standardized input format for ACF calculation, supporting both FCS and RICS data sets.<sup>66</sup> After computation, the resulting ACFs are saved in HDF5 format, enabling seamless reloading for further analysis or visualization. The fitted ACF results are also stored in HDF5 format and can be reloaded for visualization of fitted curves, residuals, or parameter maps. For Bayesian inference, posterior samples can additionally be saved in NetCDF (nc) format following the Arviz data storage standards.<sup>67</sup>

### Implementation

The software implements ACF calculations on both CPU and GPU, using NumPy for CPU-based processing and CuPy for GPU acceleration.<sup>68–70</sup> GPU computation provides substantially faster analysis, particularly for RICS and multitrace FCS data sets. Integration over the experimentally measured PSF is accelerated with Cython, enabling efficient computation. Parameter estimation is supported under both frequentist and Bayesian frameworks. Nonlinear least-squares (NLS) optimization was performed using the SciPy library.<sup>71</sup> Bayesian posterior sampling relied on nested sampling algorithms<sup>72,73</sup> provided by UltraNest, which also computes the log-evidence ( $\log Z$ ) for model comparison.<sup>60</sup> Posterior diagnostics, including parameter correlations, are displayed using corner plots implemented in the UltraNest package.<sup>60</sup> Visualization is handled through Matplotlib figure window.

### Parameter Constraints and Prior Bounds

The software applies bounded priors to all fitted parameters in both NLS and Bayesian frameworks, constraining them to physically meaningful ranges with enforced non-negativity to prevent non-physical solutions. By default, diffusion coefficients are constrained to  $0\text{--}5000 \mu\text{m}^2 \text{s}^{-1}$ , concentrations to  $0\text{--}1000$  nM, triplet-state amplitudes to  $0\text{--}1$ , triplet-state relaxation times to  $0.01\text{--}10^4 \mu\text{s}$ , and the PSF scaling factor to  $0\text{--}2$ . For two-component diffusion models, identifiability constraints (e.g.,  $DC_1 < DC_2$ ) prevent label-

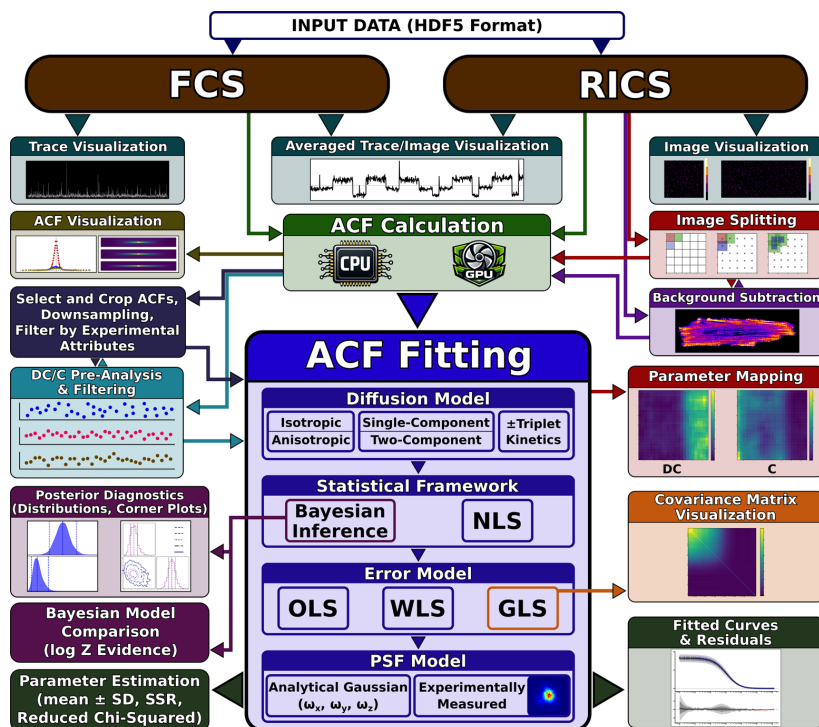


**Figure 2.** IOCBIO FCS analysis workflow. Schematic overview of the complete analysis pipeline from data input through results visualization. The platform accepts fluorescence correlation spectroscopy (FCS) photon time traces and raster image correlation spectroscopy (RICS) image stacks in HDF5 format, supporting both techniques within a unified framework. Quality control via trace/image visualization precedes GPU- or CPU-accelerated ACF calculation. Post-correlation processing includes flexible ACF selection and cropping, logarithmic downsampling, and filtering by experimental attributes (scanning angle, speed). DC- and C-based pre-analysis enables quality screening and filtering before main fitting. The ACF fitting module provides comprehensive model selection (diffusion type, statistical framework, error model, point spread function (PSF) treatment). Bayesian inference yields posterior diagnostics and model comparison via log-evidence, while both Bayesian and nonlinear least-squares (NLS) approaches produce fitted curves with residuals and parameter estimates. RICS-specific features include image splitting for spatial parameter mapping and background subtraction. Outputs include covariance matrix visualization for generalized least-squares (GLS), parameter maps, and comprehensive fit diagnostics.

switching during parameter estimation. All prior ranges can be adjusted by the user via command-line options or configuration files to reflect system-specific knowledge.

### Goodness-of-Fit Assessment

Goodness-of-fit is quantified using the chi-squared statistic evaluated at the fitted parameters,  $\chi^2(\hat{\theta})$  (eq 10), and the reduced chi-squared

$$\chi_v^2 = \chi^2(\hat{\theta}) / (n - p) \quad (15)$$

where  $n$  is the number of data points and  $p$  the number of fitted parameters. The definition of  $\chi^2(\hat{\theta})$  naturally depends on the assumed error model through the weight matrix  $W$  (OLS, WLS, or GLS; see *Fitting Frameworks*). The software reports the sum of squared raw residuals (SSR), the chi-squared statistic based on the specified error model, as well as the reduced chi-squared, which normalizes  $\chi^2(\hat{\theta})$  by the degrees of freedom and provides a scale-independent measure of fit quality. For Bayesian inference, these metrics are computed using median posterior parameter samples. While these summary statistics provide overall fit quality measures, visual inspection of residual patterns as a function of lag time (or pixel displacement for RICS) remains essential for detecting systematic deviations. For Bayesian inference, posterior credible intervals (shown as shaded regions in figures) provide additional assessment of model adequacy.

## RESULTS

The software is designed to analyze both FCS and RICS data, enabling studies of diffusion in cells and various solutions. The analysis integrates multiple capabilities, including visualization for data inspection, flexible model selection for diffusion and photophysical processes, robust fitting strategies, error modeling, and spatial parameter mapping. To demonstrate its performance and versatility, we applied the software to synthetic and experimental data sets using the full set of diffusion models described in the *Methods* section, with parameter estimation performed by both nonlinear least-squares (NLS) and Bayesian approaches under different error assumptions.

Figure 2 shows the complete analysis workflow, illustrating how the platform integrates FCS and RICS analyses within a unified, modular pipeline. Some of these features are described below and demonstrated in *Application Examples*.

### Software Features

#### Experimental Data Handling and ACF Calculation.

The software supports both FCS and RICS with options for visualizing individual fluorescence traces, averaged traces

across multiple measurements (FCS), single image frames, and averaged images from multiframe acquisitions (RICS). These modes enable detection of bleaching, drifts, illumination inhomogeneity, or sample motion, and together provide diagnostic tools for assessing measurement stability before correlation. Unstable traces or frames can then be excluded to ensure that only representative data contribute to the ACF.

The software computes the ACF for both FCS and RICS, with options that provide flexibility in trace/image selection. Prior to ACF calculation, images can be split into smaller regions to enable parameter mapping or grouped by acquisition conditions to enable background subtraction in RICS. For FCS, the photon count trace can be restricted to a chosen time interval to exclude unstable segments. After ACF computation, cropping options allow restriction to a defined  $\tau$ -range (FCS) or truncation of the central portion of the 2D-ACF (RICS), retaining the region containing molecular dynamics information.

The software also provides multiple visualization modes for ACF inspection. Temporal ACFs can be plotted as a function of  $\tau$  on linear or logarithmic axes for both FCS and RICS techniques. In RICS, temporal profiles can be extracted line by line from the 2D-ACF, with the option to select additional lines to probe spatial variations. The software also supports inspection of spatial correlations, where the ACF is plotted as a function of pixel shift ( $\Delta x$ ) across lines. Curves may be downsampled logarithmically to preserve detail at short delays while compressing longer delays. For global assessment, the 2D-ACF can be displayed as a heatmap, providing an overview of correlation amplitudes and anisotropy.

**Data Filtering and Fitting.** The software incorporates a multistage filtering strategy after ACF calculation. Users can select specific ACFs from FCS or RICS data sets without recalculating, and may exclude initial ACF points to remove contributions from detector shot noise and triplet-state kinetics. The fitting range can be further restricted to a defined number of ACF points per line or to selected lines in the spatial correlation (RICS), providing fine control over which portions of the correlation data are analyzed. Data sets can also be filtered by acquisition attributes such as scanning angle, speed, or other experiment-specific keys, ensuring that only measurements obtained under consistent conditions contribute to the final analysis.

In addition, the software can compute values of  $DC$  and  $C$  for each individual trace/image and visualizes them as scatter plots. This pre-analysis enables assessment of parameter distributions, identification of systematic trends, and exclusion of data with distorted  $DC$  or  $C$  values prior to the main fitting. When RICS frames are divided into smaller sectors, the number of ACFs increases, allowing finer-grained filtering. This is particularly useful for identifying problematic regions in samples with large, slow-moving particles; excluding only the affected sectors improves robustness and reduces bias in diffusion estimates. An early version of this software and filtering approach was previously applied to such large-particle filtering.<sup>74</sup> This tiered workflow ensures that downstream fitting is based on reproducible, high-quality data while allowing users to tailor filtering strategies to experimental conditions.

For fitting, users may choose between frequentist and Bayesian paradigms. The frequentist approach yields point estimates of model parameters, while Bayesian inference provides full posterior distributions for comprehensive

uncertainty quantification. Both paradigms support ordinary least-squares (OLS), weighted least-squares (WLS), and generalized least-squares (GLS, applied to FCS), corresponding to uniform, weighted, and correlated error structures, respectively. In Bayesian inference, integration over the parameter space yields the log-evidence ( $\log Z$ ), which serves as a quantitative criterion for model comparison. This metric naturally penalizes overly complex models by distributing probability mass over larger parameter regions, favoring simpler models unless the added complexity is justified by improved data fit.<sup>60</sup>

**Visualization of Fitting Results.** After fitting, the software overlays model curves onto the experimental ACF and can display residuals for both NLS and Bayesian approaches. For Bayesian inference, an additional uncertainty band is drawn around the median fit to represent the quantile ranges (QRs), which correspond to Bayesian credible intervals. Further visualization modes include posterior diagnostics, angular dependence plots in RICS, and spatially resolved parameter maps from sector analysis, enabling detection of heterogeneities in molecular transport.

### Application Examples

**FCS—Single Trace.** To demonstrate the FCS technique, a synthetic fluorescence trace was generated with a diffusion coefficient of  $DC = 100 \mu\text{m}^2 \text{s}^{-1}$  (without triplet-state component), with the resulting intensity fluctuations shown in Figure 3A and the corresponding ACFs in Figure 3B. Both Bayesian inference and NLS fitting were applied to fit the ACF using a 3D isotropic diffusion model. Bayesian OLS (uniform errors) fitting estimated  $DC = 102.3 \pm 1.5 \mu\text{m}^2 \text{s}^{-1}$  (mean  $\pm$  standard deviation, same notation is used throughout the *Examples*), in close agreement with  $DC$  value used in the simulations generating the synthetic data. The corresponding residuals are presented to illustrate the quality of the fit.

**FCS—Multiple Traces.** To illustrate the effect of errors and their correlation on fitting results, 2000 synthetic traces were generated for freely diffusing particles with diffusion coefficient  $DC = 20 \mu\text{m}^2 \text{s}^{-1}$  (without triplet-state component). The covariance matrix of the resulting ACFs, shown in Supplementary Figure 1A (Supporting Information), reveals the correlation structure of noise across lag times. Both Bayesian inference and NLS fitting were applied using a 3D isotropic diffusion model. Supplementary Figure 1B shows the fit curve and residuals for the 3D model with Bayesian GLS fitting under correlated errors, yielding a diffusion coefficient of  $DC = 20.4 \pm 1.8 \mu\text{m}^2 \text{s}^{-1}$ , in close agreement with  $DC$  value used in the simulations generating the synthetic data. Posterior distributions obtained from Bayesian GLS, WLS, and OLS approaches (Supplementary Figure 1D) highlight the impact of accounting for error correlation in parameter estimation. While OLS produces artificially narrow posteriors, GLS captures the variability in parameter estimates, yielding statistically rigorous inference. This capability to explicitly incorporate error correlations is an important feature of our framework and represents a significant improvement over commonly used OLS and WLS approaches.

In addition, four diffusion models were compared by Bayesian GLS fitting: 3D ( $\log Z = 19.0 \pm 0.3$ ), 3D two-component ( $\log Z = 8.2 \pm 0.3$ ), 3D with triplet-state ( $\log Z = 16.8 \pm 0.4$ ), and 3D two-component with triplet-state ( $\log Z = 6.3 \pm 0.5$ ). Bayesian model selection based on the log-evidence favored the simple 3D isotropic diffusion model, which

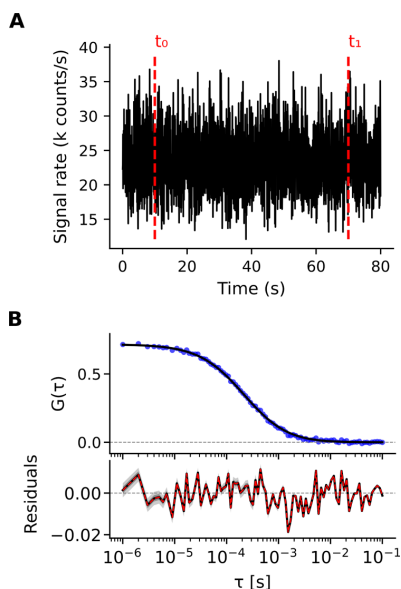


**Figure 3.** Demonstration of FCS using a synthetic fluorescence trace generated for particles with diffusion coefficient  $DC = 100 \mu\text{m}^2\text{s}^{-1}$ . (A) Time-resolved photon signal rate (in k counts/s), computed by temporal binning and normalization of photon counts, allowing visualization of fluorescence intensity fluctuations over time. The red dashed lines mark the selected time window (from  $t_0 = 10$  s to  $t_1 = 70$  s) used for autocorrelation analysis. (B) Top: Autocorrelation  $G(\tau)$  (blue circles) plotted against lag time ( $\tau$ ), along with the median Bayesian ordinary least-squares (OLS) fit (black line) using a 3D isotropic diffusion model. Bottom: Posterior predictive residuals, with the black line representing the median and shaded regions, shown in dark and light gray, denote the 68.3% and 95.5% quantile ranges (QRs), respectively. The narrow uncertainty bands make the shading barely visible along the fit curve (top). The dashed red line denotes the residuals from the NLS method (with uniform errors) fit.

provided the highest evidence score, demonstrating that the simplest model best explains the synthetic data.

To further evaluate performance under experimental conditions, Alexa Fluor 647-labeled Dextran 10K was measured diffusing in a 60% glycerol/water mixture. A total of 2000 traces were recorded, each with a trace duration of 2 min and a pixel time of 3  $\mu\text{s}$ , and 1800 stable traces were selected for ACF calculation. Figure 4A shows the covariance matrix of the resulting ACFs. Both Bayesian inference and NLS fitting were applied using a 3D isotropic diffusion model with a triplet-state component which provided the highest evidence score and an experimentally measured PSF (Figure 4B). Bayesian GLS fitting with correlated errors estimated  $DC = 9.8 \pm 1.1 \mu\text{m}^2\text{s}^{-1}$ ,  $TSA = 0.11 \pm 0.02$ , and  $\tau_T = 116 \pm 78 \mu\text{s}$ . NLS fitting (with correlated errors) estimated similar parameters:  $DC = 10.5 \pm 0.3 \mu\text{m}^2\text{s}^{-1}$ ,  $TSA = 0.11 \pm 0.01$ , and  $\tau_T = 40.9 \pm 7.1 \mu\text{s}$ .

The estimated triplet-state relaxation time—or, in this case, the more general dark-state relaxation time—warrants discussion. Bayesian GLS fitting with correlated errors estimated  $\tau_T = 116 \pm 78 \mu\text{s}$ , while NLS fitting yielded  $\tau_T = 40.9 \pm 7.1 \mu\text{s}$ . The discrepancy between these estimates reflects the challenge of parameter estimation in systems with

strong correlation structure. Examination of the posterior distribution (Figure S4A) reveals that the mode occurs near 40  $\mu\text{s}$ , in good agreement with the NLS estimate as well as estimate of  $\tau_T$  for Alexa Fluor 647 obtained in the same mixture by others.<sup>75</sup> However, the distribution exhibits a long tail extending to higher values, which shifts the mean to larger values. In addition to the viscosity-dependent increase in  $\tau_T$  observed previously<sup>76,77</sup> this extended tail could be a reflection of complex interactions between the dye and glycerol.<sup>78</sup>

Posterior distributions obtained from Bayesian GLS, WLS, and OLS approaches (Figure 4D) again highlight that while OLS produces overly narrow posteriors, GLS appropriately accounts for correlated errors, yielding a more faithful representation of parameter uncertainty.

Four diffusion models were compared by Bayesian GLS fitting: 3D ( $\log Z = 270.0 \pm 0.2$ ), 3D two-component ( $\log Z = 278.0 \pm 0.3$ ), 3D with triplet-state ( $\log Z = 279.4 \pm 0.2$ ), and 3D two-component with triplet-state ( $\log Z = 277.1 \pm 0.2$ ). Bayesian model selection based on the log-evidence favored the 3D isotropic diffusion model with a triplet-state component, which yielded the highest evidence score among the tested models. The curve fits and corner plots of all four diffusion models are presented in Figures S2–S5 in the Supporting Information, while only the results corresponding to the model with the highest Bayesian evidence are shown in Figure 4.

The covariance matrix for Alexa-Dextran 10K in a 60% glycerol/water mixture, where diffusion is substantially slowed, exhibits pronounced off-diagonal terms, reflecting strong correlations between lag times (Figure 4A). Such correlations propagate into the posterior distributions of diffusion parameters, broadening the inferred uncertainty (Figure 4D). For comparison, measurements of Alexa-Dextran 10K in water, where diffusion is relatively faster, were performed under otherwise identical conditions. Similar to the 60% glycerol/water mixture, a total of 2000 traces were recorded, and 1800 stable traces were selected for ACF calculation. The corresponding covariance matrix displays much weaker off-diagonal correlations (Figure S6A). Both Bayesian inference and NLS fitting were applied using a 3D isotropic diffusion model with a triplet-state component and an experimentally measured PSF (Figure 4B). Bayesian GLS fitting with correlated errors estimated  $DC = 84.8 \pm 3.1 \mu\text{m}^2\text{s}^{-1}$ ,  $TSA = 0.19 \pm 0.01$ , and  $\tau_T = 10.2 \pm 2.5 \mu\text{s}$ . NLS fitting (with correlated errors) estimated similar parameters:  $DC = 85.1 \pm 1.5 \mu\text{m}^2\text{s}^{-1}$ ,  $TSA = 0.19 \pm 0.01$ , and  $\tau_T = 9.4 \pm 0.9 \mu\text{s}$ . In contrast to the long  $\tau_T$  observed in the glycerol/water mixture, both Bayesian GLS and NLS fitting for Alexa-Dextran 10K in water yielded consistent and smaller triplet-state relaxation times, accompanied by narrower posterior distributions and lower parameter uncertainty (Figure S6C).

Posterior distributions obtained from Bayesian GLS, WLS, and OLS approaches (Figure S6D) exhibit more similar shapes compared to the case with strong off-diagonal terms, reflecting the reduced influence of noise correlations. These results highlight the direct relationship between diffusion dynamics, the structure of noise correlations, and the reliability of the estimated diffusion coefficients. The corresponding corner plot and fitted ACF curves are shown in Figure S6.

**RICS—Laser Scanning Speeds.** The software supports analysis of RICS data acquired at different laser scanning speeds. To illustrate this, diffusion of Alexa-Dextran 10K in water was recorded (600 RICS frames) within a  $20 \times 20 \mu\text{m}^2$

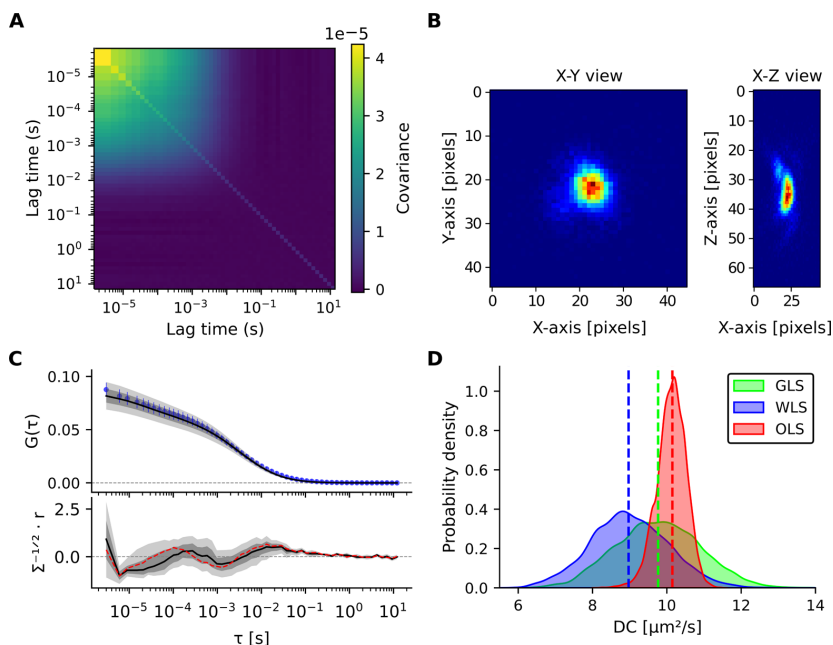


**Figure 4.** FCS measurements using 1800 experimental traces recorded for diffusion of Alexa-Dextran 10K in a 60% glycerol/water mixture. (A) Covariance matrix of the ACF computed from the 1800 individual traces, illustrating the correlation structure of noise across lag times. (B) Experimentally measured PSF used in model fitting, shown in X–Y and X–Z projections. Each pixel corresponds to a size of  $\approx 50$  nm. (C) Top: Mean autocorrelation  $G(\tau)$  (blue circles) plotted versus  $\tau$ , along with the median Bayesian GLS fit (black line) based on a 3D isotropic diffusion model including a triplet-state. Error bars represent the standard deviation (SD) of the mean. Bottom: Decorrelated residuals calculated from the ACF posterior predictive residual ( $r$ ) and covariance matrix ( $\Sigma$ ), with the black line showing the median residual. The dashed red line indicates the decorrelated residuals from the NLS method (with correlated errors) fit. Shaded regions (top and bottom), shown in dark and light gray, denote the 68.3% and 95.5% QRs, respectively. (D) Posterior distributions of  $DC$  obtained from three fitting approaches: Bayesian GLS (green, correlated errors), Bayesian weighted least-squares (WLS) (blue, weighted errors), and Bayesian OLS (red, uniform errors). Dashed lines indicate the medians of the respective distributions.

scanning area at three scanning speeds, fast, medium, and slow, corresponding to 1000, 1732, and 3000 pixels per line along the X-axis (line times of 2, 3.5, and 6 ms, including flyback), respectively. Slower scanning enables acquisition of more pixels per line, providing finer spatial sampling (Figure 5). Both Bayesian inference and NLS fitting were applied to fit the ACF from three experimental conditions using a 3D isotropic diffusion model that included a triplet-state component. Bayesian WLS fitting with weighted errors yielded  $DC = 81 \pm 17 \mu\text{m}^2 \text{s}^{-1}$ ,  $TSA = 0.29 \pm 0.13$ , and  $\tau_T = 3.41 \pm 2.05 \mu\text{s}$ . NLS fitting (with weighted errors) estimated similar parameters:  $DC = 73.9 \pm 1.3 \mu\text{m}^2 \text{s}^{-1}$ ,  $TSA = 0.34 \pm 0.01$ , and  $\tau_T = 1.94 \pm 0.14 \mu\text{s}$ . The experimentally measured PSF shown in Figure 4B was used for all fits. Posterior distributions of  $DC$ , obtained using Bayesian WLS and OLS approaches (Figure 5H) highlight the impact of accounting for measurement errors in parameter estimation.

**RICS—Laser Scanning Angles.** The software enables analysis of RICS data acquired at multiple laser scanning angles, which is essential for characterizing anisotropic diffusion in complex cellular environments. As a demonstration, diffusion of Alexa-Dextran 10K in a single live rat cardiomyocyte (CM) was recorded within a  $20 \times 20 \mu\text{m}^2$  scanning area (Figure 6A) at seven different scanning angles from  $0^\circ$  to  $180^\circ$  in  $30^\circ$  steps (Figure 6B) and at three different scanning speeds (21 conditions in total). A total of 4560 RICS

frames were recorded; the first 568 frames were excluded due to unstable intensity. Both Bayesian inference and NLS fitting approaches were applied using a 3D anisotropic diffusion model that included a triplet-state component, accounting for diffusion along the X-axis (longitudinal) and Y-axis (transverse), with diffusion along the Z-axis assumed equal to the transverse component. Bayesian WLS fitting with weighted errors yielded  $DC_x = 19.2 \pm 5.7 \mu\text{m}^2 \text{s}^{-1}$ ,  $DC_y = 13.2 \pm 3.3 \mu\text{m}^2 \text{s}^{-1}$ ,  $TSA = 0.34 \pm 0.05$ , and  $\tau_T = 4.5 \pm 5.9 \mu\text{s}$ . NLS fitting (with weighted errors) estimated similar parameters:  $DC_x = 18.5 \pm 0.6 \mu\text{m}^2 \text{s}^{-1}$ ,  $DC_y = 13.4 \pm 0.4 \mu\text{m}^2 \text{s}^{-1}$ ,  $TSA = 0.35 \pm 0.01$ , and  $\tau_T = 2.8 \pm 0.1 \mu\text{s}$ . The experimentally measured PSF shown in Figure 4B was used for all fits. The obtained diffusion coefficients for CMs are similar to our earlier estimates ( $DC_x = 19 \pm 3 \mu\text{m}^2 \text{s}^{-1}$  and  $DC_y = 16 \pm 2 \mu\text{m}^2 \text{s}^{-1}$ ).<sup>27</sup> Representative curve fits and residuals for two example conditions  $-60^\circ$  and  $90^\circ$  angles at medium scanning speed—are shown in Figure 6C and D. Posterior distributions of  $DC_x$  and  $DC_y$  from all 21 experimental conditions, obtained using Bayesian WLS and OLS approaches (Figure 6E, F), highlight the importance of explicitly accounting for measurement errors in anisotropic diffusion parameter estimation. These results demonstrate that the software enables rigorous Bayesian inference for anisotropic diffusion analysis in living cells.

**Spatial Mapping of RICS-Derived Parameters.** The software enables spatial mapping of molecular transport by

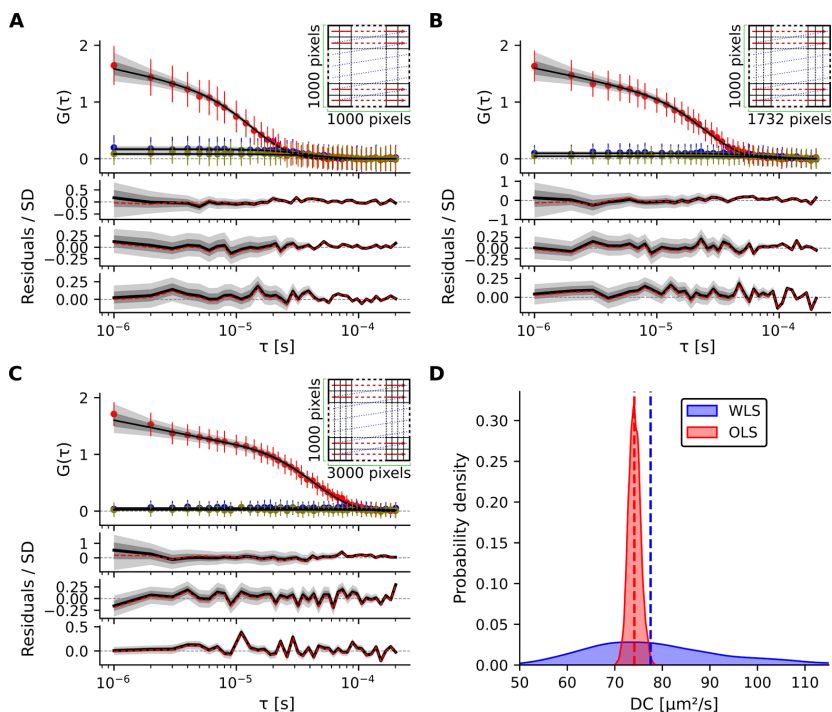


**Figure 5.** RICS analysis at varying laser scanning speeds, recorded for diffusion of Alexa-Dextran 10K in water. (A, B, C) Schematic illustrations of fast, medium, and slow scanning speeds, corresponding to line times of 2, 3.5, and 6 ms (including flyback), respectively, and corresponding analysis results for each scanning scheme. Red arrows indicate the laser scanning direction. The mean autocorrelation  $G(\tau)$  (colored circles) of three lines plotted versus  $\tau$ , along with the median Bayesian WLS fit (black line) based on a 3D isotropic diffusion model including a triplet-state component. Error bars represent the SD of the mean. Standardized posterior predictive residuals, with the black line showing the median residual are shown in bottom. The dashed red lines indicate the standardized residuals from the NLS method (weighted errors) fit. Shaded regions, shown in dark and light gray, denote the 68.3% and 95.5% QRs, respectively. (D) Posterior distributions of DC obtained from two fitting approaches: Bayesian WLS (blue, weighted errors) and Bayesian OLS (red, uniform errors). Dashed lines indicate the medians of the respective distributions.

dividing RICS images into user-defined sectors and computing the ACF within each region. This approach provides flexibility in resolution and supports detailed characterization of parameter heterogeneity across cellular areas of interest. As an example of the second configuration (larger-area self-correlation in Figure 1B), Figure 7 illustrates the spatial mapping of Alexa-Dextran 10K in a fixed mouse CM. The cell was mechanically permeabilized by localized poking and stained with Mitotracker Green to visualize mitochondria (Figure 7A). The pseudocolor image highlights the cellular structure, with a dashed square indicating the  $20 \times 20 \mu\text{m}^2$  scanning area selected for RICS analysis. As shown, the scanning window encompasses both part of the cell and the surrounding solution, enabling direct comparison of intracellular and extracellular diffusion within the same acquisition. A total of 3700 RICS frames were recorded; the first 700 frames were excluded due to unstable intensity. Subsequent fitting was performed using a 3D isotropic diffusion model including a triplet-state component, with the PSF experimentally determined in Figure 4B. For this analysis, three scanning speeds (2, 3.5, and 6 ms) were applied at a single scanning angle of  $0^\circ$ . The resulting diffusion coefficient map (Figure 7B) and concentration map (Figure 7C) clearly illustrate local variations in molecular mobility and Alexa-Dextran 10K concentration within the scanned area, which

spans both intracellular and extracellular solution regions. This example demonstrates the ability of the software to transform RICS recordings into quantitative parameter maps, providing both a spatially resolved view of molecular transport and insight into the heterogeneity of the intracellular environment.

### Performance Benchmarks

ACF calculation performance was evaluated using the hardware and software specifications described in *Methods*. GPU acceleration substantially improves ACF calculation speed (Table 1), achieving 19-fold speedup for FCS analysis of 100 traces (100 s each with  $10^8$  time points per trace at  $1 \mu\text{s}$  resolution) and 8-fold speedup for RICS processing of 350 images ( $1000 \times 1732$  pixels with  $1 \mu\text{s}$  pixel dwell time). The greater FCS acceleration reflects larger data set size ( $10^{10}$  total time points vs  $6 \times 10^8$  pixels). These speedups are critical for high-throughput experiments, reducing processing from hours to minutes.

The impact of using analytical Gaussian or experimentally measured PSF was evaluated using the same hardware and software. Experimentally measured PSFs substantially improve fit quality compared to the use of analytical Gaussian PSF (Table 2). For FCS analysis of 200 traces from Figure 4 (using NLS-GLS fitting with correlated errors) and RICS analysis of 600 frames from Figure 5 (using NLS-WLS fitting with

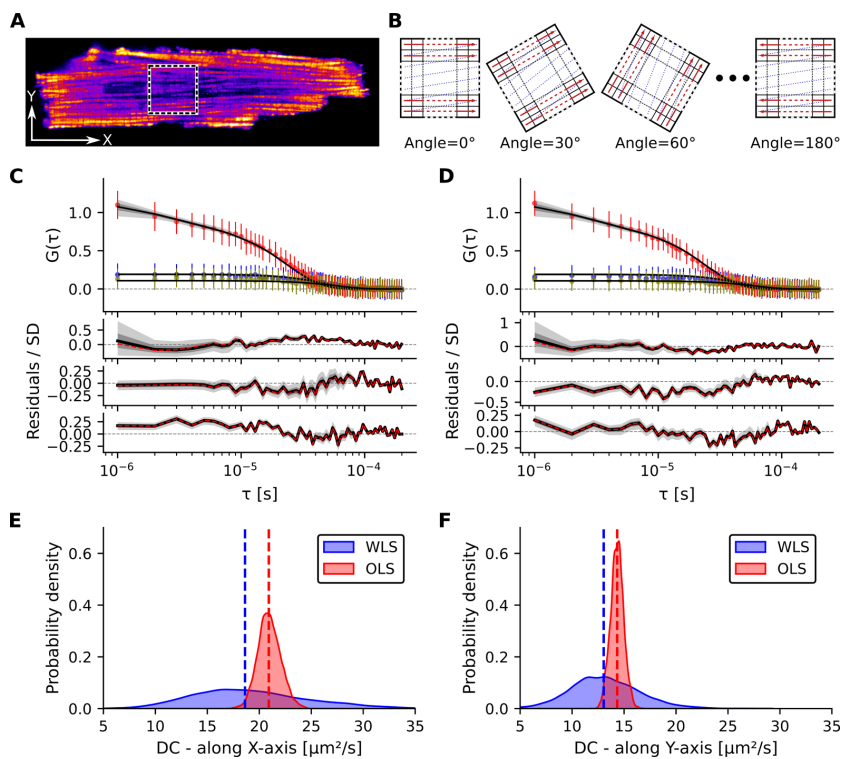


**Figure 6.** Anisotropic diffusion analysis using RICS with multiple scanning angles and speeds, recorded for diffusion of Alexa-Dextran 10K in a single rat cardiomyocyte (CM). (A) Confocal image of a live rat CM mechanically permeabilized by localized poking, shown in pseudocolor depicting mitochondria (Mitotracker Green). White arrows indicate the physical  $X$  and  $Y$  directions. The dashed square marks the  $20 \times 20 \mu\text{m}^2$  scanning area. (B) Schematic illustrations of different scanning angles from  $0^\circ$  to  $180^\circ$  in  $30^\circ$  steps. (C, D) Top: Mean autocorrelation  $G(\tau)$  (colored circles) of three lines plotted versus  $\tau$ , along with the median Bayesian WLS fits (black lines) based on a 3D anisotropic diffusion model including a triplet-state component, for the  $60^\circ$  and  $90^\circ$  scanning angles, respectively, at medium scanning speed (line time of 3.5 ms). Error bars represent the SD of the mean. Bottom: Standardized posterior predictive residuals, with the black line showing the median residual. The dashed red lines indicate standardized residuals from the NLS method (weighted errors) fit. Shaded regions, shown in dark and light gray, denote the 68.3% and 95.5% QRs, respectively. (E, F) Posterior distributions of  $DC_x$  and  $DC_y$ , from all 21 experimental conditions, obtained from two fitting approaches: Bayesian WLS (blue) and Bayesian OLS (red). Dashed lines indicate the medians of the respective distributions.

weighted errors), measured PSFs led to a 2–6-fold decrease in the chi-squared statistic ( $\chi^2(\hat{\theta})$ ) relative to Gaussian approximations, demonstrating the importance of capturing real optical aberrations and asymmetries. The Gaussian PSF parameters ( $\omega_x$ ,  $\omega_y$ ,  $\omega_z$ ) were obtained by fitting the same experimentally measured 3D PSF to a Gaussian function, ensuring a fair comparison between analytical Gaussian and experimentally measured PSF. The computational overhead scales with data set complexity: for Figure 5 with 3 scan configurations, use of the full experimental PSF during fitting required 3.8 s versus 1.3 s for models that use Gaussian approximation for PSF; for the larger data set in Figure 6 with 21 configurations (3 speeds  $\times$  7 angles), this increased to 30 s versus 1.4 s. The FCS benchmark used the first 200 traces from Figure 4, as larger data sets would introduce substantial preprocessing overhead (covariance matrix computation and memory management) that could obscure PSF-specific performance differences.

To understand the computational overhead of using experimentally measured PSF for fitting ACF, we quantified its contribution to the fitting stage of the analysis workflow,

which consists of data loading, model fitting, and output writing. Data loading and output writing introduce a fixed overhead that is independent of the PSF used. For fits using Gaussian PSFs, the model fitting step represents only a negligible fraction of total fitting runtime (<2%). In contrast, when using experimentally measured PSFs, model fitting becomes a substantial component of the fitting stage for complex data sets (e.g.,  $\sim 60\%$  of fitting time for RICS with 3 configurations and  $\sim 95\%$  for 21 configurations), while remaining more moderate for FCS (e.g.,  $\sim 20\%$  for FCS data set in Table 2). Overall, using experimentally measured PSFs during fitting substantially increases the fitting-stage duration.

To balance accuracy and computational efficiency, the software allows flexible voxel downsampling of the PSF, reducing resolution in the lateral ( $x$ ,  $y$ ) or axial ( $z$ ) dimensions independently while preserving the PSF's overall shape and lowering computational cost. Table 2 demonstrates uniform downsampling by factors of 2 $\times$  and 3 $\times$  in all three dimensions, showing that moderate downsampling reduces numerical integration cost while preserving essential optical characteristics. For high-resolution PSFs with hundreds of voxels per

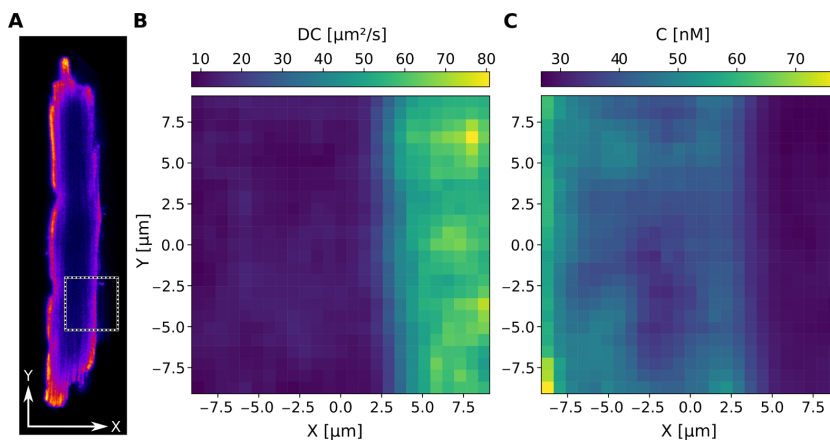


**Figure 7.** Spatial mapping of RICS-derived parameters, recorded for diffusion of Alexa-Dextran 10K in a single mouse CM at  $C \approx 50$  nM (Alexa-Dextran 10K + solution + cell). (A) The confocal image of a fixed mouse CM, shown in pseudocolor depicting mitochondria (Mitotracker Green), with white arrows indicating the physical  $X$  and  $Y$  directions. The dashed square indicates the  $20 \times 20 \mu\text{m}^2$  scanning area used for RICS analysis, covering both a portion of the cell and the surrounding solution. (B) Diffusion coefficient map of the recorded scanning area, and (C) corresponding concentration map. Each map consists of  $25 \times 25$  equally sized spatial sectors ( $0.8 \times 0.8 \mu\text{m}^2$ ). For each sector, ACF was computed using the fluorescence signals within a  $3 \times 3 \mu\text{m}^2$  area (larger-area self-correlation), and fitted using a 3D isotropic diffusion model including a triplet-state component to extract the respective parameter values. For fitting, the NLS method (uniform errors) was applied, using the PSF determined in Figure 4B. Color bars indicate the parameter scales in physical units.

**Table 1.** GPU Vs CPU Performance for ACF Calculation

Data set	CPU (s)	GPU (s)	Speedup
FCS (100 traces, $10^8$ points each)	799.1	41.8	19×
RICS (350 images, $1000 \times 1732$ pixels)	38.6	4.8	8×

**Table 2.** Comparison of Model Fits Using Analytical Gaussian and Experimentally Measured PSF: Fit Quality and Computational Cost

Data set	PSF	PSF Size	$\chi^2(\hat{\theta})^a$	Time (s)
FCS (200 traces)	Full measured	$(x, y, z)$ : $35 \times 35 \times 43$ voxels	10.32	3.5
	Downsampled 2×	$(x, y, z)$ : $17 \times 17 \times 21$ voxels	20.27	3.1
	Downsampled 3×	$(x, y, z)$ : $11 \times 11 \times 14$ voxels	23.52	2.8
	Gaussian	$(\omega_x, \omega_y, \omega_z)$ : (0.36, 0.38, 1.08) $\mu\text{m}$	57.46	2.4
RICS (600 frames)	Full measured	$(x, y, z)$ : $35 \times 35 \times 43$ voxels	3.04	3.8
	Downsampled 2×	$(x, y, z)$ : $17 \times 17 \times 21$ voxels	3.23	3.4
	Downsampled 3×	$(x, y, z)$ : $11 \times 11 \times 14$ voxels	4.13	3.4
	Gaussian	$(\omega_x, \omega_y, \omega_z)$ : (0.36, 0.38, 1.08) $\mu\text{m}$	6.55	1.3

<sup>a</sup>The chi-squared statistic ( $\chi^2(\hat{\theta})$ ) computed using decorrelated residuals (GLS fitting) for FCS and standardized residuals (WLS fitting) for RICS.

dimension, downsampling provides more pronounced computational benefits. This flexibility allows users to optimize the accuracy-speed trade-off based on PSF resolution, data set characteristics, and computational resources.

An important consideration when selecting a PSF representation for fitting is how analysis time contributes to the overall experimental workflow. The computational analysis

phase, including GPU-accelerated ACF calculation and model fitting, is substantially shorter than the data acquisition time. For example, irrespective of whether analytical or experimental PSF is used, analyzing a single 120 s FCS trace requires only 2–3 s of computation (ACF calculation plus fitting), while large data sets such as 200 FCS traces (6.5 h of acquisition) or 600 RICS images (1 h of acquisition) require on the order of 10 s to analyze, corresponding to well below 1% of the acquisition time. Even for the most computationally demanding data set (21 RICS configurations;  $\sim 10$  h of acquisition), the total analysis time is on the order of 1 min. Thus, although fitting with experimentally measured PSFs increases the computational cost relative to models using Gaussian PSFs, the absolute runtime remains acceptable for routine analysis, particularly given the substantial improvements in fit quality demonstrated in Table 2.

## DISCUSSION

We present a unified open-source Python platform for the analysis of FCS and RICS experiments to extract molecular transport parameters including diffusion coefficients, triplet dynamics, and concentrations from fluorescence fluctuation data. The platform integrates GPU-accelerated ACF calculation, rigorous statistical inference (frequentist and Bayesian approaches), support for experimentally measured PSFs, and analysis of anisotropic diffusion in cellular environments, addressing key limitations in current correlation spectroscopy workflows.

The analysis of FCS and RICS data is inherently challenging due to biological heterogeneity, experimental noise, and the need for statistically robust parameter extraction. The developed platform systematically addresses these challenges through several key features, as discussed below.

## Advanced Features for Complex Biological Systems

The ability to incorporate experimentally measured PSFs is particularly important in systems where optical aberrations significantly affect parameter extraction. The software supports both Gaussian and experimentally measured PSFs. While Gaussian PSFs are widely used for simplicity, experimentally measured PSFs yield more realistic fits by capturing aberrations, asymmetries, and other optical characteristics that analytical models cannot represent, as demonstrated in Table 2. However, experimentally measured PSFs demand greater computational effort due to their 3D complexity and higher spatial sampling requirements. To balance accuracy and efficiency, the software allows voxel downsampling of the PSF, reducing computational cost while preserving overall PSF shape.

Multiangle RICS analysis enables characterization of anisotropic diffusion in structured biological samples such as cardiomyocytes, where molecular transport is spatially constrained. The platform enables analysis of experiments where multiple scanning protocols (different angles, speeds) were performed on the same sample, leveraging complementary information to reduce parameter degeneracy. When ACFs are acquired at different scanning speeds, the platform validates model consistency by jointly fitting across all speeds. When ACFs are acquired at different scanning angles, the platform estimates anisotropic diffusion within cells. As shown in Figure 6, the angularly resolved RICS can uncover directional dependencies of diffusion processes that remain hidden in isotropic analyses.<sup>27,37</sup>

Furthermore, splitting RICS images into smaller regions (Figure 1) enables spatial mapping of diffusion and concentration (Figure 7). Such maps reveal subcellular domains with slower diffusion or higher concentration, which often correlate with structural features such as organelles or cytoskeletal barriers.

## Model Selection Strategies and Challenges

Fitting ACF data requires selecting among three model categories: statistical framework (Bayesian inference or NLS), error structure (OLS/WLS/GLS), and diffusion type (isotropic/anisotropic, single/two-component,  $\pm$ triplet kinetics). These choices strongly influence parameter estimation and uncertainty quantification.

Bayesian inference and NLS often yield similar mean parameter estimates but differ substantially in uncertainty quantification, as demonstrated in our experimental results where mean values are comparable while Bayesian standard deviations are substantially broader, more accurately reflecting parameter uncertainty. Bayesian inference yields full posterior distributions that reveal parameter correlations via corner plots and enable principled model comparison through evidence evaluation. The posterior distributions naturally quantify uncertainty through their spread, with broader distributions indicating greater parameter uncertainty and narrower distributions indicating well-constrained parameters. However, Bayesian inference requires substantially longer computation than NLS—typically 2 to several hundred times longer depending on model complexity and data set size—due to the need for extensive posterior sampling via nested sampling algorithms.

The choice between statistical frameworks depends on research priorities. NLS is appropriate for rapid parameter screening, high-throughput analysis, or when point estimates

with approximate uncertainties suffice. Bayesian inference is essential when rigorous uncertainty quantification is required, when comparing competing models, when parameter correlations must be characterized, or when decisions depend critically on confidence in parameter estimates. For systematic studies requiring model selection across many data sets, the computational investment in Bayesian inference is typically justified by the reliability of the resulting conclusions.

For distinguishing among diffusion models (single vs two-component,  $\pm$ triplet state), two quantitative approaches are available: Bayesian model comparison via log evidence ( $\log Z$ ) and frequentist hypothesis testing using the F-test. Bayesian evidence provides the most robust criterion, particularly when using GLS with the full covariance matrix. Following standard interpretation scales for natural logarithm differences,<sup>39,79</sup>  $|\Delta \log Z| < 1$  indicates models are effectively indistinguishable,  $|\Delta \log Z| = 1-3$  provides positive evidence,  $|\Delta \log Z| = 3-5$  constitutes strong evidence, and  $|\Delta \log Z| > 5$  represents very strong evidence favoring one model over another. The  $\log Z$  values reported by the software include uncertainty estimates from the nested sampling procedure, allowing rigorous error propagation in model comparison.<sup>60</sup>

Nested diffusion models can be compared using the F-test, which assesses whether the reduction in residual variance achieved by a more complex model is statistically significant. The software reports the reduced chi-squared for each fitted model, from which the F-statistic can be directly constructed. Unlike Bayesian evidence, the F-test is restricted to nested models and assumes Gaussian residuals.<sup>80</sup>

The Bayesian evidence is most effective with GLS using decorrelated residuals; WLS with standardized residuals provides intermediate reliability, while OLS can lead to incorrect model selection due to neglected error correlations. GLS accounts for both heteroscedasticity and temporal correlations, providing the most reliable metrics when covariance can be estimated from replicate measurements. WLS accounts for heteroscedastic errors using point-wise variance estimates, offering a practical compromise applicable to both FCS and RICS. OLS assumes identical error across all ACF points and independence between measurements, leading to artificially narrow parameter distributions and an underestimation of uncertainty, but remains useful for rapid preliminary analysis or when only single measurements exist. For RICS data, GLS is currently not applicable (see *Limitations and Future Directions* below), restricting model comparison to WLS-based metrics or visual residual assessment.

The importance of proper error modeling is illustrated with synthetic data (Figure S1), where traces of freely diffusing particles without triplet kinetics were generated. When multiple traces were fitted using GLS with the full covariance matrix, the correct 3D isotropic model yielded the highest Bayesian evidence. However, fitting a single trace with OLS did not allow reliable model discrimination: the 3D model with triplet state ( $\log Z = -24.7 \pm 0.4$ ) and the true 3D isotropic model ( $\log Z = -25.6 \pm 0.4$ ) yielded statistically indistinguishable evidence ( $|\Delta \log Z| = 0.9$ ). This demonstrates how ignoring noise structure can lead to incorrect model selection, consistent with previous reports emphasizing the importance of proper error modeling in fluctuation spectroscopy.<sup>32,40</sup>

Determining whether diffusion is isotropic or anisotropic requires multiangle RICS measurements. In isotropic systems (e.g., solution-phase experiments), anisotropic fitting should

Table 3. Comparison of Open-Source FCS/RICS Analysis Platforms

Capability	IOCBIO FCS	Imaging FCS <sup>a</sup>	fcsSOFI <sub>b</sub>	PyCorrFit <sub>c</sub>	FoCuS-scan <sub>d</sub>	Group C <sup>e,f,g</sup>	Fiji RICS <sup>h</sup>
1. Fitting framework:							
Bayesian inference	✓	×	×	×	×	×	×
Nonlinear least squares	✓	✓	✓	✓	✓	✓	✓
2. Error models:							
OLS	✓	✓	✓	✓	✓	✓	✓
WLS	✓	×	×	✓	×	✓	×
GLS	✓	×	×	×	×	×	×
3. Diffusion models:							
3D diffusion	✓	✓	✓	✓	✓	✓	✓
Triplet-state kinetics	✓	✓	×	✓	✓	✓	✓
2-component diffusion	✓	✓	✓	✓	✓	✓	✓
4. Scanning features:							
Multiple angles	✓	×	×	×	×	×	×
Multiple speeds	✓	×	×	N/A	✓	N/A	×
5. PSF:							
Analytical Gaussian	✓	✓	✓	✓	✓	✓	✓
Experimentally measured	✓	×	×	×	×	×	×
6. $DC$ and $C$ pre-analysis							
✓	×	×	×	×	×	×	×
7. Image splitting/mapping							
✓	✓	✓	✓	N/A	✓	N/A	✓
8. GPU-accelerated ACF calculation							
✓	✓	×	×	×	×	×	×

<sup>a</sup>Sankaran et al., 2021 [50]; <sup>b</sup>Yoshida et al., 2021 [49]; <sup>c</sup>Müller et al., 2014 [45]; <sup>d</sup>Waithé et al., 2018 [46]; Group C (FCS-focused):

<sup>e</sup>ImFCS [42], <sup>f</sup>PAM [81], <sup>g</sup>FCSlib [48]; <sup>h</sup>Fiji RICS plugins [43, 44]. N/A: Not Applicable (FCS-only software without imaging/scanning capabilities).

yield nearly identical diffusion coefficients across all scan directions ( $DC_x \approx DC_y$ , within uncertainty). Anisotropic systems such as cardiomyocytes show clear directional dependence (Figure 6). However, weak anisotropy can be challenging to establish confidently, as directional differences may approach the magnitude of systematic uncertainties in PSF characterization or be obscured by noise correlations. A key limitation is that PSFs are characterized in solution rather than within live cells, as described in PSF Characterization. This measured PSF is then applied to fit both solution and live-cell experiments. Refractive index mismatches and optical aberrations introduced by cellular structures can alter the PSF shape compared to solution measurements, potentially contributing additional systematic uncertainty to extracted diffusion coefficients. Distinguishing genuine anisotropy from experimental artifacts—including PSF-related systematic errors—requires careful experimental design with multiple scan angles and sufficient statistical power.

### Comparison with Existing Software

Several open-source tools have been developed for FCS and RICS analysis over the past two decades, each contributing valuable capabilities while exhibiting specific limitations (Table 3). ImFCS introduced imaging-based correlation methods supporting both point FCS and scanning FCS configurations.<sup>42</sup> PyCorrFit provided a Python-based framework for generic FCS data evaluation with multiple diffusion models and WLS fitting.<sup>45</sup> FCSlib offers FCS and scanning FCS analysis in R with functions for mobility and molecular brightness estimation.<sup>48</sup> Specialized Python tools for optimized FCS

and scanning FCS analysis have been developed for conventional confocal microscopy data.<sup>46</sup> The Imaging FCS plugin for Fiji/ImageJ implements GPU-accelerated with PSF calibration capabilities, supporting FCS and scanning FCS.<sup>50</sup> For RICS analysis, several implementations exist within the Fiji/ImageJ ecosystem<sup>43,44</sup> providing accessible tools for spatial correlation analysis. Several MATLAB-based tools have been developed for fluorescence fluctuation analysis. These include the PAM framework, which integrates FCS and RICS analysis with ensemble and single-molecule fluorescence methods.<sup>81</sup> Another example is a quantitative 4D imaging approach that uses FCS calibration.<sup>47</sup> Additionally, fcsSOFI provides the spatiotemporal correlation method for scanning FCS, featuring GPU acceleration for the fitting stage.<sup>49</sup> While these MATLAB-based tools are open-source, their dependence on MATLAB as a proprietary environment limits broad accessibility.

Table 3 systematically compares correlation-based FCS and RICS platforms across key analytical capabilities. While existing software provide diverse features, critical limitations remain. None of these tools support multiple-angle RICS analysis for characterizing anisotropic diffusion in biological systems. While PSF calibration has been implemented in some packages<sup>50</sup> based on our knowledge no open-source tool incorporates experimentally measured 3D PSFs into the fitting procedure, and available frameworks remain limited to analytical Gaussian approximations. Only Imaging FCS currently supports GPU acceleration for ACF calculation, enabling order-of-magnitude speedups.<sup>50</sup> Based on our knowledge, Bayesian inference for fitting ACF data is not available in

any of the existing packages, and our implementation is unique in this regard. Furthermore, while available software relies on OLS or WLS for NLS fitting, our framework extends both Bayesian and NLS fitting by providing support for OLS, WLS, and GLS. Additionally, the platform introduces diffusion-concentration pre-analysis and filtering to identify and exclude poor-quality measurements before main parameter estimation. Our platform unifies FCS and RICS analysis within a single framework, with the flexibility to perform scanning FCS by setting the line scan displacement to zero ( $\Delta y = 0$ ) in the RICS, thereby covering the full spectrum of correlation-based fluorescence techniques.

### Machine Learning and Direct Trace Analysis

In recent years, machine learning (ML) and deep learning (DL) techniques have been explored for FCS and imaging-FCS applications.<sup>82</sup> Tang et al. introduced FCSNet and ImFCSNet, convolutional neural networks (CNN) trained on simulated data that predict diffusion parameters directly from intensity traces, reducing data requirements and enabling near real-time inference.<sup>83</sup> ML approaches have also been applied for artifact filtering<sup>36</sup> and anomalous diffusion classification.<sup>84</sup> However, these approaches face limitations: training on simulated data may not generalize to real experimental conditions that vary from one microscope to another; learned representations lack physical interpretability, hindering failure diagnosis; and integrated uncertainty quantification is limited. ML/DL methods are thus complementary to correlation-based approaches—excelling at rapid screening when training data exist, while correlation methods provide interpretable, physically grounded parameters with rigorous statistical inference.

An emerging alternative to conventional FCS is the class of methods based on direct fitting of experimental data using stochastic models. One of these methods, fluorescence intensity trace statistical analysis (FITSA), is a Bayesian framework that directly analyzes fluorescence intensity traces rather than derived autocorrelations.<sup>65</sup> Earlier Bayesian approaches introduced by Jazani and colleagues<sup>85–88</sup> established the conceptual basis for direct statistical analysis of photon traces, but their initial implementations<sup>86</sup> faced challenges related to computational efficiency and convergence.<sup>65</sup> FITSA addresses these limitations by offering faster and more stable convergence, enabling robust parameter estimation from substantially shorter measurements than FCS, minimizing laser exposure and phototoxicity, and accounting for statistical dependencies often overlooked in standard FCS fitting. By requiring fewer photons and avoiding problematic assumptions of autocorrelation analysis, FITSA and similar methods represent a major conceptual advance in fluctuation spectroscopy. However, FITSA is currently limited to relatively simple diffusion models (e.g., 3D single-component isotropic diffusion without triplet dynamics), requires low fluorophore concentrations, and is computationally demanding for more complex data sets. Addressing these FITSA issues will take some time, and this class of methods still has to prove itself in the field to fully fulfill their great potential.

The choice among approaches depends on experimental constraints and scientific goals. Our correlation-based platform is optimal for anisotropic diffusion characterization, multi-component diffusion, triplet-state kinetics, spatial parameter mapping, and moderate-to-high concentrations. Current FITSA implementation excels for brief measurements at low

concentrations with simple single-component isotropic diffusion. ML/DL methods suit real-time analysis and classification tasks. As direct trace analysis extend to handle anisotropic diffusion, multicomponent models, and higher concentrations, they may provide future alternatives to correlation-based analysis for broader applications.

### Limitations and Future Directions

Despite the advances described above, several limitations remain, ranging from practical software constraints to fundamental experimental challenges inherent to FCS and RICS. The software currently relies on HDF5 format for standardized input and output of raw data, correlation results, and fitted parameters. While HDF5 is an open format, future development is needed to facilitate conversion of user data sets into this format. This development is planned to be demand-driven, with either direct data import support or dedicated converters created through collaboration between developers and users.

Bayesian inference, while powerful for model selection and quantifying parameter uncertainty, remains computationally demanding for complex models. Future development could extend GPU acceleration to the Bayesian inference framework to improve computational efficiency.<sup>89</sup>

To take full advantage of GLS-based fitting, the covariance matrix must be estimated. This enables full implementation of Bayesian GLS fitting with rigorous uncertainty quantification and allows model comparison while accounting for correlated errors. In our current implementation, GLS-based fitting is supported only for FCS, where a single 1D intensity trace can be repeated thousands of times (much larger than the dimension of the ACF) to robustly estimate the covariance across lag times. Such estimation imposes several practical challenges to ensure the stability of the experimental setup. In the example shown in Figure 4, experiments took approximately 100 h. Over this time window, special precautions were necessary to prevent temperature fluctuations due to air conditioning and to minimize airflow variability in the microscopy room caused by ventilation cycles. These experiments were performed in solution and would be impossible—or at least exceptionally difficult—to perform on live cells due to phototoxicity, cell movement, and viability constraints. When such large numbers of repeats are not available, shrinkage-based approaches for estimating noise correlations from multiple ACFs can be applied.<sup>40</sup> However, whether this shrinkage fully reflects covariances through its approximation of the full covariance matrix is unclear. An alternative is to implement segmented and randomized ACF approaches, which reduce correlations between data points and allow standard goodness-of-fit evaluation with shorter experiments.<sup>32</sup> While not currently implemented, this is a promising approach for future development.

GLS fitting is not implemented for RICS due to experimental limitations, which are even more pronounced than for FCS. For RICS, after recording image stacks (e.g., 2000 frames of  $1000 \times 1000$  pixels), the 2D spatiotemporal ACF is cropped, and one quadrant containing positive time lags is selected for fitting. By default, this yields three correlation lines with approximately 100 ACF points each, which are flattened into a 1D vector (about 300 points total). Reliable estimation of such a covariance matrix would require thousands of independent RICS frames acquired under identical conditions (frame size, scanning speed, and angle),

which we expect is practically impossible in live-cell experiments. Additionally, RICS data acquisition is slower than FCS due to flyback periods during scanning when no data are collected, further extending the required experimental time.

As discussed earlier, PSFs are currently characterized in solution rather than within live cells. Future development of methods for in-cell PSF characterization would improve accuracy, particularly for detecting anisotropy where systematic PSF errors can approach or exceed the magnitude of directional diffusion differences. As a current practical solution, the platform allows PSF scale as an additional free parameter during fitting to accommodate calibration uncertainties or systematic PSF size deviations without requiring remeasurement.

## CONCLUSION

The presented open-source Python platform (IOC BIO FCS) unifies the analysis of FCS and RICS within a statistically rigorous and computationally efficient framework. By integrating GPU-accelerated ACF computation, support for arbitrary scan angles and speeds, and image splitting for spatial parameter mapping, the software enables analysis of large data sets and provides the ability to study anisotropic diffusion. Incorporation of experimentally measured PSFs, advanced filtering strategies, and robust fitting approaches—including both frequentist and Bayesian inference under explicit noise models—distinguishes the platform from existing tools. Comprehensive visualization of fitted results, residuals, posterior distributions, and spatial maps further ensures reproducibility and interpretability. Together, these capabilities establish a versatile framework for quantitative correlation-based fluorescence methods, with broad relevance to biophysics, biochemistry, and cellular biology research.

## STATISTICS AND REPRODUCIBILITY

All FCS and RICS data were analyzed using the statistical frameworks implemented in the IOC BIO FCS software. Parameter estimation was performed using NLS and Bayesian inference, with uncertainty quantified through posterior distributions. Model comparison was based on the Bayesian evidence ( $Z$ ). The number of traces or image frames used for analysis is indicated in the *Results* section.

## ASSOCIATED CONTENT

### Data Availability Statement

The data supporting the findings of this study are available from the corresponding author upon reasonable request. Representative FCS and RICS example data sets are accessible at: <https://iocbio.gitlab.io/fcs/example-datasets>. The source code and documentation are publicly available through the GitLab project at: <https://iocbio.gitlab.io/fcs/>.

### Supporting Information

The Supporting Information is available free of charge at <https://pubs.acs.org/doi/10.1021/acsomega.5c12269>.

Additional synthetic FCS validation data and covariance structure of autocorrelation noise; Bayesian model comparison of one- and two-component diffusion models with and without triplet-state contributions; additional experimental FCS analysis of Alexa Fluor 647-labeled Dextran; corresponding corner plots for all analyses (Figures S1–S6) (PDF)

## AUTHOR INFORMATION

### Corresponding Author

Marko Vendelin – Laboratory of Systems Biology, Department of Cybernetics, Tallinn University of Technology, Tallinn 12618, Estonia; [orcid.org/0000-0002-6459-0391](https://orcid.org/0000-0002-6459-0391); Email: [markov@sysbio.ioc.ee](mailto:markov@sysbio.ioc.ee)

### Authors

Hamed Karimi – Laboratory of Systems Biology, Department of Cybernetics, Tallinn University of Technology, Tallinn 12618, Estonia; [orcid.org/0000-0003-0275-5311](https://orcid.org/0000-0003-0275-5311)

Otto Gustavson – Laboratory of Systems Biology, Department of Cybernetics, Tallinn University of Technology, Tallinn 12618, Estonia; [orcid.org/0009-0005-1579-6923](https://orcid.org/0009-0005-1579-6923)

Irina Česnokova – Laboratory of Systems Biology, Department of Cybernetics, Tallinn University of Technology, Tallinn 12618, Estonia; [orcid.org/0000-0002-8590-2278](https://orcid.org/0000-0002-8590-2278)

Jelena Branovets – Laboratory of Systems Biology, Department of Cybernetics, Tallinn University of Technology, Tallinn 12618, Estonia; [orcid.org/0000-0001-7970-8543](https://orcid.org/0000-0001-7970-8543)

Rikke Birkedal – Laboratory of Systems Biology, Department of Cybernetics, Tallinn University of Technology, Tallinn 12618, Estonia; [orcid.org/0000-0001-6777-7031](https://orcid.org/0000-0001-6777-7031)

Martin Laasmaa – Laboratory of Systems Biology, Department of Cybernetics, Tallinn University of Technology, Tallinn 12618, Estonia; [orcid.org/0000-0002-6663-6947](https://orcid.org/0000-0002-6663-6947)

Complete contact information is available at: <https://pubs.acs.org/10.1021/acsomega.5c12269>

### Author Contributions

Conceptualization: H.K., M.L., M.V. Data curation: H.K., O.G. Formal analysis: H.K., M.V. Funding acquisition: M.V. Investigation: H.K., O.G., M.V. Methodology: H.K., M.L., M.V. Project administration: M.V. Resources: I.C., J.B., M.L., R.B. Software: H.K., M.V. Supervision: M.L., M.V. Validation: H.K., M.V. Visualization: H.K., M.V. Writing—original draft: H.K. Writing—review and editing: H.K., M.L., M.V.

### Funding

This work was supported by the Estonian Research Council (PRG1127).

### Notes

The authors declare no competing financial interest.

## ACKNOWLEDGMENTS

Text was edited with the assistance of ChatGPT (OpenAI, San Francisco, CA).

## REFERENCES

- (1) Han, S. S.; Holmstedt, J. O. *Cell Biology*; McGraw-Hill: New York, 1979.
- (2) Alberts, B.; Hopkin, K.; Johnson, A. D.; Morgan, D.; Raff, M.; Roberts, K.; Walter, P. *Essential Cell Biology: Fifth International Student edition*; W.W. Norton, 2018.
- (3) Birkedal, R.; Laasmaa, M.; Vendelin, M. The Location of Energetic Compartments Affects Energetic Communication in Cardiomyocytes. *Front. Physiol.* **2014**, *5*, 376.
- (4) Birkedal, R.; Laasmaa, M.; Branovets, J.; Vendelin, M. Ontogeny of cardiomyocytes: ultrastructure optimization to meet the demand for tight communication in excitation–contraction coupling and energy transfer. *Philos. Trans. R. Soc., B* **2022**, *377* (1864), 20210321.

- (5) Kaasik, A.; Veksler, V.; Boehm, E.; Novotova, M.; Minajeva, A.; Ventura-Clapier, R. Energetic Crosstalk between Organelles: Architectural Integration of Energy Production and Utilization. *Circ. Res.* **2001**, *89*, 153–159.
- (6) Zaccolo, M.; Pozzan, T. Discrete Microdomains with High Concentration of cAMP in Stimulated Rat Neonatal Cardiac Myocytes. *Science* **2002**, *295*, 1711–1715.
- (7) Sepp, M.; Vendelin, M.; Vija, H.; Birkedal, R. ADP Compartmentation Analysis Reveals Coupling between Pyruvate Kinase and ATPases in Heart Muscle. *Biophys. J.* **2010**, *98*, 2785–2793.
- (8) Goonasekera, S. A.; Molkentin, J. D. Unraveling the Secrets of a Double Life: Contractile versus Signaling Ca<sup>2+</sup> in a Cardiac Myocyte. *J. Mol. Cell. Cardiol.* **2012**, *52*, 317–322.
- (9) Mika, D.; Leroy, J.; Vandecasteele, G.; Fischmeister, R. PDEs Create Local Domains of cAMP Signaling. *J. Mol. Cell. Cardiol.* **2012**, *52*, 323–329.
- (10) Jephthina, N.; Beraud, N.; Sepp, M.; Birkedal, R.; Vendelin, M. Permeabilized Rat Cardiomyocyte Response Demonstrates Intracellular Origin of Diffusion Obstacles. *Biophys. J.* **2011**, *101*, 2112–2121.
- (11) Simson, P.; Jephthina, N.; Laasmaa, M.; Peterson, P.; Birkedal, R.; Vendelin, M. Restricted ADP Movement in Cardiomyocytes: Cytosolic Diffusion Obstacles Are Complemented with a Small Number of Open Mitochondrial Voltage-Dependent Anion Channels. *J. Mol. Cell. Cardiol.* **2016**, *97*, 197–203.
- (12) Richards, M.; Lomas, O.; Jalink, K.; Ford, K. L.; Vaughan-Jones, R. D.; Lefkimmiatis, K.; Swietach, P. Intracellular Tortuosity Underlies Slow cAMP Diffusion in Adult Ventricular Myocytes. *Cardiovasc. Res.* **2016**, *110*, 395–407.
- (13) Ghigo, A.; Mika, D. cAMP/PKA Signaling Compartmentalization in Cardiomyocytes: Lessons from FRET-based Biosensors. *J. Mol. Cell. Cardiol.* **2019**, *131*, 112–121.
- (14) Birkedal, R.; Branovets, J.; Vendelin, M. Compartmentalization in Cardiomyocytes Modulates Creatine Kinase and Adenylate Kinase Activities. *FEBS Lett.* **2024**, *598*, 2623–2640.
- (15) Lin, T.-Y.; et al. Cardiac Contraction and Relaxation Are Regulated by Distinct Subcellular cAMP Pools. *Nat. Chem. Biol.* **2024**, *20*, 62–73.
- (16) Elson, E. L.; Magde, D. Fluorescence correlation spectroscopy. I. Conceptual basis and theory. *Biopolymers* **1974**, *13*, 1–27.
- (17) Petrov, E. P.; Schwille, P. *Standardization and Quality Assurance in Fluorescence Measurements II: Bioanalytical and Biomedical Applications*; Springer Series on Fluorescence, Resch-Genger, U.eds.; Springer: Berlin, Heidelberg; 2008, pp. 145–197.
- (18) Elson, E. L. Fluorescence Correlation Spectroscopy: Past, Present, Future. *Biophys. J.* **2011**, *101*, 2855–2870.
- (19) Digman, M. A.; Brown, C. M.; Sengupta, P.; Wiseman, P. W.; Horwitz, A. R.; Gratton, E. Measuring Fast Dynamics in Solutions and Cells with a Laser Scanning Microscope. *Biophys. J.* **2005**, *89*, 1317–1327.
- (20) Digman, M. A.; Gratton, E. Analysis of Diffusion and Binding in Cells Using the RICS Approach. *Microsc. Res. Tech.* **2009**, *72*, 323–332.
- (21) Lenne, P.-F.; et al. Dynamic Molecular Confinement in the Plasma Membrane by Microdomains and the Cytoskeleton Meshwork. *EMBO J.* **2006**, *25*, 3245–3256.
- (22) Hausteiner, E.; Schwille, P. Fluorescence Correlation Spectroscopy: Novel Variations of an Established Technique. *Annu. Rev. Biophys.* **2007**, *36*, 151–169.
- (23) Betaneli, V.; Schwille, P. *Lipid-Protein Interactions: Methods and Protocols*; Kleinschmidt, J. H. eds.; Humana Press: Totowa, NJ, 2013; pp. 253–278.
- (24) Mouttou, A.; Bremaud, E.; Noero, J.; Dibs, R.; Arone, C.; Mak, J.; Muriaux, D.; Berry, H.; Favard, C. Quantifying Membrane Binding and Diffusion with Fluorescence Correlation Spectroscopy Diffusion Laws. *Biophys. J.* **2023**, *122*, 2216–2229.
- (25) Wachsmuth, M.; Waldeck, W.; Langowski, J. Anomalous Diffusion of Fluorescent Probes inside Living Cell Nuclei Investigated by Spatially-Resolved Fluorescence Correlation Spectroscopy. *J. Mol. Biol.* **2000**, *298*, 677–689.
- (26) Weiss, M.; Hashimoto, H.; Nilsson, T. Anomalous Protein Diffusion in Living Cells as Seen by Fluorescence Correlation Spectroscopy. *Biophys. J.* **2003**, *84*, 4043–4052.
- (27) Illaste, A.; Laasmaa, M.; Peterson, P.; Vendelin, M. Analysis of Molecular Movement Reveals Latticelike Obstructions to Diffusion in Heart Muscle Cells. *Biophys. J.* **2012**, *102*, 739–748.
- (28) Li, H.; Zheng, K.; Yang, J.; Zhao, J. Anomalous Diffusion Inside Soft Colloidal Suspensions Investigated by Variable Length Scale Fluorescence Correlation Spectroscopy. *ACS Omega* **2020**, *5*, 11123–11130.
- (29) Bacia, K.; Kim, S. A.; Schwille, P. Fluorescence Cross-Correlation Spectroscopy in Living Cells. *Nat. Methods* **2006**, *3*, 83–89.
- (30) Kim, S. A.; Heinze, K. G.; Schwille, P. Fluorescence Correlation Spectroscopy in Living Cells. *Nat. Methods* **2007**, *4*, 963–973.
- (31) Koppel, D. E. Statistical Accuracy in Fluorescence Correlation Spectroscopy. *Phys. Rev. A* **1974**, *10*, 1938–1945.
- (32) Kohler, J.; Hur, K.-H.; Mueller, J. D. Statistical Analysis of the Autocorrelation Function in Fluorescence Correlation Spectroscopy. *Biophys. J.* **2024**, *123*, 667–680.
- (33) Oceau, V.; Cognet, L.; Duchesne, L.; Lasne, D.; Schaeffer, N.; Fernig, D. G.; Lounis, B. Photothermal Absorption Correlation Spectroscopy. *ACS Nano* **2009**, *3*, 345–350.
- (34) Hodges, C.; Kafle, R. P.; Hoff, J. D.; Meiners, J.-C. Fluorescence Correlation Spectroscopy with Photobleaching Correction in Slowly Diffusing Systems. *J. Fluoresc.* **2018**, *28*, 505–511.
- (35) Zhang, L.; Perez-Romero, C.; Dostajni, N.; Fradin, C. Using FCS to Accurately Measure Protein Concentration in the Presence of Noise and Photobleaching. *Biophys. J.* **2021**, *120*, 4230–4241.
- (36) Seltmann, A.; Carravilla, P.; Reglinski, K.; Eggeling, C.; Waithe, D. Neural Network Informed Photon Filtering Reduces Fluorescence Correlation Spectroscopy Artifacts. *Biophys. J.* **2024**, *123*, 745–755.
- (37) Vendelin, M.; Birkedal, R. Anisotropic Diffusion of Fluorescently Labeled ATP in Rat Cardiomyocytes Determined by Raster Image Correlation Spectroscopy. *Am. J. Physiol. Cell Physiol.* **2008**, *295*, C1302–C1315.
- (38) Sengupta, P.; Garai, K.; Balaji, J.; Periasamy, N.; Maiti, S. Measuring Size Distribution in Highly Heterogeneous Systems with Fluorescence Correlation Spectroscopy. *Biophys. J.* **2003**, *84*, 1977–1984.
- (39) He, J.; Guo, S.-M.; Bathe, M. Bayesian Approach to the Analysis of Fluorescence Correlation Spectroscopy Data I: Theory. *Anal. Chem.* **2012**, *84*, 3871–3879.
- (40) Guo, S.-M.; He, J.; Monnier, N.; Sun, G.; Wohland, T.; Bathe, M. Bayesian Approach to the Analysis of Fluorescence Correlation Spectroscopy Data II: Application to Simulated and In Vitro Data. *Anal. Chem.* **2012**, *84*, 3880–3888.
- (41) Sun, G.; Guo, S.-M.; Teh, C.; Korzh, V.; Bathe, M.; Wohland, T. Bayesian Model Selection Applied to the Analysis of Fluorescence Correlation Spectroscopy Data of Fluorescent Proteins in Vitro and in Vivo. *Anal. Chem.* **2015**, *87*, 4326–4333.
- (42) Sankaran, J.; Shi, X.; Ho, L. Y.; Stelzer, E. H. K.; Wohland, T. ImFCS: A Software for Imaging FCS Data Analysis and Visualization. *Opt. Express* **2010**, *18*, 25468–25481.
- (43) Rossow, M. J.; Sasaki, J. M.; Digman, M. A.; Gratton, E. Raster Image Correlation Spectroscopy in Live Cells. *Nat. Protoc.* **2010**, *5*, 1761–1774.
- (44) Schindelin, J.; et al. Fiji: An Open-Source Platform for Biological-Image Analysis. *Nat. Methods* **2012**, *9*, 676–682.
- (45) Müller, P.; Schwille, P.; Weidemann, T. PyCorrFit—Generic Data Evaluation for Fluorescence Correlation Spectroscopy. *Bioinformatics* **2014**, *30*, 2532–2533.
- (46) Waithe, D.; Schneider, F.; Chojnacki, J.; Clausen, M. P.; Shrestha, D.; de la Serna, J. B.; Eggeling, C. Optimized Processing and Analysis of Conventional Confocal Microscopy Generated Scanning FCS Data. *Methods* **2018**, *140–141*, 62–73.

- (47) Politi, A. Z.; Cai, Y.; Walther, N.; Hossain, M. J.; Koch, B.; Wachsmuth, M.; Ellenberg, J. Quantitative Mapping of Fluorescently Tagged Cellular Proteins Using FCS-calibrated Four-Dimensional Imaging. *Nat. Protoc.* **2018**, *13*, 1445–1464.
- (48) Pinto-Cámara, R.; Linares, A.; Moreno-Gutiérrez, D. S.; Hernández, H. O.; Martínez-Reyes, J. D.; Rendón-Mancha, J. M.; Wood, C. D.; Guerrero, A. FCSlib: An Open-Source Tool for Fluorescence Fluctuation Spectroscopy Analysis for Mobility, Number and Molecular Brightness in R. *Bioinformatics* **2021**, *37*, 1930–1931.
- (49) Yoshida, S.; Schmid, W.; Vo, N.; Calabrese, W.; Kislely, L. Computationally-Efficient Spatiotemporal Correlation Analysis Super-Resolves Anomalous Diffusion. *Opt. Express* **2021**, *29*, 7616–7629.
- (50) Sankaran, J.; Balasubramanian, H.; Tang, W. H.; Ng, X. W.; Röllin, A.; Wohland, T. Simultaneous Spatiotemporal Super-Resolution and Multi-Parametric Fluorescence Microscopy. *Nat. Commun.* **2021**, *12*, 1748.
- (51) Scipioni, L.; Bona, M. D.; Vicidomini, G.; Diaspro, A.; Lanzaò, L. Local Raster Image Correlation Spectroscopy Generates High-Resolution Intracellular Diffusion Maps. *Commun. Biol.* **2018**, *1* (1), 10.
- (52) Cole, R. W.; Jinadasa, T.; Brown, C. M. Measuring and Interpreting Point Spread Functions to Determine Confocal Microscope Resolution and Ensure Quality Control. *Nat. Protoc.* **2011**, *6*, 1929–1941.
- (53) Zhang, B.; Zerubia, J.; Olivo-Marin, J.-C. Gaussian Approximations of Fluorescence Microscope Point-Spread Function Models. *Appl. Opt.* **2007**, *46*, 1819–1829.
- (54) Hess, S. T.; Webb, W. W. Focal Volume Optics and Experimental Artifacts in Confocal Fluorescence Correlation Spectroscopy. *Biophys. J.* **2002**, *83*, 2300–2317.
- (55) Seber, G. A. F.; Wild, C. J. *Nonlinear Regression*; Wiley: New York, 1989.
- (56) Davidson, R.; MacKinnon, J. G. *Econometric Theory and Methods*; Oxford University Press: New York, 2004.
- (57) Carroll, R. J.; Ruppert, D.; Stefanski, L. A.; Crainiceanu, C. M. *Measurement Error in Nonlinear Models: A Modern Perspective*; 2nd ed.; Chapman and Hall/CRC: New York, 2006.
- (58) Berger, J. O.; Jefferys, W. H. The Application of Robust Bayesian Analysis to Hypothesis Testing and Occam's Razor. *J. Ital. Stat. Soc.* **1992**, *1*, 17–32.
- (59) Kass, R. E.; Raftery, A. E. Bayes Factors. *J. Am. Stat. Assoc.* **1995**, *90*, 773–795.
- (60) Buchner, J. UltraNest - a robust, general purpose Bayesian inference engine. *J. Open Source Software* **2021**, *6*, 3001.
- (61) Frisk, M.; Koivumäki, J. T.; Norseng, P. A.; Maleckar, M. M.; Sejersted, O. M.; Louch, W. E. Variable T-Tubule Organization and Ca<sup>2+</sup> Homeostasis across the Atria. *Am. J. Physiol. Heart Circ. Physiol.* **2014**, *307*, H609–H620.
- (62) Laasmaa, M.; Branovets, J.; Barsunova, K.; Karro, N.; Lygate, C. A.; Birkedal, R.; Vendelin, M. Altered Calcium Handling in Cardiomyocytes from Arginine-Glycine Amidinotransferase-Knockout Mice Is Rescued by Creatine. *Am. J. Physiol. Heart Circ. Physiol.* **2021**, *320*, H805–H825.
- (63) Branovets, J.; Karro, N.; Barsunova, K.; Laasmaa, M.; Lygate, C. A.; Vendelin, M.; Birkedal, R. Cardiac Expression and Location of Hexokinase Changes in a Mouse Model of Pure Creatine Deficiency. *Am. J. Physiol. Heart Circ. Physiol.* **2021**, *320*, H613–H629.
- (64) Laasmaa, M.; Vendelin, M.; Peterson, P. Application of Regularized Richardson-Lucy Algorithm for Deconvolution of Confocal Microscopy Images. *Biophys. J.* **2011**, *100*, 139a.
- (65) Karimi, H.; Laasmaa, M.; Pihlak, M.; Vendelin, M. Statistical Analysis of Fluorescence Intensity Transients with Bayesian Methods. *Sci. Adv.* **2025**, *11* (16), No. eads4609.
- (66) Folk, M.; Heber, G.; Kozioł, Q.; Pourmal, E.; Robinson, D. An Overview of the HDF5 Technology Suite and Its Applications. *Proceedings Of The EDBT/ICDT 2011 Workshop On Array Databases* ACM201136–47
- (67) Rew, R.; Davis, G. NetCDF: An Interface for Scientific Data Access. *IEEE Comput. Graphics Appl.* **1990**, *10*, 76–82.
- (68) Teodoro, G.; Kurc, T. M.; Pan, T.; Cooper, L. A.; Kong, J.; Widener, P.; Saltz, J. H. Accelerating Large Scale Image Analyses on Parallel, CPU-GPU Equipped Systems. *2012 IEEE 26th International Parallel and Distributed Processing Symposium* IEEE201220121093–1104
- (69) Wu, G.; Nowotny, T.; Chen, Y.; Li, D. D.-U. GPU Acceleration of Time-Domain Fluorescence Lifetime Imaging. *J. Biomed. Opt.* **2016**, *21*, 017001.
- (70) Lu, G.; et al. A Real-Time GPU-accelerated Parallelized Image Processor for Large-Scale Multiplexed Fluorescence Microscopy Data. *Front. Immunol.* **2022**, *13*, 981825.
- (71) Virtanen, P.; et al. SciPy 1.0 Contributors, SciPy 1.0: Fundamental Algorithms for Scientific Computing in Python. *Nat. Methods* **2020**, *17*, 261–272.
- (72) Buchner, J. A Statistical Test for Nested Sampling Algorithms. *Stat. Comput.* **2016**, *26*, 383–392.
- (73) Buchner, J. Collaborative Nested Sampling: Big Data vs. Complex Physical Models. *Publ. Astron. Soc. Pac.* **2019**, *131*, 108005.
- (74) Risti, R.; et al. Combined Action of Albumin and Heparin Regulates Lipoprotein Lipase Oligomerization, Stability, and Ligand Interactions. *PLoS One* **2023**, *18*, No. e0283358.
- (75) Barulin, A.; Kim, Y.; Oh, D. K.; Jang, J.; Park, H.; Rho, J.; Kim, I. Dual-Wavelength Metalens Enables Epi-fluorescence Detection from Single Molecules. *Nat. Commun.* **2024**, *15*, 26.
- (76) Lee, J.; Fujii, F.; Kim, S. Y.; Pack, C.-G.; Kim, S. W. Analysis of Quantum Rod Diffusion by Polarized Fluorescence Correlation Spectroscopy. *J. Fluoresc.* **2014**, *24*, 1371–1378.
- (77) Widengren, J.; Schwille, P. Characterization of Photoinduced Isomerization and Back-Isomerization of the Cyanine Dye Cy5 by Fluorescence Correlation Spectroscopy. *J. Phys. Chem. A* **2000**, *104*, 6416–6428.
- (78) Feldman, H.; Iron, M. A.; Fixler, D.; Moshkov, S.; Zurgil, N.; Afrimzon, E.; Deutsch, M. Fluorophore Spectroscopy in Aqueous Glycerol Solution: The Interactions of Glycerol with the Fluorophore. *Photochem. Photobiol. Sci.* **2021**, *20*, 1397–1418.
- (79) Jeffreys, S. H.; Jeffreys, S. H. *The Theory of Probability*; 3th ed.; Oxford Classic Texts in the Physical Sciences, Oxford University Press: Oxford, NY, 1998.
- (80) Bevington, P. R. *Data Reduction and Error Analysis for the Physical Sciences*; McGraw-Hill: Boston, 2003.
- (81) Schrimpf, W.; Barth, A.; Hendrix, J.; Lamb, D. C. PAM: A Framework for Integrated Analysis of Imaging, Single-Molecule, and Ensemble Fluorescence Data. *Biophys. J.* **2018**, *114*, 1518–1528.
- (82) Enderlein, J. Machine Learning and Advanced Statistical Analysis for Fluorescence Correlation Spectroscopy. *Biophys. J.* **2024**, *123*, 651–652.
- (83) Tang, W. H.; Sim, S. R.; Aik, D. Y. K.; Nelanuthala, A. V. S.; Athilingam, T.; Röllin, A.; Wohland, T. Deep Learning Reduces Data Requirements and Allows Real-Time Measurements in Imaging FCS. *Biophys. J.* **2024**, *123*, 655–666.
- (84) Quiblier, N.; Rye, J.-M.; Leclerc, P.; Truong, H.; Hannou, A.; Heliot, L.; Berry, H. Enhancing Fluorescence Correlation Spectroscopy with Machine Learning to Infer Anomalous Molecular Motion. *Biophys. J.* **2025**, *124*, 844–856.
- (85) Jazani, S.; Sgouralis, I.; Pressé, S. A Method for Single Molecule Tracking Using a Conventional Single-Focus Confocal Setup. *J. Chem. Phys.* **2019**, *150*, 114108.
- (86) Jazani, S.; Sgouralis, I.; Shafraz, O. M.; Levitus, M.; Sivasankar, S.; Pressé, S. An Alternative Framework for Fluorescence Correlation Spectroscopy. *Nat. Commun.* **2019**, *10*, 3662.
- (87) Tavakoli, M.; Jazani, S.; Sgouralis, I.; Shafraz, O. M.; Sivasankar, S.; Donaphon, B.; Levitus, M.; Pressé, S. Pitching Single-Focus Confocal Data Analysis One Photon at a Time with Bayesian Nonparametrics. *Phys. Rev. X* **2020**, *10*, 011021.
- (88) Jazani, S.; Xu, L. W. Q.; Sgouralis, I.; Shepherd, D. P.; Pressé, S. Computational Proposal for Tracking Multiple Molecules in a Multifocus Confocal Setup. *ACS Photonics* **2022**, *9*, 2489–2498.

(89) Beam, A. L.; Ghosh, S. K.; Doyle, J. Fast Hamiltonian Monte Carlo Using GPU Computing. *J. Comput. Graph. Stat.* **2016**, *25*, S36–S48.



CAS BIOFINDER DISCOVERY PLATFORM™

## CAS BIOFINDER HELPS YOU FIND YOUR NEXT BREAKTHROUGH FASTER

Navigate pathways, targets, and  
diseases with precision

Explore CAS BioFinder





## Appendix 2

### II

Robert Risti, Kathryn H. Gunn, Kristofer Hiis-Hommuk, Natjan-Naatan Seeba, **Hamed Karimi**, Ly Villo, Marko Vendelin, Saskia B. Neher, and Aivar Lõokene. Combined action of albumin and heparin regulates lipoprotein lipase oligomerization, stability, and ligand interactions. *PLOS ONE*, 18(4):e0283358, 2023



## RESEARCH ARTICLE

# Combined action of albumin and heparin regulates lipoprotein lipase oligomerization, stability, and ligand interactions

Robert Risti<sup>1</sup>, Kathryn H. Gunn<sup>2</sup>, Kristofer Hiis-Hommuk<sup>3</sup>, Natjan-Naatan Seeba<sup>1</sup>, Hamed Karimi<sup>3</sup>, Ly Villo<sup>1</sup>, Marko Vendelin<sup>3</sup>, Saskia B. Neher<sup>2</sup>, Aivar Lõokene<sup>1\*</sup>

**1** Department of Chemistry and Biotechnology, Tallinn University of Technology, Tallinn, Estonia, **2** Department of Biochemistry and Biophysics, The University of North Carolina at Chapel Hill, Chapel Hill, North Carolina, United States of America, **3** Laboratory of Systems Biology, Department of Cybernetics, Tallinn University of Technology, Tallinn, Estonia

\* [aivar.lookene@taltech.ee](mailto:aivar.lookene@taltech.ee)



## Abstract

Lipoprotein lipase (LPL), a crucial enzyme in the intravascular hydrolysis of triglyceride-rich lipoproteins, is a potential drug target for the treatment of hypertriglyceridemia. The activity and stability of LPL are influenced by a complex ligand network. Previous studies performed in dilute solutions suggest that LPL can appear in various oligomeric states. However, it was not known how the physiological environment, that is blood plasma, affects the action of LPL. In the current study, we demonstrate that albumin, the major protein component in blood plasma, has a significant impact on LPL stability, oligomerization, and ligand interactions. The effects induced by albumin could not solely be reproduced by the macromolecular crowding effect. Stabilization, isothermal titration calorimetry, and surface plasmon resonance studies revealed that albumin binds to LPL with affinity sufficient to form a complex in both the interstitial space and the capillaries. Negative stain transmission electron microscopy and raster image correlation spectroscopy showed that albumin, like heparin, induced reversible oligomerization of LPL. However, the albumin induced oligomers were structurally different from heparin-induced filament-like LPL oligomers. An intriguing observation was that no oligomers of either type were formed in the simultaneous presence of albumin and heparin. Our data also suggested that the oligomer formation protected LPL from the inactivation by its physiological regulator angiopoietin-like protein 4. The concentration of LPL and its environment could influence whether LPL follows irreversible inactivation and aggregation or reversible LPL oligomer formation, which might affect interactions with various ligands and drugs. In conclusion, the interplay between albumin and heparin could provide a mechanism for ensuring the dissociation of heparan sulfate-bound LPL oligomers into active LPL upon secretion into the interstitial space.

## OPEN ACCESS

**Citation:** Risti R, Gunn KH, Hiis-Hommuk K, Seeba N-N, Karimi H, Villo L, et al. (2023) Combined action of albumin and heparin regulates lipoprotein lipase oligomerization, stability, and ligand interactions. PLoS ONE 18(4): e0283358. <https://doi.org/10.1371/journal.pone.0283358>

**Editor:** Maria Gasset, Consejo Superior de Investigaciones Científicas, SPAIN

**Received:** December 21, 2022

**Accepted:** March 7, 2023

**Published:** April 12, 2023

**Copyright:** © 2023 Risti et al. This is an open access article distributed under the terms of the [Creative Commons Attribution License](https://creativecommons.org/licenses/by/4.0/), which permits unrestricted use, distribution, and reproduction in any medium, provided the original author and source are credited.

**Data Availability Statement:** All relevant data are within the manuscript and its [Supporting Information](#) files.

**Funding:** This work was supported by Tallinn University of Technology (grant SS22005 to A.L), Estonian Research Council (Grant No PRG1127 to M.V) and by National Institutes of Health (Grant No. R01-HL12565 to S.B.N) and American Heart Association (Grant No. 900354 to K.H.G). The funders had no role in study design, data collection

## Introduction

Lipoprotein lipase (LPL) is a crucial enzyme in the intravascular hydrolysis of triglyceride-rich lipoproteins (TLRs). LPL deficiency causes hypertriglyceridemia, which is causally linked to

and analysis, decision to publish, or preparation of the manuscript.

**Competing interests:** The authors have declared that no competing interests exist.

cardiovascular disease (CVD) and pancreatitis[1–5]. LPL and its regulators are potential drug targets for the treatment of hypertriglyceridemia[6–8]. LPL is mainly produced by adipose and muscle parenchymal cells and secreted into the interstitial space where a capillary endothelial protein called glycosylphosphatidylinositol-anchored high-density lipoprotein-binding protein 1 (GPIHBP1) transports LPL to the endothelium of the vascular lumen[9, 10]. At this site, LPL catalyzes the hydrolytic degradation of triglycerides in chylomicrons (CM) and very low-density lipoproteins (VLDL). In addition to GPIHBP1 and lipoproteins, secreted LPL is known to interact with apolipoprotein CII[11], fatty acids[12, 13], heparan sulfates [14], and angiopoietin-like proteins (ANGPTLs) 3, 4, and 8 [15]. LPL activity is also indirectly affected by apolipoproteins CIII, CI [16], and AV [17]. Combined action of these ligands may play a key role in the extracellular regulation of LPL activity [17, 18]. Regulators and ligands can affect LPL in a variety of extracellular regions, including the interstitial space and vascular endothelium. In the postprandial state, LPL is also associated with circulating TRLs and is involved in the uptake of remnant lipoproteins by the liver [19].

Although significant progress has been made in understanding the complex regulation system of LPL, there are still several aspects that require further investigation. This is because the basic mechanistic knowledge about LPL and its regulators is primarily based on experiments performed with purified proteins and synthetic lipid substrates in conventional buffer solutions. However, it should be considered that in the native capillary plasma environment, which contains thousands of proteins and other molecules, extracellular effects on LPL can occur. The high plasma protein content (80 g/liter) is sufficient to produce a macromolecular crowding effect [20] that may affect LPL and its ligands. Many studies indicate that the stability, structure, and aggregation of proteins in general can be significantly affected by the macromolecular crowding effect [21–23]. In addition to the crowding effect, LPL may be affected by plasma components which have not been identified yet.

Numerous studies indicate that LPL can exist in different conformational and oligomeric states. It has been shown by several studies that purified and active LPL appears as a dimer. These dimers rapidly exchange subunits and can irreversibly dissociate into inactive monomers [24, 25]. According to this mechanism, a part of the active LPL pool is always in monomeric form. Recent studies have indicated that LPL can be in an active monomeric form under certain conditions [26]. In addition, based on recent x-ray crystal studies, monomeric LPL forms a stable 1:1 complex with its transporter GPIHBP1 [27, 28]. This state has been proposed to be the active form of LPL at the vascular endothelium [29]. Under physiological salt concentration, temperature and pH, isolated LPL is very unstable and loses most of its activity within minutes. This inactivation occurs due to conformational changes in the N-terminal domain of LPL and leads to the irreversible formation of inactive monomers that can form amorphous aggregates [25]. The inactive monomeric LPL has lower affinity for heparin than the active form, this difference is used for their separation using heparin-chromatography [30]. ANGPTL3, 4 and 8 actively regulate the ratio between inactive and active LPL as a means of post-translational regulation of LPL in tissues [31]. Similar to the thermal inactivation, ANGPTL4 induces conformational changes in the N-terminal domain of LPL [32]. However, the states of LPL are not limited to dimer and monomer, as recent data revealed that natively folded LPL can form helical oligomers at high concentrations, which are stabilized by the presence of heparin [33]. These oligomers are composed of dihedral LPL dimers, and unlike the amorphous irreversible aggregates of LPL, their dissociation restores the catalytic activity of LPL. The existence of inactive, helical form of LPL raises the question of under which conditions is LPL activity irreversibly vs. reversibly lost. In addition, there is the question of where different oligomeric forms of LPL are present in the body, and how LPL transitions between these forms.

LPL oligomerization varies as it travels through the cell, interstitial space, and vascular endothelium. Prior to secretion, it has been shown that LPL forms helical oligomers in the presence of heparan sulfate proteoglycans (HSPG) attached to syndecan-1 (SDC1) inside of adipose cell vesicles [33]. Following secretion, LPL has been found to linger at the cell surface in HeLa cells, tethered there by HSPGs [34]. This raises the question of what precipitates LPL dissociation from the HSPG, permitting LPL to transfer across the interstitial space and reach GPIHBP1. During this time in the interstitial space, it is crucial that LPL does not degrade prior to binding GPIHBP1, which facilitates LPL's transfer into the capillaries. LPL is known to be stabilized by heparin, which is comparable to HSPGs [14, 33], which are present in the interstitial space. However, it begs the question whether there are additional components that influence LPL in the interstitial space, given the propensity of LPL to oligomerize in the presence of HSPGs.

In the present study we show that albumin, the major protein in blood plasma, forms a complex with LPL and has a significant effect on LPL stability and oligomerization. Surface plasmon resonance (SPR) measurements revealed that the LPL-albumin complex is dynamic, with a lifetime of less than few seconds. The equilibrium dissociation constant of the complex is 30–70  $\mu\text{M}$ , which is comparable to the albumin concentration in the interstitial space [35], suggesting the physiological relevance of the LPL-albumin interaction. Negative stain transmission electron microscopy (nsTEM) and raster image correlation spectroscopy (RICS) measurements indicate that albumin, like heparin, induces reversible concentration dependent oligomerization of LPL. However, the oligomers decomposed when both heparin and albumin were present, indicating that albumin may play a role in liberating LPL from HSPGs allowing LPL to transit across the interstitial space. The reversible oligomerization also protected LPL from inactivation by its physiological regulator ANGPTL4. Based on these observations, we conclude that the role of albumin in the LPL system is more diverse than the previously known role of binding lipolysis-derived fatty acids in the capillaries.

## 2. Materials and methods

### 2.1 Reagents

Normolipidemic non-fasting plasma samples were purchased from Tallinn Blood Centrum, aliquoted and stored at  $-80^{\circ}\text{C}$ . Triglyceride-rich lipoprotein fractions (CM/VLDL) were isolated from human plasma by density gradient ultracentrifugation. Goat serum as a source of apoC-II was obtained from Invitrogen (#10000C). Bovine LPL was purified from bovine milk [36] and dialyzed against 1 M NaCl and 20 mM  $\text{NaH}_2\text{PO}_4$ , pH 7.4 or 20 mM Bis-Tris, pH 6.5. Recombinant human LPL was purchased from Bio-Techne (#9888-LL) with a specific activity of  $>2,500$  pmol/min/ $\mu\text{g}$  as determined with 4-nitrophenyl butyrate. Recombinant N-terminal domain of ANGPTL4 (nANGPTL4<sup>26-184</sup>) was expressed in *E. coli* and purified as previously described [37]. Full-length ANGPTL4 was purchased from BioVendor (#RD172073100-HEK). Human GPIHBP1 was purchased from Sino Biological (#15388-H02H). Both proteins were assessed by reducing and non-reducing SDS-PAGE prior to use. 1,2-Di-O-lauryl-rac-glycero-3-glutaric acid 6-methylresorufin ester (DGGR) (#30058) and bovine serum albumin (#A7906) were purchased from Sigma Aldrich. Na-deoxycholate (#218590250) and heparin (#411212500) were purchased from Acros Organics. Polyethylene glycol 6000 (PEG 6) was purchased from Alfa Aesar (#A17541) and dextran 40000 (dextran 40) from Sigma Aldrich (#31389). The amino coupling kit (containing N-hydroxysuccinimide, N-ethyl-N9 [(diethylamino)propyl]carbodiimide, 1M ethanolamine) and BIAcore sensor chips were purchased from GE Healthcare. Fluorescence reagent ATTO610-NHS ester was purchased from Merck (#93259). Lipoprotein free human plasma (LFHP) from a single donor was obtained by

flotation ultracentrifugation at  $d = 1.215$  g/ml [38] and dialyzed against 150 mM NaCl. Residual triglyceride and cholesterol concentrations in LFPH were respectively 40  $\mu$ M and 10.34  $\mu$ M.

## 2.2 Determination of LPL activity using isothermal titration calorimetry (ITC)

Catalytic activity of LPL was measured using an ITC assay that allows to determine LPL activity in complex substrate systems including undiluted human plasma [39]. The assay is based on the detection of changes in heat rate as a result of LPL catalyzed hydrolysis of lipids. The heat rate detected by ITC corresponds to the release of fatty acids and is related to the catalytic activity of LPL. There is a linear correlation between heat production and the number of fatty acids released. LPL activity is expressed as  $\mu$ J/s (microjoule per second). The experiments in this study were performed on a MicroCal PEAQ-ITC (Malvern) as previously described [40]. In a standard measurement, the calorimetric cell (200  $\mu$ l) was filled with a substrate mixture and the syringe (40  $\mu$ l) contained 200 nM LPL in 150 mM NaCl, 20 mM HEPES, pH 7.4 buffer with 50 mg/ml BSA and 10 IU/ml heparin. The reference cell was filled with MilliQ water (200  $\mu$ l). The stirring speed in the sample cell was set to 1000 rpm in all experiments. Automatic baseline stabilization took 5–12 min, after which a 0.4  $\mu$ l LPL injection was made. Following that, a 5  $\mu$ l LPL injection was made, which increased LPL concentration in the cell by 5 nM and the new baseline was measured for 3 min. All incubations and measurements were carried out at room temperature. The sample cell and syringe were washed with 10% Decon 90 and rinsed with MilliQ water after each experiment. The syringe was additionally rinsed with methanol.

## 2.3 Determination of LPL activity with DGGR

LPL activity was determined with fluorogenic substrate DGGR, using a spectrofluorophotometer (Shimadzu RF-5301 PC, Shimadzu Corporation, Japan). The reaction was followed for 3 minutes at 25°C, using an excitation wavelength of 572 nm and an emission wavelength of 605 nm. Samples were prepared by incubating 200 nM LPL at room temperature in a 150 mM NaCl, 20 mM HEPES, pH 7.4 buffer with various supplements or in LFHP. The incubation mixture was diluted to 10 nM LPL in a measurement buffer containing 150 mM NaCl, 20 mM HEPES, 10 IU/ml heparin, 24  $\mu$ M DGGR and 0.5% Triton X-100. A 4 mM stock solution of DGGR was prepared in ethanol.

## 2.4 Determination of the affinity for the interaction of LPL-BSA using ITC

The binding affinity between bLPL and BSA was determined using MicroCal PEAQ-ITC. The calorimetric cell was filled with 1.695  $\mu$ M bLPL and 10 IU/ml heparin in 20 mM HEPES, 150 mM NaCl, pH 7.4 buffer. The syringe contained 752  $\mu$ M BSA in the same conditions and the reference cell was filled with degassed MilliQ water. Titration was carried out at 25°C with a reference power set to 41.9  $\mu$ J/s and at a stirring speed of 750 rpm. Binding affinity was estimated based on 38 sequential injections of BSA where each injection increased BSA concentration in the cell by 3.76  $\mu$ M. A control experiment (dilution of BSA) was carried out in the same conditions but without bLPL in the measurement cell. Data analysis and  $K_D$  estimation was performed with MicroCal PEAQ-ITC Analysis Software (Malvern).

## 2.5 Stabilization measurements for estimation of affinity for the interaction of LPL-BSA

Human or bovine LPL (200 nM) was preincubated alone or with various concentrations of BSA at room temperature in a solution of 20 mM HEPES, 150 mM NaCl, pH 7.4. After 60

minutes, LPL activity was determined at 25°C using DGGR as a substrate. Stabilization effect of BSA was calculated by subtracting the LPL activity at 60 minutes from the initial LPL activity. The affinity (expressed as  $K_D$ ) of BSA for bLPL or hLPL was calculated by the equation:

$$v = \frac{V_m \cdot [BSA]}{K_D + [BSA]} + v_0 \quad (1)$$

where  $v$  is the catalytic activity of hLPL or bLPL at any BSA concentration,  $[BSA]$ —BSA concentration,  $v_0$ —catalytic activity of bLPL or hLPL in the absence of BSA,  $V_m$ —maximal bLPL or hLPL activity achievable by increasing the BSA concentration. To obtain estimation for  $K_D$ , SigmaPlot software (SPSS, Chicago, IL, USA) and its hyperbolic curve fit function was used for fitting the experimental data according to Eq 1.

## 2.6 Surface plasmon resonance measurements

SPR experiments were performed on a Biacore 3000 instrument using CM5 sensorchips (GE Healthcare). The binding of BSA to bLPL was analyzed using two experimental set ups. In one experiment, biotinylated bLPL was attached to the surface of a CM5 sensor chip in 20 mM HEPES, 150 mM NaCl, pH 7.4 buffer via neutravidin that was covalently pre-immobilized using the amino coupling kit (GE Healthcare). It has been previously demonstrated that bLPL immobilized in this manner retains its ability to bind lipoproteins and ANGPTL4 [41]. 1074 RU of biotinylated bLPL was bound to the surface of the sensor which corresponded to a surface density of 19.5 fmol/mm<sup>2</sup>. In the other experiment, bLPL in 20 mM HEPES, 150 mM NaCl, 10 IU/ml heparin, 2 mg/ml BSA, pH 7.4 buffer was attached to GPIHBP1 that was covalently pre-immobilized in 10 mM acetic acid (pH 3.5) using the amino coupling kit. In this case, 215 RU of bLPL was bound to the immobilized GPIHBP1 corresponding to surface density of 3.9 fmol/mm<sup>2</sup>. Anti-LPL monoclonal antibody 5D2 was immobilized to a sensor chip according to Mysling et al. [42]. In this case, bLPL was bound to the immobilized 5D2 in 20 mM HEPES, 150 mM NaCl, 10 IU/ml heparin, pH 7.4. The surface density of bound LPL was 1.7 fmol/mm<sup>2</sup>. Binding of BSA to the sensor chips with bLPL were carried out at 25°C in a buffer that contained 20 mM HEPES, 150 mM NaCl, pH 7.4. For data analysis, nonspecific binding and bulk effect was subtracted from the total binding.

For calculation the number of BSA molecules bound to immobilized LPL ( $n$ ), we used the following equation:

$$n = \frac{RU_A/Mw_A}{RU_L/Mw_L} \quad (2)$$

where  $RU_A$  is the response for binding of BSA to the immobilized bLPL at the steady state;  $RU_L$  is the amount of immobilized LPL expressed in response units;  $Mw_A$  and  $Mw_L$  are molecular weights of BSA (66 kDa) and bLPL (55 kDa), respectively.

## 2.7 Determination of diffusion coefficients using raster image correlation spectroscopy

LPL was labelled with ATTO610-NHS ester for these experiments. This LPL conjugate was prepared as follows: LPL was dialyzed against 200 mM NaHCO<sub>3</sub>, 1 M NaCl, pH 8.4 buffer, after which LPL was incubated with ATTO610 at a 1:5 molar ratio for 2 h at 4°C. The active fluorescent LPL was purified using heparin chromatography and the concentration and degree of labeling was determined by measuring optical densities at  $\lambda_{280}$  and  $\lambda_{616}$ . Samples for RICS were prepared by incubating 10 nM LPL-ATTO610 with 190 nM unlabeled LPL at room

temperature for up to 2 hours in buffer containing 20 mM HEPES pH 7.4, 150 mM NaCl and either 2 or 50 mg/ml BSA or 10 IU/ml heparin. Heparin was added after 15 minutes into LPL incubation with BSA in measurements with both BSA and heparin. LPL was incubated for at least 2 hours in incubations with 1 M GuHCl to allow for monomerization of LPL to happen [43].

Raster image correlation spectroscopy (RICS) was used to determine diffusion coefficient assuming that the sample consisted of a single component. Previously developed RICS extensions were used [44, 45]. Namely, sample was scanned at three different line scanning frequencies and imaging a region of 20 x 20 μm. The signal was acquired during half of the scan time with the other half used for flyback with each image containing 1000 lines and pixel time set to 1 μs. Images were acquired in sets of 90 (line scanning frequency 500 Hz), 60 (289 Hz), and 30 (167 Hz) frames with the order of the used frequencies randomized. Measurements were performed on custom built confocal microscope as previously described [45]. Analysis of the samples involved in this work required additional filtering step. Namely, samples contained a small fraction of large particles that were visible on some of the images. Such large particles disturbed the correlation analysis and were removed from overall diffusion coefficient determination, as described in Results. To filter the images with the large particles, each acquired image was split into four equal sections and correlation functions (CF) for each section was found. CF from each section was fitted by single-component diffusion model and the diffusion coefficient together with the number of particles in the confocal volume. For image sections with the large particles, estimated diffusion coefficient and number of particles in confocal volume were much smaller than for the image sections without such particles (see Results for examples). The sections without large particles were later analyzed by finding CF on the basis of all data and fitting CF obtained for each line scanning frequency with the same model parameters. The used models assumed Gaussian form of the point spread function and triplet state. Measurements and analysis of RICS data was done blindly with the samples prepared and enumerated by personnel not involved in the measurements and analysis of RICS data to avoid any bias.

## 2.8 Negative stain transmission electron microscopy (nsTEM)

Samples were prepared as described for RICS. Briefly, LPL was diluted to 200 nM in buffer containing 20 mM HEPES pH 7.4, 150 mM NaCl, and 2 mg/ml BSA (A7906, Sigma) or 10 IU/ml Heparin (H19, Fisher scientific) and incubated for 30 min. For samples with both BSA and heparin, heparin was added 15 min into incubation. For samples with both heparin and triton X-100, triton X-100 was added 15 min into incubation. Following incubation, 5 μl of each sample was applied to a glow discharged ultrathin carbon nsTEM grid (CF300\_CU\_UL, EMS). Grids were glow discharged with a PELCO easiGlow for 25 seconds to ensure hydrophilization of the grid carbon. Sample was incubated on the grid for 1 min followed by a wash with 100 μl of 20 mM HEPES pH 7.4 and 150 mM NaCl. The grid was then stained for 1 min with a filtered 2% uranyl acetate solution in 50% ethanol, blotted, and allowed to dry. Grids were imaged using a TECNAI T12 microscope equipped with a Gatan Rio camera. Images were collected using DigitalMicrograph and analyzed with ImageJ.

## 3. Results

### 3.1 Effect of BSA on LPL stability

LPL irreversibly loses most of its catalytic activity in ordinary buffers within minutes but is stable for several hours in undiluted human plasma as shown by the measurements of ITC [39]. This stabilization could be due to the binding of LPL to lipoprotein surfaces, as this effect has

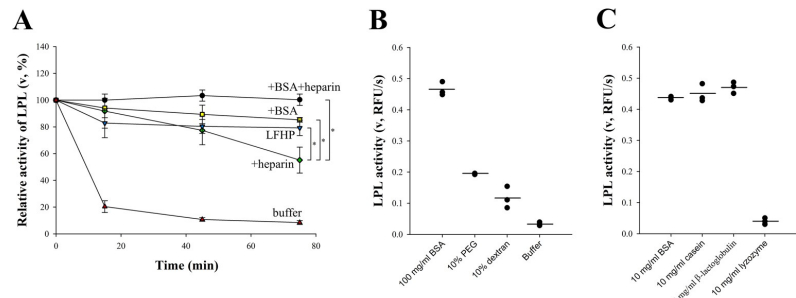


**Fig 1. Catalytic activity of LPL measured with DGGR after incubation in various conditions.** (A) 200 nM LPL was incubated in buffer A ( $\blacktriangle$ ), which contained 10 IU/ml heparin ( $\blacklozenge$ ), 50 mg/ml BSA ( $\blacksquare$ ) or both ( $\bullet$ ). Alternatively, LPL was incubated in LFHP ( $\blacktriangledown$ ). LPL activity is expressed relative to the initial activity of the experiment that contained both heparin and BSA. Results at 75 minutes were compared by two-tailed Student's *t*-test. \* $P < 0.05$ . LPL loses its activity quickly in plain buffer but is stabilized by lipoprotein free human plasma (LFHP) or its main constituent albumin (BSA). The most significant stabilization was observed when both BSA and heparin were used together. (B) 200 nM LPL was incubated in macromolecularly crowded buffer A. LPL activity is expressed as relative fluorescence units per second (RFU/s). PEG 6 nor dextran 40 could stabilize LPL like BSA, indicating that macromolecular crowding alone is not sufficient for LPL stabilization. (C) 200 nM LPL was incubated in buffer A with various proteins. Casein and  $\beta$ -lactoglobulin were as efficient as BSA in stabilizing LPL, however lysozyme failed to exert any effect. This suggests that LPL stabilization by proteins depends on their specific characteristics such as charge or hydrophobicity.

<https://doi.org/10.1371/journal.pone.0283358.g001>

also been observed in some artificial substrate emulsions [46]. To examine whether other plasma components affect LPL stability, incubations were performed in lipoprotein free human plasma (LFHP), and in various other solutions for comparison: a) 150 mM NaCl, 20 mM HEPES, pH 7.4 buffer (buffer A), b) buffer A supplemented with BSA, the main plasma protein, c) buffer A supplemented with heparin (a well-known stabilizer of LPL), d) buffer A supplemented with both BSA and heparin. LPL activity was measured at multiple time-points using the fluorogenic substrate DGGR. As seen in Fig 1A, LPL lost almost 80% of its initial activity within 15 min in buffer A. Significant stabilization was recorded in all other solutions used. LFHP and BSA were somewhat more effective stabilizers than heparin. The most significant LPL stabilization was observed when both BSA and heparin were present, as LPL was completely stable for 75 minutes in this case. The similar stabilization effect of BSA and LFHP suggests that albumin is a major stabilizer of LPL in plasma.

We next wanted to address the mechanism by which BSA might stabilize LPL. We first investigated whether BSA was acting as a macromolecular crowder, effectively stabilizing LPL by altering the properties of the surrounding buffer environment. For this purpose, BSA was replaced with 10% PEG or 10% dextran in the LPL incubation mixture with buffer A. The concentration of 10% for PEG or dextran was chosen to produce a crowding effect that is comparable or higher than that of BSA at the concentration 100 mg/ml [47]. The results of these experiments are presented as residual LPL activity determined after 60 minutes of incubation (Fig 1B). The loss of LPL activity was greater in buffer conditions without crowders, but neither PEG nor dextran stabilized LPL to the extent BSA did. LPL activity was at least two-fold higher when incubated with BSA instead of PEG or dextran. This observation suggests that macromolecular crowding alone is not sufficient to cause the stabilization of LPL.

We did find that BSA was not the only protein that stabilized LPL as the milk proteins casein and  $\beta$ -lactoglobulin had a similar ability (Fig 1C). However, lysozyme, a small antibacterial protein, lacked this property. Thus, the stabilization of LPL seems not to be a general property of proteins, but rather depends on their specific characteristics. The effect of casein agrees with previous studies (casein stabilizes LPL in milk [48]) and  $\beta$ -lactoglobulin may also

play a similar role. These proteins were chosen for comparison randomly based on their stability and solubility at room temperature.

The above experiments suggest that albumin plays a role in stabilizing LPL in the absence of substrate, the situation that occurs *in vivo* in the interstitial space after secretion of LPL from parenchymal cells. However, albumin is also required as a fatty acid acceptor to keep LPL active on triglycerides of long chain fatty acids. *In vivo* this occurs at the vascular endothelium when LPL binds lipoproteins and hydrolyzes their triglycerides. In the absence of albumin, long chain fatty acids inhibit LPL activity [12]. Here, we investigated whether the effect of albumin on LPL is limited to the fatty acid binding during lipolysis of lipoproteins by replacing BSA with another fatty acid acceptor,  $\beta$ -cyclodextrin, in the calorimetric assay (Fig 2). LPL activity was determined with ITC using a mixture of isolated triglyceride-rich lipoproteins CM/VLDL (adjusted to 0.5 mM triglycerides) accompanied by BSA, PEG or dextran. The concentrations of BSA (0.75 mM) and  $\beta$ -cyclodextrin (8.81 mM) were chosen to be well above the required limit to bind all FFAs released during lipolysis. The lack of difference in LPL activity between the use of two different FFA acceptors, BSA and  $\beta$ -cyclodextrin, allows to conclude that the role of albumin during endothelial lipolysis is confined to binding released FFAs. Introducing a crowded environment did not seem to significantly affect LPL activity towards TRLs. Only a 20% increase in LPL activity was noticed when dextran was used as a macromolecular crowder, and no change was detected when BSA or PEG was involved. This implies that the role of albumin in stabilizing LPL is likely to occur prior to its movement onto the endothelial surface.

### 3.2 LPL forms a complex with BSA

Next, we investigated whether LPL was able to form a direct complex with BSA. The formation of the bLPL-BSA complex was first demonstrated by ITC by titrating BSA into a solution with

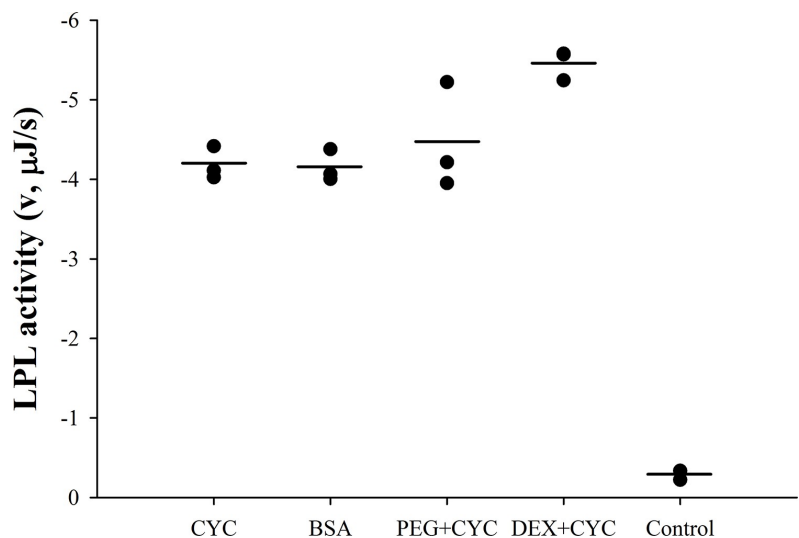


**Fig 2. Catalytic activity of LPL on triglyceride-rich lipoproteins in the presence of fatty acid acceptors and macromolecular crowders.** Measurements were performed using ITC. LPL activity is expressed as heat rate ( $\mu$ J/s). The substrate mixture contained CM/VLDL (adjusted to 0.5 mM triglycerides), 50 mg/ml BSA (0.75 mM) or 10 mg/ml  $\beta$ -cyclodextrin (8.81 mM) (CYC) and either 10% PEG 6 or 10% dextran 40 (DEX).

<https://doi.org/10.1371/journal.pone.0283358.g002>

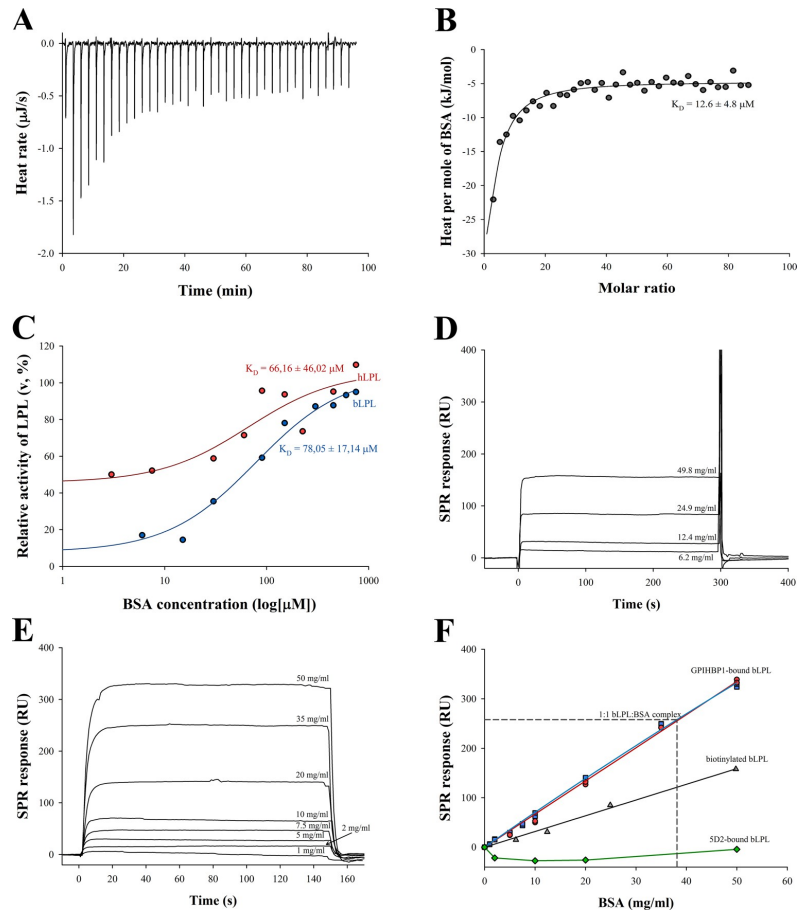


**Fig 3. Interaction of LPL with BSA as studied using ITC, stabilization of LPL, and SPR.** (A) An example ITC thermogram for the titration of BSA into a solution with bLPL, obtained after subtraction of the BSA dilution effect. The concentration of bLPL in the cell was 1.695  $\mu\text{M}$ . (B) Fitted isotherm for the binding between BSA and bLPL from the ITC experiment on panel A. (C) Enzymatic stability of LPL in the presence of BSA as determined with DGGR. 200 nM bLPL or hLPL was incubated for 60 minutes in buffer A at various BSA concentrations. The values are calculated relative to the initial activity of LPL in the same conditions. BSA stabilized both bLPL and hLPL in a concentration-dependent manner. (D) SPR sensorgrams showing binding of BSA to biotinylated bLPL that was attached to pre-immobilized neutravidin. (E) SPR sensorgrams showing BSA binding to bLPL that was attached to pre-immobilized GPIHBP1. In D and E, BSA concentrations are shown on sensorgrams. Non-specific binding sensorgrams of BSA to streptavidin and GPIHBP1, respectively, have been subtracted. (F) Plateau values of sensorgrams plotted against BSA concentration. ●—Binding of BSA with 0.1 IU/ml heparin to GPIHBP1-bound bLPL. ▲—Binding of BSA to biotinylated bLPL. ◆—Binding of BSA to 5D2-bound bLPL. Dashed line—1:1 ratio of immobilized bLPL to bound BSA in the experiment with GPIHBP1-bound bLPL. The results indicate that BSA can bind to neutravidin-bound LPL or GPIHBP1-bound LPL but not 5D2-bound LPL.

<https://doi.org/10.1371/journal.pone.0283358.g003>

bLPL (Fig 3A and 3B). This experiment was performed in the presence of heparin to stabilize bLPL. The bLPL-BSA interaction was exothermic and BSA concentrations above 3  $\mu\text{M}$  were required to record a measurable heat effect. The low solubility of bLPL, the weakness of the interaction, and the solubility limit of BSA did not allow us to perform experiments under

optimal conditions where all the parameters characterizing the interaction could be determined. Therefore, the ITC titration data could only be used to estimate the apparent affinity of the BSA-bLPL interaction. These data suggested a complex type of interaction: after an initial saturable binding phase, additional and almost constant heat production was recorded at higher BSA concentrations. The second weaker binding event was not well-defined to allow for the estimation of  $K_D$ . When the second weaker binding phase was not taken into account, the calculated apparent  $K_D$  for the initial binding was 12.6  $\mu\text{M}$ . However, our various simulations involving both phases confirmed that any additional binding has a negligible effect on the  $K_D$  of initial binding.

We also investigated the interaction between LPL and BSA by measuring the enzymatic stability of bovine LPL (bLPL) and human LPL (hLPL) at different BSA concentrations (Fig 3C). BSA stabilized both LPL homologs in a concentration-dependent manner and the stabilization effect was already detectable when BSA concentration was as low as 6  $\mu\text{M}$  (0.4 mg/ml). A hyperbolic relationship was observed between the relative increase of bLPL or hLPL activity and BSA concentration. The calculated apparent  $K_D$  for the interaction between bLPL-BSA and hLPL-BSA were 78  $\mu\text{M}$  (5.2 mg/ml) and 66  $\mu\text{M}$  (4.4 mg/ml), respectively. The reason for the difference in the  $K_D$  values between the ITC and the stabilization study is likely due to the presence of heparin in the ITC study.

In addition to ITC and enzymatic stability measurements, the interaction between bLPL and BSA was investigated by SPR. Three separate BSA binding experiments were performed using a Biacore 3000 (GE Healthcare): 1) with biotinylated bLPL non-covalently attached to neutravidin that was directly pre-immobilized on the sensor chip 2) with bLPL non-covalently attached to the chip surface via pre-immobilized GPIHBP1 3) with bLPL non-covalently attached to pre-immobilized 5D2 antibody. In all systems, dissociation of bLPL from the sensor chip was negligible. In the experiments with the neutravidin-bound biotinylated bLPL, a detectable association of BSA was observed when its concentration was above 6 mg/ml (91  $\mu\text{M}$ ) (Fig 3D) while in the case of GPIHBP1-bound bLPL, a detectable binding of BSA was observed at just 1 mg/ml (Fig 3E). In the case of 5D2-bound bLPL, at lower BSA concentrations of 5–20 mg/ml, the non-specific binding to 5D2 was higher than the binding to bLPL-5D2, however, minor association was observed when BSA concentration was as high as 50 mg/ml. We conclude that 5D2 strongly hinders association of BSA with LPL. The rectangular shape of the sensorgrams of the systems with GPIHBP1 and neutravidin indicated very fast off-kinetics, BSA was completely dissociated within few seconds. Such rapid dissociation made the correct calculation of rate constants impossible. The rapid dissociation kinetics also indicated that the lifetime of the bLPL-BSA complex is very short, less than a few seconds. For estimation of the equilibrium dissociation constant  $K_D$ , the plateau values were plotted against the BSA concentrations in the injected solutions (Fig 3F). In both systems, this relationship remained linear over the range of BSA concentrations used (0–910  $\mu\text{M}$ ), meaning that no saturation was achieved. Higher BSA concentrations were not possible with the BIAcore system. Additionally, the presence of 0.1 IU/ml heparin did not affect the binding of BSA to GPIHBP1-bound bLPL (Fig 3F, red circles). Although the apparent binding kinetics of BSA to neutravidin-bound LPL and to GPIHBP1-bound LPL were similar, much less of the GPIHBP1-bound LPL than the neutravidin-bound LPL was required for detectable BSA binding. The surface density 3.9 fmol/mm<sup>2</sup> of the GPIHBP1 bound LPL was sufficient to observe the interaction while a measurable association was detected when the surface density of neutravidin-bound biotin-bLPL was 19.5 fmol/mm<sup>2</sup>. When measuring 50 mg/ml BSA binding, the steady-state bound BSA/LPL molar ratio was 0.12:1 for neutravidin-bound LPL and 1.2:1 for GPIHBP1-bound LPL. This indicates that the main part of the neutravidin-bound LPL was not able to interact with BSA. At the same time, a significant fraction, if not all, of the LPL

bound to GPIHBP1 interacted with BSA. Non-saturable linear binding, as well as a greater than one molar ratio of bound BSA/LPL, suggest that each molecule of LPL attached to GPIHBP1 can simultaneously interact with multiple BSA molecules. In summary, all three different binding studies confirm that LPL forms a complex with BSA at physiologically relevant concentrations, as circulating albumin concentrations range from 35 to 50 mg/ml and 4.4–15.7 mg/ml in the interstitial space, the latter depending on the tissue [35].

### 3.3 Interplay between albumin and heparin differs from their individual effects

Building on the data that LPL forms a complex with BSA and previous works showing that LPL interacts with heparin, we wanted to investigate the independent and combined effects of BSA and heparin on LPL when LPL activity is determined with a natural substrate. When 200 nM LPL was incubated for 15 minutes with BSA or heparin alone, its activity on TRLs in human plasma, as measured by ITC, was much lower than when incubated in the presence of both heparin and BSA (Fig 4A). Our data therefore shows that when acting on a natural substrate, both heparin and BSA are needed during incubation for maximum LPL activity. This difference was not observed in the DGGR assay (Fig 1A) under the same incubation conditions, nor when LPL activity was measured using the tributyrin/gum arabic substrate system (S1 Fig). To elucidate the reason for this discrepancy between the assays, effects of various incubation conditions were tested. We found that LPL, which has been incubated with heparin alone for 15 minutes regains its maximal activity after dilution to a solution containing BSA (Fig 4B). A similar increase in LPL activity was also observed when the dilution was carried out into LFHP or Triton X-100 (Fig 4B). These data suggest that the low activity of LPL measured in human plasma when preincubated with heparin (Fig 4A) was due to reversible changes in the state of LPL. It has recently been shown that heparin induces formation of reversible inactive helical LPL oligomers that dissociate into active LPL in the presence of the

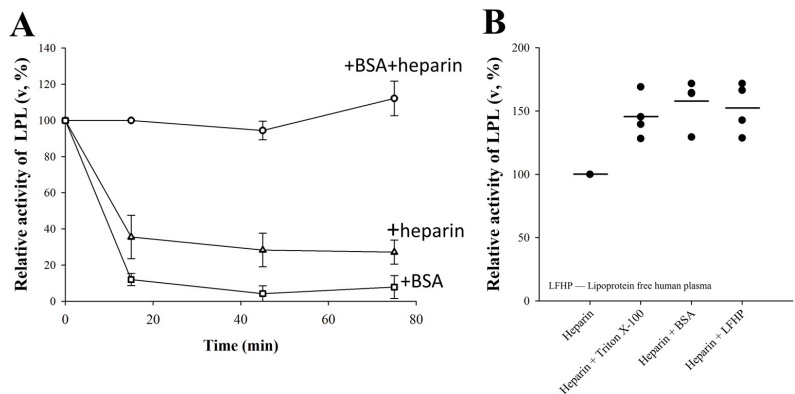


**Fig 4. Effect of BSA, Triton X-100 or LFHP on LPL activity in the presence of heparin.** (A) 200 nM LPL was incubated for the indicated timepoints with 50 mg/ml BSA, 10 IU/ml heparin or both in buffer A. The remaining activity (expressed as heat rate,  $\mu$ J/s) was determined with ITC after a single 5 nM LPL injection into human plasma that contained 1.31 mM triglycerides. LPL activity is expressed relative to the initial activity of the experiment that contained both heparin and BSA and the data is presented as mean  $\pm$  SD of three independent measurements. LPL activity was significantly lower when only BSA or heparin was used. (B) 1  $\mu$ M LPL was incubated with 10 IU/ml heparin in buffer A and diluted 5-fold to buffer A with heparin and 0.5% Triton X-100, 50 mg/ml BSA or LFHP. The remaining LPL activity was determined in the same manner as panel A. LPL activity was restored equally with every additive.

<https://doi.org/10.1371/journal.pone.0283358.g004>

surfactant deoxycholate [33]. Our data here indicate that the LPL helical oligomers do not dissociate into the active form in undiluted human plasma but do so in the substrate systems containing surfactants such as Triton X-100 in the DGGR assay or gum arabic in the tributyrin assay. The LPL helical oligomers also dissociated in the substrate-free preincubation solutions with Triton X-100, BSA, or LFHP. The observation that the oligomers did not dissolve in undiluted human plasma but did when lipoproteins were removed from plasma—that is, in LFHP,—suggests that the presence of lipoproteins hindered this process.

When LPL at various concentrations was preincubated with BSA alone prior to activity determination in human plasma by ITC, the observed catalytic activity of LPL was higher at its lower preincubation concentrations. A significant increase in the activity of LPL was observed when preincubation concentration was reduced from 200 nM to 20 nM (Fig 5). This sharp change in LPL activity suggests that BSA, like heparin, causes reversible oligomerization of LPL. Like heparin induced LPL oligomers, BSA induced LPL oligomers did not dissociate into active form in human plasma. The LPL concentration effect on its activity disappeared when heparin was combined with BSA during preincubation. In this case, LPL activity was the same for every concentration (Fig 5).

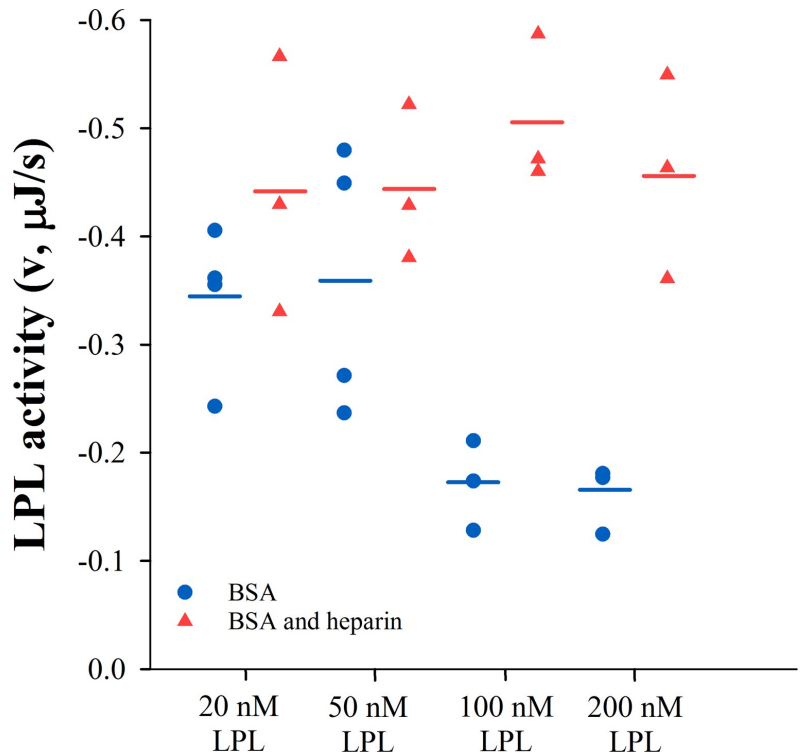


**Fig 5. Effect of LPL incubation concentration on its activity as measured with ITC.** LPL activity, expressed as heat rate ( $\mu\text{J/s}$ ), after incubation of LPL at various concentrations with 50 mg/ml BSA with ( $\blacktriangle$ ) or without ( $\bullet$ ) 10 IU/ml heparin in buffer A. The changes in residual LPL activity suggest that LPL oligomerization triggered by BSA is dependent on LPL concentration. This dependence disappears with the combined use of heparin and BSA which blocks the formation of LPL oligomers.

<https://doi.org/10.1371/journal.pone.0283358.g005>

### 3.4 Oligomerization of LPL as studied by RICS and Transmission Electron Microscopy (TEM)

To further characterize the LPL oligomerization occurring in the presence of heparin and BSA, we used RICS technology to determine diffusion coefficients ( $D$ ) and estimate the relative content of LPL species with different sizes. Larger particles will have a lower  $D$  value while smaller particles are characterized by high  $D$  values. We chose RICS technology instead of the previously used standard sedimentation method [14, 26] because the high sucrose concentration used in the latter would cause additional crowding effect [49, 50]. In the RICS experiments, LPL was labelled with the fluorescent marker ATTO610, and measurements were performed in the presence of either BSA, heparin, or both. No fluorescence correlation was observed in measurements performed with BSA alone in solution. Straightforward fitting of autocorrelation functions, as a part of RICS analysis, produced poor fits (results not shown). This was caused by the presence of a population of large bright particles which disturbed autocorrelation significantly and made it impossible to fit with the diffusion models. To resolve this issue, the recorded images were split into subsections and the diffusion coefficient with the number of particles ( $N$ ) in the confocal volume was estimated for each of these subsections. As it is shown in [S2A Fig](#), the estimated  $D$  varied from subsection to subsection throughout the experiment, including some with relatively small values. When plotting  $D$  against  $N$ , one can observe that there is a fraction of subsections with small  $D$  that have small  $N$  (bottom left corner of [Fig 6A, 6C and 6E](#)). This is consistent with large bright particles moving through the experimental area—leading to low  $D$  and small  $N$  values. The high variability of  $D$  and  $N$  estimates is expected as we used small datasets to make those estimations. Subsections with the small estimated  $D$  and  $N$  were removed and the average correlation functions for the remaining subsections were found and fitted with the diffusion model ([S2B Fig](#)). Analysis of the LPL diffusion coefficients for different samples is summarized in [Table 1](#), the average diffusion coefficient takes into account all observed larger and smaller species. RICS experiments were conducted using both 200 nM and 10 nM LPL to observe differences in the average diffusion coefficients resulting from LPL concentration.

LPL at 200 nM formed larger particles in the presence of 50 mg/ml BSA, as indicated by a low average  $D$  ( $7.4 \pm 1.2 \mu\text{m}^2/\text{s}$ ). In addition, as shown in [Fig 6A](#), the sample was heterogeneous, leading to formation of tail-like structure on  $N$ - $D$  scatter plot (red circle). We predict that the large particles represent the reversible oligomerized state of LPL identified with BSA. Oligomerization of LPL was also seen with 10 IU/ml heparin ([Fig 6C](#)), albeit in a smaller proportion as indicated by larger average  $D$  of  $\sim 20 \mu\text{m}^2/\text{s}$  ([Table 1](#)). Similar average  $D$  ( $\sim 22 \mu\text{m}^2/\text{s}$ ) was recorded after addition of 10 IU/ml heparin to the LPL+BSA mixture homogenized the LPL distribution ([Fig 6E](#)). This agrees with ITC measurements that show LPL activity of ATTO610 labeled LPL is restored after addition of heparin to an LPL-BSA incubation ([S3 Fig](#)), similarly to how BSA was previously able to restore LPL activity in a heparin containing solution ([Fig 4B](#)). The same pattern was observed at 2 mg/ml BSA concentration ([Table 1](#)). However, on the basis of  $D$  measurements, it is impossible to explain the differences in activity of LPL with heparin alone and BSA with heparin. In solution, LPL is likely in a similar size, but inactive conformation, in the presence of heparin at this LPL concentration, as indicated by activity measurements.

TEM experiments were used to examine the appearance of LPL aggregates under the conditions used in the RICS measurements, but without ATTO610 labeled LPL. LPL aggregates were observed with BSA ([Fig 6B](#)), which were not seen with BSA alone ([S4A Fig](#)). LPL helical oligomers were observed when incubated with heparin ([Fig 6D](#)). LPL aggregates were not observed when combined with both BSA and heparin ([Fig 6F](#)), although combining heparin

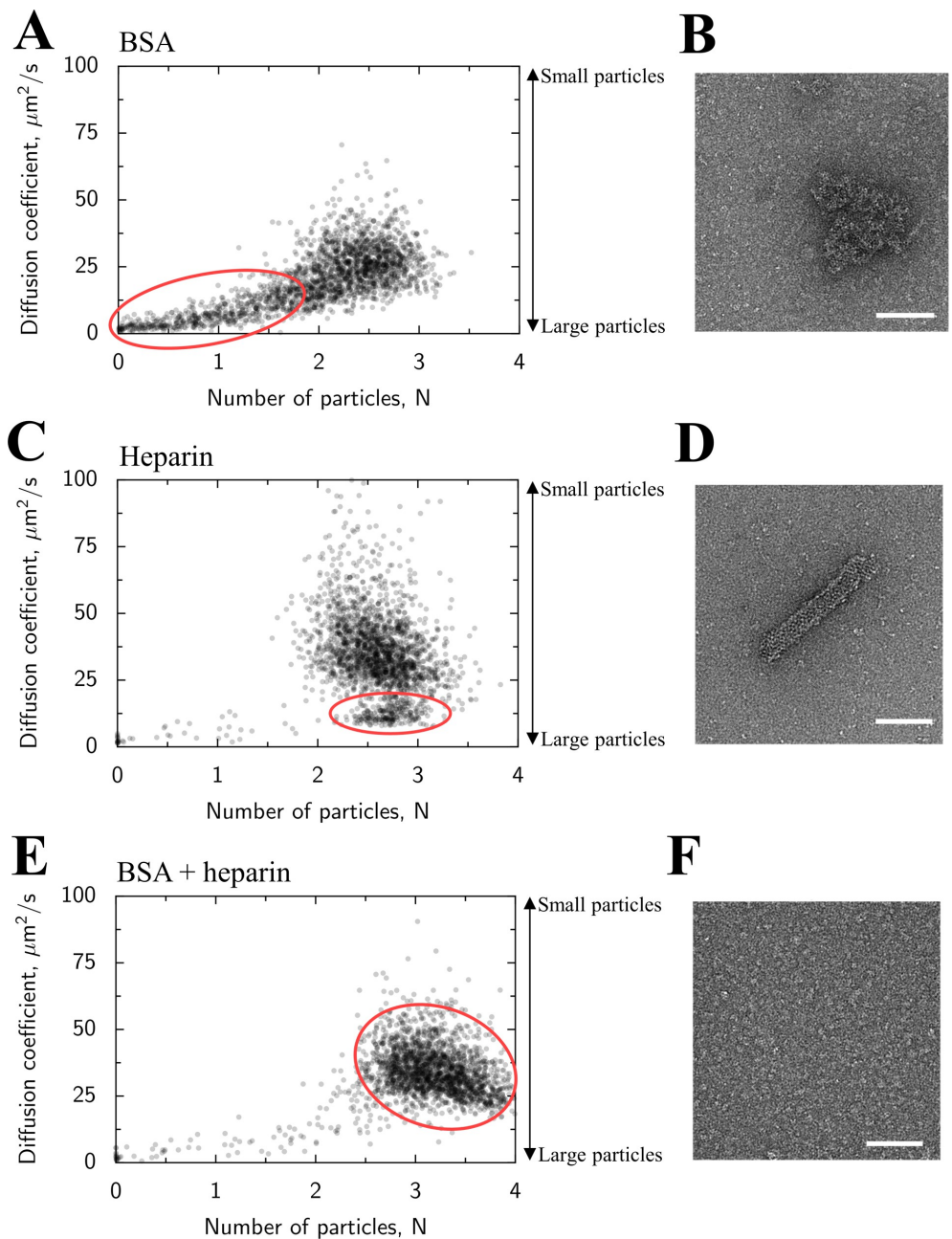


**Fig 6. Oligomerization of LPL as studied by RICS and TEM.** 10 nM LPL-ATTO610 with 190 nM unlabeled LPL was incubated in buffer A with the indicated supplements for up to two hours at room temperature. (A) Relationship between diffusion coefficient (D) and number of particles (N) in confocal volume (proportional to concentration) for image sectors recorded in an experiment with 200 nM LPL and 50 mg/ml BSA. Larger particles have lower D values. Notice that a large fraction of measurements leads to estimates with low D and N values (red circle)

(B), (D), (F) Representative nsTEM micrographs of unlabeled LPL in similar conditions as RICS experiments. Scale bars are 100 nm. (C) Interaction of LPL and heparin leads to formation of a fraction of estimates with lower D values at N values between 2–3. This is visible in the plot as a smaller set of points grouped around  $D = 10 \mu\text{m}^2/\text{s}$  (red circle) with the larger set of estimates above it. (E) Relationship between D and N for an experiment with LPL, BSA and heparin. Notice that most of the image sectors lead to D and N estimates in a certain region of the plot (red circle).

<https://doi.org/10.1371/journal.pone.0283358.g006>

and BSA did lead to some aggregation of the BSA (S4B Fig). The data from RICS supports that these BSA aggregates in the presence of heparin do not contain LPL. LPL aggregates were also observed with 200 nM LPL by itself (S4D Fig). Finally, LPL oligomers in the presence of heparin were dissolved by treatment with Triton X-100 (S5 Fig), which is in agreement with LPL activity measurements that show an increase in LPL activity after introduction of Triton X-100 to oligomeric LPL conditions (Fig 4B).

To test the effect of LPL concentration on formation of LPL oligomers, measurements were performed with 10 nM LPL and 50 mg/ml BSA, in the absence or presence of 10 IU/ml heparin. Measurements with 10 nM LPL and 50 mg/ml BSA exhibited only slight oligomerization (Table 1, average  $D \sim 20 \mu\text{m}^2/\text{s}$ ) and the results were comparable to 10 nM LPL with BSA and heparin together. This agrees with the concentration dependence demonstrated in Fig 5A. Finally, 10 nM LPL was denatured with 1 M GuHCl to produce partially unfolded monomeric LPL [43] as a comparison (S2C Fig). In this case, the LPL solution is inhabited by smaller particles whose average Ds were approximately twice as high as that observed when LPL was incubated with heparin and BSA.

### 3.5 Oligomeric form of LPL is more resistant to inactivation by ANGPTL4

We next asked if ANGPTL4 inactivation of LPL could be influenced by the formation of the LPL-BSA and LPL-heparin oligomers. At a relatively low LPL concentration of 20 nM where we do not expect to see significant oligomerization, we found the rate of inactivation by ANGPTL4 was similar in all conditions (Fig 7A). When the LPL concentration was raised to 200 nM (Fig 7B), the difference between the incubation conditions was noticeable—after 130 minutes of incubation, the residual LPL activity was 55% of the initial activity in the presence of heparin or BSA alone and 35% in the presence of both. These results indicate that conditions that promote oligomer formation, such as higher LPL concentrations and the presence of either BSA or heparin alone, reduce the rate of ANGPTL4 inactivation. Thus, it is reasonable to assume that LPL oligomers are resistant or less affected by the action of ANGPTL4. LPL was not fully resistant to inactivation by ANGPTL4, likely due to our previous observation that LPL is not entirely oligomeric in these conditions. Some fraction of total LPL remains catalytically active in these cases as seen in Figs 4 and 5A.

**Table 1. Calculated diffusion coefficients of main LPL component from RICS measurements.**

LPL	BSA	10 IU/ml heparin	Diffusion coefficient (D, $\mu\text{m}^2/\text{s}$ )
200 nM	50 mg/ml		$7.0 \pm 1.2$
	2 mg/ml		$13.0 \pm 2.9$
		+	$19.9 \pm 3.4$
	50 mg/ml	+	$21.7 \pm 0.8$
	2 mg/ml	+	$25.7 \pm 2.6$
10 nM	50 mg/ml		$20.5 \pm 1.4$
	2 mg/ml		$28.7 \pm 2.2$
	50 mg/ml	+	$24.0 \pm 1.0$
10 nM LPL + 1 M GuHCl			$42.5 \pm 7.2$

<https://doi.org/10.1371/journal.pone.0283358.t001>

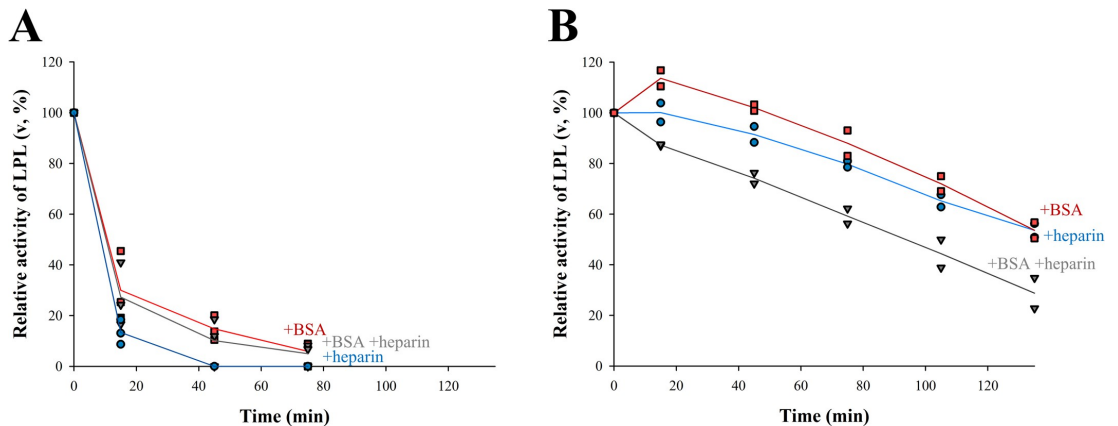


**Fig 7. Inactivation of oligomeric LPL by ANGPTL4.** 20 nM LPL (A) or 200 nM LPL (B) was incubated in the presence of 1  $\mu$ M ANGPTL4 and 10 IU/ml heparin (●) or 50 mg/ml BSA (■) or both (▼) in buffer A. Remaining LPL activity was determined by ITC using undiluted pooled human plasma (0.89 mM triglycerides,  $n = 5$ ). LPL activity is expressed relative to initial activity in the same conditions without ANGPTL4. Symbols represent individual measurements and lines correspond to their average values. The results suggest that the rate of LPL inactivation by ANGPTL4 depends on the degree of LPL oligomerization.

<https://doi.org/10.1371/journal.pone.0283358.g007>

### 3.6 Albumin amplifies the inactivation of LPL by nANGPTL4 in the presence of substrate

In addition to the interstitial space, ANGPTL4 can affect LPL at the surface of lipoproteins [51]. To investigate whether albumin affects the ANGPTL4/LPL interaction in this case, inactivation kinetics of LPL by ANGPTL4 were measured at various BSA concentrations. These measurements were performed by ITC using a mixture of triglyceride-rich lipoproteins as substrate. We found that the rate of inactivation of LPL by nANGPTL4 was increased at higher BSA concentrations (Fig 8A). The inactivation curves followed the first-order kinetics and the inactivation rate constant ( $k_i$ ) in the presence of 10 mg/ml or 50 mg/ml BSA was about 1.6 time higher than for 2 mg/ml BSA. Since albumin does not affect LPL activity and stability at substrate surfaces, we wondered if there might be a direct interaction between albumin and nANGPTL4. Indeed, SPR measurements showed association between human serum albumin (HSA) and immobilized nANGPTL4 (Fig 8B). This interaction was rather weak ( $K_D = 500 \pm 51 \mu$ M), but still sufficient to have physiological significance in the capillary.

## Discussion

In the present study, we show that albumin, the major protein component of plasma, increases the stability of LPL via reversible oligomerization, dissolves heparin-induced LPL oligomers, and can affect the LPL-ANGPTL4 interaction. Thus, our results suggest that the role of albumin in the LPL system is more diverse than the previously known role of binding lipolysis-derived fatty acids. Albumin, usually as BSA, has been also previously included in LPL assays [52–54] but its specific role has never been studied before this study. Although most of the experiments in this study were performed with bovine LPL and BSA, it is likely that the results of the proteins from other sources will not differ because our experiments with human LPL and BSA did not differ significantly from those with bovine LPL. Also, LFHP, which contains HSA, affected LPL stability similarly to BSA. LPL is exposed to albumin and other plasma components in the vascular endothelium, interstitial space, the surface of parenchymal cells,

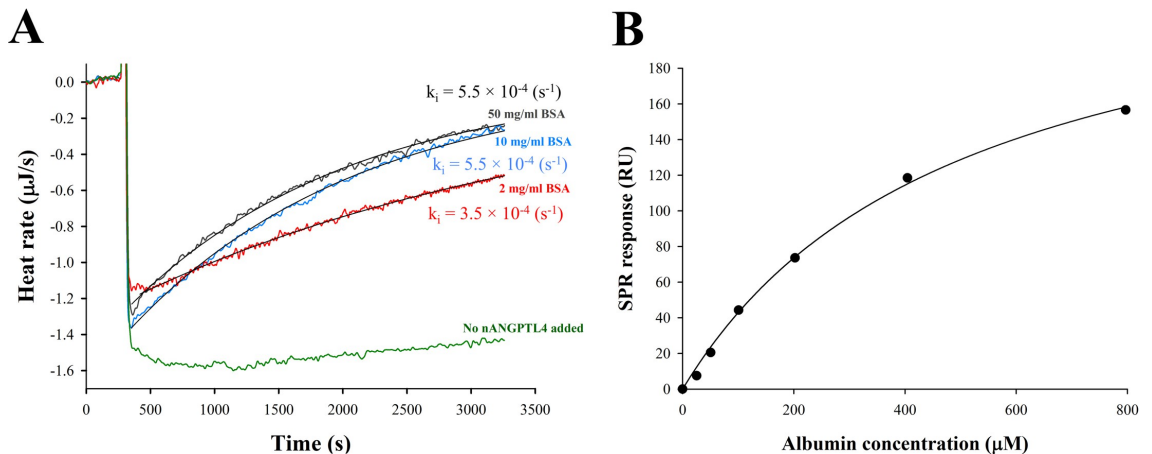


**Fig 8. Interaction of albumin with nANGPTL4.** (A) Effect of BSA at various concentrations on nANGPTL4-induced inactivation of LPL during lipolysis of triglyceride-rich lipoproteins. Raw ITC thermograms of lipolysis of CM/VLDL (adjusted to 0.75 mM triglycerides) by LPL in the presence of 100 nM nANGPTL4 and various concentrations of BSA (2 mg/l, 10 mg/ml, 50 mg/ml). The lipolysis rate is expressed as heat rate,  $\mu$ J/s. The control experiment was performed in the absence of nANGPTL4 and presence of 50 mg/ml BSA.  $k_i$  represents inhibition rate constant of LPL by nANGPTL4 calculated from the data ( $n = 2$ ). The results demonstrate that the rate of LPL inactivation by nANGPTL4 is increased at higher BSA concentrations. (B) SPR analysis of binding of various concentrations of HSA to immobilized nANGPTL4. Plateau values of SPR sensorgrams were plotted against HSA concentrations after subtracting non-specific binding. The results indicate that HSA interacts with nANGPTL4.

<https://doi.org/10.1371/journal.pone.0283358.g008>

and when attached to lipoprotein remnants [55]. The plasma concentration of albumin is 35–50 mg/ml and its concentration in the interstitial space of adipose tissue and skeletal muscle is 4.4–10 mg/ml and 9.7–15.7 mg/ml, respectively [35]. Since the  $K_D$  values of the LPL-albumin complexes were lower than or comparable to albumin concentrations in all extracellular locations of LPL, it is reasonable to assume that albumin affects LPL *in vivo*. Our data also indicate that albumin affects LPL stability via direct interaction, and macromolecular crowding may have only a limited role in the effect. The short lifetime of the LPL-albumin complex, as seen in the SPR experiment, may be important for the rapid transition of LPL to other complexes in the interstitial space to enable efficient shuttling of LPL to the vascular endothelium.

The observation that casein and  $\beta$ -lactoglobulin also stabilize LPL, but lysozyme does not, raises the question of what properties are required for a protein to interact with LPL. Our measurements were performed at pH 7.4, where albumin, casein and  $\beta$ -lactoglobulin are negatively charged due to their low pI, while lysozyme with its very high pI (11.1) is positively charged. The overall positive charge of LPL may explain its interaction with negatively charged albumin, casein and  $\beta$ -lactoglobulin, and also the avoidance of positively charged lysozyme. Exposed hydrophobicity, which plays a role in the thermal stabilization of several proteins, is likely not the only reason for stabilization of LPL by these proteins. This is mainly because lysozyme has a significantly large exposed hydrophobic area. However, the structural properties of proteins that determine their ability to stabilize LPL require further investigation.

The most intriguing observation in this study was the interplay of BSA and heparin in the reversible aggregation / oligomerization of LPL. As shown by ITC, TEM, and RICS measurements, both heparin and albumin alone induced reversible oligomerization of LPL. The LPL aggregates disappeared when both heparin and BSA were present in the incubation solution. This observation suggests that albumin binds to the LPL region involved in heparin-induced oligomerization and that heparin binds to the LPL region that plays a role in albumin-induced

aggregation. TEM analysis revealed that albumin-induced LPL aggregates differed from that of heparin-induced LPL helices (Fig 6). Unlike heparin-induced higher-order structure helices, albumin-induced aggregates did not have a well-defined regular structure. Despite structural differences, both oligomers were soluble in detergents such as Triton X-100, gum arabic or deoxycholate and dissociated at low LPL concentrations. The solubilization effect of the detergents suggests that the hydrophobic effect may play a role in the formation of both types of oligomers. LFHP was as effective as albumin in dissolving the LPL oligomers induced by heparin, indicating that albumin is the major component of plasma responsible for this effect.

LPL is mainly synthesized by parenchymal cells of adipose tissue and skeletal muscles, secreted into the interstitial space, and transported by GPIHBP1 to the vascular endothelium. Prior to secretion from cells, LPL has been shown to be transported in intracellular vesicles in which it is complexed with HSPG SDC1 [34] and has acquired filamentous distribution [33]. Upon secretion, the LPL filaments arrive in the interstitial space where vast amounts of albumin and glucose-aminoglycans, including HSPGs, are present. To become enzymatically active, the filaments must dissociate into an active form of LPL. This dissociation can be ensured by the coaction of interstitial albumin and HSPG. Thus, albumin can have a role in creating a suitable environment that turns oligomerized LPL into its active form (Fig 9).

It is possible that ANGPTL4 can act on LPL either in the cells that produce them [56], in the subendothelial space right after their secretion [57] or at the luminal side of vascular endothelium [41, 51, 58]. Our experiments show that the ANGPTL4 induced inactivation of LPL occurs faster when both albumin and heparin are present, i.e. in an environment in which LPL is not oligomerized. Both heparin-induced and albumin-induced oligomerization protected LPL from the action of ANGPTL4. It has been shown that nANGPTL4 binds to the lid-domain and the lid-proximal helix of LPL [59]. According to the cryo-EM structure of helical oligomers of LPL, the lid region is involved in the formation of LPL helices. Thus, the ANGPTL4 binding region could be occluded in oligomeric LPL, and this might prove to be a fail-safe to protect vesicle-stored LPL in adipose tissue. Inversely, albumin and HSPG are present in the subendothelial space, which might provide a suitable environment for the action of ANGPTL4 on LPL.

Albumin acts as a FFA acceptor *in vivo* during lipolysis and has to be used *in vitro* with substrates that contain long-chain triglycerides to bind released FFAs which would otherwise inhibit LPL. We did not observe any changes to LPL activity when another fatty acid acceptor, cyclodextrin, was used in place of albumin. This indicates that when LPL is in the presence of substrate, the role of albumin is limited to its ability to bind FFAs—and does not rely on a direct physical interaction between LPL and albumin. Further suggesting that the realm of LPL-albumin interactions might be prior to transfer to the vascular endothelium. LPL stabilization has been previously observed when LPL is bound to surfaces of artificial substrate emulsions [46]. It is likely that LPL is also stable on the surface of lipoproteins and is not influenced by albumin or macromolecular crowding of plasma.

A model for describing our observations on the oligomerization of LPL is proposed in Fig 9. Depending on the conditions, LPL can appear as an irreversible aggregate, a heparin-induced reversible helical oligomer [33], a reversible albumin-induced aggregate, or in its active form—which could be a properly folded monomer or dimer. The presence of both heparin and albumin leads to dissociation of both reversible type aggregates [42].

In summary, this study suggests that albumin can strongly affect the action and properties of LPL. Albumin may play a role in the decomposition of helical LPL oligomers induced by heparin or HSPGs. The dissociation of LPL oligomers or the avoidance of their formation can be crucial for LPL's interaction with its ligands as it transits the interstitial space. *In vitro*, both albumin alone and heparin alone promote the concentration-dependent formation of LPL

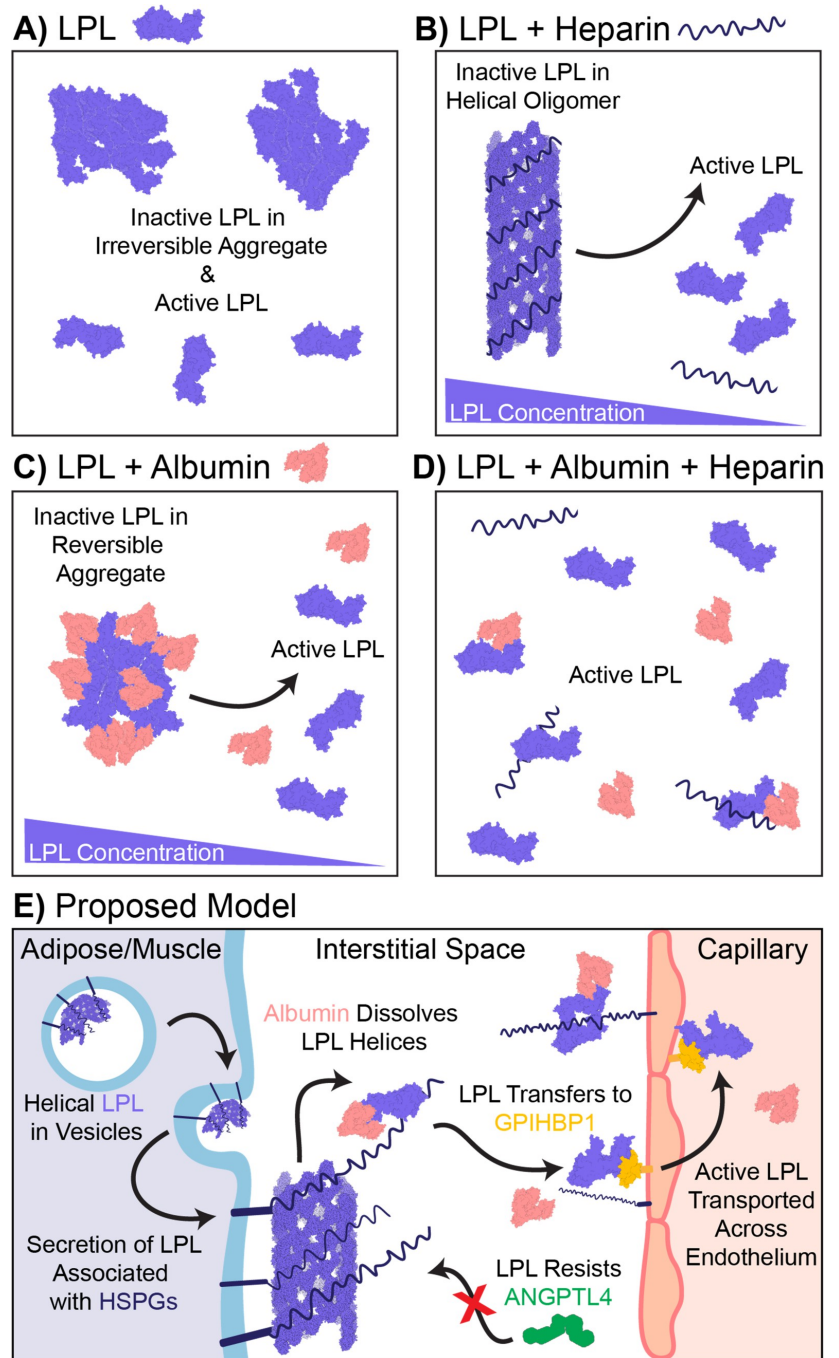


**Fig 9. Summarized results and proposed model for oligomerization of LPL.** The model describes possible states of LPL according to in vitro investigations.

<https://doi.org/10.1371/journal.pone.0283358.g009>

oligomers. These oligomers are reversible and dissociate into catalytically active LPL upon dilution and/or treatment with Triton X-100. Great consideration into LPL concentration and buffer environment should be taken in studies to distinguish between irreversible inactivation or aggregation and reversible LPL oligomer formation, which might affect interactions with various ligands and drugs.

## Supporting information

**S1 Fig. LPL activity measured in various substrate systems.** LPL activity was measured in substrate systems with increasing complexity: soluble fluorescent substrate DGGR < Tributyrin < Intralipid < Isolated triglyceride-rich lipoproteins (CM/VLDL) < Undiluted human plasma. 200 nM LPL was incubated for 15, 45 or 75 min in 20 mM HEPES, 150 mM NaCl, pH 7.4 buffer with 50 mg/ml BSA. Remaining LPL activity was determined with ITC for all substrates except DGGR, where fluorimetry was used instead. A single 5 nM LPL injection was made in the ITC experiments and the final concentration of LPL with DGGR was 10 nM. Results are presented as mean  $\pm$  SD of three independent measurements and calculated relative to measurements where heparin was added in addition to albumin. (TIF)

**S2 Fig. Determining diffusion coefficients of LPL using RICS.** (A) Estimation of diffusion coefficient (D) for all image sectors acquired with 200 nM LPL, 50 mg/ml BSA and 10 IU/ml heparin. Notice the spread of Ds and that some of the estimates had rather low value, corresponding to images with the larger particles. (B) Fit of fluorescence autocorrelation obtained in RICS experiment at 289 Hz scanning speed after analyzing average correlation and filtering the data (see main text for details). C—10 nM LPL-ATTO610 incubated in 1 M GuHCl for 2 hours at room temperature. There are only a few bright particles in these conditions (red circle). (TIF)

**S3 Fig. Addition of heparin to LPL incubation with albumin.** 190 nM LPL with 10 nM LPL-ATTO610 was incubated at room temperature in 20 mM HEPES, 150 mM NaCl, pH 7.4 buffer with 50 mg/ml BSA to mimic conditions used for FCS measurements. After 15 minutes, final concentration of 10 IU/ml heparin or water was added to the mixture. LPL activity expressed as heat rate was measured with ITC at 25°C in 1.31 mM triglycerides human plasma after a 5 nM LPL injection. Data is presented as mean of two independent measurements. (TIF)

**S4 Fig. BSA and heparin occasionally form aggregates.** (A) Aggregates of BSA were not observed when 2 mg/ml BSA was applied to a TEM grid. (B) However, aggregates were sometimes observed when 2 mg/ml BSA and 10 IU/ml heparin were mixed together. (C) These BSA/heparin aggregates were also seen in a minority of 200 nM LPL with 2 mg/mL BSA and 10 IU/mL heparin micrographs. Scale bars 100 nm. D—200 nM LPL in 20 mM HEPES, 150 mM NaCl, pH 7.4 buffer. (TIF)

**S5 Fig. Incubation of heparin treated LPL with triton X-100 abolishes formation of LPL helices.** When 200 nM of LPL is mixed with 10 IU/ml heparin, the formation of LPL helices was observed (Fig 6D). When 200 nM LPL with 10 IU/ml heparin was treated with increasing

concentrations of the detergent triton X-100, the LPL helices were progressively dissolved. (A)—At 0.005% triton X-100 concentration the beginning of LPL helix dissolution can be observed, with the helices pulling apart (upper panel) or dissolving from one end of the helix (lower panel). (B)—At 0.05% triton X-100 LPL helices are no longer observed, although some clumps of LPL are visible. (C)—at 0.5% triton X-100 the LPL particles are disperse and do not appear aggregated. Scale bars are 100 nm. (TIF)

## Acknowledgments

We acknowledge the UNC Hooker Imaging Core.

## Author Contributions

**Conceptualization:** Robert Risti, Kathryn H. Gunn, Saskia B. Neher, Aivar Löökene.

**Data curation:** Robert Risti.

**Investigation:** Robert Risti, Kathryn H. Gunn, Kristofer Hiis-Hommuk, Natjan-Naatan Seeba, Hamed Karimi, Ly Villo, Marko Vendelin.

**Methodology:** Robert Risti.

**Supervision:** Marko Vendelin, Aivar Löökene.

**Visualization:** Robert Risti, Kathryn H. Gunn.

**Writing – original draft:** Robert Risti, Aivar Löökene.

**Writing – review & editing:** Robert Risti, Kathryn H. Gunn, Marko Vendelin, Saskia B. Neher, Aivar Löökene.

## References

1. Wang H, Eckel RH. Lipoprotein lipase: from gene to obesity. *Am J Physiol Endocrinol Metab.* 2009; 297(1522–1555):E271–88. <https://doi.org/10.1152/ajpendo.90920.2008> PMID: 19318514
2. Boullart ACI, de Graaf J, Stalenhoef AF. Serum triglycerides and risk of cardiovascular disease. *Biochim Biophys Acta Mol Cell Biol Lipids.* 2012; 1821(5):867–75. <https://doi.org/10.1016/j.bbalip.2011.10.002> PMID: 22015388
3. Nordestgaard BG. Triglyceride-Rich Lipoproteins and Atherosclerotic Cardiovascular Disease: New Insights From Epidemiology, Genetics, and Biology. *Circ Res.* 2016 Feb 19; 118(4):547–63. <https://doi.org/10.1161/CIRCRESAHA.115.306249> PMID: 26892957
4. Sarwar N, Sandhu MS, Ricketts SL, Butterworth AS, di Angelantonio E, Mattheijs Boekholdt S, et al. Triglyceride-mediated pathways and coronary disease: Collaborative analysis of 101 studies. *The Lancet.* 2010; 375(9726):1634–9. [https://doi.org/10.1016/S0140-6736\(10\)60545-4](https://doi.org/10.1016/S0140-6736(10)60545-4) PMID: 20452521
5. Borén J, Taskinen MR, Björnson E, Packard CJ. Metabolism of triglyceride-rich lipoproteins in health and dyslipidaemia. *Nature Reviews Cardiology* 2022 19:9. 2022 Mar 22;19(9):577–92. <https://doi.org/10.1038/s41569-022-00676-y> PMID: 35318466
6. Wolska A, Yang ZH, Remaley AT. Hypertriglyceridemia: New approaches in management and treatment. Vol. 31, *Current Opinion in Lipidology.* 2020. p. 331–9. <https://doi.org/10.1097/MOL.0000000000000710> PMID: 33027225
7. Sathiyakumar V, Kapoor K, Jones SR, Banach M, Martin SS, Toth PP. Novel Therapeutic Targets for Managing Dyslipidemia. *Trends Pharmacol Sci.* 2018; 39(8):733–47. <https://doi.org/10.1016/j.tips.2018.06.001> PMID: 29970260
8. Wiczorek E, Cwiklińska A, Jankowski M. Hypertriglyceridemia, a causal risk factor for atherosclerosis, and its laboratory assessment. *Clin Chem Lab Med.* 2022; 60(8). <https://doi.org/10.1515/cclm-2022-0189> PMID: 35687325

9. Davies BSJ, Beigneux AP, Barnes RH, Tu Y, Gin P, Weinstein MM, et al. GPIHBP1 is responsible for the entry of lipoprotein lipase into capillaries. *Cell Metab*. 2010 Jul 7; 12(1):42–52. <https://doi.org/10.1016/j.cmet.2010.04.016> PMID: 20620994
10. Davies BSJ, Goulbourne CN, Barnes RH, Turlo KA, Gin P, Vaughan S, et al. Assessing mechanisms of GPIHBP1 and lipoprotein lipase movement across endothelial cells. *J Lipid Res*. 2012 Dec; 53(12):2690–7. <https://doi.org/10.1194/jlr.M031559> PMID: 23008484
11. LaRosa JC, Levy RI, Herbert P, Lux SE, Fredrickson DS. A specific apoprotein activator for lipoprotein lipase. *Biochem Biophys Res Commun*. 1970 Oct 9; 41(1):57–62. [https://doi.org/10.1016/0006-291x\(70\)90468-7](https://doi.org/10.1016/0006-291x(70)90468-7) PMID: 5459123
12. Bengtsson G, Olivecrona T. Lipoprotein Lipase: Mechanism of Product Inhibition. *Eur J Biochem*. 1980; 106(2):557–62.
13. Saxena U, Witte LD, Goldberg IJ. Release of endothelial cell lipoprotein lipase by plasma lipoproteins and free fatty acids. *Journal of Biological Chemistry*. 1989 Mar 15; 264(8):4349–55. PMID: 2925647
14. Lookene A, Chevreuil O, Østergaard P, Olivecrona G. Interaction of lipoprotein lipase with heparin fragments and with heparan sulfate: stoichiometry, stabilization, and kinetics. *Biochemistry*. 1996; 35(37):12155–63. <https://doi.org/10.1021/bi960008e> PMID: 8810923
15. Kersten S. New insights into angiotensin-like proteins in lipid metabolism and cardiovascular disease risk. *Curr Opin Lipidol*. 2019 Mar; 1. <https://doi.org/10.1097/MOL.0000000000000600> PMID: 30893111
16. Jong MC, Hofker MH, Havekes LM. Role of ApoCs in Lipoprotein Metabolism. *Arterioscler Thromb Vasc Biol*. 1999; 19(3):472 LP– 484.
17. Chen YQ, Pottanat TG, Zhen EY, Siegel RW, Ehsani M, Qian YW, et al. ApoA5 lowers triglyceride levels via suppression of ANGPTL3/8-mediated LPL inhibition. *J Lipid Res*. 2021 Apr 1; 62. <https://doi.org/10.1016/j.jlr.2021.100068> PMID: 33762177
18. Chi X, Britt EC, Shows HW, Hjelmaas AJ, Shetty SK, Cushing EM, et al. ANGPTL8 promotes the ability of ANGPTL3 to bind and inhibit lipoprotein lipase. *Mol Metab*. 2017 Oct 1; 6(10):1137–49. <https://doi.org/10.1016/j.molmet.2017.06.014> PMID: 29031715
19. Zheng C, Murdoch SJ, Brunzell JD, Sacks FM. Lipoprotein lipase bound to apolipoprotein B lipoproteins accelerates clearance of postprandial lipoproteins in humans. *Arterioscler Thromb Vasc Biol*. 2006 Apr; 26(4):891–6. <https://doi.org/10.1161/01.ATV.0000203512.01007.3d> PMID: 16410459
20. Busher JT. Serum Albumin and Globulin. *Clinical Methods: The History, Physical, and Laboratory Examinations*. Butterworths; 1990.
21. Ellis RJ. Macromolecular crowding: obvious but underappreciated. *Trends Biochem Sci*. 2001 Oct; 26(10):597–604. [https://doi.org/10.1016/s0968-0004\(01\)01938-7](https://doi.org/10.1016/s0968-0004(01)01938-7) PMID: 11590012
22. Tokuriki N, Kinjo M, Negi S, Hoshino M, Goto Y, Urabe I, et al. Protein folding by the effects of macromolecular crowding. *Protein Sci*. 2004 Jan 1; 13(1):125–33. <https://doi.org/10.1110/ps.03288104> PMID: 14691228
23. Kuznetsova IM, Turoverov KK, Uversky VN. What macromolecular crowding can do to a protein. *Vol. 15, International Journal of Molecular Sciences*. 2014. 23090–23140 p.
24. Olivecrona T, Bengtsson-Olivecrona G, Osborne JC, Kempner ES. Molecular size of bovine lipoprotein lipase as determined by radiation inactivation. *Journal of Biological Chemistry*. 1985; 260(11):6888–91. PMID: 3888985
25. Lookene A, Zhang L, Hultin M, Olivecrona G. Rapid subunit exchange in dimeric lipoprotein lipase and properties of the inactive monomer. *Journal of Biological Chemistry*. 2004; 279(48):49964–72. <https://doi.org/10.1074/jbc.M407419200> PMID: 15385564
26. Beigneux AP, Allan CM, Sandoval NP, Cho GW, Heizer PJ, Jung RS, et al. Lipoprotein lipase is active as a monomer. *Proceedings of the National Academy of Sciences*. 2019; 116(13):6319–28. <https://doi.org/10.1073/pnas.1900983116> PMID: 30850549
27. Arora R, Nimonkar A V., Baird D, Wang C, Chiu CH, Horton PA, et al. Structure of lipoprotein lipase in complex with GPIHBP1. *Proc Natl Acad Sci U S A*. 2019; 116(21):10360–5. <https://doi.org/10.1073/pnas.1820171116> PMID: 31072929
28. Birrane G, Beigneux AP, Dwyer B, Strack-Logue B, Kristensen KK, Francone OL, et al. Structure of the lipoprotein lipase-GPIHBP1 complex that mediates plasma triglyceride hydrolysis. *Proc Natl Acad Sci U S A*. 2019; 116(5):1723–32. <https://doi.org/10.1073/pnas.1817984116> PMID: 30559189
29. Goulbourne CN, Gin P, Tatar A, Nobumori C, Hoenger A, Jiang H, et al. The GPIHBP1–LPL complex is responsible for the margination of triglyceride-rich lipoproteins in capillaries. *Cell Metab*. 2014 May 6; 19(5):849. <https://doi.org/10.1016/j.cmet.2014.01.017> PMID: 24726386
30. Bergö M, Olivecrona G, Olivecrona T. Forms of lipoprotein lipase in rat tissues: in adipose tissue the proportion of inactive lipase increases on fasting. *Biochemical Journal*. 1996 Feb 1; 313(Pt 3):893. <https://doi.org/10.1042/bj3130893> PMID: 8611172

31. Kersten S. New insights into angiotensin-like proteins in lipid metabolism and cardiovascular disease risk. *Curr Opin Lipidol*. 2019 Jun 1; 30(3):205–11. <https://doi.org/10.1097/MOL.0000000000000600> PMID: 30893111
32. Kristensen KK, Leth-Espensen KZ, Young SG, Ploug M. ANGPTL4 inactivates lipoprotein lipase by catalyzing the irreversible unfolding of LPL's hydrolase domain. *J Lipid Res*. 2020 Sep 1; 61(9):1253. <https://doi.org/10.1194/jlr.ILR120000780> PMID: 32327484
33. Gunn KH, Roberts BS, Wang F, Strauss JD, Borgnia MJ, Egelman EH, et al. The structure of helical lipoprotein lipase reveals an unexpected twist in lipase storage. *Proc Natl Acad Sci U S A*. 2020 May 12; 117(19):10254–64. <https://doi.org/10.1073/pnas.1916555117> PMID: 32332168
34. Sundberg EL, Deng Y, Burd CG. Syndecan-1 mediates sorting of soluble lipoprotein lipase with sphingomyelin-rich membrane in the Golgi apparatus. *Dev Cell*. 2019 Nov 4; 51(3):387. <https://doi.org/10.1016/j.devcel.2019.08.014> PMID: 31543446
35. Ellmerer M, Schaupp L, Brunner GA, Sendhofer G, Wutte A, Wach P, et al. Measurement of interstitial albumin in human skeletal muscle and adipose tissue by open-flow microperfusion. *American Journal Of Physiology-Endocrinology And Metabolism*. 2000; 278:352–6. <https://doi.org/10.1152/ajpendo.2000.278.2.E352> PMID: 10662720
36. Bengtsson-Olivecrona G, Olivecrona T. Phospholipase activity of milk lipoprotein lipase. *Methods Enzymol*. 1991; 197:345–56. [https://doi.org/10.1016/0076-6879\(91\)97160-z](https://doi.org/10.1016/0076-6879(91)97160-z) PMID: 2051931
37. Robal T, Larsson M, Martin M, Olivecrona G, Lookene A. Fatty acids bind tightly to the N-terminal domain of angiotensin-like protein 4 and modulate its interaction with lipoprotein lipase. *Journal of Biological Chemistry*. 2012 Aug 24; 287(35):29739–52. <https://doi.org/10.1074/jbc.M111.303529> PMID: 22773878
38. Goldstein JL, Basu SK, Brown MS. Receptor-Mediated Endocytosis of Low-Density Lipoprotein in Cultured Cells. *Methods Enzymol*. 1983 Jan 1; 98(C):241–60. [https://doi.org/10.1016/0076-6879\(83\)98152-1](https://doi.org/10.1016/0076-6879(83)98152-1) PMID: 6321901
39. Reimund M, Kovrov O, Olivecrona G, Lookene A. Lipoprotein lipase activity and interactions studied in human plasma by isothermal titration calorimetry. *J Lipid Res*. 2017 Jan 1; 58(1):279–88. <https://doi.org/10.1194/jlr.D071787> PMID: 27845686
40. Reimund M, Wolska A, Risti R, Wilson S, Sviridov D, Remaley AT, et al. Apolipoprotein C-II mimetic peptide is an efficient activator of lipoprotein lipase in human plasma as studied by a calorimetric approach. *Biochem Biophys Res Commun*. 2019; 519(1). <https://doi.org/10.1016/j.bbrc.2019.08.130> PMID: 31477272
41. Sukonina V, Lookene A, Olivecrona T, Olivecrona G. Angiotensin-like protein 4 converts lipoprotein lipase to inactive monomers and modulates lipase activity in adipose tissue. *Proceedings of the National Academy of Sciences*. 2006; 103(46):17450–5. <https://doi.org/10.1073/pnas.0604026103> PMID: 17088546
42. Mysling S, Kristensen KK, Larsson M, Kovrov O, Bensadoun A, Jørgensen TJ, et al. The angiotensin-like protein ANGPTL4 catalyzes unfolding of the hydrolase domain in lipoprotein lipase and the endothelial membrane protein GPIHBP1 counteracts this unfolding. *Elife*. 2016 Dec 8; 5. <https://doi.org/10.7554/eLife.20958> PMID: 27929370
43. Zhang L, Lookene A, Wu G, Olivecrona G. Calcium triggers folding of lipoprotein lipase into active dimers. *Journal of Biological Chemistry*. 2005 Dec 30; 280(52):42580–91. <https://doi.org/10.1074/jbc.M507252200> PMID: 16179346
44. Vendelin M, Birkedal R. Anisotropic diffusion of fluorescently labeled ATP in rat cardiomyocytes determined by raster image correlation spectroscopy. *Am J Physiol Cell Physiol*. 2008; 295:1302–15. <https://doi.org/10.1152/ajpcell.00313.2008> PMID: 18815224
45. Illaste A, Laasmaa M, Peterson P, Vendelin M. Analysis of molecular movement reveals latticelike obstructions to diffusion in heart muscle cells. *Biophys J*. 2012 Feb 22; 102(4):739–48. <https://doi.org/10.1016/j.bpj.2012.01.012> PMID: 22385844
46. Rapp D, Olivecrona T. Kinetics of Milk Lipoprotein Lipase. Studies with Tributyrin. *Eur J Biochem*. 1978; 91:379–85. <https://doi.org/10.1111/j.1432-1033.1978.tb12690.x> PMID: 32030
47. Jing W, Qin Y, Tong J. Effects of macromolecular crowding on the folding and aggregation of glycosylated MUC5AC. *Biochem Biophys Res Commun*. 2020 Sep 3; 529(4):984–90. <https://doi.org/10.1016/j.bbrc.2020.06.156> PMID: 32819609
48. Sundheim G, Bengtsson-Olivecrona G. Hydrolysis of bovine and caprine milk fat globules by lipoprotein lipase. Effects of heparin and of skim milk on lipase distribution and on lipolysis. *J Dairy Sci*. 1987; 70(12):2467–75. [https://doi.org/10.3168/jds.S0022-0302\(87\)80313-2](https://doi.org/10.3168/jds.S0022-0302(87)80313-2) PMID: 3448103
49. Erwin N, Patra S, Dwivedi M, Weise K, Winter R. Influence of isoform-specific Ras lipidation motifs on protein partitioning and dynamics in model membrane systems of various complexity. *Biol Chem*. 2017 May 1; 398(5–6):547–63. <https://doi.org/10.1515/hsz-2016-0289> PMID: 27977396

50. Benton LA, Smith AE, Young GB, Pielak GJ. Unexpected effects of macromolecular crowding on protein stability. *Biochemistry*. 2012 Dec 11; 51(49):9773–5. <https://doi.org/10.1021/bi300909q> PMID: 23167542
51. Gunn KH, Gutgsell AR, Xu Y, Johnson C v., Liu J, Neher SB. Comparison of angiotensin-like protein 3 and 4 reveals structural and mechanistic similarities. *Journal of Biological Chemistry*. 2021; 296:100312.
52. Reimund M, Larsson M, Kovrov O, Kasvandik S, Olivecrona G, Lookene A. Evidence for Two Distinct Binding Sites for Lipoprotein Lipase on Glycosylphosphatidylinositol-anchored High Density Lipoprotein-binding Protein 1 (GPIHBP1). *Journal of Biological Chemistry*. 2015 May 29; 290(22):13919–34. <https://doi.org/10.1074/jbc.M114.634626> PMID: 25873395
53. Kristensen KK, Leth-Espensen KZ, Mertens HDT, Birrane G, Meiyappan M, Olivecrona G, et al. Unfolding of monomeric lipoprotein lipase by ANGPTL4: Insight into the regulation of plasma triglyceride metabolism. *Proc Natl Acad Sci U S A*. 2020; 117(8):4337–46. <https://doi.org/10.1073/pnas.1920202117> PMID: 32034094
54. Sonnenburg WK, Yu D, Lee EC, Xiong W, Gololobov G, Key B, et al. GPIHBP1 stabilizes lipoprotein lipase and prevents its inhibition by angiotensin-like 3 and angiotensin-like 4. *J Lipid Res*. 2009; 50(12):2421–9. <https://doi.org/10.1194/jlr.M900145-JLR200> PMID: 19542565
55. Karpe F, Olivecrona T, Walldius G, Hamsten A. Lipoprotein lipase in plasma after an oral fat load: relation to free fatty acids. *Journal Lipid Research*. 1992; 33:975–84. PMID: 1431589
56. Dijk W, Ruppert PMM, Oost LJ, Kersten S. Angiotensin-like 4 promotes the intracellular cleavage of lipoprotein lipase by PCSK3/furin in adipocytes. *J Biol Chem*. 2018 Sep 7; 293(36):14134–45. <https://doi.org/10.1074/jbc.RA118.002426> PMID: 30021841
57. Makoveichuk E, Sukonina V, Kroupa O, Thulin P, Ehrenborg E, Olivecrona T, et al. Inactivation of lipoprotein lipase occurs on the surface of THP-1 macrophages where oligomers of angiotensin-like protein 4 are formed. *Biochem Biophys Res Commun*. 2012; 425(2):138–43. <https://doi.org/10.1016/j.bbrc.2012.07.048> PMID: 22820186
58. Lafferty MJ, Bradford KC, Erie DA, Neher SB. Angiotensin-like protein 4 inhibition of lipoprotein lipase: Evidence for reversible complex formation. *Journal of Biological Chemistry*. 2013; 288(40):28524–34. <https://doi.org/10.1074/jbc.M113.497602> PMID: 23960078
59. Gutgsell AR, Ghodge S v, Bowers AA, Neher SB. Mapping the sites of the lipoprotein lipase (LPL)-angiotensin-like protein 4 (ANGPTL4) interaction provides mechanistic insight into LPL inhibition. *J Biol Chem*. 2019;(8):2678–89. <https://doi.org/10.1074/jbc.RA118.005932> PMID: 30591589

## Appendix 3

### III

**Hamed Karimi**, Martin Laasmaa, Margus Pihlak, and Marko Vendelin. Statistical analysis of fluorescence intensity transients with Bayesian methods. *Science Advances*, 11(16):eads4609, 2025



## BIOPHYSICS

# Statistical analysis of fluorescence intensity transients with Bayesian methods

Hamed Karimi<sup>1</sup>, Martin Laasmaa<sup>1</sup>, Margus Pihlak<sup>2</sup>, Marko Vendelin<sup>1\*</sup>

Molecular movement and interactions at the single-molecule level, particularly in live cells, are often studied using fluorescence correlation spectroscopy (FCS). While powerful, FCS has notable drawbacks: It requires high laser intensities and long acquisition times, increasing phototoxicity, and often relies on problematic statistical assumptions in data fitting. We introduce fluorescence intensity trace statistical analysis (FITSA), a Bayesian method that directly analyzes fluorescence intensity traces. FITSA offers faster, more stable convergence than previous approaches and provides robust parameter estimation from far shorter measurements than conventional FCS. Our results demonstrate that FITSA achieves comparable precision to FCS while requiring substantially fewer photons. This advantage becomes even more pronounced when accounting for statistical dependencies in FCS analysis, which are often overlooked but necessary for accurate error estimation. By reducing laser exposure, FITSA minimizes phototoxicity effects, representing a major advancement in the quantitative analysis of molecular processes across fields.

## INTRODUCTION

Fluorescence correlation spectroscopy (FCS) is an established technique used in many disciplines to study the movement of molecules and changes at the single-molecule level (1, 2). The method is based on recording fluorescence intensity transient changes in a small volume using confocal microscopy and analyzing these transients through autocorrelations. Depending on the physical processes causing the fluorescence intensity fluctuations, it is possible to determine diffusion coefficients (DCs) of fluorescent molecules and their concentrations and characterize reactions leading to changes in their fluorescence state (1, 2). As measurements can be performed in live cells, FCS is one of the few methods capable of revealing details about intracellular environment properties under conditions approximating *in vivo*, thereby providing crucial information for a mechanistic understanding of intracellular processes and their regulation. FCS has been extended by a family of methods to address some of its shortcomings or to study the aspects that were not possible with the classical FCS (3–10). As the fields progress toward an understanding that the intracellular environment is highly compartmentalized rather than a well-mixed solution (11–13), resolution requirements for methods probing this environment have increased. However, FCS and related methods use relatively high laser intensities in measurements, which means that performing measurements to explore regional differences in the intracellular environment would require even longer overall exposure of cells to laser radiation, potentially increasing phototoxicity effects (14). Thus, alternative methods are needed to study the intracellular environment with reduced exposure to laser illumination.

In addition to high laser illumination requirements, FCS has a well-known flaw in how it is commonly used to obtain properties of the environment or fluorescent molecules. After FCS measurements, the autocorrelation function (ACF) is typically fitted with a model using the least-squares or maximum likelihood methods.

This fit is performed under the assumption that the residuals for different lag times are statistically independent. However, this assumption is incorrect and leads to overconfident estimates of model parameters (15–17). In turn, this has a major implication for using FCS when this assumption is made—it becomes impossible to judge the goodness of fit in a statistically sound manner or compare models of different complexities. For example, it becomes challenging to determine whether the measurements indicate single- or multiple-component diffusion.

One approach to address issues with fitting ACF by FCS models is to account for cross-correlation between residuals corresponding to different lag times. This requires covariance estimation between different lag times, which can be achieved through a larger number of measurements or by using approximation techniques (15, 16). Alternatively, measurements can be repeated many times, composing an overall ACF by taking values for each lag time from a different trace, leading to their independence (18). However, while improving the statistical properties of the fits, these methods would require even longer laser exposure than classical FCS, which is often impractical for many experiments.

Several years ago, an alternative framework was proposed by Pressé and colleagues (19–22). Instead of fitting the calculated ACF of a measurement to a model, they used the Bayesian paradigm and applied the same physical principles as FCS to describe signal formation. In this approach, a Bayesian model was constructed to represent the movement of particles through the confocal volume and fitted against the recorded fluorescence intensity transient. As a result of the fit, posterior probability distributions were obtained for parameters such as diffusion coefficient and molecular brightness. Several variants of the models were tested, all resulting in a remarkable reduction of the required experimental time (20, 21). However, when testing the available implementation of the method (20), we found it to be very slow to be used in practice and, as shown in the results of this work, sometimes either failing to converge or converging to an incorrect solution. Thus, while the approach is very promising, major obstacles must be overcome before it can be used in practice.

In this work, we introduce a fluorescence intensity trace statistical analysis (FITSA) method based on the Bayesian paradigm. The

Copyright © 2025 The Authors, some rights reserved; exclusive licensee American Association for the Advancement of Science. No claim to original U.S. Government Works. Distributed under a Creative Commons Attribution License 4.0 (CC BY).

<sup>1</sup>Laboratory of Systems Biology, Department of Cybernetics, Tallinn University of Technology, Tallinn, Estonia. <sup>2</sup>Division of Mathematics, Department of Cybernetics, Tallinn University of Technology, Tallinn, Estonia.

\*Corresponding author. Email: markov@sysbio.ioc.ee

implemented method is compared with the model of Jazani *et al.* (20), and we demonstrate that FITSA achieves faster and more stable convergence. In addition, we quantitatively compare FITSA and FCS requirements, demonstrating that the same precision of diffusion coefficient estimates can be achieved by FITSA using much shorter experiments than those required by FCS.

## RESULTS

### Overall description of the method

To provide context for the subsequent simulation and experimental results, we present a concise overview of the FITSA method, outlining its underlying principles. In the experiment, a fluorescent particle passes through the laser-illuminated area (Fig. 1A) and generates photons detected by the microscope hardware (Fig. 1B). The detected signal can originate from particles passing through the confocal volume or from background emissions. The FITSA method distinguishes between these signal components by identifying portions of the signal with high photon counts, which contain the most information about particle movement. Signal segments with photon rates higher than the expected background emission rate are isolated for further analysis. This separation enables two distinct analytical approaches: studying overall emitted photons by binning the signal into larger bins to examine background emissions or analyzing rapid changes by tracking short-timescale variations to decode molecular movements.

This dual analytical approach is implemented through the signal binning process. As illustrated in the zoomed area in Fig. 1C, binning tracks the number of photons in each interval. Regions with high photon counts are binned into smaller intervals, while areas

with predominantly background emissions are binned into larger intervals. The algorithm creates smooth transitions between these different bin sizes, allowing FITSA to track not only particles within the confocal volume but also their entry and exit (Fig. 1D).

Given the single confocal volume recording, we cannot uniquely determine a particle's location, as identical photon signals could result from multiple positions within the point spread function (PSF). Instead, we can determine what effectively amounts to a normalized distance from the focal point (Fig. 1E). Under an analytical three-dimensional (3D) Gaussian PSF, this normalized distance varies between lateral and axial directions because of PSF shape asymmetry.

Particle events near the PSF are typically brief and characterized by elevated photon detection rates. Figure 1F schematically shows three possible particle passes through the PSF—these could represent different particles or the same particle entering and exiting during the high-photon detection period. Because particle diffusion is assumed to be independent, FITSA treats these local events as statistically independent and analyzes them separately. This fundamental assumption allows the experimental signal to be divided into distinct subsections for detailed analysis.

Subsection borders are determined by analyzing signal bin durations (Fig. 1G). Regions dominated by background photon emissions, characterized by longer signal bins, serve as natural division points. To estimate particle trajectory and diffusion coefficient, the method selects a seed point at the maximum photon emission within each subsection—typically corresponding to the particle's closest approach to the focal point. The trajectory calculation begins at the particle's location in the seed point and follows statistical diffusion properties in both forward and backward time directions. The predicted trajectory shows minimal uncertainty during

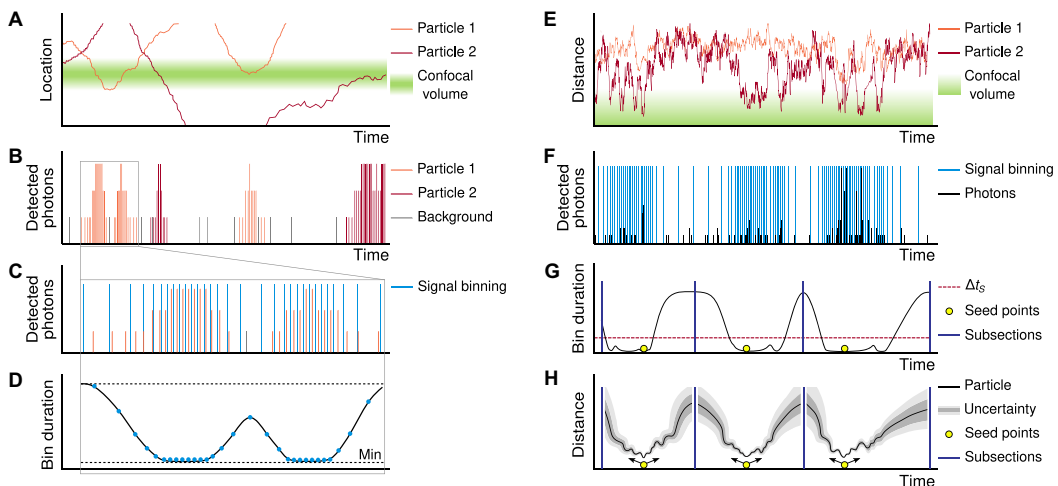


**Fig. 1. Overall description of the method.** Schematic illustration of the FITSA approach for analyzing particle movement near the confocal recording volume. Note that left panels (A to D) and right panels (E to H) show different examples to illustrate distinct aspects of the method. (A) Representation of the laser-illuminated confocal volume and movement of particles next to it. (B) Time-resolved photon detection trace recorded by the microscope detection system. (C) Zoomed section of the signal from (B), showing binning based on recorded photon emission rates. (D) Demonstration of smooth transitions between bin sizes, illustrating the adaptive binning approach. (E and F) Normalized distance of particles from the focal point (E) and representative fluorescence intensity trace (F) showing multiple particle transit events through the confocal volume. (G) Segmentation of the signal trace from (F) into subsections, each containing a distinct high-photon detection period. (H) FITSA trajectory reconstruction within a subsection, demonstrating position estimates and their associated uncertainties. Detailed explanation is provided in the main text.

high-signal transients and maximal uncertainty at subsection boundaries (Fig. 1H).

In the following sections, we demonstrate how this method's systematic binning, subsection splitting, and trajectory prediction enable robust recovery of diffusion coefficients from short recordings. While the method is described for single-particle contributions to subsection signals, it can be extended to account for multiple-particle scenarios.

**Demonstration with simulated data**

To demonstrate the FITSA protocol, we generated a synthetic fluorescence intensity trace (Fig. 2A) by simulating 25 point sources with a diffusion coefficient of  $10 \mu\text{m}^2/\text{s}$  within a small box around the focal point. The trace was relatively short for an FCS analysis,

even when correcting for trace duration (23). The ACFs calculated for the first 0.2 s and the full 1-s trace were fitted with a 3D motion model, yielding diffusion coefficients higher than the simulation input (Fig. 2, B and C). These ACF fits used FCS models without accounting for the uncertainty heterogeneity or the covariance between ACF values (15, 16), assuming a uniform SD for all ACF values. Consistent with an earlier study (15), we found that the classical FCS fit is overfitting the data as it overestimates precision while producing diffusion coefficients that significantly deviate from the true value.

In our FITSA analysis, we examined the synthetic trace (Fig. 2A) in its full length and in shorter segments of 0.1 and 0.2 s. The initial step of FITSA involves dividing the trace into smaller subsections, assuming that a limited number of particles contribute to the signal

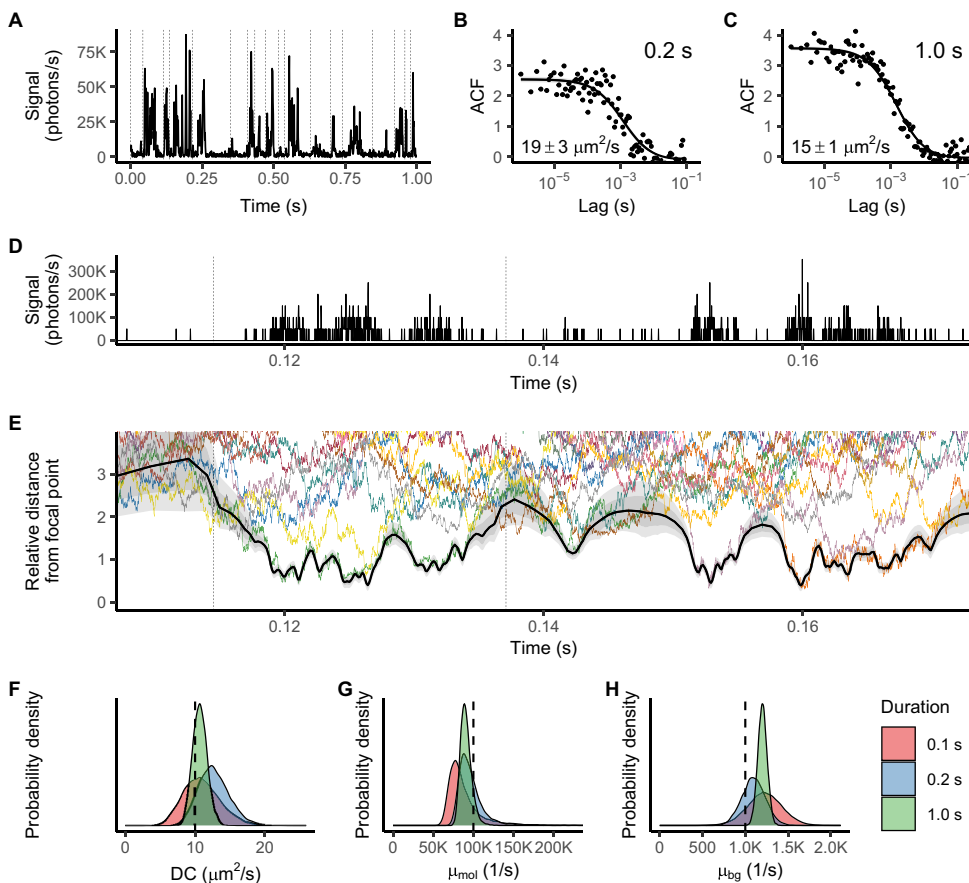


**Fig. 2. Demonstration of FITSA using the synthetic trace generated with the particles having a diffusion coefficient (DC) of  $10 \mu\text{m}^2/\text{s}$ .** (A) Fluorescence intensity trace analyzed by FITSA and FCS. In the plot, the signal is reported as an average rate per 1 ms for visibility. Vertical dashed lines denote splitting of the trace into sub-traces for FITSA. (B and C) Time ACFs calculated for the 0.2-s trace start (B) and full trace (C), fitted with the FCS 3D diffusion model. Insets show FCS-derived DCs (mean  $\pm$  SD). (D and E) Trace section (D) (average rate per 20  $\mu\text{s}$ ) and relative particle distances from the focal point (E). In (E), distances are normalized by PSF waist in each coordinate. Colored lines show particle trajectories used for trace generation; black line (median) with gray areas ( $\pm 25$  and  $\pm 40\%$ ) shows the FITSA-estimated trajectory. (F to H) Posterior probability densities for DC (F), molecular brightness (G), and background photon emission rate (H) for different trace durations (0.1, 0.2, and 1 s). Vertical dashed lines indicate true parameter values. Note uncertainty reduction with increased data amount.

within each subsection. For this study, we restricted this number to one particle per subsection. Figure 2D illustrates how this approach translates into the identified trajectory by showing a portion of the trace, while Fig. 2E displays the derived trajectory with its associated uncertainty for FITSA performed on the full 1-s trace.

To compare the estimated trajectory with those of all particles used in trace generation, we calculated the relative distance of each particle from the focal point. This distance was found by normalizing contributions of displacements in  $x$ ,  $y$ , and  $z$  from the focal point by the corresponding PSF waist dimensions in the same coordinates. After this normalization, it becomes evident that the particle trajectory identified by FITSA closely tracks the particle nearest to the focus at any given moment (Fig. 2E). As demonstrated in Fig. 2E, FITSA switches between tracked particles when one leaves the confocal volume and another enters it (see, for example, the behavior just below 0.16 s in Fig. 2E). In addition, in regions with minimal fluorescence signal, the predicted trajectory exhibits larger uncertainty compared to regions with high signal rates.

This implementation of FITSA generates trajectories along with estimates of the diffusion coefficient, molecular brightness, and background photon emission rate. The resulting posterior distributions for these parameters depend on the length of the analyzed fluorescence trace, as illustrated in Fig. 2 (F to H). As expected, increasing the analyzed trace duration improves the precision of the estimates. While all estimated parameters approximated the true values used in the trace synthesis, closer examination reveals slight deviations of the posterior distribution maxima for both the diffusion coefficient and molecular brightness from the values used in generating the synthetic trace. Such deviations are expected when analyzing very short traces, as demonstrated later in our systematic analysis of both synthetic and experimental data. For background emissions, we observe overestimation of the rate, although the underlying reasons for this bias remain unclear.

Regardless of the trace duration, the true value of the diffusion coefficient consistently fell within the posterior distribution estimated by FITSA. This contrasts with the estimates produced by classical FCS. Such performance demonstrates FITSA's excellent capability to analyze short traces.

### Comparison with an alternative Bayesian fitting approach

FITSA is similar to the Jazani *et al.* method (20) in terms of fitting the fluorescence intensity trace directly by models. We compared FITSA's performance to the reference implementation of the Jazani *et al.* method (20) using the same dataset as in Fig. 2.

To assess convergence, we performed sampling in six chains, evaluating the potential scale reduction factor  $\hat{R}$  and bulk and tail effective sample sizes (ESSs), which quantify the independent information content of the samples and help validate the reliability of posterior estimates (24). We used slightly looser convergence criteria than proposed in (24), as the Jazani *et al.* method required many iterations to pass even these criteria (Fig. 3, A and B). FITSA needed far fewer iterations than the Jazani *et al.* method. Figure 3C illustrates the last 1500 iterations by six chains for both approaches. FITSA chains show good mixing and sample similar distributions, while Jazani *et al.* samples exhibit strong within-chain correlation, resulting in slow ESS growth and prolonged posterior sampling.

These sampling differences stem from the algorithms used: FITSA uses Hamiltonian Monte Carlo with the No U-Turn Sampler (NUTS), while the Jazani *et al.* method partly uses Gibbs sampling

(20). Although FITSA's per-iteration cost is expected to be higher because of NUTS's calculations, it achieves convergence faster. To compare performance, we determined the number of FITSA iterations required to match Jazani *et al.* solution after 90,000 iterations (18,000 burn-in and 72,000 sampling). FITSA exceeded the convergence parameters ( $\hat{R} \leq 1.015$ , bulk ESS  $\geq 250$ , and tail ESS  $\geq 420$ ) after just 600 iterations (300 burn-in and 300 sampling). On the same PC, the Jazani *et al.* method took  $101 \pm 5$  min per chain, while FITSA took  $14 \pm 2$  min ( $t$  test,  $P < 0.001$ ), making FITSA more than seven times faster. In this comparison, FITSA sampled all chains in parallel, while the Jazani *et al.* implementation was limited to sequential chain sampling. Parallel sampling for the Jazani *et al.* method would have required multiple MATLAB instances, which was infeasible on the test PC because of high random-access memory demands. This sequential testing approach using the Jazani *et al.* implementation inherently disadvantaged the FITSA implementation, as its six chains had to simultaneously share central processing unit cores and random-access memory resources, whereas in the Jazani *et al.* implementation, each chain had exclusive access to PC resources. It is important to note that the performance, as reported here, depends on the underlying algorithms and implementation. For this comparison, we used the reference implementation of the Jazani *et al.* method, as published in (20).

Both algorithms produced similar distributions for the diffusion coefficient, encompassing the true value (Fig. 3D). However, the Jazani *et al.* method significantly underestimated molecular brightness, unlike FITSA (Fig. 3E). Both slightly overestimated the background emission rate (Fig. 3F).

We found the Jazani *et al.* algorithm to be sensitive to the molecular brightness prior. For the synthetic trace generated with a diffusion coefficient of  $20 \mu\text{m}^2/\text{s}$ , using priors from (20) led to convergence failure (fig. S1). Increasing the prior mean to match the synthetic trace generation value allowed convergence but resulted in underestimated diffusion coefficient and molecular brightness (fig. S2). In contrast, FITSA converged to true values for both priors (figs. S1 and S2) as well as with the priors having mean values of 10,000 and 1000 1/s. FITSA only failed to converge after 1500 burn-in and 1500 sampling iterations when the molecular brightness prior mean was reduced to 100 1/s, a thousand-fold decrease from the true value.

Thus, compared to the Jazani *et al.* method (20), FITSA demonstrated superior speed and robustness to prior differences, consistently satisfying strict recommended convergence criteria (24) for the studied traces.

### Comparing precision with FCS

To compare FITSA and FCS performance, we used identical data for both methods. We generated synthetic traces with known diffusion coefficients and fitted the same trace segments using either FITSA or FCS. Classical FCS does not account for covariance between ACF values, which can lead to overfitting (15). Therefore, we performed two types of FCS estimates: one considering ACF covariance and one without. To determine ACF value covariance, we generated 2000 synthetic traces and calculated ACFs for each trace at time points matching those in the selected segment. From these, we estimated the covariance matrix, which was then used alongside the ACF calculated from the first trace for FCS fitting. To ensure a fair comparison, we used a Bayesian approach for both FITSA and FCS model fits (see Materials and Methods), allowing us to obtain

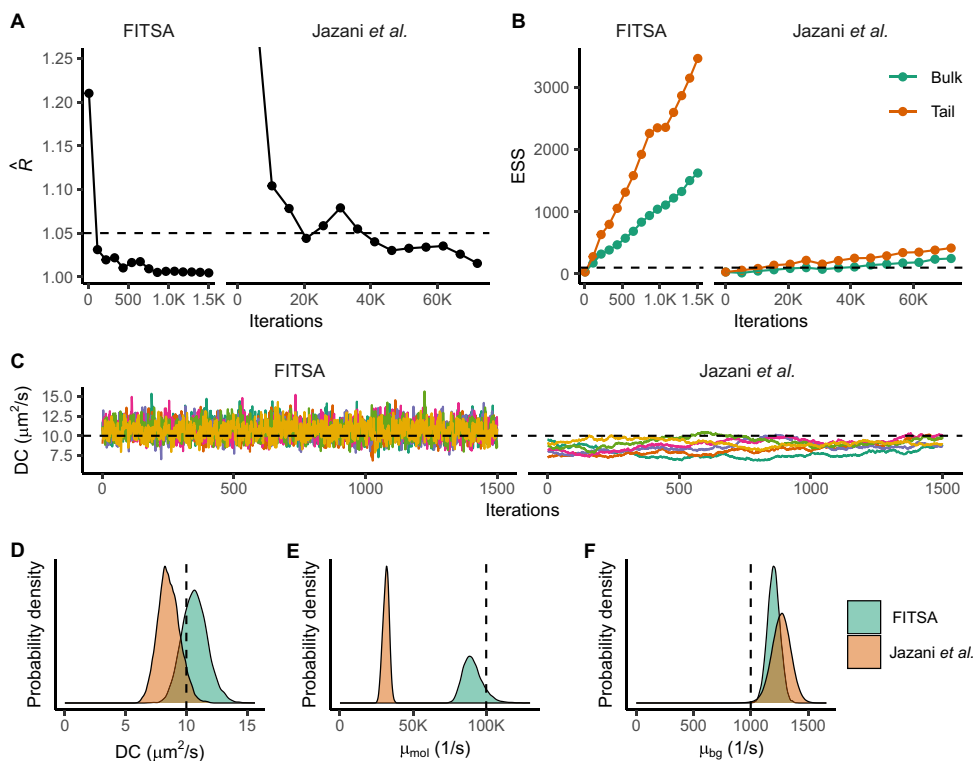


**Fig. 3. Comparing performance of FITSA with the algorithm by Jazani *et al.* (20).** Here, the synthetic trace from Fig. 2 was fitted using FITSA or the Jazani *et al.* algorithm. (A and B) Convergence assessment using potential scale reduction factor  $\hat{R}$  (A) and ESSs (B) for iterations after burn-in. Dashed lines show convergence criteria. (C) Last 1500 iterations for six chains (color-coded) for FITSA and the Jazani *et al.* method. The dashed line indicates expected DC. (D to F) Posterior probability densities for DC (D), molecular brightness (E), and background emission rate (F) from FITSA and the Jazani *et al.* method. Vertical dashed lines show true parameter values.

posterior distributions for diffusion coefficient estimates in both cases. In addition, unless stated otherwise, for all FCS fits in this study, we applied corrections for trace duration (23) to enhance FCS fits for short traces.

Figure 4A illustrates the performance of different methods in estimating diffusion coefficients. FITSA shows rapid convergence to the true diffusion coefficient value with high precision, even for short traces. FCS estimates depended on whether ACF value covariance was considered. Assuming independent ACF values with uniform variance resulted in high-confidence FCS model estimates but for shorter traces, these estimates often excluded the true diffusion coefficient value. Given the importance of ACF value covariance, we focused on comparing FITSA with FCS fits that account for covariance. As shown in Fig. 4A, FCS estimates with covariance require longer traces to achieve similar confidence as FITSA.

To quantify the photon efficiency of FITSA compared to FCS, we targeted a relative precision of 10 (SD 10 times smaller than the true value). Figure 4B shows the relative precision obtained by different methods. In line with previous findings on FCS overfitting when ignoring ACF value covariance, the simplified FCS model estimated much higher precision than the complete model accounting for

covariance (Fig. 4B). FITSA required about four times fewer photons than the complete FCS model to reach a precision of 10 (Fig. 4B). Figure 4C shows the corresponding diffusion coefficient posterior probability densities for FITSA and FCS estimates near the relative precision of 10, which largely overlap [FCS estimate marked as “FCS (E)”]. For comparison, the posterior distribution for the FCS estimate using the same trace length as FITSA was much wider [“FCS (D)” in Fig. 4C]. This demonstrates FITSA’s superior precision with shorter trace lengths.

We repeated this analysis for synthetic traces with diffusion coefficients of 2 and 200  $\mu\text{m}^2/\text{s}$  (figs. S3 and S4). Results were consistent: FITSA achieved the desired precision using shorter traces than FCS when accounting for ACF value covariance. To reach a relative precision of 10, FITSA required 2 (fig. S3) to 11 (fig. S4) times fewer photons than FCS depending on the trace.

For the 200  $\mu\text{m}^2/\text{s}$  diffusion coefficient trace (fig. S3), the difference between FCS and FITSA in required photons was the smallest. In this case, particles passed the focal point quickly, emitting relatively few photons per event. While the photon count was low, the number of events sufficed for ACF composition and covariance estimation, allowing FCS model fitting to recover the diffusion coefficient.

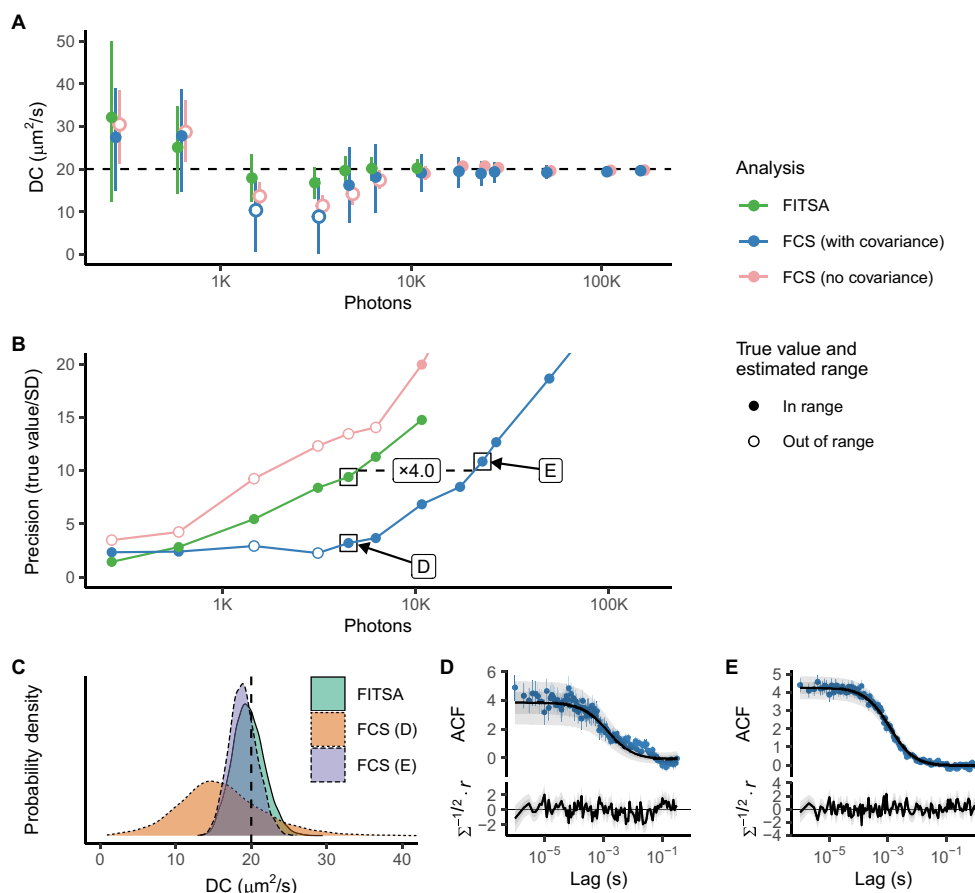


**Fig. 4. Precision of the estimated DC achieved by FITSA and FCS.** Synthetic fluorescence traces were generated with particles having a DC of  $20 \mu\text{m}^2/\text{s}$ . Analysis was performed on the initial section of these traces with varying durations. **(A)** The estimated DC is plotted as a function of photons in the trace exceeding background emission. DC was estimated using FITSA and FCS, with FCS either accounting for ACF covariance (with covariance) or assuming independent ACF values with uniform SD (no covariance). Ranges represent the highest density interval (HDI) of 88%. Points are filled if the HDI contains the true value and the estimated mean value is within the HDI. DC estimates from the same trace are slightly offset to prevent overlap. FITSA estimates DC with shorter traces and demonstrates higher precision than FCS when ACF covariance is considered. See the main text for a discussion on FCS estimates without covariance. **(B)** The precision of DC estimates by different methods is shown as the true value divided by the SD. The same notation is used as in (A). FITSA achieves a relative precision of 10 with shorter traces compared to FCS (with covariance), requiring 4x fewer photons (indicated by the dashed line and label). Estimates marked by black boxes were selected to illustrate the posterior probability density for DC estimated by FITSA (precision close to 10) and FCS for the same trace duration as FITSA or when a precision of 10 was reached. **(C)** Posterior probability densities for DC estimates marked in (B). **(D)** and **(E)** ACF and its predictive posterior by the FCS model (the solid line is median;  $\pm 25$  and  $\pm 40\%$  regions indicated by gray areas) are shown for selected FCS estimates. Below, standardized residuals calculated using the ACF predictive posterior are found from residual ( $r$ ) and covariance ( $\Sigma$ ).

The  $2 \mu\text{m}^2/\text{s}$  diffusion coefficient trace (fig. S4) showed a more pronounced difference, with FITSA recovering the diffusion coefficient using 11 times fewer photons than FCS. For shorter traces, FCS fits accounting for ACF covariance were poor, resulting in wide posterior distributions for estimated diffusion coefficients. FITSA, however, converged to the correct diffusion coefficient and achieved the required precision using a short trace.

In the previous comparison, the number of photons was considered a primary factor determining the estimation precision. However, the duration of the analyzed signal could also potentially

influence the results, as the number of analyzed photons increased with signal duration. To systematically distinguish between the contributions of photon count and signal duration, we conducted an additional analysis by varying molecular brightness from 100,000 1/s to 10,000 1/s (Fig. 5). The comparison of Fig. 5 (A and B) reveals that the number of photons more accurately describes the estimation precision for both FITSA and FCS methods. As illustrated in Fig. 5B, both analytical approaches required progressively longer signal durations when molecular brightness decreased to achieve comparable precision. Notably, across all molecular brightness levels,

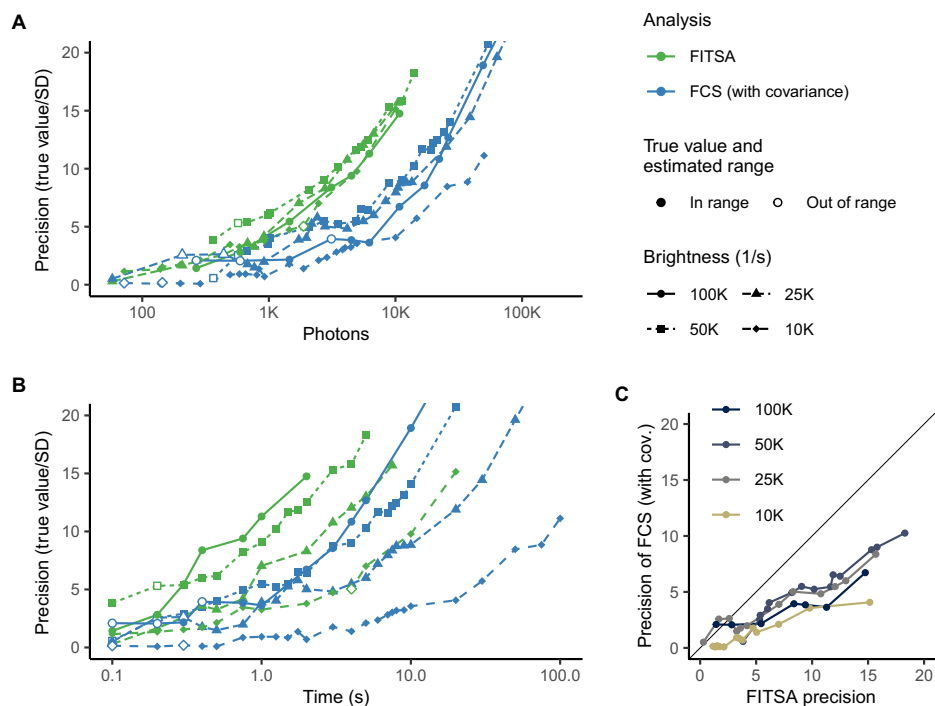


**Fig. 5. Impact of molecular brightness on estimation precision.** As in Fig. 4, synthetic fluorescence traces were generated with particles having molecular brightness reduced from 100,000 1/s to 10,000 1/s and a DC of  $20 \mu\text{m}^2/\text{s}$ . The precision of DC estimation achieved by FITSA and FCS (with covariance) is shown as a function of photons in the trace exceeding background emission (A) or the duration of the analyzed trace (B). Note that for both methods, precision was mainly determined by the number of photons. In (C), the precision of FCS is plotted against the precision of FITSA, following a similar data representation approach as in [(A) and (B)]. Each data point represents a specific simulated condition, and lines connect points obtained under the same molecular brightness, revealing the comparative performance of the two estimation methods across different conditions.

FITSA consistently demonstrated superior precision compared to FCS, as evidenced in Fig. 5C.

In the comparison above, we demonstrated that FITSA achieves desired precision using several times fewer photons than FCS, assuming known ACF covariance without additional measurements. As discussed later, this improvement likely underestimates FITSA's actual advantage by orders of magnitude.

### Demonstration with experimental data

We recorded fluorescence traces under various conditions to demonstrate FITSA's application to experimental data analysis. In Fig. 6, we show traces and analysis results obtained with Alexa Fluor 647 Dextran 10K in a glycerol-water mixture. The fluorescence peaks are heterogeneously distributed throughout the experiment (Fig. 6A). As more data are analyzed, FITSA's estimation of the diffusion coefficient becomes more precise (Fig. 6C). However, because of signal heterogeneity, equal trace durations do not necessarily yield identical posterior probability densities for the diffusion coefficient, especially for shorter durations (Fig. 6D).

To characterize estimate variability, we divided a 120-s trace into shorter intervals of different durations. We estimated the diffusion coefficient for each interval using both FITSA and FCS (without covariance) and summarized the results in Fig. 6E. FITSA estimates

show notably less variability than FCS estimates. To achieve the same precision as FITSA, FCS would require approximately five times longer measurements. This is illustrated by SD of the estimates for FITSA and FCS at different interval durations (Fig. 6F). Notice that FITSA estimates using 1-s intervals had an SD ( $6.6 \mu\text{m}^2/\text{s}$ ) comparable to FCS estimates using 5-s intervals ( $7.0 \mu\text{m}^2/\text{s}$ ), with this trend consistently observed when comparing FITSA estimates at 2 s with FCS at 10 s and FITSA at 5 s with FCS at 20 s.

In a second set of experiments (Fig. 7), we recorded 120-s fluorescence traces with Alexa Fluor 647 Dextran 10K in water, resulting in faster diffusion ( $\sim 70 \mu\text{m}^2/\text{s}$ ), in agreement with the earlier measurement of  $62 \mu\text{m}^2/\text{s}$  by raster image correlation spectroscopy (8) and reported values of diffusion coefficient ( $60$  to  $70 \mu\text{m}^2/\text{s}$ ) for similar-sized dextran conjugated with other fluorophores (25–27). We varied laser power and dye concentration, which strongly affected trace intensity (Fig. 7A). Despite these differences, FITSA-estimated diffusion coefficient posteriors showed similar median values across conditions (Fig. 7B). However, these conditions affected estimate precision for both 5-s traces analyzed by FITSA and 120-s traces analyzed by FCS. Increased laser power led to higher precision in FITSA estimates.

For low dye concentrations (0.1 nM), we carefully selected representative traces to reflect average FITSA estimates. We chose 120-s

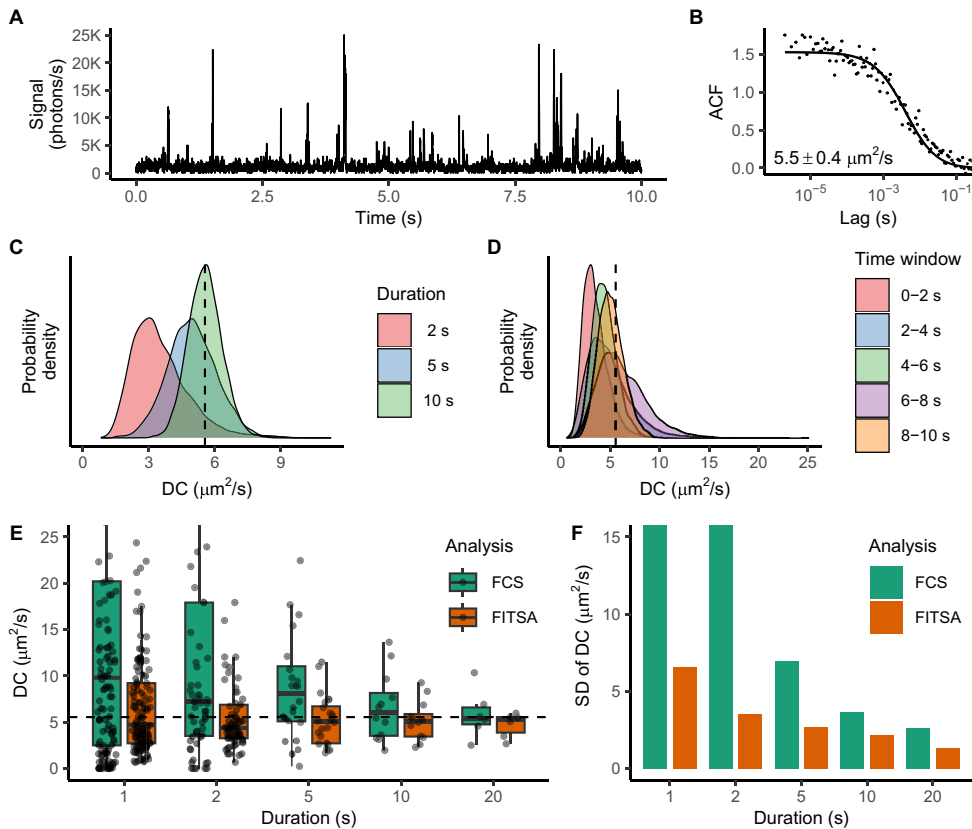


**Fig. 6. Analysis of the experimental trace recorded for Alexa Fluor 647 Dextran 10K in the 60% glycerol/water mixture.** (A) Signal obtained during 10 s of 120-s recording for the dye in a 0.1 nM concentration. (B) ACF calculated for the 120-s signal trace and fitted by the 3D diffusion FCS model with the estimated diffusion coefficient shown in the inset. In (B), FCS analysis was performed without correcting for the analyzed segment duration, as the experiment's duration was sufficiently long. (C) Diffusion coefficient estimation by FITSA using the first 2, 5, or 10 s of the trace in (A). Note how the posterior of the diffusion coefficient is getting more compact with the increase in the amount of analyzed data. (D) For shorter time traces, the diffusion coefficient posterior depends on which part of the signal is analyzed. Here, 2-s traces were taken from the 10-s trace (A) at the different time windows, as indicated by color. (E) 120-s trace analyzed by FCS and FITSA using smaller subsections of the trace with the results grouped by the duration of the subsections. For FITSA, the mean value of the diffusion coefficient posterior was shown in this comparison. For clarity, shown diffusion coefficients are limited to  $25 \mu\text{m}^2/\text{s}$ . (F) SD of the diffusion coefficient estimations shown in (E) for FCS and FITSA with the vertical axis limited to  $15 \mu\text{m}^2/\text{s}$  for clarity. Note that the spread of the estimated values is considerably smaller for FITSA than for FCS. In [(C) to (E)], the diffusion coefficient value estimated by FCS for the 120-s trace is indicated by a dashed line.

traces on the basis of FCS-estimated diffusion coefficients close to the median among all estimates for the same concentration and laser power. We then partitioned these traces into 5-s intervals for FITSA analysis, selecting intervals with median FITSA-estimated diffusion coefficients to show as representative posteriors in Fig. 7.

Higher dye concentrations improved precision for estimates from the same time interval because of more particle passage events. However, at a 1 nM concentration, FITSA faced challenges. The current implementation assumes single-particle passages through the confocal volume, which does not hold at higher concentrations. This led to elevated background emission rate estimates. Furthermore, we had to limit the length of subsections used in the fits, as there were no clear phases in the transients corresponding to stages where no particles were near the confocal volume. Consequently,

without this imposed limit, the automatic partitioning of the trace was unable to isolate single-particle passages and instead joined multiple passages into a single subsection. This automatic partitioning had been effective in other tests with lower concentrations. Addressing these challenges for higher concentration traces will be the focus of future studies.

In additional experiments, we evaluated FITSA's ability to determine diffusion coefficients in cardiomyocytes. We created holes in an intact cardiomyocyte by puncturing it using a sharp glass pipette, allowing Alexa Fluor 647 Dextran 10K from the external solution to enter the cell. For each selected cellular location (Fig. 8A), we recorded three 120-s fluorescence intensity traces. For FITSA, we analyzed the middle portion of the second trace (out of three) at each location because it displayed stable fluorescence

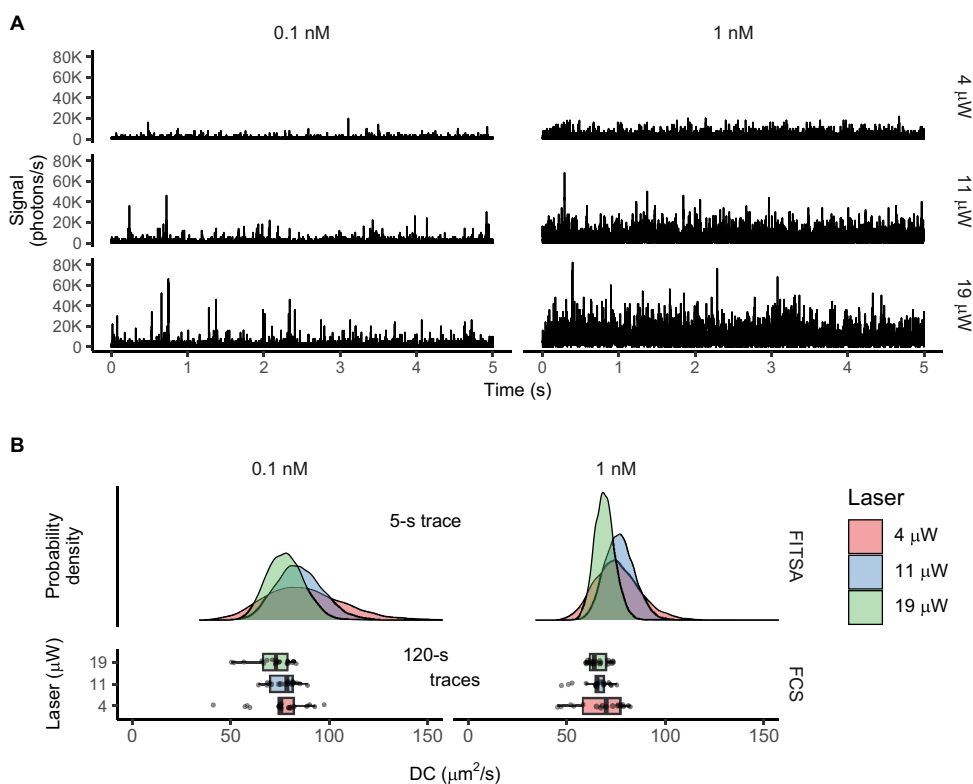


**Fig. 7. Determination of the diffusion coefficient at different laser powers and Alexa Fluor 647 Dextran 10K concentrations in water.** (A) Sample 5-s-traces analyzed by FITSA and measured with 0.1 nM (left) or 1 nM (right) solutions of Alexa Fluor 647 Dextran 10K at different laser powers (4 to 19  $\mu\text{W}$  from top to bottom). (B) Diffusion coefficient posterior probability densities from FITSA (5-s traces, top) compared to FCS results (120-s traces, bottom). For FCS, each point represents one 120-s trace analysis (17 to 18 traces per condition). Here, FCS analysis was performed without correcting for the analyzed segment duration, as the experiment's duration was sufficiently long. Left and right columns show different dye concentrations. Colors encode laser power. Note the increased estimate precision with higher laser power and concentration.

levels, while, for FCS, we used the final 60 s of all stable traces to estimate the diffusion coefficient (Fig. 8). The first trace typically showed an initial decline in overall fluorescence that stabilized before the second half of recording, except at location “2.” This decline could be attributed to bleaching of weak autofluorescence (observed in experiments without dye), bleaching of dye molecules, or other contributing factors.

In cardiomyocytes, FCS revealed a larger contribution of the triplet state compared to water (Fig. 8B). The fractional population of the triplet state in the studied cardiomyocyte ( $0.50 \pm 0.04$ ,  $n = 6$ ) was significantly larger than in water ( $0.29 \pm 0.04$ ,  $n = 26$ ;  $P < 0.0001$ , likelihood ratio test). The triplet relaxation time showed no significant difference between the cell ( $4.1 \pm 1.2 \mu\text{s}$ ,  $n = 6$ ) and water ( $6.0 \pm 3.8 \mu\text{s}$ ,  $n = 26$ ;  $P = 0.21$ , likelihood ratio test). Here, we included only transients that resulted in fits with triplet relaxation times between 2 and 15  $\mu\text{s}$ , avoiding cases where triplet contribution improved ACF fit outside the expected range of 4 to 7  $\mu\text{s}$  for the used dye (8). In addition, for the analyzed transient recorded in the glycerol-water mixture (Fig. 6), the contribution of triplet states was negligible, with FCS model fits showing a triplet relaxation time of

1  $\mu\text{s}$ . Thus, compared to the other experimental cases in this study, analysis in cardiomyocytes is complicated by substantial contributions of triplet states.

Despite these challenges, FITSA successfully recovered diffusion coefficients from relatively short transients (10 s), with the posterior distribution of diffusion coefficients encompassing the range predicted by FCS (Fig. 8C). Because current FITSA models do not incorporate triplet states, the predicted posterior of diffusion coefficients shows a slight shift toward larger values compared to FCS models that account for triplet state contribution:  $21.8 \pm 2.8 \mu\text{m}^2/\text{s}$  (FCS,  $n = 8$ ) versus  $24.9 \pm 2.7 \mu\text{m}^2/\text{s}$  (FITSA posterior medians for 10-s traces,  $n = 3$ ); this difference was not significant ( $P = 0.099$ , likelihood ratio test). This shift toward larger diffusion coefficients in models without triplet state contribution is expected, as demonstrated by larger diffusion coefficients predicted by FCS ( $26.5 \pm 3.5 \mu\text{m}^2/\text{s}$ ,  $n = 8$ ) when fitting ACF at lag times larger than 2  $\mu\text{s}$  (significant difference between FCS models with and without the triplet state,  $P = 0.005$ , likelihood ratio test). The estimates by both FITSA and FCS are similar, although slightly higher, compared to previous measurements using raster image correlation spectroscopy

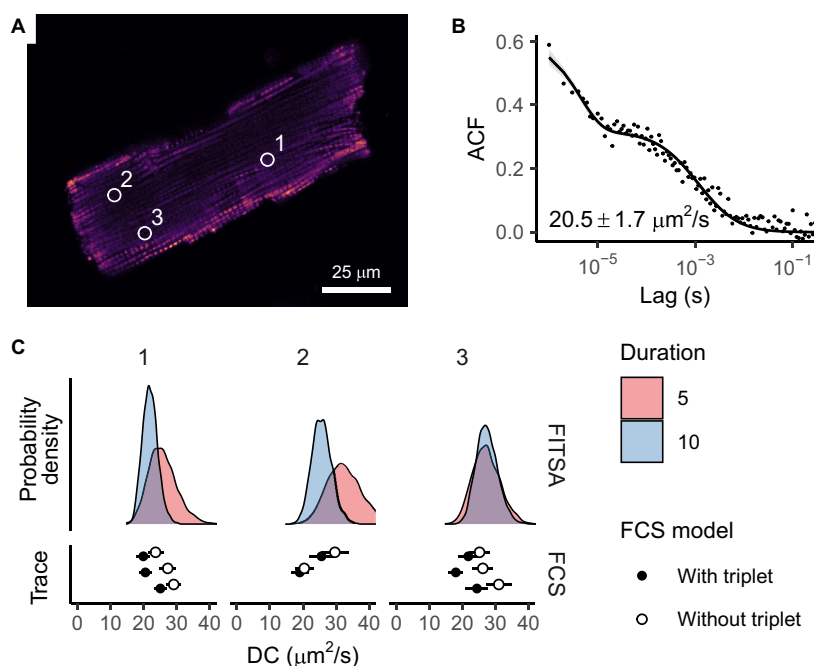


**Fig. 8. Determination of diffusion coefficients of Alexa Fluor 647 Dextran 10K in the rat cardiomyocyte.** (A) Confocal image of an adult rat cardiomyocyte depicting mitochondria (MitoTracker Green), along with the diffusion measurement locations of Alexa Fluor 647 Dextran 10K indicated by circles. (B) ACF with its predictive posterior calculated using an FCS model that accounts for both diffusion and triplet state dynamics (median shown as a solid line, with  $\pm 25$  and  $\pm 40\%$  probability regions in gray). The ACF was calculated using the last 60 s of the final two traces from location 1 to demonstrate the presence of triplet states. (C) Diffusion coefficients determined by FITSA (using 5- and 10-s traces) compared with FCS results (using 60-s traces). FCS estimates are presented as the means with SD for each analyzed trace using models either considering or excluding triplet state contributions. At location "2," one of three traces was excluded from analysis because of fluorescence instability. Here, FCS analysis was performed without correcting for the analyzed segment duration, as the experiment's duration was sufficiently long.

(8) for the same dye in rat cardiomyocytes:  $16 \pm 2 \mu\text{m}^2/\text{s}$  in the transversal direction and  $19 \pm 3 \mu\text{m}^2/\text{s}$  in the longitudinal direction. This example demonstrates FITSA's capability to recover diffusion coefficients in live cells using short fluorescence transients, achieving results similar to those obtained by FCS analysis of 60-s traces.

Looking ahead, we anticipate that extending FITSA models to include transitions between molecular states would improve estimate precision. The development of FITSA models incorporating various physical aspects of real-life measurements will be addressed in future studies.

## DISCUSSION

Fluorescence intensity traces from FCS experiments encode rich information about molecular movement around and within the confocal volume. Recent Bayesian approaches have shown promise in directly analyzing these traces compared to traditional FCS analysis using ACFs (20, 21). Compared to earlier Bayesian approach-based methods (20), FITSA converges much faster and demonstrates greater robustness. Rigorous analysis shows that FITSA can estimate diffusion coefficients using much shorter fluorescence traces than FCS, overcoming difficulties in statistical analysis of FCS results.

A major advance of FITSA, enabling it to outperform earlier approaches for direct fitting of fluorescence intensity traces (20),

stems from its treatment of fluorescence traces as collections of smaller sections. Each section represents an experimental phase where independent particles enter the vicinity of the focal point and subsequently leave it. This conceptual approach of handling the experiment as a series of local events begins with adaptive signal binning based on fluorescent particle proximity to the focal point, facilitating the subsequent division of the transient into smaller sections. Furthermore, FITSA's strategic selection of seed points at maximum photon emission rates enables efficient sampling of posterior distributions around well-constrained positions, reducing the impact of parameter cross-correlations. These advances result in demonstrably improved convergence speed and greater robustness to priors far from the posterior compared to earlier methods, as evidenced in our validation studies (Fig. 3 and figs. S1 and S2). Both improvements make FITSA more suitable for practical applications and enable the analysis of longer transients than was achievable with earlier approaches (20).

The advantages of FITSA's sectioning approach and strategic seed point selection become evident when considering posterior sampling. When reconstructing particle trajectories, the algorithm first draws coordinates for a seed point and then reconstructs the trajectory by drawing possible particle steps based on elapsed time and proposed diffusion coefficient. Because each consecutive particle position depends on the previous one, the coordinates become

strongly correlated throughout the trajectory. Methods analyzing whole transients, as in (20), face a substantial challenge: Any change in particle position at the beginning of a trajectory affects all subsequent positions. This challenge is further complicated by varying precision in position estimation—high when particles are near the focal point and low when they are distant, where limited information leads to wide posterior distributions. This creates a particularly difficult sampling problem: When analyzing long trajectories, any large changes in particle coordinates before the particle enters the focal region must remain consistent with the subsequent well-confined positions where the particle produces a measurable signal. FITSA overcomes these challenges by treating particle movements in separate sections as independent events and selecting seed points at maximum fluorescence intensity. This approach confines coordinate cross-correlations within individual sections and starts from positions with minimal posterior uncertainty, substantially improving sampling efficiency and method performance.

FITSA's sectioning approach also mitigates limitations associated with using unbound diffusion processes in the model. While bound diffusion descriptions exist, their implementation is impractical because of infinite series in coordinate posterior calculations. The unbound diffusion model, used in both FITSA and earlier methods (20, 21), inherently allows particles to drift away from the seed point. FITSA minimizes this effect through its short sections and strategic seed point selection. In contrast, methods analyzing complete transients must compensate for this particle dispersion to maintain particles near the focal point, potentially leading to artificial adjustments such as underestimation of diffusion coefficients, as demonstrated in our comparison with the Jazani *et al.* method (fig. S2).

Before comparing FITSA with FCS, it is important to stress that as pointed out in Introduction, FCS is commonly used assuming statistically independent residuals in ACF values when fitted with models. This assumption is incorrect and leads to data overfitting, as shown in earlier studies (15, 16) and in Fig. 4. To address this, one can estimate covariance between different lag times (15) or perform separate measurements for each ACF value (18). These approaches are expected to yield better error estimates and enable discrimination between models of different complexities, such as single- or multicomponent diffusion.

When applied to FCS, estimation of covariance or composition of ACF requires a much larger dataset than commonly used and stable preparation throughout the longer experiment required to acquire it. For instance, in our covariance matrix estimation to compare FITSA and FCS performance (Figs. 4 and 5 and figs. S3 and S4), we used 2000 traces for each condition. If we had composed an ACF by taking one point from each trace as in (18), we would have used 130 traces in our analysis. These requirements were not accounted for in the comparison between FITSA and FCS. When considering these requirements, FITSA can estimate the diffusion coefficient using 300 to 21,000 times fewer photons than FCS depending on the dataset and approach used to estimate FCS errors.

While the statistical properties of ACF used in FCS have been known for some time, FCS and its derived techniques typically ignore cross-correlation between ACF values in practical applications. Current FCS measurements already require stable background conditions, and extending these measurements 100-fold or more is often impossible in practice. This limitation, considering the wide range of problems where FCS has been applied, makes the

determination of intracellular molecular properties, such as diffusion coefficients, a major open scientific challenge. FITSA addresses this challenge in a statistically sound manner and, as we demonstrate with experimental traces (Fig. 6), enables the use of even shorter fluorescence transients than commonly used FCS. This makes it possible to determine diffusion coefficients in cases that were previously considered impractical using FCS with statistically correct ACF fitting. While FITSA does require longer simulation times than conventional FCS, we argue that this is a necessary trade-off for solving the problem in a statistically rigorous way.

From the comparison of FITSA and FCS performance using synthetic data, we observed that their performance gap depends on diffusion coefficient, with FITSA's advantage over FCS becoming more pronounced for slower diffusion. Taking into account the fact that molecular diffusion in cells is frequently relatively slow—even for smaller molecules such as ATP (adenosine 5'-triphosphate) and cAMP (adenosine 3',5'-monophosphate), which exhibit diffusion coefficients around  $30 \mu\text{m}^2/\text{s}$  (8, 28, 29)—FITSA is expected to have a major impact on improving studies of the intracellular environment by reducing the time required for measurements. This reduction in measurement time would consequently minimize laser-induced phototoxic effects on cells during experiments.

Given FITSA's ability to estimate diffusion coefficients from small amounts of data, it was crucial to recognize the inherent heterogeneity in estimated model parameters because of trace variability. This is illustrated in Fig. 6, where transients of the same duration led to different diffusion coefficient estimates for different short time traces. When comparing FCS performance with FITSA (Fig. 4 and figs. S3 and S4), we ensured that exactly the same transient section was analyzed using a Bayesian approach to fit ACF by the FCS model to obtain confidence levels in estimated diffusion coefficients.

Our approach differs from that used in (20), where FCS result variability was analyzed by performing fits on different sections of the trace. Such an approach potentially combines FCS analysis uncertainty with trace heterogeneity. By analyzing the same transient section for both methods, we were able to accurately quantify the performance of FITSA and FCS, isolating methodological differences from trace-to-trace variability. This approach allowed us to precisely estimate the differences in photon requirements between the two methods, providing a more rigorous comparison of their relative efficiencies.

FITSA estimates not only diffusion coefficients but also molecular brightness and background emissions, making it comparable to methods that analyze photon count distributions rather than temporal domain measurements like FCS. The photon counting histogram (PCH) analysis and fluorescence-intensity distribution analysis (FIDA) are two such methods that determine molecular brightness and molecular concentrations in samples (30, 31), and these approaches have been demonstrated to be mathematically equivalent (32). An extension of FIDA, called fluorescence intensity multiple distributions analysis (FIMDA), analyzes the same fluorescence trace using photon count histograms obtained at different time intervals. This approach combines the strengths of FIDA and PCH with FCS capabilities, enabling the determination of diffusion coefficients (33). To our knowledge, the impact of error covariance in fits for FIDA, FIMDA, and PCH has not been analyzed as extensively as it has for FCS (15). However, we anticipate that FIMDA likely faces similar challenges. Specifically, because FIMDA reuses the same underlying recording data by rebinning them at different

time intervals, these measurements are unlikely to be statistically independent. Consequently, we expect that ignoring error covariance in FIMDA would affect diffusion coefficient estimations in a manner similar to FCS.

FITSA shares certain similarities with single-particle tracking methods but offers distinct advantages. Most notably, FITSA can effectively analyze particles with much higher diffusion coefficients than those typically studied using single-particle tracking, which is usually limited to coefficients below and around  $1 \mu\text{m}^2/\text{s}$  (although some setups have achieved measurements up to 10 to  $20 \mu\text{m}^2/\text{s}$ ) (34, 35). Furthermore, when particle tracking is used to study small molecules, careful consideration must be given to potential optical trapping effects that might influence molecular motion (36). This concern is largely mitigated in FITSA and FCS, as these methods record fluorescence changes at a fixed spot rather than tracking individual particles.

In our validation tests, FITSA successfully recovered a diffusion coefficient of  $500 \pm 35 \mu\text{m}^2/\text{s}$  from synthetic traces generated with a true value of  $500 \mu\text{m}^2/\text{s}$ . For faster-moving molecules (synthetic trace with  $750 \mu\text{m}^2/\text{s}$ ), FITSA showed a slight underestimation, yielding  $690 \pm 50 \mu\text{m}^2/\text{s}$ . While we have not tested FITSA with even faster-moving molecules, the main challenge in analyzing such rapid diffusion lies in distinguishing particle passages through the confocal volume from background emissions. This limitation can be addressed by lowering the prior background emission rate during signal preprocessing. Although this adjustment increases computational demands by expanding the number of bins requiring analysis, it enables accurate recovery of diffusion coefficients. Thus, FITSA extends the range of molecular mobility studies beyond what is typically achievable with single-particle tracking methods.

FITSA's performance depends not only on model equations but also on fluorescence transient preprocessing. While preprocessing parameters can be modified from our tested values, they should be chosen on the basis of the studied system and expected particle dynamics. For slow-moving particles, longer time intervals can be used for binning, reducing computational requirements. On the basis of our testing, time intervals should be substantially shorter than the time a particle takes to traverse the microscope's PSF volume; otherwise, the diffusion coefficient will be underestimated because of missing information about particle dynamics. The expected background emission rate should not be overestimated, as this would lead to consideration of only larger fluorescence transient peaks. Missing smaller peaks would cause FITSA to underestimate the diffusion coefficient, interpreting the data as particles remaining in the focal point vicinity for longer periods on average. When fluorescence peaks are clearly visible, we used a wide range of data points per subsection with automatic split determination. However, with overlapping peaks from multiple particles, smaller subsection sizes become crucial to analyze independent events separately. These adjustments should still capture particle movement while maintaining sufficient length to avoid missing longer-term dynamics.

FITSA represents a major advancement in shifting from traditional FCS data analysis to direct fitting of fluorescence traces, proving highly effective in many practical applications. However, like most emerging approaches, it has limitations that need to be addressed in future work. The primary challenges we have encountered relate to fitting data from experiments requiring multiparticle models, particularly those involving higher concentrations or multicomponent systems. These challenges manifest in two main

aspects. First, the local events, as specified by fluorescence transient subsections, are caused by multiple particles simultaneously passing through the detection volume. A potential solution is to use a non-parametric approach, as demonstrated in previous studies (20, 21), to determine both the number of contributing particles and their trajectories. The second aspect concerns signal analysis when multiple particles contribute continuously to the fluorescence signal. In such cases, there are no periods in the transient that are dominated by background emissions, making it difficult to determine the background emission level from the same transient. Consequently, either the background level must be established in a separate experiment or the dye concentration must be limited. As a practical solution at this stage, until FITSA can handle multiparticle cases, we recommend reducing the concentration of fluorescent dye to levels that are more suitable for analysis in the experimental setup.

Similar to the evolution of FCS over decades, we anticipate that FITSA's underlying models will require further refinement to better reflect observed phenomena. These refinements include accounting for triplet state formation, chemical reactions, deviations of microscope PSF from the used analytical form, and analysis of background emissions. Because FITSA relies on the same physical principles as FCS, these refinements can build upon numerous previously established studies in the field, accelerating FITSA development. As FITSA analyzes fluorescence traces differently from FCS, further optimization of imaging and other experimental conditions is needed. We expect that these optimizations will greatly improve our ability to study intracellular molecular properties in future studies.

Although FITSA is faster and less memory intensive than previous methods, it still demands considerable computational resources. To address this limitation, we can leverage FITSA's use of state-of-the-art numerical libraries to potentially accelerate simulations on graphics processing units (GPUs). However, in our test cases, GPU utilization did not yield faster simulation times, suggesting that further optimization of the implementation is necessary to better harness GPU capabilities.

In conclusion, FITSA allows estimation of diffusion coefficients and other parameters from short fluorescence intensity traces. The reference implementation provides a set of applications and model libraries for practical analysis and future development. We anticipate that FITSA and similar approaches will become attractive alternatives for studying molecular events in experiments currently performed using FCS and related techniques. By avoiding correlation calculations and their inherent fitting issues, methods like FITSA that rely on statistical fitting of original datasets are more robust and provide uncertainty estimation for fitted parameters. Given the markedly reduced photon requirements to achieve precision comparable to FCS, we expect that direct data fitting methods will enable more detailed descriptions of intracellular environments and molecular interactions than previously possible.

## MATERIALS AND METHODS

### Model overview

The mathematical model used by FITSA assumes that particles diffuse freely in the 3D space and emit fluorescence because of laser illumination in the confocal microscopy setup. As the model is using a Bayesian approach, its objective is to find the posterior distributions for the parameters of interest given priors and likelihood. In

this case, the model estimates the posterior distributions for particle trajectories, their diffusion coefficient  $D$ , molecular brightness  $\mu_{\text{mol}}$ , and background emission rate  $\mu_{\text{bg}}$ . For that, the likelihood is formulated using the measured fluorescence intensity trace. To improve convergence, FITSA preprocesses the signal by splitting it into smaller subsections to separate parts where a single particle moves through the confocal volume. The overall likelihood is formulated assuming that each subsection reflects an independent measurement with the particles trajectories being uncorrelated between subsections.

**Signal processing**

As outlined in Results, FITSA preprocesses the fluorescence signal through adaptive binning followed by subsection splitting.

**Signal binning**

FITSA preprocesses the fluorescence trace using an adaptive binning strategy that distinguishes between background emissions and particle-originated signals near the confocal volume. The complete binning procedure is illustrated in fig. S8. Consider particles traversing the confocal volume (fig. S8A) and their corresponding detected photon signals (fig. S8B).

The binning process begins with calculating the signal’s rolling average using two time windows: twin1 (10 ms) and twin2 (50 ms). Regions where both rolling averages exceed the expected background emission rate by a binning factor  $f_{\text{bin}}$  (set to 2) are designated as candidates for smaller bins. These regions, termed “accepted areas,” are highlighted in green in fig. S8C, with the acceptance rate defined as  $f_{\text{bin}}$  times the background emission rate.

The signal is then analyzed sequentially in time, with bin size selection adapting to different scenarios. Within accepted areas, bin duration is determined by counting photons until a predefined threshold is reached ( $I_{\text{thr}}$ ) (fig. S8D). In high-emission rate regions, bin duration is set to the predefined minimum ( $\Delta t_{\text{min}}$ ) when the photon rate would otherwise result in bins smaller than  $\Delta t_{\text{min}}$  (fig. S8E). When exiting accepted areas, the photon count is reset, and bin duration is set to either the predefined maximum ( $\Delta t_{\text{max}}$ ) or, at most,  $\text{bin}_{\text{increase}}$  (set to 2) times the previous bin duration (fig. S8F). Upon entering accepted areas, photon counting begins anew, with bin duration determined by either the threshold or maximum duration increase (fig. S8G).

Following the forward analysis, the signal undergoes multiple reverse passes to refine bin transitions, particularly where bin duration changes abruptly upon entering accepted areas. The reverse processing continues until consecutive bins maintain the maximum duration ratio  $\text{bin}_{\text{increase}}$  in both time directions, ensuring smooth transitions throughout the signal. The resulting adaptively binned signal  $I_b(t)$  features gradual transitions between different bin sizes and serves as input for subsequent analysis.

**Binned signal splitting**

The binned signal was divided into subsections on the basis of bin durations, with splits occurring in regions containing the largest bins, which primarily represent background emissions. The splitting process analyzes the signal in the forward direction, evaluating bin sizes within a moving window of  $N_s^{\text{min}}$  to  $N_s^{\text{max}}$  bins. Within this window, the bins exceeding a minimum duration threshold  $\Delta t_s$  are found. If no bins exceed  $\Delta t_s$ , the bin with the longest duration was selected as a split point. When multiple bins had durations exceeding  $\Delta t_s$ , the first such bin was selected as a candidate. To ensure robust splitting, the algorithm verifies the first potential split point

by examining the subsequent  $N_s^{\text{seq}}$  bins (five used in the current implementation) and selecting the furthest bin within these  $N_s^{\text{seq}}$  bins that exceeds  $\Delta t_s$ . This process repeats from each established split point until the entire signal is segmented into distinct subsections.

Within each subsection  $s$ , the algorithm identifies a seed time point  $t_s^{\text{seed}}$  by locating the maximum of the rolling average calculated over a time window  $\Delta t_{\text{seed}}$ . This seed point typically corresponds to the moment when a particle is the closest to the confocal volume center.

**Model**

**Likelihood**

We assumed that the photon counts in the binned fluorescence trace were described by Poisson statistics (19, 20, 37, 38). With this assumption, the likelihood of the observed intensity  $I_b(t_k)$  for the  $k$ -th bin is determined as

$$I_b(t_k) \sim \text{Poisson}(\Delta t_k \mu_k) \tag{1}$$

where  $\Delta t_k = t_k - t_{k-1}$  is the duration of the  $k$ -th bin, and  $\mu_k$  is the projected photon emission rate during that bin, as detected by the detector.

**Emission rate**

The emission rate  $\mu_k$  is the sum of background emissions and emissions by  $N$  particles

$$\mu_k = \mu_{\text{bg}} + \mu_{\text{mol}} \sum_{n=1}^N \text{PSF}[x_n(t_k), y_n(t_k), z_n(t_k)] \tag{2}$$

where  $x_n(t_k)$ ,  $y_n(t_k)$ , and  $z_n(t_k)$  are the positions of particle  $n$  in the 3D space relative to the focal point at time moment  $t_k$ , and the PSF describes the spatial distribution of detected photons from a single point source (1). Here, the  $z$  axis is parallel to the optical axis of the microscope objective. For the confocal setup used in this study, PSF was approximated by a 3D Gaussian ellipsoid (1, 39)

$$\text{PSF}(x, y, z) = \exp\left(-2\frac{x^2+y^2}{\omega_{xy}^2} - 2\frac{z^2}{\omega_z^2}\right) \tag{3}$$

where  $\omega_{xy}$  is the lateral waist of the PSF, and  $\omega_z$  is the axial waist along the  $z$  axis. Note that in this model, molecular brightness is determined not only by the intrinsic brightness of the particle but also by the detection efficiency of the microscope, which includes the optical system and the detector. The same applies to the background emission rate.

**Diffusion**

Diffusion of particles in the 3D space was defined by propagators (40) for each particle

$$\begin{aligned} x_n(t_k) &\sim \text{Normal}[x_n(t_{k-1}), 2D\Delta t_k] \\ y_n(t_k) &\sim \text{Normal}[y_n(t_{k-1}), 2D\Delta t_k] \\ z_n(t_k) &\sim \text{Normal}[z_n(t_{k-1}), 2D\Delta t_k] \end{aligned} \tag{4}$$

Because of the symmetry of the propagators, a chance of observing a sequence of coordinates in the forward direction [as in  $\dots, x_n(t_{k-2}), x_n(t_{k-1}), x_n(t_k), \dots$ ] is equal to observing the same sequence in the opposite direction [as in  $\dots, x_n(t_k), x_n(t_{k-1}), x_n(t_{k-2}), \dots$ ].

**Priors and inference**

We used the same type of priors for the diffusion coefficient, molecular brightness, and background emission rate as in (20)

$$\begin{aligned}
 D &\sim \text{Inverse gamma}(\alpha_D, \beta_D) \\
 \mu_{bg} &\sim \text{Gamma}(\alpha_{bg}, \beta_{bg}) \\
 \mu_{mol} &\sim \text{Gamma}(\alpha_{mol}, \beta_{mol})
 \end{aligned}
 \tag{5}$$

where  $\alpha_D = \beta_D = 1$ ,  $\alpha_{bg} = \alpha_{mol} = 2.25$ ,  $\beta_{bg} = \alpha_{bg} / \mu_{bg}$ , and  $\beta_{mol} = \alpha_{mol} / \mu_{mol}$ . Used probability density functions are defined in table S1.

Diffusion of the particles was considered separately in each subsection, with coordinates defined from the first time moment of the subsection to the last time moment before the first time moment of the next subsection. Within each subsection, a seed time moment  $t_s^{seed}$  was selected as described above, and particle coordinate priors for that time moment were

$$\begin{aligned}
 x_n(t_s^{seed}) &\sim B_{xy} \cdot \text{Normal}(0, 1) + \left[1 + \frac{(n-1)}{N}\right] \cdot \frac{B_{xy}}{2} \\
 y_n(t_s^{seed}) &\sim B_{xy} \cdot \text{Normal}(0, 1) + \left[1 + \frac{(n-1)}{N}\right] \cdot \frac{B_{xy}}{2} \\
 z_n(t_s^{seed}) &\sim B_z \cdot \text{Normal}(0, 1) + \left[1 + \frac{(n-1)}{N}\right] \cdot \frac{B_z}{2}
 \end{aligned}
 \tag{6}$$

where  $B_{xy}$  and  $B_z$  were used to shift and scale the priors; the particle index  $n$  was from 1 to  $N$ . As the used PSF was symmetric (Eq. 3), priors were set to preferentially shift particles into the positive coordinates. Because of the symmetry of the PSF and the assumption that particles do not interact with each other in the model, our selection of priors does not introduce bias. However, if the PSF is asymmetric or if processes depend on the precise location of particles, such as interparticle interactions, these priors would need to be revised.

Priors for other positions within each subsection  $s$  were determined on the basis of diffusion propagators (Eq. 4) using the diffusion coefficient as a hyperprior (Eq. 5). For particle positions after the seed time moment, the diffusion propagators were applied according to Eq. 4 in the forward direction. Conversely, for particle coordinates before the seed time moment  $t_s^{seed}$ , the symmetry of the propagators was used

$$\begin{aligned}
 x_n(t_{k-1}) &\sim \text{Normal}[x_n(t_k), 2D\Delta t_k] \\
 y_n(t_{k-1}) &\sim \text{Normal}[y_n(t_k), 2D\Delta t_k] \\
 z_n(t_{k-1}) &\sim \text{Normal}[z_n(t_k), 2D\Delta t_k]
 \end{aligned}
 \tag{7}$$

Inference was done by sampling priors for diffusion coefficient, molecular brightness, and background emission rate priors first. Next, priors for particle positions were sampled individually for each subsection and merged to reconstruct particle trajectories across the entire binned signal. Last, using these samples, the likelihood was evaluated. Posterior distributions were then derived on the basis of the likelihood and the priors, as described in the implementation below. In the performed simulations, the number of particles  $N$  was set to one.

**Implementation**

FITSA is implemented as a set of applications and a library in Python. For FITSA simulations presented here, models were implemented

and sampled using NumPyro (41, 42). Sampling was performed by NumPyro’s implementation of NUTS, an extension of the Hamilton Monte Carlo.

The sampling was performed using six parallel chains, consisting of two phases: burn-in and sampling. The burn-in phase comprises initial iterations during which the algorithm stabilizes, while the sampling phase includes iterations used to estimate the posterior distribution. The number of burn-in and sampling iterations was selected to ensure convergence, as indicated by a potential scale reduction factor  $\hat{R}$  close to 1 (below 1.05), and reliability of the estimates, verified by bulk and tail ESSs exceeding 100, following standard recommendations (24).

The convergence was checked for diffusion coefficient  $D$ , molecular brightness  $\mu_{mol}$ , and background emission rate  $\mu_{bg}$ . Particle positions were not checked for convergence because multiple combinations of coordinates could yield the same photon emission rate, as determined by the used PSF. In the simulations presented, typically 1500 burn-in and 1500 sampling iterations were used, as these generally met the convergence criteria. However, in the instances with very short transients, the number of sampling and burn-in iterations was increased until convergence was confirmed.

Convergence was checked by processing posterior samples using ArviZ (43). In addition, Hamilton Monte Carlo divergences (44, 45) were found to be low during sampling of the formulated model, indicating that the sampler was able to explore the posterior distribution effectively.

**Synthetic traces**

Synthetic traces were generated by simulating the Brownian motion of  $K$  particles inside a box with dimensions  $B_{xy} \times B_{xy} \times B_z$  (parallel to the focal plane and along the optical axis). At the beginning of the simulations, particles were randomly seeded in the box following a uniform distribution, and the trajectories were calculated using a specified diffusion coefficient  $D$ . It was ensured that particles could not cross the boundaries and rebounded upon contact. The size of the box was selected to be sufficiently large to avoid interference through long-term cross-correlations of the signal. The interference was tested by estimating the diffusion coefficient using FCS, and the box was increased if the estimated diffusion coefficient was different from the one used in the simulations.

Fluorescence was sampled using Poisson distribution (Eq. 1) with PSF (Eq. 3) focused at the center of the box, incorporating set molecular brightness and background emission rates. Trajectories and fluorescence trace were computed with a time step of 1  $\mu$ s, consistent with the experiments described below. Simulations were implemented in Python using NumPy.

**Simulation parameters**

Used simulation parameters for synthetic trace generation and FITSA are given in tables S2 and S3, respectively. For synthetic traces analyzed in Results, the same background emission rate was used as was applied during trace generation, while experimental data analysis required background estimation. The initial background level was estimated by assuming that approximately half of the detected photons originated from background emissions. This estimate was then refined through visual inspection of signal binning over a short segment of experimental data (typically 2 s). During this inspection, the background level was adjusted to ensure proper detection of signal peaks, characterized by successful binning of visually

identifiable fluorescence intensity increases. The background level was considered appropriately set when the algorithm detected all observed peaks, and this calibrated value was then applied to the entire recording.

For synthetic traces used to test the upper limit of the FITSA detection range, the background level was lowered four times to make sure that particle passages through confocal volume would not be mistaken for background emissions. The parameters governing signal splitting into subsections were selected as follows.  $N_S^{\min}$  was set to 50 sequential bins to prevent formation of excessively short subsections.  $N_S^{\max}$  was assigned a large value (1000) to accommodate cases where particles remained near the confocal volume for extended periods. A split point was established when bin durations exceeded  $\Delta t_S$ . Given the selected  $I_{\text{thr}}$  value of 1 used for binning, this criterion indicated periods without photon detection. We assumed that if no photons were recorded within the millisecond range (1 ms for slower particles and 0.5 ms for faster particles), then the particle had left the vicinity of the focal point, and any subsequent peaks were attributed to different particles. For one specific case with a reduced molecular brightness of 10000 1/s, we increased  $N_S^{\min}$  to 150 to prevent FITSA from splitting the signal into excessively short subsections. The maximal number of bins in subsection  $N_S^{\max}$  was reduced to 200 in the analysis of 1 nM dextran diffusion in water to prevent merging of the segments. This parameter combination provided FITSA with sufficient flexibility to accurately recover diffusion coefficients across the wide range of values investigated in this study.

**Fluorescence correlation spectroscopy**

The FCS data were analyzed by fitting the ACF with a model corresponding to 3D free diffusion of a fluorescent particle without triplet states (46). Here, ACF  $G(\tau)$  (2, 46) was found from the experimental fluorescence trace

$$G(\tau) = \frac{\langle \delta I(t)\delta I(t+\tau) \rangle}{\langle I(t) \rangle^2} \tag{8}$$

where  $\delta$  denotes fluctuations, and  $\tau$  is the lag time.

For a single component diffusing in three dimensions, without considering the triplet state,  $G(\tau)$  is

$$G(\tau) = \frac{1}{V_{\text{eff}} \langle C \rangle} \frac{1}{1 + \frac{4D\tau}{\omega_{xy}^2}} \frac{1}{\sqrt{1 + \frac{4D\tau}{\omega_z^2}}} \tag{9}$$

where  $\langle C \rangle$  is the average concentration of fluorescent molecules in the focal volume, and  $V_{\text{eff}}$  is the effective focal volume (1). The effective volume is defined by PSF (Eq. 3)

$$V_{\text{eff}} = \frac{\int \int \text{PSF}(r) dV}{\int \text{PSF}^2(r) dV} \tag{10}$$

where integration is performed around the focal point (47). When analyzed considering the contribution of the triplet state, the compensation factor

$$1 + \frac{T}{1-T} \exp\left(-\frac{\tau}{\tau_T}\right) \tag{11}$$

was incorporated into  $G(\tau)$  as in (1, 8). Here,  $T$  is the fraction of molecules in triplet state and  $\tau_T$  is the triplet state relaxation time.

In this work, FCS analysis was applied to relatively short segments. Unless specified otherwise, to prevent bias in estimating the diffusion coefficient, we implemented corrections accounting for shot noise and photon count correlations within the segment (23). The second-order binning function used to correct photon counts within the segment for the 3D observation volume was taken from (48).

To compare estimated diffusion coefficients between FITSA and FCS, a Bayesian approach was used to fit ACF with the model, as described in (15). The fits were conducted either by assuming that ACF consists of independent individual measurements or by using a general multivariate Gaussian distribution with covariance (15). Wide, noninformative priors were used for the diffusion coefficient and concentration.

The FCS models were implemented in Python using three different approaches. Least-squares fitting with the Trust Region Reflective algorithm (49) was used for the analysis presented in Fig. 6E. For Bayesian analyses, we used either UltraNest (50) or PyMC (51) implementations. The UltraNest implementation was used for analyses shown in Figs. 2, 6B, 7, and 8, while the PyMC implementation was applied to all other analyses, specifically those considering ACF covariance.

**Experiments**

**Confocal setup**

Measurements were performed using a custom confocal setup described in (8) using a water-immersion 60x objective (UPLSAPO; numerical aperture, 1.2; Olympus). For diffusion measurements, a 633-nm laser (05-LHP-151, Melles Griot, US) was focused on the sample. Emission was detected through a long-pass filter (F76-631, Semrock, Rochester, NY) by an avalanche photodiode (SPCM-AQRH-54, Excelitas Technologies, Pittsburgh, PA) and recorded by a data acquisition card (PCIe-6353, National Instruments, Austin, TX) every 1  $\mu$ s. For imaging mitochondria, a 488-nm laser (0488L-11A-NI-NT-NE, Integrated Optics UAB, Lithuania) was used to excite MitoTracker Green-stained cells and emission was collected through a 550/88-nm filter (FF01-550/88-25, Semrock, Rochester, NY) at a sampling rate of 10  $\mu$ s.

**Experiments on solutions**

Experiments were performed using Alexa Fluor 647 Dextran 10K in water or glycerol/water mix at room temperature (22°C). Used concentrations were 1 and 0.1 nM, diluted in the presence of 0.5% Tween-20, as suggested in (52).

**Experiments on cardiomyocytes**

All animal procedures were carried out according to the guidelines of Directive 2010/63/EU of the European Parliament on the protection of animals used for scientific purposes and had been approved by the Project Authorisation Committee for Animal Experiments in the Estonian Ministry of Rural Affairs (permission no 1.2-17/169, 2023).

Freshly isolated rat (Wistar Han, female, 257 days old; animal supplier: Envigo RMS, 5961 NM Horst, the Netherlands) ventricular cardiomyocytes used to determine diffusion coefficients in different locations in the cell. Cells were isolated as described in (53). Before a measurement, isolated cells were first stained with MitoTracker Green FM (M7514, Invitrogen, Eugene, OR) with a final concentration of 250 nM for 10 min to label mitochondria. Then, stained cells were placed in a reusable silicon insert (94.6077.434, flexiPERM, SARSTEDT AG & Co. KG, Nümbrecht, Germany)

attached to a coverslip containing intracellular fluid mimicking solution. The solution contained 0.5 mM EGTA, 3.0 mM  $\text{KH}_2\text{PO}_4$ , 3.0 mM  $\text{MgCl}_2$ , 20 Hepes, 110 mM sucrose, 20 mM taurine, 0.5 mM dithiothreitol, 60 mM lactobionate, 5 mM glutamate, 2 mM malate, 5.0 mM MgATP, 10 mM PCR, and 10 nM Alexa Fluor 647 Dextran 10K. In addition, bovine serum albumin (5 mg/ml) was added, and pH was adjusted to 7.1 at 25°C with KOH.

After about 5 min of cell sedimentation in the silicon insert under the microscope, a cell attached to the coverslip was located. The outer membrane of the cell was then mechanically permeated using a glass microneedle, which was controlled by a micromanipulator (SMXS-K-L-EUR, Sensapex, Oulu, Finland). The microneedle, with a tip size of around 0.5  $\mu\text{m}$ , was made from 1.0-mm-diameter glass rods (TW100F-3, World Precision Instruments, Sarasota, US) using a pipette puller (PC-10, Narishige, Japan). Following the permeation, the internal and external environments of the cell were allowed to equilibrate for 5 min. First, a confocal image of adult rat cardiomyocyte mitochondria was recorded, after which different locations inside the cell were selected for diffusion measurements.

### PSF estimation

The microsphere slides for measuring PSFs were prepared as in (54). Briefly, a 10,000-fold dilution of the original suspension of microspheres (TetraSpeck, T7279, Invitrogen, Eugene, OR) was made using water. A small drop of this diluted solution was then placed on a cover glass with a thickness of 0.17 mm and allowed to air dry. Once the sample was dry, a small drop of immersion oil (Carl Zeiss Immersol W, Oberkochen, Germany), with a refractive index of 1.334 at 23°C, was added to the spot and secured with a glass slide.

Under the microscope, an area containing several microspheres was selected so that Airy patterns would not overlap on either side of the focus. For measurement, the voxel size in the  $xy$  plane was set to less than 40 nm and, in the  $z$  plane, it was 100 nm, and several  $z$ -stacks were recorded. From the  $z$ -stacks, point sources were identified and averaged according to center positions found from the least-square fitting with Eq. 3. Last, the average point source was fitted with Eq. 3 to determine the PSF lateral waist and axial waist used in analysis.

### Statistics

If not stated otherwise, statistics are reported using the means  $\pm$  SD. For experiments repeated on the same location several times, we used linear mixed models to quantify the impact of the fixed factors. The models were composed with random intercepts, location considered as random factor. To determine the significance of the fixed factor(s) and their interaction(s), we composed models with and without the corresponding factor and  $P$  values were obtained by the likelihood ratio test of the full and simplified models. Statistical analysis was performed in R using lme4 (55) for linear mixed model analysis.  $P < 0.05$  was considered statistically significant.

### Use of artificial intelligence tools

Text was edited with the assistance of large language models: Claude 3.5 Sonnet (Anthropic, San Francisco, CA) and ChatGPT 4.0 (OpenAI, San Francisco, CA). Artificial intelligence tools were used for correcting grammar and improving the clarity of the text sections. The full prompt used was as follows: "I would like to ask you to help with English and edit text for clarity if needed," with the corresponding text added after this prompt. Before incorporating any artificial intelligence-suggested changes into the manuscript,

all proposed edits were reviewed by the authors to ensure that the original meaning was preserved.

### Supplementary Materials

This PDF file includes:

Figs. S1 to S8

Tables S1 to S3

### REFERENCES AND NOTES

- E. P. Petrov, P. Schwille, "State of the art and novel trends in fluorescence correlation spectroscopy" in *Standardization and Quality Assurance in Fluorescence Measurements II: Bioanalytical and Biomedical Applications*, U. Resch-Genger, Ed., Springer Series on Fluorescence (Springer, 2008), pp. 145–197.
- E. L. Elson, Fluorescence correlation spectroscopy: Past, present, future. *Biophys. J.* **101**, 2855–2870 (2011).
- K. Bacia, S. A. Kim, P. Schwille, Fluorescence cross-correlation spectroscopy in living cells. *Nat. Methods* **3**, 83–89 (2006).
- P. Schwille, F. J. Meyer-Almes, R. Rigler, Dual-color fluorescence cross-correlation spectroscopy for multicomponent diffusional analysis in solution. *Biophys. J.* **72**, 1878–1886 (1997).
- K. M. Berland, P. T. So, E. Gratton, Two-photon fluorescence correlation spectroscopy: Method and application to the intracellular environment. *Biophys. J.* **68**, 694–701 (1995).
- M. A. Digman, P. Sengupta, P. W. Wiseman, C. M. Brown, A. R. Horwitz, E. Gratton, Fluctuation correlation spectroscopy with a laser-scanning microscope: Exploiting the hidden time structure. *Biophys. J.* **88**, L33–L36 (2005).
- M. Vendelin, R. Birkedal, Anisotropic diffusion of fluorescently labeled ATP in rat cardiomyocytes determined by raster image correlation spectroscopy. *Am. J. Physiol. Cell Physiol.* **295**, C1302–C1315 (2008).
- A. Illaste, M. Laasmaa, P. Peterson, M. Vendelin, Analysis of molecular movement reveals lattice-like obstructions to diffusion in heart muscle cells. *Biophys. J.* **102**, 739–748 (2012).
- J. W. Krieger, A. P. Singh, N. Bag, C. S. Garbe, T. E. Saunders, J. Langowski, T. Wohland, Imaging fluorescence (cross-) correlation spectroscopy in live cells and organisms. *Nat. Protoc.* **10**, 1948–1974 (2015).
- C. Di Rienzo, E. Gratton, F. Beltram, F. Cardarelli, Fast spatiotemporal correlation spectroscopy to determine protein lateral diffusion laws in live cell membranes. *Proc. Natl. Acad. Sci. U.S.A.* **110**, 12307–12312 (2013).
- J. N. Weiss, P. Korge, The cytoplasm: No longer a well-mixed bag. *Circ. Res.* **89**, 108–110 (2001).
- R. Birkedal, M. Laasmaa, M. Vendelin, The location of energetic compartments affects energetic communication in cardiomyocytes. *Front. Physiol.* **5**, 376 (2014).
- K. Luby-Phelps, The physical chemistry of cytoplasm and its influence on cell function: An update. *Mol. Biol. Cell* **24**, 2593–2596 (2013).
- J. Icha, M. Weber, J. C. Waters, C. Norden, Phototoxicity in live fluorescence microscopy, and how to avoid it. *Bioessays* **39**, 1700003 (2017).
- J. He, S.-M. Guo, M. Bathe, Bayesian approach to the analysis of fluorescence correlation spectroscopy data I: Theory. *Anal. Chem.* **84**, 3871–3879 (2012).
- S.-M. Guo, J. He, N. Monnier, G. Sun, T. Wohland, M. Bathe, Bayesian approach to the analysis of fluorescence correlation spectroscopy data II: Application to simulated and in vitro data. *Anal. Chem.* **84**, 3880–3888 (2012).
- G. Sun, S.-M. Guo, C. Teh, V. Korzh, M. Bathe, T. Wohland, Bayesian model selection applied to the analysis of fluorescence correlation spectroscopy data of fluorescent proteins in vitro and in vivo. *Anal. Chem.* **87**, 4326–4333 (2015).
- J. Kohler, K.-H. Hur, J. D. Mueller, Statistical analysis of the autocorrelation function in fluorescence correlation spectroscopy. *Biophys. J.* **123**, 667–680 (2012).
- S. Jazani, I. Sgouralis, S. Pressé, A method for single molecule tracking using a conventional single-focus confocal setup. *J. Chem. Phys.* **150**, 114108 (2019).
- S. Jazani, I. Sgouralis, O. M. Shafraz, M. Levitus, S. Sivasankar, S. Pressé, An alternative framework for fluorescence correlation spectroscopy. *Nat. Commun.* **10**, 3662 (2019).
- M. Tavakoli, S. Jazani, I. Sgouralis, O. M. Shafraz, S. Sivasankar, B. Donaphon, M. Levitus, S. Pressé, Pitching single-focus confocal data analysis one photon at a time with Bayesian nonparametrics. *Phys. Rev. X* **10**, 011021 (2020).
- S. Jazani, L. W. Q. Xu, I. Sgouralis, D. P. Shepherd, S. Pressé, Computational proposal for tracking multiple molecules in a multifocus confocal setup. *ACS Photonics* **9**, 2489–2498 (2022).
- J. Kohler, K.-H. Hur, J. D. Mueller, Autocorrelation function of finite-length data in fluorescence correlation spectroscopy. *Biophys. J.* **122**, 241–253 (2023).
- A. Vehtari, A. Gelman, D. Simpson, B. Carpenter, P.-C. Bürkner, Rank-normalization, folding, and localization: An improved  $\hat{R}$  for assessing convergence of MCMC (with discussion). *Bayesian Anal.* **16**, 667–718 (2021).

25. P. Xia, P. M. Bungay, C. C. Gibson, O. N. Kovbansjuk, K. R. Spring, Diffusion coefficients in the lateral intercellular spaces of Madin-Darby canine kidney cell epithelium determined with caged compounds. *Biophys. J.* **74**, 3302–3312 (1998).
26. F. Meunier, K. J. Wilkinson, Nonperturbing fluorescent labeling of polysaccharides. *Biomacromolecules* **3**, 857–864 (2002).
27. S. Noel, J. Buffle, N. Fatin-Rouge, J. Labille, Factors affecting the flux of macromolecular, labile, metal complexes at consuming interfaces, in water and inside agarose gel: SSCP study and environmental implications. *J. Electroanal. Chem.* **595**, 125–135 (2006).
28. P. Simson, N. Jephthina, M. Laasmaa, P. Peterson, R. Birkedal, M. Vendelin, Restricted ADP movement in cardiomyocytes: Cytosolic diffusion obstacles are complemented with a small number of open mitochondrial voltage-dependent anion channels. *J. Mol. Cell. Cardiol.* **97**, 197–203 (2016).
29. M. Richards, O. Lomas, K. Jalink, K. L. Ford, R. D. Vaughan-Jones, K. Lefkimiatis, P. Swietach, Intracellular tortuosity underlies slow cAMP diffusion in adult ventricular myocytes. *Cardiovasc. Res.* **110**, 395–407 (2016).
30. Y. Chen, J. D. Müller, P. T. C. So, E. Gratton, The photon counting histogram in fluorescence fluctuation spectroscopy. *Biophys. J.* **77**, 553–567 (1999).
31. P. Kask, K. Palo, D. Ullmann, K. Gall, Fluorescence-intensity distribution analysis and its application in biomolecular detection technology. *Proc. Natl. Acad. Sci. U.S.A.* **96**, 13756–13761 (1999).
32. F. Meng, H. Ma, A comparison between photon counting histogram and fluorescence intensity distribution analysis. *J. Phys. Chem. B* **110**, 25716–25720 (2006).
33. K. Palo, U. Mets, S. Jäger, P. Kask, K. Gall, Fluorescence intensity multiple distributions analysis: Concurrent determination of diffusion times and molecular brightness. *Biophys. J.* **79**, 2858–2866 (2000).
34. S. Hou, J. Exell, K. Welsher, Real-time 3D single molecule tracking. *Nat. Commun.* **11**, 3607 (2020).
35. K. McHale, A. J. Berglund, H. Mabuchi, Quantum dot photon statistics measured by three-dimensional particle tracking. *Nano Lett.* **7**, 3535–3539 (2007).
36. V. Levi, Q. Ruan, E. Gratton, 3-D particle tracking in a two-photon microscope: Application to the study of molecular dynamics in cells. *Biophys. J.* **88**, 2919–2928 (2005).
37. M. Hirsch, R. J. Wareham, M. L. Martin-Fernandez, M. P. Hobson, D. J. Rolfe, A stochastic model for electron multiplication charge-coupled devices – From theory to practice. *PLOS ONE* **8**, e53671 (2013).
38. M. Fazel, K. S. Grussmayer, B. Ferdman, A. Radenovic, Y. Shechtman, J. Enderlein, S. Pressé, Fluorescence microscopy: A statistics-optics perspective. *Rev. Mod. Phys.* **96**, 025003 (2024).
39. B. Zhang, J. Zerubia, J.-C. Olivo-Marin, Gaussian approximations of fluorescence microscope point-spread function models. *Appl. Optics* **46**, 1819–1829 (2007).
40. C. H. Ziener, T. Kampf, F. T. Kurz, Diffusion propagators for hindered diffusion in open geometries. *Concepts Magn. Reson. Part A* **44**, 150–159 (2015).
41. D. Phan, N. Pradhan, M. Jankowiak, Composable effects for flexible and accelerated probabilistic programming in NumPyro. arXiv:1912.11554 (2019).
42. E. Bingham, J. P. Chen, M. Jankowiak, F. Obermeyer, N. Pradhan, T. Karaletsos, R. Singh, P. Szerlip, P. Horsfall, N. D. Goodman, Pyro: Deep universal probabilistic programming. *J. Mach. Learn. Res.* **20**, 1–6 (2019).
43. R. Kumar, C. Carroll, A. Hartikainen, O. Martin, ArviZ a unified library for exploratory analysis of Bayesian models in Python. *J. Open Source Softw.* **4**, 1143 (2019).
44. M. Betancourt, A conceptual introduction to Hamiltonian Monte Carlo. arXiv:1701.02434 (2018).
45. M. Betancourt, Diagnosing suboptimal cotangent disintegrations in Hamiltonian Monte Carlo. arXiv:1604.00695 (2016).
46. P. Schwille, E. Haustein, “Fluorescence correlation spectroscopy - An introduction to its concepts and applications” in *Biophysics Textbook Online* (Biophysical Society, 2001), pp. 1–33.
47. S. T. Hess, W. W. Webb, Focal volume optics and experimental artifacts in confocal fluorescence correlation spectroscopy. *Biophys. J.* **83**, 2300–2317 (2002).
48. J. D. Müller, Cumulant analysis in fluorescence fluctuation spectroscopy. *Biophys. J.* **86**, 3981–3992 (2004).
49. M. A. Branch, T. F. Coleman, Y. Li, A subspace, interior, and conjugate gradient method for large-scale bound-constrained minimization problems. *SIAM J. Sci. Comput.* **21**, 1–23 (1999).
50. J. Buchner, UltraNest – A robust, general purpose Bayesian inference engine. arXiv:2101.09604 (2021).
51. O. Abril-Pla, V. Andreani, C. Carroll, L. Dong, C. J. Fannesbeck, M. Kochurov, R. Kumar, J. Lao, C. C. Luhmann, O. A. Martin, M. Osthege, R. Vieira, T. Wiecki, R. Zinkov, PyMC: A modern, and comprehensive probabilistic programming framework in Python. *PeerJ Comput. Sci.* **9**, e1516 (2023).
52. V. Buschmann, B. Krämer, F. Koberling, R. Macdonald, S. Rüttinger, “Quantitative FCS: Determination of the confocal volume by FCS and bead scanning with the MicroTime 200,” in *Application Note: Quantitative FCS v. 1.1* (PicoQuant GmbH, 2009).
53. M. Frisk, J. T. Koivumäki, P. A. Norseng, M. M. Maleckar, O. M. Sejersted, W. E. Louch, Variable t-tubule organization and Ca<sup>2+</sup> homeostasis across the atria. *Am. J. Physiol. Heart Circ. Physiol.* **307**, H609–H620 (2014).
54. M. Laasmaa, M. Vendelin, P. Peterson, Application of regularized Richardson-Lucy algorithm for deconvolution of confocal microscopy images. *J. Microsc.* **243**, 124–140 (2011).
55. D. Bates, M. Mächler, B. Bolker, S. Walker, Fitting linear mixed-effects models using lme4. *J. Stat. Softw.* **67**, 1–48 (2015).

**Acknowledgments:** We would like to acknowledge R. Birkedal, J. Branovets, and I. Česnokova (Laboratory of Systems Biology, Department of Cybernetics, Tallinn University of Technology) for providing cardiomyocytes. Some simulations were carried out in the High Performance Computing Center of TalTech. Text was edited with the assistance of large language models: Claude (Anthropic, San Francisco, CA) and ChatGPT (OpenAI, San Francisco, CA). **Funding:** This work was supported by the Estonian Research Council (PRG1127). **Author contributions:** Conceptualization: H.K., M.L., M.P., and M.V. Methodology: H.K. and M.V. Software: H.K. and M.V. Validation: H.K. and M.V. Formal analysis: H.K. and M.V. Experiments: H.K., M.L., and M.V. Resources: H.K., M.L., and M.V. Data curation: H.K. and M.V. Visualization: H.K. and M.V. Writing—original draft: M.V. Writing—review and editing: H.K., M.L., and M.V. Supervision: M.L. and M.V. Project administration: M.V. Funding acquisition: M.V. **Competing interests:** The authors declare that they have no competing interests. **Data and materials availability:** All data needed to evaluate the conclusions in the paper are present in the paper and/or the Supplementary Materials. The datasets generated and analyzed during the current study are available via archive <https://doi.org/10.5061/dryad.80gb5mm11>. FITSA implementation is available at <https://github.com/iocbio/fitisa> under the GNU General Public License version 3 (GPLv3). The software version used in this study is also available at the archive <https://doi.org/10.5281/zenodo.14742211>.

Submitted 14 August 2024

Accepted 13 March 2025

Published 18 April 2025

10.1126/sciadv.ads4609

# Curriculum Vitae

## Personal Data

Name Hamed Karimi  
Date of birth 5 February 1993  
Place of birth Mahabad, Iran  
Nationality Iranian

## Contact Information

Address Tallinn University of Technology, School of Science,  
Department of Cybernetics,  
Akadeemia tee 15, 12618 Tallinn, Estonia  
E-mail hamed@sysbio.ioc.ee

## Education

2022–2026 Tallinn University of Technology, School of Science, Estonia,  
Applied Physics and Data Science, PhD  
2017–2020 University of Kurdistan, Faculty of Science, Iran,  
Physics, Fundamental–Theoretical, MSc  
2012–2017 Bu–Alisina University, Faculty of Science, Iran,  
Nuclear Physics, BSc

## Language Competence

English Fluent  
Kurdish native  
Persian native

## Defended Theses

- 2020, Entropic Splitter for Particle Separation, MSc, supervisor: Prof. Mohammad Reza Setare, University of Kurdistan, Faculty of Science, Iran

## Supervised Dissertation

- 2025, Otto Gustavson, Master's thesis, "Studies of diffusion in cardiac muscle cells"
- 2023, Kaarel Beljaev, Bachelor's thesis, "Diffusion in fixed cardiomyocytes"

## Publications

1. **Hamed Karimi**, Otto Gustavson, Irina Česnokova, Jelena Branovets, Rikke Birkedal, Martin Laasmaa, and Marko Vendelin. A Unified Platform for FCS and RICS Analysis with Advanced Statistical Inference. *ACS Omega*, 2026
2. **Hamed Karimi**, Martin Laasmaa, Margus Pihlak, and Marko Vendelin. Statistical analysis of fluorescence intensity transients with Bayesian methods. *Science Advances*, 11(16):eads4609, 2025

3. Robert Risti, Kathryn H. Gunn, Kristofer Hiis-Hommuk, Natjan-Naatan Seeba, **Hamed Karimi**, Ly Villo, Marko Vendelin, Saskia B. Neher, and Aivar Lõokene. Combined action of albumin and heparin regulates lipoprotein lipase oligomerization, stability, and ligand interactions. *PLOS ONE*, 18(4):e0283358, 2023
4. **Hamed Karimi**, Mohammad Reza Setare, and Ali Moradian. Rod Separation by Sawtooth Channel, *Phys. Rev. E* 102, 012610, 2020

### Conferences

- 2025      15th European Biophysics CONGRESS, Rome, Italy,  
from the 30th of June to the 4th of July 2025,  
Oral presentation: FITSA: A Robust Bayesian Method for Analysis of  
Detected Photons in Single-Molecule Measurements
- 2025      Nordic Computational Biology Conference 2025, Tallinn, Estonia,  
October 23-24th, 2025,  
Poster presentation: Beyond FCS: Bayesian Single-Molecule Analysis with FITSA

### Awards

- 2026      Best Research Article of the Year (2025) in the Field of Engineering and  
Technology, TalTech, Article: Karimi et al (Sci Adv 2025)
- 2025      EBSA Bursary, European Biophysics Societies Association Fellowship

# Elulookirjeldus

## Isikuandmed

Nimi Hamed Karimi  
Sünniaeg 5. veebruar 1993  
Sünnikoht Mahabad, Iraan  
Kodakondsus Iraani

## Kontaktandmed

Aadress Tallinna Tehnikaülikool, Loodusteaduskond,  
Küberneetika instituut,  
Akadeemia tee 15, 12618 Tallinn, Eesti  
E-post hamed@sysbio.ioc.ee

## Haridus

2022–2026 Tallinna Tehnikaülikool, Loodusteaduskond, Eesti,  
Rakendusfüüsika ja andmeteadus, PhD  
2017–2020 Kurdistani Ülikool, Loodusteaduskond, Iraan,  
Füüsika, fundamentaal-teoreetiline, MSc  
2012–2017 Bu–Alisina Ülikool, Loodusteaduskond, Iraan,  
Tuumafüüsika, BSc

## Keelteoskus

Inglise keel sorav  
Kurdi keel emakeel  
Pärsia keel emakeel

## Teenistuskäik

- 2020, Entropic Splitter for Particle Separation, magistritöö, juhendaja: prof. Mohammad Reza Setare, Kurdistani Ülikool, Loodusteaduskond, Iraan

## 9. Kaitstud lõputööd

- 2025, Otto Gustavson, magistritöö, “Difusiooni uuringud südamelihaskudedes”
- 2023, Kaarel Beljaev, bakalaureusetöö, “Difusioon fikseeritud südamelihaskudedes”

## Publikatsioonid

1. **Hamed Karimi**, Otto Gustavson, Irina Česnokova, Jelena Branovets, Rikke Birkedal, Martin Laasmaa, and Marko Vendelin. A Unified Platform for FCS and RICS Analysis with Advanced Statistical Inference. *ACS Omega*, 2026
2. **Hamed Karimi**, Martin Laasmaa, Margus Pihlak, and Marko Vendelin. Statistical analysis of fluorescence intensity transients with Bayesian methods. *Science Advances*, 11(16):eads4609, 2025
3. Robert Risti, Kathryn H. Gunn, Kristofer Hiis-Hommuk, Natjan-Naatan Seeba, **Hamed Karimi**, Ly Villo, Marko Vendelin, Saskia B. Neher, and Aivar Löökene. Combined action of albumin and heparin regulates lipoprotein lipase oligomerization, stability, and ligand interactions. *PLOS ONE*, 18(4):e0283358, 2023

4. **Hamed Karimi**, Mohammad Reza Setare ja Ali Moradian. Rod Separation by Sawtooth Channel, *Phys. Rev. E* 102, 012610, 2020

### **Konverentsid**

- 2025 15. Euroopa Biofüüsika Kongress, Rooma, Itaalia,  
30. juunist kuni 4. juulini 2025,  
Suuline ettekanne: FITSA: A Robust Bayesian Method for Analysis of  
Detected Photons in Single-Molecule Measurements
- 2025 Nordic Computational Biology Conference 2025, Tallinn, Eesti,  
23.-24. oktoober 2025,  
Posterisitlus: Beyond FCS: Bayesian Single-Molecule Analysis with FITSA

### **Auhinnad**

- 2026 Aasta parim teadusartikkel (2025) tehnika ja tehnoloogia valdkonnas,  
TalTech, Artikkel: Karimi et al (Sci Adv 2025)
- 2025 EBSA stipendium, Euroopa Biofüüsika Seltside Assotsiatsioon stipendium

ISSN 2585-6901 (PDF)  
ISBN 978-9916-80-492-6 (PDF)